Variational multiscale stabilization and local preconditioning for compressible flow

PhD Thesis by

Margarida Moragues Ginard

Thesis supervisor

Dr. Mariano Vázquez

Submitted to

Universitat Politècnica de Catalunya

Barcelona, November 2015

Panta rhei, "Everything flows"

aphorism attributed to Heraclitus

Abstract

This thesis is about the stabilization of the numerical solution of the Euler and Navier-Stokes equations of compressible flow. When simulating numerically the flow equations, if no stabilization is added, the solution presents non-physical (but numerical) oscillations. For this reason the stabilization of partial differential equations and of the fluid dynamics equations is of great importance. In the framework of the so-called variational multiscale stabilization, we present here a stabilization method for compressible flow. The method assessment is done first of all on a batch of academic examples for different Mach numbers, for viscous and inviscid, steady and transient flow. Afterwards the method is applied to atmospheric flow simulations. To this end we solve the Euler equations for dry and moist atmospheric flow. In the presence of moisture a set of transport equations for water species should be solved as well. This domain of application is a real challenge from the stabilization point of view because the correct amount of stabilization must be added in order to preserve the physical properties of the atmospheric flow. At this point, in order to even improve our method, we turn towards local preconditioning. Local preconditiong permits to reduce the stiffness problems that present the flow equations and cause a bad and slow convergence to the solution. With this purpose in mind we combine our stabilization method with local preconditioning and present a stabilization method for the preconditioned Navier-Stokes equations of compressible flow, that we call P-VMS. This method is tested over several examples at different Mach numbers and proves a significant improvement not only in the convergence to the solution but also in the accuracy and robustness of the method. Finally, the benefits of P-VMS are theoretically assessed using Fourier stability analysis. As a result of this analysis a modification on the computation of the time step is done even improving the convergence of the method.

Publications related to this thesis

International Journals

- M. Moragues, G. Bernardino, M. Vázquez, and G. Houzeaux. Fourier stability analysis and local Courant number of the preconditioned variational multiscale stabilization (P-VMS) for Euler compressible flow. Accepted for publication at Computer Methods in Applied Mechanics and Engineering, 2015

- M. Moragues, M. Vázquez, and G. Houzeaux. Local preconditioning and variational multiscale stabilization for Euler compressible steady flow. Submitted at Computer Methods in Applied Mechanics and Engineering, 2015

- Simone Marras, James F. Kelly, Margarida Moragues, Andreas Müller, Michal A. Kopera, Mariano Vázquez, Francis X. Giraldo, Guillaume Houzeaux, and Oriol Jorba. A review of element-based Galerkin methods for numerical weather prediction: Finite elements, spectral elements, and discontinuous Galerkin. *Archives of Computational Methods in Engineering*, pages 1–50, 2015. ISSN 1134-3060. doi: 10.1007/s11831-015-9152-1. URL http://dx.doi.org/10.1007/s11831-015-9152-1

- Simone Marras, Margarida Moragues, Mariano Vázquez, Oriol Jorba, and Guillaume Houzeaux. Simulations of moist convection by a variational multiscale stabilized finite element method. *Journal of Computational Physics*, 252:195 – 218, 2013b. ISSN 0021-9991. doi: http://dx.doi.org/10.1016/j.jcp.2013.06.006

- Simone Marras, Margarida Moragues, Mariano Vázquez, Oriol Jorba, and Guillaume Houzeaux. A variational multiscale stabilized finite element method for the solution of the Euler equations of nonhydrostatic stratified flows. *Journal of Computational Physics*, 236:380 – 407, 2013a. ISSN 0021-9991. doi: http://dx.doi.org/10.1016/j.jcp.2013.06.006

Conference contributions

- M. Moragues, M. Vázquez, G. Bernardino, and G. Houzeaux. Preconditioned VMS for compressible flow. In *Proceedings: Platform for advanced Scientific Computing Conference PASC*, Zurich, Switzerland, 2015

- M. Vázquez, M. Pérez, M. Moragues, and G. Houzeaux. Parallel monolithic implicit solver for compressible flows. In *Proceedings: PANACM Conference*, Buenos Aires, Argentina, 2015b

- M. Moragues, M. Vázquez, and G. Houzeaux. Preconditioned VMS for compressible flow I: steady problems. In *Proceedings: ECCOMAS CFD Conference*, Barcelona, Spain, 2014a

- M. Moragues, M. Vázquez, and G. Houzeaux. Preconditioned VMS for compressible flow II: transient problems. In *Proceedings: ECCOMAS CFD Conference*, Barcelona, Spain, 2014b

- Margarida Moragues, Simone Marras, Mariano Vázquez, and Guillaume Houzeaux. A variational multiscale stabilized finite element method to solve the Euler equations for nonhydrostatic stratified benchmarks. In *Proceedings: Solution of Partial Differential Equations on the Sphere Workshop (AMMW02), Newton Institute for Mathematical Science*, Cambridge, UK, 2012

- Simone Marras, Margarida Moragues, Mariano Vázquez, Oriol Jorba, and Guillaume Houzeaux. 3D simulations of convective storms using finite elements with variational multiscale stabilization. In *Proceedings: Solution of Partial Differential Equations on the Sphere Workshop (AMMW02), Newton Institute for Mathematical Science*, Cambridge, UK, 2012

- M. Moragues, M. Vázquez, and G. Houzeaux. Variational multiscale stabilization of compressible Navier-Stokes equations. In *Proceedings: Finite Elements in Flow Problems FEF*, Munich, Germany, 2011

- Mariano Vázquez, Simone Marras, Margarida Moragues, Oriol Jorba, Guillaume Houzeaux, and Romain Aubry. A massively parallel variational multiscale FEM scheme applied to nonhydrostatic atmospheric dynamics. In *Proceedings: EGU Annual Meeting, EGU-2010-9060*, Vienna, Austria, 2010

- M. Moragues, M. Vázquez, and G. Houzeaux. Variational multiscale stabilization method for compressible flow. In *Proceedings: Argentinian Congress on Computational Mechanics*, Buenos Aires, Argentina, 2010a

- M. Vázquez, M. Moragues, G. Houzeaux, R. Aubry, and S. Marras. Variational multiscale method for compressible flows. In *Proceedings: ECCOMAS CFD Conference*, Lisbon, Portugal, 2010

- M. Moragues, M. Vázquez, G. Houzeaux, and R. Aubry. Variational multiscale stabilization of compressible flows in parallel architectures. In *Proceedings: Int. Conf. on Parallel CFD*, Kaoshiung, Taiwan, 2010b

Contents

Chapter 1

Introduction

In this thesis we investigate on the stabilization of the Euler and Navier-Stokes equations of compressible fluid dynamics, which represents a crucial subject in the numerical solution of this set of equations and of partial differential equations in general. In particular we concentrate on the variational multiscale stabilization (VMS). We develop a particular stabilization technique that we apply to some selected fluid dynamics benchmarks and to a more realistic case of atmospheric flow simulation. In order to improve the stability and performance of the numerical method, we combine this stabilization technique with two other powerful tools: local preconditioning and Fourier stability analysis.

All the methods developed in this thesis are implemented in Alya, the in-house multi-physics parallel finite elements code, that runs in parallel and scales up to 100000 of processors Casoni et al. [2014], Gövert et al. [2015], Houzeaux et al. [2009, 2014], Puzyrev et al. [2013], Samaniego et al. [2015], Vázquez et al. [2015a]. Our motivation with Alya is to solve efficiently multi-physics problems in large supercomputers, covering a full range of fluid mechanics problems in complex geometries and unstructured meshes.

1.1 VMS for compressible flow

When convection dominates, as it is the case of the Euler and Navier-Stokes equations, the finite elements discretization (2.11) presents some instabilities that should be treated in order to avoid non-physical oscillations or blow-up of the solution Quarteroni and Valli [1994]. These instabilities can be treated by means of different stabilization procedures. The *Streamline Upwind Petrov-Galerkin* (SUPG) Hughes and Mallet [1986b], Hughes and Tezduyar [1984], Le Beau et al. [1993], Tezduyar and Senga [2006] and the *Galerkin/Least-Squares* (GLS) Shakib et al. [1991] are some of the most used stabilization

techniques for finite elements for compressible flow. Due to its high efficiency, robustness, and validity at all Mach regimes, in this paper we focus on the variational multiscale approach pioneered by Hughes [1995], Hughes et al. [1998], and firstly introduced for the advection-diffusion equations. A review of residual-based stabilization methods for compressible flows can be found in Hughes et al. [2010]. A review of the most common stabilization techniques for Galerkin methods are described in a recent article Marras et al. [2015].

In the 90's a group of researchers lead by Hughes proposed a theory to explain the reasons of instabilities and a new way to attack the problem. They state that the instabilities appear because the effect of the unresolved scales is not captured by the numerical method. The unresolved scales is the part of the solution that is under the resolution of the grid and consequently can not be solved by the numerical method. They conclude that the effects of the unresolved scales must be introduced in the formulation of the discrete problem, by modeling them in some way, using the information that we have at the grid scale level. Based on this idea they designed a new stabilization framework, the so-called variational multiscale stabilization method Hughes [1995], Hughes et al. [1998], and applied it to the advection-diffusion equations. This approach allows the development of new schemes but also the understanding of previous stabilization techniques as SUPG, GLS, etc. The VMS method relies on the splitting of the solution into a resolved, large scale component, $\mathbf{\Phi}^h$, and a sub-grid scale, unresolved component, $\tilde{\mathbf{\Phi}}$, to give $\mathbf{\Phi} = \mathbf{\Phi}^h + \tilde{\mathbf{\Phi}}$. The large scale is the part of the unknown that is solved explicitely, while the subscale as well as its effect on the large scale problem are modeled by the VMS method.

VMS has been widely applied to advection-diffusion-reaction problems (e.g. Codina and Blasco [2002], Corsini et al. [2005], Houzeaux et al. [2009], Hughes [1995], Hughes et al. [1998]) as well as to the incompressible Navier-Stokes equations (e.g. Avila et al. [2014], Bazilevs et al. [2007], Codina [2002], Gravemeier [2003], Hughes et al. [2000]). Its application to compressible flow is more restricted. To our knowledge, VMS for compressible flows appears in Rispoli and Saavedra [2006], Rispoli et al. [2007], for computational fluid dynamics (CFD) simulations. A hybrid VMS for large eddy simulation of turbulent compressible flows can be found in Collis and Chang [2002], Farhat et al. [2006], Koobus and Charbel [2004], Levasseur et al. [2006], Ouvrard et al. [2010], and van der Bos et al. [2007], this represents a different approach of VMS.

A VMS method for the Euler and Navier-Stokes equations of compressible flow is developed in this thesis. This method, with all its different options, is tested through several test cases of viscous and inviscid, steady and transient flow at different Mach numbers.

1.2 Compressible VMS applied to low-Mach problems: atmospheric flows

After its assessment through academic benchmarks, the developed VMS method for compressible flow is applied into the particular domain of atmospheric flow. This work is done in collaboration with an expert in the meteorological field, Simone Marras. Taking profit of his expertise in the physics of the atmosphere, the contribution of the present thesis in this atmospheric flow simulation is on the stabilization and numerical treatment of the problem. The application of the finite elements method and VMS into the field of atmospheric simulations is of especial interest because of the reasons given below.

The past decade has seen an important growth in the development of faster and cheaper supercomputers for high-performance computing (HPC). This trend is such that many research groups can now enhance their models in terms of efficiency and accuracy through higher resolution, by limiting the time of computation. Among many fields of computational mechanics, this is even more so in the context of atmospheric simulations, where the wall-clock time is a discriminant metric in the selection of the underlying algorithm. It has been widely proved that, to effectively see an improvement in computation on these architectures, the numerical algorithm at hand should have certain characteristics. Of these, being local by construction, which implies the smallness of the communication foot-print, is maybe the most important.

The use of finite element schemes in atmospheric simulations began four decades ago with Holmstrom [1963] and Simons [1968] in the 60s. However, as far as we know, VMS for the finite element method is firstly applied to atmospheric flow in our work.

1.3 Compressible VMS and local preconditioning: P-VMS

Local preconditioning is considered in this thesis in order to overcome the stiffness problems that arise as consequence of the bad conditioning of the equations, for example, at very low speeds, as it is the case of the atmospheric simulations. To this end, local preconditioning is combined with the compressible VMS. The compressible VMS is adapted to solve the preconditioned system obtaining a method that we call P-VMS.

As it is well known, the characteristic propagation speeds of the Euler system of equations, $\{cM, c(M+1), c(M-1)\}$, being c the speed of sound and M the Mach number, lead to highly disparate values especially when the Mach number approaches 0 or 1. This disparity is paired with a strong increase in the system's stiffness and a consequent loss

in convergence speed. As this behavior precedes the discretization, it happens regardless of the numerical method that is used.

The goal of local preconditioning is the uniformization of the characteristic propagation speeds of the system. This entails a gain in the convergence speed to a steady state, or to the transient solution at a given time step when a pseudo-time technique Jameson [1991], Merkle and Athavale [1987] is used. Local preconditioning also gives accuracy to the solution as it is shown, for example, in Turkel and Vatsa [2005] for finite difference methods. Local preconditioning is applied to the set of equations before any discretization is done. The extra computational cost is minimal. It consists of transforming the original convective jacobians and diffusive matrices of the Navier-Stokes system into the preconditioned ones, in such a way that the non-preconditioned and the preconditioned equations share the same solution. In the case of steady flow problems, they will have different time evolutions but reach the same steady state.

Based on the idea of artificial compressibility of Chorin Chorin [1967], local preconditioning is first set up by Turkel [1987] for incompressible and low speed compressible flow. Other local preconditioners have been presented since then. *Van Leer-Lee-Roe*'s (VLR) preconditioner is introduced by Lee [1991], van Leer et al. [1991] for Euler steady flow covering a wide range of Mach numbers. It is extended to Navier-Stokes in Lee [1996, 1998a]. In Choi and Merkle [1993], *Choi-Merkle*'s (CM) preconditioner is presented for low Mach number steady flow, suitable for both the Euler and Navier-Stokes equations with a single parameter change. It is extended to transient flows in Nigro et al. [1998]. Weiss and Smith [1995] propose a preconditioner to solve incompressible and variable density transient flows in transonic and low-speed regimes. The diagonal preconditioner defined by Briley et al. [2003] is applicable to unsteady viscous flows, for Mach numbers ranging from essentially incompressible to supersonic. Local preconditioning is independent of the space discretization method; in all the references listed above the finite differences and finite volumes methods are used. In the context of the finite volume discretization, the Roe's flux is adapted to the preconditioned equations, for example, in Darmofal and van Leer [1999], Godfrey et al. [1993] for the VLR preconditioner. For the central difference scheme, the artificial viscosity should be based on the preconditioned equations as well Turkel [1993]. As far as we know, there are two precedents in the use of FE and local preconditioners: Nigro et al. [1998] and López et al. [2012], where CM preconditioner is used for the solution of compressible viscous flow in steady and transient problems, respectively.

1.4 Fourier stability analysis of the compressible P-VMS

In order to theoretically analyze the stiffness reduction that completes the local preconditioning on the discretized system, a Fourier stability analysis of P-VMS is finally done, for the Euler equations of steady flow problems. After this analysis the method is even improved in terms of convergence by defining an alternative way of computing the time steps.

Fourier stability analysis Vichnevetsky and Bowles [1982] represents a basic tool to study the numerical solutions of partial differential equations and it is performed by introducing a discrete Fourier mode in the discretized equations. The purpose of Fourier analysis is to study the nature of the discrete operator, in particular the error propagation that arises during the numerical approximation. The precedents of Fourier stability analysis for the preconditioned Euler and Navier-Stokes equations are in the context of finite volumes and finite differences schemes. See for example Darmofal and van Leer [1998], Godfrey [1994], Lee [1996, 1998a,b, 1991], Lynn and van Leer [1993], van Leer et al. [1991] for the VLR preconditioner, Choi and Merkle [1993] for the CM preconditioner, Allmaras [1993, 1995], Pierce and B. [1996] for the block-Jacobi preconditioner, and Sheng [2010], Wang [2005] for Briley's (Briley et al. [2003]) preconditioner.

1.5 Contributions of this thesis

- A variational multiscale stabilization of the finite element solution of the Euler and Navier-Stokes equations of compressible flow is presented in this work and assessed on different problems for viscous and inviscid, steady and transient flow, for low Mach to supersonic regimes. This method is presented in Chapter 2 of this thesis and presented in different international conferences such as:

  M. Moragues, M. Vázquez, G. Houzeaux, and R. Aubry. Variational multiscale stabilization of compressible flows in parallel architectures. In *Proceedings: Int. Conf. on Parallel CFD*, Kaoshiung, Taiwan, 2010b

- The compressible VMS method is applied to the solution of the compressible Euler equations of dry and moist atmospheric flows, and assessed through several standard benchmarks. In the presence of moisture the Euler equations need to be coupled to a set of transport equations for water species. In this context, the finite element algorithm proposed here is, at our knowledge, the first continuous Galerkin method with VMS stabilization applied to stratified non-hydrostatic flows. This work is presented in Chapter 3 of this thesis and done in collaboration with Simone Marras, an expert in the physics of the atmosphere. The related publications are:

Simone Marras, James F. Kelly, Margarida Moragues, Andreas Müller, Michal A. Kopera, Mariano Vázquez, Francis X. Giraldo, Guillaume Houzeaux, and Oriol Jorba. A review of element-based Galerkin methods for numerical weather prediction: Finite elements, spectral elements, and discontinuous Galerkin. *Archives of Computational Methods in Engineering*, pages 1–50, 2015. ISSN 1134-3060. doi: 10.1007/s11831-015-9152-1. URL http://dx.doi.org/10.1007/s11831-015-9152-1

Simone Marras, Margarida Moragues, Mariano Vázquez, Oriol Jorba, and Guillaume Houzeaux. Simulations of moist convection by a variational multiscale stabilized finite element method. *Journal of Computational Physics*, 252:195 – 218, 2013b. ISSN 0021-9991. doi: http://dx.doi.org/10.1016/j.jcp.2013.06.006

Simone Marras, Margarida Moragues, Mariano Vázquez, Oriol Jorba, and Guillaume Houzeaux. A variational multiscale stabilized finite element method for the solution of the Euler equations of nonhydrostatic stratified flows. *Journal of Computational Physics*, 236:380 – 407, 2013a. ISSN 0021-9991. doi: http://dx.doi.org/10.1016/j.jcp.2013.06.006

- P-VMS method is developed: compressible VMS is combined with local preconditioning, improving the convergence, accuracy and robustness of the method for all Mach regimes. Its performance is assessed for compressible flow problems including viscous and inviscid, transient and steady flow, for a wide range of Mach numbers. P-VMS is presented in Chapter 4 of this thesis and submitted for publication in:

  M. Moragues, M. Vázquez, and G. Houzeaux. Local preconditioning and variational multiscale stabilization for Euler compressible steady flow. Submitted at Computer Methods in Applied Mechanics and Engineering, 2015

- Fourier stability analysis of P-VMS for Euler steady flow is performed in order to study its behavior in terms of error propagation and convergence. As consequence a local Courant-Friedrichs-Lewy (CFL) number (computed using local parameters) is defined improving even more the convergence of P-VMS method. The benefits of the local CFL compared to the constant one are assessed through numerical examples covering a large range of Mach numbers. This analysis is presented in Chapter 5 of this thesis and accepted for plublication in:

  M. Moragues, G. Bernardino, M. Vázquez, and G. Houzeaux. Fourier stability analysis and local Courant number of the preconditioned variational multiscale stabilization (P-VMS) for Euler compressible flow. Accepted for publication at Computer Methods in Applied Mechanics and Engineering, 2015

Chapter 2

VMS for compressible flow

In this chapter we present a variational multiscale stabilization for the finite element numerical solution of the Euler and Navier-Stokes equations of compressible flow. We propose two versions of variational multiscale stabilization. The first version is a straight adaptation of what is set in Codina [2002] in the context of the advection-diffusion equation. The second version, inspired by what is done in Codina and Blasco [2002], uses the Fourier transform in order to model the stabilization parameter, but without assuming the classical structure of τ times the residual. We compare these two versions of the numerical method through several benchmark cases of different complexity in viscous and inviscid flows, covering a wide range of Mach numbers.

2.1 Navier-Stokes equations

Let d be the space dimension that we take to be two or three in this work. From the conservation principles of momentum, mass, and energy result the Navier-Stokes equations, which can be written in three dimensions in conservative form as follows:

$$\frac{\partial \boldsymbol{\Phi}}{\partial t} + \frac{\partial \mathbf{F}^i(\boldsymbol{\Phi})}{\partial x_i} = 0 \,, \tag{2.1}$$

for $i = 1, \ldots, d$ which labels the space dimension. We use the Einstein summation convention that implies summation over repeated indexes in the same term. We take in (2.1) the conservative set of unknowns or conservative variables that in three dimensions read:

$$\boldsymbol{\Phi} = (U_1 \; U_2 \; U_3 \; \rho \; E)^{\mathrm{T}} \,, \tag{2.2}$$

where $\mathbf{U} = (U_1, U_2, U_3)$ is the momentum, ρ is the density, and E is the total energy per unit volume, all of them are functions of space $\mathbf{x} = (x_1, x_2, x_3)$ and time t. The superscript $^{\mathrm{T}}$ represents the transposed vector. For a comparative of different sets of variables for the solution of compressible and incompressible flow, refer to Hauke and Hughes [1998]. Other important physical variables are: the velocity $\mathbf{u} = \frac{\mathbf{U}}{\rho}$, the temperature $T = i/c_v = \frac{1}{c_{\mathrm{v}}\rho}(E - \frac{1}{2}\frac{U_k U_k}{\rho})$, the internal energy per unit mass $i = e - \frac{1}{2}\|\mathbf{u}\|^2$, the total energy per unit mass $e = \frac{E}{\rho}$, the Mach number $M = \frac{\|\mathbf{u}\|}{c}$, the speed of sound $c = \sqrt{\gamma \frac{p}{\rho}}$, the pressure $p = \rho R T = \frac{R}{c_{\mathrm{v}}}(E - \frac{1}{2}\frac{U_k U_k}{\rho})$, the constant of perfect gases $R = c_{\mathrm{p}} - c_{\mathrm{v}}$, the specific heat ratio $\gamma = \frac{c_{\mathrm{p}}}{c_{\mathrm{v}}}$, and the coefficients of specific heat at constant pressure and volume, c_{p} and c_{v}, respectively. In this work $\|\cdot\|$ represents the L^2 norm. Vectors $\mathbf{F}^i$ in (2.1) are the fluxes, which are the sum of a convective part $\mathbf{F}^{\mathrm{conv,i}}$ and a diffusive part $\mathbf{F}^{\mathrm{diff,i}}$, in three dimensions they write:

$$\mathbf{F}^{\mathrm{conv},1} = \begin{bmatrix} \frac{U_1 U_1}{\rho} + p \\ \frac{U_2 U_1}{\rho} \\ \frac{U_3 U_1}{\rho} \\ U_1 \\ \frac{U_1}{\rho}(E+p) \end{bmatrix}, \quad \mathbf{F}^{\mathrm{conv},2} = \begin{bmatrix} \frac{U_1 U_2}{\rho} \\ \frac{U_2 U_2}{\rho} + p \\ \frac{U_3 U_2}{\rho} \\ U_2 \\ \frac{U_2}{\rho}(E+p) \end{bmatrix}, \quad \mathbf{F}^{\mathrm{conv},3} = \begin{bmatrix} \frac{U_1 U_3}{\rho} \\ \frac{U_2 U_3}{\rho} \\ \frac{U_3 U_3}{\rho} + p \\ U_3 \\ \frac{U_3}{\rho}(E+p) \end{bmatrix}, \tag{2.3}$$

and

$$\mathbf{F}^{\mathrm{diff},1} = \begin{bmatrix} \tau_{11} \\ \tau_{21} \\ \tau_{31} \\ 0 \\ \frac{U_k \tau_{k1}}{\rho} - q_1 \end{bmatrix}, \quad \mathbf{F}^{\mathrm{diff},2} = \begin{bmatrix} \tau_{12} \\ \tau_{22} \\ \tau_{32} \\ 0 \\ \frac{U_k \tau_{k2}}{\rho} - q_2 \end{bmatrix}, \quad \mathbf{F}^{\mathrm{diff},3} = \begin{bmatrix} \tau_{13} \\ \tau_{23} \\ \tau_{33} \\ 0 \\ \frac{U_k \tau_{k3}}{\rho} - q_3 \end{bmatrix}, \tag{2.4}$$

where

$$\begin{aligned} \tau_{ij} &= \mu \left[\left(\frac{\partial u_i}{\partial x_j} + \frac{\partial u_j}{\partial x_i} \right) - \delta_{ij} \frac{2}{3} \frac{\partial u_k}{\partial x_k} \right] \\ &= \frac{\mu}{\rho} \left(\frac{\partial U_i}{\partial x_j} + \frac{\partial U_j}{\partial x_i} - \frac{U_i}{\rho}\frac{\partial \rho}{\partial x_j} - \frac{U_j}{\rho}\frac{\partial \rho}{\partial x_i} \right) - \delta_{ij} \frac{2}{3} \frac{\mu}{\rho} \left(\frac{\partial U_k}{\partial x_k} - \frac{U_k}{\rho}\frac{\partial \rho}{\partial x_k} \right), \end{aligned} \tag{2.5}$$

$$q_j = -\kappa \frac{\partial T}{\partial x_j} = -\frac{\kappa}{c_{\mathrm{v}}\rho} \left[\left(\frac{U_k U_k}{\rho^2} - \frac{E}{\rho}\frac{\partial \rho}{\partial x_j} \right) - \frac{U_k}{\rho}\frac{\partial U_k}{\partial x_j} + \frac{\partial E}{\partial x_j} \right], \tag{2.6}$$

where $i, j = 1, \ldots, 3$, μ is the viscosity, and κ is the coefficient of heat conductivity. μ and κ are supposed constant exept where it is otherwise indicated. It is useful to define the Prandtl number $Pr = \frac{c_{\mathrm{p}}\,\mu}{\kappa}$ and the Reynolds number $Re = \frac{\rho \|\mathbf{u}_{\mathrm{ch}}\| L}{\mu}$, where L and $\mathbf{u}_{\mathrm{ch}}$ are, respectively, a characteristic length and velocity of the problem.

The three-dimensional Navier-Stokes equations can be re-written in non-conservative form as follows:

$$\frac{\partial \mathbf{\Phi}}{\partial t} + \mathbf{A}^i(\mathbf{\Phi})\,\frac{\partial \mathbf{\Phi}}{\partial x_i} - \frac{\partial}{\partial x_i}\left(\mathbf{K}^{ir}(\mathbf{\Phi})\,\frac{\partial \mathbf{\Phi}}{\partial x_r}\right) = 0\,, \tag{2.7}$$

where $\mathbf{A}^i(\mathbf{\Phi}) = \frac{\partial \mathbf{F}^i}{\partial \mathbf{\Phi}}$ are the Euler jacobian matrices and $\mathbf{K}^{ir}$ are the diffusion matrices that verify $\mathbf{F}^{\text{diff,i}} = \mathbf{K}^{ir}\frac{\partial \mathbf{\Phi}}{\partial x_r}$. $\mathbf{A}^i$ and $\mathbf{K}^{ir}$ are $(d+2)\times(d+2)$ matrices whose explicit expressions in three dimensions can be found in Appendix A. Given a bounded domain $\Omega \subset \mathbb{R}^3$, and a time interval $(0,T)$, $T \in \mathbb{R}$, $T > 0$, the problem is to find $\mathbf{\Phi}(\mathbf{x},t)$ verifying equation (2.7) with proper initial and boundary conditions, for all $(\mathbf{x},t) \in \Omega \times (0,T)$. Boundary and initial conditions depend on the problem under study.

2.2 Euler equations

The Euler equations are the inviscid equations of compressible flow. They are a particular case of the Navier-Stokes equations (2.7) for which the viscosity is assumed to be zero, that is $\mu = 0$. Thus the three-dimensional Euler equations can be written in non-conservative form as follows:

$$\frac{\partial \mathbf{\Phi}}{\partial t} + \mathbf{A}^i(\mathbf{\Phi})\,\frac{\partial \mathbf{\Phi}}{\partial x_i} = 0\,, \tag{2.8}$$

where $i = 1,\ldots,3$ labels the space dimension and $\mathbf{\Phi}$ is the vector of the unknowns in conservative variables (2.2). As analogously stated for the Navier-Stokes equations, the problem is to find $\mathbf{\Phi}(\mathbf{x},t)$ verifying equation (2.8) with proper initial and boundary conditions, for all $(\mathbf{x},t) \in \Omega\times(0,T)$. The Euler equations (2.8) are hyperbolic equations, which means that for any linear combination of the form $\mathbf{A_k} = k_i\,\mathbf{A}^i$, with $k_i \in \mathbb{R}$, $\mathbf{A_k}$ is diagonalizable with real eigenvalues.

2.3 Numerical formulation

2.3.1 Variational form

Let $L^2(\Omega)$ be the space of square-integrable real-valued functions over Ω. The variational or weak form of the Navier-Stokes equations (2.7) is obtained by projection of (2.7) by the L^2 scalar product on a chosen test or trial function space $W \subset L^2(\Omega)$,

$$\int_\Omega \psi\,\frac{\partial \mathbf{\Phi}}{\partial t}\,d\Omega + \int_\Omega \psi\,\mathbf{A}^i(\mathbf{\Phi})\,\frac{\partial \mathbf{\Phi}}{\partial x_i}\,d\Omega - \int_\Omega \psi\,\frac{\partial}{\partial x_i}\left(\mathbf{K}^{ir}(\mathbf{\Phi})\,\frac{\partial \mathbf{\Phi}}{\partial x_r}\right)\,d\Omega = 0\,, \tag{2.9}$$

for all $\psi \in W$. As we take the same test function ψ for all the equations of our system (2.7), we write ψ as a scalar function. In order to relax the derivation requirements of the unknown, $\mathbf{\Phi}$, we can integrate by parts the diffusion term and obtain

$$\int_\Omega \psi \, \frac{\partial \mathbf{\Phi}}{\partial t} \, d\Omega + \int_\Omega \psi \, \mathbf{A}^i(\mathbf{\Phi}) \, \frac{\partial \mathbf{\Phi}}{\partial x_i} \, d\Omega + \int_\Omega \frac{\partial \psi}{\partial x_i} \, \mathbf{K}^{ir}(\mathbf{\Phi}) \, \frac{\partial \mathbf{\Phi}}{\partial x_r} \, d\Omega - \int_\Gamma \psi \, \mathbf{K}^{ir}(\mathbf{\Phi}) \, \frac{\partial \mathbf{\Phi}}{\partial x_r} \, n_i \, d\Gamma = 0 \, . \quad (2.10)$$

The resulting boundary term is used to impose Neumann-like conditions on the fluxes, being $\Gamma = \partial\Omega$ the domain boundary and n_r its exterior unit normal vector. In all this work we consider a zero Neumann boundary condition, i.e. $\int_\Gamma \psi \, \mathbf{K}^{ir}(\mathbf{\Phi}) \, \frac{\partial \mathbf{\Phi}}{\partial x_r} \, n_i \, d\Gamma = 0$ in (2.10). The problem consists in finding $\mathbf{\Phi} \in L^2(0,T;\, W)^{d+2}$ verifying (2.10) for all $\psi \in W$.

2.3.2 Finite element discretization

The finite element discretization is set up by choosing a suitable finite-dimensional function space, noted W^h, for the variational form of the problem (2.10). Let Ω^h be a polyhedral approximation of Ω. We consider a partition $\mathcal{P}^h = \{K^m\}_{m=1,\dots,N_{el}}$ of Ω^h in N_{el} elements, $K^m \subset \Omega^h$, of characteristic length h^m. In this work, h^m is defined as the shortest edge of the element. Let $\{\mathbf{x}^p\}_{p=1,\dots,N}$ be the N nodes of the grid associated to $\mathcal{P}^h$ and ψ_p^h the Lagrange polynomial corresponding to node $\mathbf{x}^p$, for $p = 1, \dots, N$. For a first order finite element discretization we consider W^h, the functions space generated by $\{\psi_p^h\}_{p=1,\dots,N}$. The weak or variational finite elements form of the Navier-Stokes equations (2.7) is written as

$$\int_{\Omega^h} \psi^h \, \frac{\partial \mathbf{\Phi}^h}{\partial t} \, d\Omega^h + \int_{\Omega^h} \psi^h \, \mathbf{A}^i(\mathbf{\Phi}^h) \, \frac{\partial \mathbf{\Phi}^h}{\partial x_i} \, d\Omega^h + \int_{\Omega^h} \frac{\partial \psi^h}{\partial x_i} \, \mathbf{K}^{ir}(\mathbf{\Phi}^h) \, \frac{\partial \mathbf{\Phi}^h}{\partial x_r} \, d\Omega^h = 0 \, , \quad (2.11)$$

for all $\psi^h \in W^h$. The function $\mathbf{\Phi}^h$ is defined as the projection of $\mathbf{\Phi}$ onto W^h and it can be expressed as

$$\mathbf{\Phi}^h(\xi, t) = \sum_{p=1}^{N} \psi_p^h(\xi) \, \mathbf{\Phi}_p^h(t) \, , \quad (2.12)$$

where $\xi \in \Omega^h$ and $\mathbf{\Phi}_p^h(t)$ is the value of $\mathbf{\Phi}^h$ at nodes $\mathbf{x}^p$ and time t.

2.3.3 Variational multiscale stabilization

In Hughes [1995], Hughes et al. [1998] they propose a way to explain and remedy the numerical oscillations that appear when a straight finite elements discretization is applied to convetion-dominated problems. They call variational multiscale the stabilization framework they propose, and firstly apply to the advection-diffusion equations. They state that the solution variable is the sum of two parts: the large scales and the subscales. The large scales can be solved by the numerical method but the subscales can not because they are small and under the resolution of the grid. They say that the instabilities appear because the effect of the subscales is not captured by the numerical method. They conclude that the effects of the subscales or unresolved scales must be introduced in the formulation of the discrete problem, by modeling them in some way, using the information that we have at the grid scale level. In the present work we will concentrate on the application of the variational multiscale stabilization (VMS) to the Euler and the Navier-Stokes equations.

Following the fundamental idea behind VMS, let $\tilde{W}$ be the space that completes W^h inside the test function space W, that is, $W = W^h \oplus \tilde{W}$. In this way, W is decomposed into the finite element space W^h, and the subscale space $\tilde{W}$ corresponding to the subscales. This translates into the decompositions $\mathbf{\Phi} = \mathbf{\Phi}_h + \tilde{\mathbf{\Phi}}$ and $\psi = \psi_h + \tilde{\psi}$ that we plug into the variational form (2.9) and obtain

$$\int_{\Omega^h} (\psi^h + \tilde{\psi}) \, \frac{\partial (\mathbf{\Phi}^h + \tilde{\mathbf{\Phi}})}{\partial t} \, d\Omega^h + \int_{\Omega^h} (\psi^h + \tilde{\psi}) \, \mathbf{A}^i(\mathbf{\Phi}) \, \frac{\partial (\mathbf{\Phi}^h + \tilde{\mathbf{\Phi}})}{\partial x_i} \, d\Omega^h + \int_{\Omega^h} (\psi^h + \tilde{\psi}) \, \frac{\partial}{\partial x_i} \left(\mathbf{K}^{ir}(\mathbf{\Phi}) \, \frac{\partial (\mathbf{\Phi}^h + \tilde{\mathbf{\Phi}})}{\partial x_r} \right) d\Omega^h = 0 \,, \quad (2.13)$$

for all $\psi = \psi_h + \tilde{\psi} \in W$. Because all ψ in W is written as the sum of its large scale, ψ_h, and sub-grid scale, $\tilde{\psi}$, components, equation (2.13) can be split in two equations as follows

$$\int_{\Omega^h} \psi^h \, \frac{\partial \mathbf{\Phi}^h}{\partial t} \, d\Omega^h + \int_{\Omega^h} \psi^h \, \mathbf{A}^i(\mathbf{\Phi}) \, \frac{\partial \mathbf{\Phi}^h}{\partial x_i} \, d\Omega^h + \int_{\Omega^h} \frac{\partial \psi^h}{\partial x_i} \, \mathbf{K}^{ir}(\mathbf{\Phi}) \, \frac{\partial \mathbf{\Phi}^h}{\partial x_r} \, d\Omega^h + \sum_{K \in \mathcal{P}_h} \left(\int_K \psi^h \frac{\partial \tilde{\mathbf{\Phi}}}{\partial t} \, dK + \int_K \psi^h \mathcal{L}(\mathbf{\Phi}) \tilde{\mathbf{\Phi}} \, dK \right) = 0 \,, \qquad \forall \psi^h \in W^h \quad (2.14a)$$

$$\sum_{K \in \mathcal{P}_h} \int_K \tilde{\psi} \left(\frac{\partial}{\partial t} + \mathcal{L}(\mathbf{\Phi}) \right) \tilde{\mathbf{\Phi}} \, dK = - \sum_{K \in \mathcal{P}_h} \int_K \tilde{\psi} \left(\frac{\partial}{\partial t} + \mathcal{L}(\mathbf{\Phi}) \right) \mathbf{\Phi}^h \, dK \,, \qquad \forall \tilde{\psi} \in \tilde{W} \quad (2.14b)$$

where

$$\mathcal{L}(\mathbf{\Phi}) = \mathbf{A}^i(\mathbf{\Phi})\frac{\partial}{\partial x_i} - \frac{\partial}{\partial x_i}\left(\mathbf{K}^{ir}(\mathbf{\Phi})\frac{\partial}{\partial x_r}\right) , \tag{2.15}$$

is the original space differential operator. We replaced $\int_{\Omega^h}$ by $\sum_{K\in\mathcal{P}_h}\int_K$ in the subscale terms of (2.14) because the subscales are defined inside the elements but not necessarily on their boundaries. As it is done in Codina [2002], Codina and Blasco [2002], we chose $\tilde{W}$ orthogonal to W^h, thus $\tilde{W} = W^{h\perp} \cap W$.

The large scale equation (2.14a) is solved numerically to compute an approximate solution to our problem. The subscale equation (2.14b) is used to model the subscales, that is to find an expression for $\tilde{\mathbf{\Phi}}$ which will be plugged into the large scale equation. In what follows, we enumerate some simplifications of the large scale and the subscale equations.

Concerning the large scale equation (2.14a), we make the following assumptions that are tested in the literature:

1. Because we took $\tilde{W}$ orthogonal to W^h, then we have

$$\int_K \psi^h \frac{\partial\tilde{\mathbf{\Phi}}}{\partial t}\, dK = 0. \tag{2.16}$$

2. To avoid the space derivatives of the subscale, we integrate by parts the last term of (2.14a) and we suppose the arising boundary terms to be zero, that is

$$\int_K \psi^h\ \mathcal{L}(\mathbf{\Phi})\tilde{\mathbf{\Phi}}\ dK = \int_K \mathcal{L}^*(\mathbf{\Phi})\psi^h\ \tilde{\mathbf{\Phi}}\ dK \tag{2.17}$$

   where

$$\begin{aligned}\mathcal{L}^*(\mathbf{\Phi})\psi^h &= -\frac{\partial}{\partial x_i}\left(\psi^h\ \mathbf{A}^i(\mathbf{\Phi})\right) - \frac{\partial}{\partial x_r}\left(\frac{\partial\psi^h}{\partial x_i}\ \mathbf{K}^{ir}(\mathbf{\Phi})\right)\\ &= -\frac{\partial\psi^h}{\partial x_i}\ \mathbf{A}^i(\mathbf{\Phi}) - \psi^h\ \frac{\partial\mathbf{A}^i(\mathbf{\Phi})}{\partial x_i} - \frac{\partial^2\psi^h}{\partial x_r\partial x_i}\ \mathbf{K}^{ir}(\mathbf{\Phi}) - \frac{\partial\psi^h}{\partial x_i}\ \frac{\partial\mathbf{K}^{ir}(\mathbf{\Phi})}{\partial x_r}\ .\end{aligned} \tag{2.18}$$

3. For the sake of algorithmic simplicity, we make the approximations $\mathbf{A}^i(\mathbf{\Phi}) \approx \mathbf{A}^i(\mathbf{\Phi}^h)$ and $\mathbf{K}^{ir}(\mathbf{\Phi}) \approx \mathbf{K}^{ir}(\mathbf{\Phi}^h)$ (see, for example, Rispoli and Saavedra [2006]). In the context of incompressible flow, the exact form is preserved in Codina [2002]; this requires the storage of the subscale at each iteration.

We observe that imposing equation (2.14a) to hold for all $\psi^h \in W^h$ is equivalent to imposing it to hold for all ψ^h_p, $p \in \{1,\dots,N\}$, because the test functions space W^h is generated by $\{\psi^h_p\}_{p=1,\dots,N}$. This observation together with the last assumptions lead to

the reformulation of (2.14a) as

$$\int_{\Omega^h} \psi_p^h \frac{\partial \mathbf{\Phi}^h}{\partial t}\, d\Omega^h + \int_{\Omega^h} \psi_p^h\, \mathbf{A}^i(\mathbf{\Phi}^h)\, \frac{\partial \mathbf{\Phi}^h}{\partial x_i}\, d\Omega^h + \int_{\Omega^h} \frac{\partial \psi_p^h}{\partial x_i}\, \mathbf{K}^{ir}(\mathbf{\Phi}^h)\, \frac{\partial \mathbf{\Phi}^h}{\partial x_r}\, d\Omega^h + \sum_{K\in\mathcal{P}_h} \int_K \mathcal{L}^*(\mathbf{\Phi}^h)\psi_p^h\, \tilde{\mathbf{\Phi}}\, dK = 0\,, \quad (2.19)$$

holding for all $p \in \{1, \ldots, N\}$. The effect of the subscale on the large scale modeling is represented by the stabilization term, consisting of the last term in equation (2.19).

Concerning the subscale equation (2.14b), we make the approximation $\mathcal{L}(\mathbf{\Phi}) \approx \mathcal{L}(\mathbf{\Phi}^h)$ (same as in the third point above). Because we took $\tilde{W}$ orthogonal to W^h, we have $\int_K \tilde{\psi} \frac{\partial \mathbf{\Phi_h}}{\partial t}\, dK = 0$. Thus (2.14b) becomes

$$\sum_{K\in\mathcal{P}_h} \int_K \tilde{\psi} \left(\frac{\partial}{\partial t} + \mathcal{L}(\mathbf{\Phi}^h) \right) \tilde{\mathbf{\Phi}}\, dK = - \sum_{K\in\mathcal{P}_h} \int_K \tilde{\psi}\, \mathcal{L}(\mathbf{\Phi}^h)\mathbf{\Phi}^h\, dK\,, \quad (2.20)$$

for all $\tilde{\psi} \in \tilde{W}$. For the modeling of the subscale, we consider the subscale equation (2.20) in the strong form, and obtain for every $K \in \mathcal{P}_h$,

$$\left(\frac{\partial}{\partial t} + \mathcal{L}(\mathbf{\Phi}^h) \right) \tilde{\mathbf{\Phi}} = \mathbf{r}(\mathbf{\Phi}^h)\,, \quad (2.21)$$

where

$$\mathbf{r}(\mathbf{\Phi}^h) = -\mathcal{L}(\mathbf{\Phi}^h)\mathbf{\Phi}^h\,, \quad (2.22)$$

is the space residual of the large scales equation.

2.3.4 Modeling the VMS subscales

Here we present two options for the modeling of the subscale, which is a topic of active research still today John and Knobloch [2007].

2.3.4.1 Diagonal τ subscale

We consider now the hypotheses of quasi-static subscales (refer to Codina and Blasco [2002]), which means that $\frac{\partial \tilde{\mathbf{\Phi}}}{\partial t} \approx 0$. This way we avoid the time tracking of the subscales. Then (2.21) becomes

$$\mathcal{L}(\mathbf{\Phi}^h)\, \tilde{\mathbf{\Phi}} = \mathbf{r}(\mathbf{\Phi}^h)\,. \quad (2.23)$$

For a description of how the subscales can be tracked when solving the incompressible equations, refer to Codina [2002]. If we call τ an approximation of $(\mathcal{L}(\mathbf{\Phi}^h))^{-1}$, the

compressible flow subscales $\tilde{\boldsymbol{\Phi}}$ can be approximated in every element $K \in \mathcal{P}^h$, as

$$\tilde{\boldsymbol{\Phi}} = \tau \, \mathbf{r}(\boldsymbol{\Phi}^h) \, . \tag{2.24}$$

Most of the models describe the subscale in the form of equation (2.24), i.e. as the product of a parameter τ times the residual of the equation. There exist, for compressible flow, many proposals for the definition of τ in the literature, some of them are found in Hughes and Tezduyar [1984], Le Beau et al. [1993], in the context of SUPG; in Shakib et al. [1991], in the context of GLS; and in Rispoli and Saavedra [2006], in the context of VMS. Following the line set for incompressible flow in Codina [2002], parameter τ, is here defined as

$$\tau = \left(\frac{\|\mathbf{u}\| + c}{h} + \frac{4\,\mu}{\rho\, h^2} \right)^{-1} \, . \tag{2.25}$$

On the one hand we note that τ depends on the speed of sound, which is not the case of the incompressible flow formulation of Codina [2002]. However it is the case of other compressible flow formulations, for instance, in Hughes and Tezduyar [1984], Le Beau et al. [1993], Rispoli and Saavedra [2006]. On the other hand it is important to see the local nature of the subscales that are meant to exist only where residuals are important. This fact is illustrated in the numerical results of Chapter 3. Expression (2.24) is plugged into equation (2.19) to find an approximate solution of problem (2.7).

2.3.4.2 Fourier subscale

Here we propose a different method, which takes as a starting point the Fourier approach of Codina and Blasco [2002]. For every $K \in \mathcal{P}_h$ the time discretized subscale equation (2.20) can be written as

$$\left(\frac{1}{\Delta t} + \mathcal{L}(\boldsymbol{\Phi}^n)(\mathbf{x}) \right) \tilde{\boldsymbol{\Phi}}^{n+1}(\mathbf{x}) = \mathbf{d}^n(\mathbf{x}) \, , \tag{2.26}$$

where superscripts n and $n+1$ account for the last and the current time steps, respectively, and

$$\mathbf{d}^n = \frac{1}{\Delta t} \tilde{\boldsymbol{\Phi}}^n \, + \, \mathbf{r}(\boldsymbol{\Phi}^{h,n}) \, . \tag{2.27}$$

Now we want to transform equation (2.26) into the Fourier space. Given an integrable function f defined on each element K, its Fourier transform writes

$$\widehat{f}(\omega) = \int_K f(\mathbf{x}) e^{-i\theta_k \omega_k x_k} \, d\mathbf{x} \, , \tag{2.28}$$

where i is the imaginary unit, ω is the Fourier parameter, $\theta_k = \frac{2\pi}{h_k}$, and h_k is the characteristic length for each space component. Its inverse transform writes

$$f(\mathbf{x}) = \int_{\mathbb{R}^d} \widehat{f}(\omega) e^{i\theta_k \omega_k x_k} \, d\omega \, . \tag{2.29}$$

The Fourier transform of its first and second degree partial derivatives write

$$\widehat{\frac{\partial f}{\partial x_i}}(\omega) = i\,\theta_i \omega_i \, \widehat{f}(\omega) + \int_\Gamma n_i \, e^{-i\theta_k \omega_k x_k} f(\mathbf{x}) \, d\mathbf{x} \, , \tag{2.30}$$

$$\begin{aligned} \widehat{\frac{\partial^2 f}{\partial x_i \partial x_r}}(\omega) = &- \theta_i \theta_r \omega_i \omega_r \, \widehat{f}(\omega) + \int_\Gamma n_i \, e^{-i\theta_k \omega_k x_k} \frac{\partial f}{\partial x_r}(\mathbf{x}) \, d\mathbf{x} \\ &+ \int_\Gamma n_r \, i\,\theta_i \omega_i \, e^{-i\theta_k \omega_k x_k} f(\mathbf{x}) \, d\mathbf{x} \, , \end{aligned} \tag{2.31}$$

respectively, where $\mathbf{n}$ is the exterior normal to K. As it is done in Codina and Blasco [2002], we assume that

$$\widehat{\frac{\partial \tilde{\boldsymbol{\Phi}}}{\partial x_i}} \approx i\,\theta_i \omega_i \, \hat{\tilde{\boldsymbol{\Phi}}} \, , \tag{2.32}$$

$$\widehat{\frac{\partial^2 \tilde{\boldsymbol{\Phi}}}{\partial x_i \partial x_r}} \approx -\theta_i \theta_r \omega_i \omega_r \, \hat{\tilde{\boldsymbol{\Phi}}} \, . \tag{2.33}$$

Thus the Fourier transform of the equation (2.26) writes

$$\left(\frac{1}{\Delta t} + L(\omega) \right) \hat{\tilde{\boldsymbol{\Phi}}}^{n+1}(\omega) = \widehat{\mathbf{d}}^n(\omega) \, , \tag{2.34}$$

and we approximate the Fourier's transform of $\mathcal{L}$ as

$$L(\omega) = i\,\theta_i \omega_i \, \bar{\mathbf{A}}^i(\boldsymbol{\Phi}^{h,n}) + \theta_i \theta_r \omega_i \omega_r \, \bar{\mathbf{K}}^{ir}(\boldsymbol{\Phi}^{h,n}) \, . \tag{2.35}$$

Bars over $\mathbf{A}^i$ and $\mathbf{K}^{ir}$ notes their mean value on K. We observe from (2.35) that the partial derivatives in $\mathcal{L}$ disappear when transforming it to the Fourier space. From (2.34) we obtain an expression for the subscale transform

$$\hat{\tilde{\boldsymbol{\Phi}}}^{n+1}(\omega) = \mathcal{T}(\omega) \, \widehat{\mathbf{d}}^n(\omega) \tag{2.36}$$

where $\mathcal{T}(\omega) = \left(\frac{1}{\Delta t} + L(\omega) \right)^{-1}$. Finally, to model the subscales, we transform back to the physical space, obtaining for all $\mathbf{y} \in K$

$$\tilde{\boldsymbol{\Phi}}^{n+1}(\mathbf{y}) = \int_{\mathbb{R}^d} \int_K \tau(\omega, \mathbf{x}, \mathbf{y}) \, \mathbf{d}^n(\mathbf{x}) \, d\mathbf{x} \, d\omega \, , \tag{2.37}$$

where

$$\tau(\omega,\mathbf{x},\mathbf{y}) = Re\left(\mathcal{T}(\omega)\right)\,\cos(\theta_k\omega_k\left(x_k-y_k\right)) + Im\left(\mathcal{T}(\omega)\right)\,\sin(\theta_k\omega_k\left(x_k-y_k\right))\,. \quad (2.38)$$

We observe that $L(-\omega)=\overline{L(\omega)}$, then $\mathcal{T}(-\omega)=\overline{\mathcal{T}(\omega)}$, $\tau(-\omega,\mathbf{x},\mathbf{y}))=\tau(\omega,\mathbf{x},\mathbf{y})$, and

$$\tilde{\boldsymbol{\Phi}}^{n+1}(\mathbf{y}) = 2\int_{(\mathbb{R}^d)^+}\int_K \tau(\omega,\mathbf{x},\mathbf{y})\,\mathbf{d}^n(\mathbf{x})\,d\mathbf{x}\,d\omega\,. \quad (2.39)$$

We discretize the integral $\int_{(\mathbb{R}^d)^+}(\cdot)\,d\omega$ and approximate it as the finite sum $\sum_{\omega\in D}(\cdot)$, where $D=D_1\cap D_2\subset\mathbb{Z}^d$ and

$$\begin{aligned} D_1 = \mathbb{Z}^d \cap \{&\{0\}\cup\{\omega_1>0\}\cup\{\omega_2>0,\,\omega_1=0\}\cup\cdots\cup \\ &\{\omega_d>0,\,\omega_k=0,\quad \forall k=1,\ldots,d-1\}\}\,, \end{aligned} \quad (2.40)$$

$$D_2 = \{|\omega_k|\le M_{\text{freq}}\}\,. \quad (2.41)$$

In the definition of D_2, $M_{\text{freq}}\in\mathbb{Z}$ limits the extension of the set D to a finite number of Fourier frequencies. In the applications, M_{freq} typically takes the value of 0, 1, 2, or 3. Finally we obtain

$$\tilde{\boldsymbol{\Phi}}^{n+1}(\mathbf{y}) = \int_K \Delta t\;\mathbf{d}^n(\mathbf{x})\,d\mathbf{x} \;+\; 2\sum_{\omega\in D\setminus\{0\}}\int_K \tau(\omega,\mathbf{x},\mathbf{y})\;\mathbf{d}^n(\mathbf{x})\,d\mathbf{x}\,. \quad (2.42)$$

Observe that when $M_{\text{freq}}=0$ we get for all $y\in K$

$$\tilde{\boldsymbol{\Phi}}^{n+1}(\mathbf{y}) = \int_K \Delta t\;\mathbf{d}^n(\mathbf{x})\,d\mathbf{x}\,. \quad (2.43)$$

In the examples we solved, we noticed that the Fourier subscale performs much better if we remove term $\frac{1}{\Delta t}\tilde{\boldsymbol{\Phi}}^n$ from (2.27). The explanation for this is not clear and more testing on that should be done.

2.3.5 Time discretization

The time discretization of (2.19) is here done by an explicit scheme, giving

$$\begin{aligned} &\int_{\Omega^h}\psi_p^h\,\frac{\boldsymbol{\Phi}^{h,n+1}-\boldsymbol{\Phi}^{h,n}}{\Delta t}\,d\Omega^h + \int_{\Omega^h}\psi_p^h\;\mathbf{A}^i(\boldsymbol{\Phi}^{h,n})\,\frac{\partial\boldsymbol{\Phi}^{h,n}}{\partial x_i}\,d\Omega^h \\ &\quad+\int_{\Omega^h}\frac{\partial\psi_p^h}{\partial x_i}\,\mathbf{K}^{ir}(\boldsymbol{\Phi}^{h,n})\,\frac{\partial\boldsymbol{\Phi}^{h,n}}{\partial x_r}\,d\Omega^h + \sum_{K\in\mathcal{P}_h}\int_K \mathcal{L}(\boldsymbol{\Phi}^{h,n})^*\psi_p^h\;\tilde{\boldsymbol{\Phi}}^{n+1}\,dK\;=0\,, \end{aligned} \quad (2.44)$$

holding for all $p\in\{1,\ldots,N\}$. The superscripts $n+1$ and n indicate the value at the current and the previous time step, respectively. The value of $\tilde{\boldsymbol{\Phi}}^{n+1}$ is computed from

the information of the previous time step n. When the diagonal τ subscale is used (2.24), the subscale at time step $n+1$ reads

$$\tilde{\mathbf{\Phi}}^{n+1} = \tau^n \, \mathbf{r}(\mathbf{\Phi}^{h,n}) \, , \tag{2.45}$$

where the residual (2.22) at time n reads

$$\mathbf{r}(\mathbf{\Phi}^{h,n}) \, = \, - \mathcal{L}(\mathbf{\Phi}^{h,n}) \mathbf{\Phi}^{h,n} = - \mathbf{A}^i(\mathbf{\Phi}^{h,n}) \frac{\partial \mathbf{\Phi}^{h,n}}{\partial x_i} + \frac{\partial}{\partial x_i} \left(\mathbf{K}^{ir}(\mathbf{\Phi}^{h,n}) \frac{\partial \mathbf{\Phi}^{h,n}}{\partial x_r} \right) \, , \tag{2.46}$$

and τ^n is the value of τ, explicetly defined in (2.25), at time n. When the Fourier subscale is used, then $\tilde{\mathbf{\Phi}}^{n+1}$ is defined from (2.42).

In this work, both local and global time steppings are considered. From the CFL condition Courant et al. [1967] a time step inside each element is defined as

$$\Delta t^{\,el} = C \, \left(\frac{\|\mathbf{u}\| + c}{h} + \frac{4\,\mu}{\rho\, h^2} \right)^{-1} \, , \tag{2.47}$$

where $C \in (0,1)$ is the CFL number and h is the smallest edge length of the element. The element time step (2.47) is interpolated on the nodes of the grid, obtaining the local time step $\Delta t^{\,p}$, $p = 1, \ldots, N$, at each node $\mathbf{x}^p$ of the grid. The global time step is computed as the minimum time step of the domain as

$$\Delta t = \min_{p=1,\ldots,N} \{ \Delta t^{\,p} \} \, . \tag{2.48}$$

Inserting equality (2.12) in (2.44), a linear system of $N(d+2)$ equations is obtained:

$$\mathbf{M} \, \frac{\mathbf{\Phi}^{h,n+1} - \mathbf{\Phi}^{h,n}}{\Delta t} = \mathbf{G}(\mathbf{\Phi}^{h,n}) + \mathbf{S}(\mathbf{\Phi}^{h,n}, \tilde{\mathbf{\Phi}}^{n+1}) \, , \tag{2.49}$$

where

1. $\mathbf{\Phi}^h$ is here the nodal vector of unknowns of dimension $N(d+2)$. It is made by assembly of the vectors $\mathbf{\Phi}^h_p$, for $p = 1, \ldots, N$.

2. $\mathbf{M}$ is the global Mass matrix, it has dimension $N(d+2) \times N(d+2)$. It is a block matrix composed of N^2 blocks $\mathbf{M}^{pq}$ of dimension $(d+2) \times (d+2)$,

$$\mathbf{M}^{pq} = \int_{\Omega^h} \psi^h_p \psi^h_q \, d\Omega^h \, \mathbf{I}_{d+2} \, , \tag{2.50}$$

where $p, q = 1, \ldots, N$ and $\mathbf{I}_{d+2}$ is the identity matrix of dimension $(d+2) \times (d+2)$.

3. $\mathbf{G}$ and $\mathbf{S}$ are the Galerkin and stabilization vector terms, respectively. They are constructed by assembly of the following N local vectors of dimension $d+2$:

$$\mathbf{G}^p = -\int_{\Omega^h} \psi_p^h \, \mathbf{A}^i(\mathbf{\Phi}^{h,n}) \, \frac{\partial \mathbf{\Phi}^{h,n}}{\partial x_i} \, d\Omega^h - \int_{\Omega^h} \frac{\partial \psi_p^h}{\partial x_i} \, \mathbf{K}^{ir}(\mathbf{\Phi}^{h,n}) \, \frac{\partial \mathbf{\Phi}^{h,n}}{\partial x_r} \, d\Omega^h \,, \quad (2.51)$$

$$\mathbf{S}^p = -\sum_{K \in \mathcal{P}_h} \int_K \mathcal{L}(\mathbf{\Phi}^{h,n})^* \psi_p^h \, \tilde{\mathbf{\Phi}}^{n+1} \, dK \,, \quad (2.52)$$

respectively, for $p = 1, \ldots, N$.

All the integrals above are approximated by the Gaussian quadrature rule that, for a function f, writes

$$\int_{K^m} f(\mathbf{x}) \, dK^m = \int_I f(\mathcal{H}^m(\xi)) \, |J^m(\xi)| \, d\xi \approx \sum_{p=1}^{N_{Gauss}} f(\mathcal{H}^m(\xi^p)) \, |J^m(\xi^p)| \, \omega^p, \quad (2.53)$$

where $I = [-1,1] \times [-1,1]$ is a reference element, $\mathcal{H}^m$ a bijection from I to the element K^m, $J^m = \frac{\mathrm{d}\mathcal{H}^m}{\mathrm{d}\xi}$ the $\mathcal{H}^m$ Jacobian matrix, $|J^m|$ its determinant, N_{Gauss} is the number of integration Gauss points ξ^p inside the element K^m, and ω^p its weight.

$\mathbf{M}$ is diagonalized by lumping techniques Hughes [2000] in order to avoid its inversion when open integration rules are used. From equation (2.49), the value of $\mathbf{\Phi}^{h,n+1}$ at each node of the computational grid is obtained as

$$\mathbf{\Phi}^{h,n+1} = \mathbf{\Phi}^{h,n} + \Delta t \, \mathbf{M}^{-1} \left(\mathbf{G}(\mathbf{\Phi}^{h,n}) + \mathbf{S}(\mathbf{\Phi}^{h,n}, \tilde{\mathbf{\Phi}}^{n+1}) \right) \,, \quad (2.54)$$

where $\tilde{\mathbf{\Phi}}^{n+1}$ is defined as explained in Subsection 2.3.4, from the values at the previous time step n.

VMS stabilization term (2.52) with the diagonal τ subscale (2.45), can be compared with the corresponding compressible SUPG (Hughes and Mallet [1986b], Hughes and Tezduyar [1984], Le Beau et al. [1993], Tezduyar and Senga [2006]), GLS (Shakib et al. [1991]), and Rispoli's VMS (Rispoli and Saavedra [2006]) stabilization terms. When the diagonal τ subscale (2.45) is used, our VMS stabilization term (2.52) reads

$$\mathbf{S}^p = -\sum_{K \in \mathcal{P}_h} \int_K \left(-\frac{\partial \psi_p^h}{\partial x_i} \, \mathbf{A}^i(\mathbf{\Phi}^{h,n}) - \psi_p^h \, \frac{\partial \mathbf{A}^i(\mathbf{\Phi}^{h,n})}{\partial x_i} \right.$$
$$\left. - \frac{\partial^2 \psi_p^h}{\partial x_r \partial x_i} \, \mathbf{K}^{ir}(\mathbf{\Phi}^{h,n}) - \frac{\partial \psi_p^h}{\partial x_i} \, \frac{\partial \mathbf{K}^{ir}(\mathbf{\Phi}^{h,n})}{\partial x_r} \right) \tau^n \, \mathbf{r}(\mathbf{\Phi}^{h,n}) \, dK \,. \quad (2.55)$$

The corresponding SUPG stabilization term reads

$$\mathbf{S}^p_{\text{SUPG}} = -\sum_{K\in\mathcal{P}_h}\int_K -\frac{\partial\psi^h_p}{\partial x_i}\,\mathbf{A}^i(\mathbf{\Phi}^{h,n})\,\tau^n_{\text{SUPG}}\,\mathbf{r}_t(\mathbf{\Phi}^{h,n})\,dK\,, \tag{2.56}$$

the GLS stabilization term reads

$$\mathbf{S}^p_{\text{GLS}} = -\sum_{K\in\mathcal{P}_h}\int_K \left(-\frac{\partial\psi^h_p}{\partial x_i}\,\mathbf{A}^i(\mathbf{\Phi}^{h,n}) + \frac{\partial^2\psi^h_p}{\partial x_i\partial x_r}\,\mathbf{K}^{ir}(\mathbf{\Phi}^{h,n}) + \frac{\partial\psi^h_p}{\partial x_r}\,\frac{\partial\mathbf{K}^{ir}(\mathbf{\Phi}^{h,n})}{\partial x_i}\right)\tau^n_{\text{GLS}}\,\mathbf{r}_t(\mathbf{\Phi}^{h,n})\,dK\,, \tag{2.57}$$

and Rispoli's VMS stabilization term (when ψ^h does not depend on the time variable t, as it is the case in our work) reads

$$\mathbf{S}^p_{\text{Rispoli}} = -\sum_{K\in\mathcal{P}_h}\int_K \left(-\frac{\partial\psi^h_p}{\partial x_i}\,\mathbf{A}^i(\mathbf{\Phi}^{h,n}) - \frac{\partial^2\psi^h_p}{\partial x_r\partial x_i}\,\mathbf{K}^{ir}(\mathbf{\Phi}^{h,n}) - \frac{\partial\psi^h_p}{\partial x_i}\,\frac{\partial\mathbf{K}^{ir}(\mathbf{\Phi}^{h,n})}{\partial x_r}\right)\tau^n_{\text{Rispoli}}\,\mathbf{r}_t(\mathbf{\Phi}^{h,n})\,dK\,. \tag{2.58}$$

The residual $\mathbf{r}(\mathbf{\Phi}^{h,n})$ in (2.58) is defined by (2.46). Remark that, as we took orthogonal subscales, the time derivatives $\frac{\partial\mathbf{\Phi}^h}{\partial t}$ do not appear in the residual, avoiding the storage of $\mathbf{\Phi}^{h,n-1}$ at each time step. However for most of the stabilization formulations, their residual include the time derivative, that is:

$$\mathbf{r}_t(\mathbf{\Phi}^h) = -\frac{\partial\mathbf{\Phi}^h}{\partial t} - \mathcal{L}(\mathbf{\Phi}^{h,n})\mathbf{\Phi}^{h,n}\,. \tag{2.59}$$

The stabilization parameter τ in (2.58) is defined by (2.25). However each formulation has his own parameter τ. Note that $\frac{\partial^2\psi^h}{\partial x_r\partial x_i} = 0$ when the test functions ψ^h are linear functions, in this work that is when triangles or tetrahedra are used. When quadrilaterals are used, ψ^h are bilinear functions and $\frac{\partial^2\psi^h}{\partial x_r\partial x_i} \neq 0$. For the sake of completeness we expand our compressible VMS term (2.58) and write it here:

$$\mathbf{S}^p = -\sum_{K\in\mathcal{P}_h}\int_K \left\{\left(-\frac{\partial\psi^h_p}{\partial x_i}\,\mathbf{A}^i(\mathbf{\Phi}^{h,n}) - \psi^h_p\,\frac{\partial\mathbf{A}^i(\mathbf{\Phi}^{h,n})}{\partial x_i} - \frac{\partial^2\psi^h_p}{\partial x_r\partial x_i}\,\mathbf{K}^{ir}(\mathbf{\Phi}^{h,n}) - \frac{\partial\psi^h_p}{\partial x_i}\,\frac{\partial\mathbf{K}^{ir}(\mathbf{\Phi}^{h,n})}{\partial x_r}\right)\left(\frac{\|\mathbf{u}\|+c}{h} + \frac{4\,\mu}{\rho\,h^2}\right)^{-1}\left(-\mathbf{A}^i(\mathbf{\Phi}^{h,n})\frac{\partial\mathbf{\Phi}^{h,n}}{\partial x_i} + \frac{\partial}{\partial x_i}\left(\mathbf{K}^{ir}(\mathbf{\Phi}^{h,n})\frac{\partial\mathbf{\Phi}^{h,n}}{\partial x_r}\right)\right)\right\}\,dK\,. \tag{2.60}$$

2.4 Numerical results

In this section we assess the proposed VMS method on a suite of benchmarks of viscous and inviscid, transient and steady flow, covering a large range of Mach numbers. Both the diagonal τ subscale and the Fourier subscale are tested and compared. We suppose a diatomic ideal gas then $\gamma = 1.4$ in all the following simulations. The problems that we solve are the following:

- Sod's shock tube (Euler transient flow at different Mach numbers)
- Carter plate (viscous steady supersonic flow)
- Scramjet (Euler steady supersonic flow)

When shocks start to appear in the supersonic regions, some sort of discontinuity capturing technique could be needed in order to avoid spurious oscillations around the discontinuities. In some of the examples that we solve, the isotropic or anisotropic shock capturing from Codina [1993], Vázquez [1998], are used. The discontinuity capturing terms, added to the right hand side of equation (2.19) are:

$$\sum_{K\in\mathcal{P}_h}\int_K \left\{ \nu_{\text{DC}}\,\frac{\partial\psi_p^h}{\partial x_i}\,\delta_{ij}\,\frac{\partial\mathbf{\Phi}^h}{\partial x_j} + (\nu_{\text{sl}}-\nu_{\text{DC}})\,\frac{\partial\psi_p^h}{\partial x_i}\left(\frac{u_i u_j}{\|\mathbf{u}\|^2}\right)\frac{\partial\mathbf{\Phi}^h}{\partial x_j}\right\} dK\ , \tag{2.61}$$

where

$$\nu_{\text{DC}} = \frac{1}{2}\,\alpha_{\text{DC}}\,h\,\|\mathbf{r}(\mathbf{\Phi}^h)\|\,\left(\left\|\frac{\partial\mathbf{\Phi}^h}{\partial x_j}\right\|\right)^{-1}\ , \tag{2.62}$$

$$\alpha_{\text{DC}} = \max\left\{0\,,\,c - \frac{2\mu}{h\,\|\mathbf{r}(\mathbf{\Phi}^h)\|}\left\|\frac{\partial\mathbf{\Phi}^h}{\partial x_j}\right\|\right\}\ , \tag{2.63}$$

$c = 0.7$ for linear interpolations and $c = 0.35$ for quadratic ones, and

$$\nu = \frac{1}{2}\frac{\Delta t}{2}\|\mathbf{u}\|^2\ . \tag{2.64}$$

For isotropic shock capturing we have:

$$\nu_{\text{sl}} = \nu_{\text{DC}}\ , \tag{2.65}$$

and for the anisotropic one we have:

$$\nu_{\text{sl}} = \max\{0\,,\,\nu_{\text{DC}} - \nu\}\ . \tag{2.66}$$

It is worth to remark that the isotropic shock capturing adds a diffusion uniformly in all the directions, while the anisotropic one only adds it in the streamline direction. Depending on the problem one or the other is seen to perform better.

2.4.1 Sod's shock tube

We solve the well known shock tube originally proposed by Sod [1978]. It is a transient case that has analytic solution. It consists of a one-dimensional tube that has a discontinuity in the initial data, the left and right sides of the tube present different density ρ and total energy E. The left density is set to 1 and the right density to 0.125, the left total energy is set to 2.5 and the right total energy is set to 2. The fluid is initially at rest, that is, it has zero initial velocity. It starts to move because of the discontinuous initial condition of the left and right states which entails a shock wave that propagates to both left and right sides. This leads to a maximum Mach number of 0.828 approximately.

Our computational domain is a two-dimensional rectangular tube. This tube is partitioned in the horizontal direction with a mesh of 400 rectangles and 802 nodes, no partition is done in the vertical direction as shown in Fig. 2.1. The one-dimensionality of the original problem is assured by considering $u_2 = 0$ on the upper and lower walls, that is in all the nodes. The left and right boundaries are left free of boundary conditions. We use a CFL number of 0.8 in the computation of the time step and 4 integration Gauss points. No shock capturing is used for this case.

In Fig. 2.2 the exact analytical solution for the density is plotted and compared to the corresponding numerical solution, using the diagonal τ subscale as well as the Fourier subscale considering different frequencies (i.e. different values for M_{freq}). We see that the shock location is correctly predicted. In some of the cases the solution has small undershoots near the shock, these oscillations are, however, very localized and do not corrupt the solution away from the shock. When $M_{\text{freq}} = 2$ is used, the instabilities near the shocks disappear and the solution is more diffusive. In Fig. 2.3 we show the behavior of the solution when the number of Fourier frequencies and Gauss points are increased. As expected, the solution is smoother when M_{freq} is increased, and slightly less diffusive when more Gauss points are used.

In order to show the operability of the scheme through a wide range of Mach numbers, the same problem with two different settings on the initial conditions has been solved as well, giving a supersonic case and a very subsonic case. The supersonic shock tube reaches a Mach number around 10 and is generated using a very large discontinuity in the initial data: the left density is set to 1 and the right density is set to 10^{-10}, and the left total energy is set to 2.5 and the right total energy is set to 2. Comparative results of the

supersonic shock tube for the diagonal τ subscale and the Fourier subscale are displayed in Fig. 2.4. We observe that the results are very similar for both cases. Concerning the very subsonic tube, it reaches a maximum Mach number around 1.4×10^{-6}. The initial conditions are: the left density is set to 1 and the right density is set to 0.99998, and the left energy is set to 2.5 and the right energy is set to 2.49999. The results obtained for this subsonic case using the diagonal τ subscale and the Fourier subscale are almost identical. In Fig. 2.5 we show the results using the diagonal τ subscale. Both shock tube configurations are solved using a CFL number of 0.8 for the time step, 4 integration Gauss points, and $M_{\text{freq}} = 1$ for the Fourier subscale. No shock capturing is used in any of the configurations for this case.

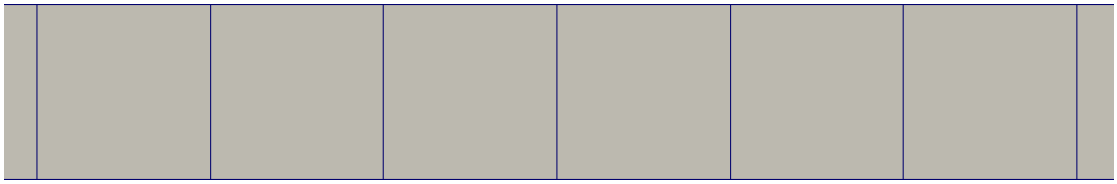

FIGURE 2.1: Sod's shock tube. Close-up of the computational mesh.

(A) Diagonal τ subscale

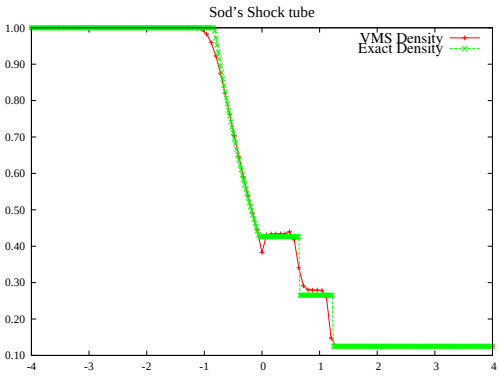

(B) Fourier subscale, $M_{\text{freq}} = 0$

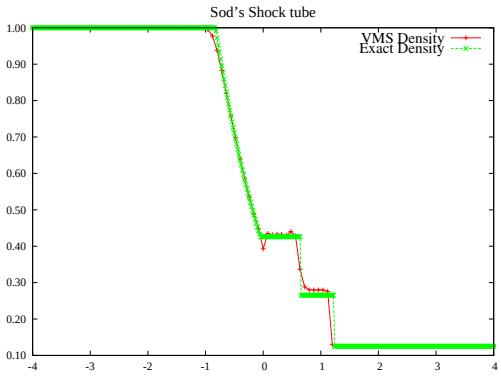

(C) Fourier subscale, $M_{\text{freq}} = 2$

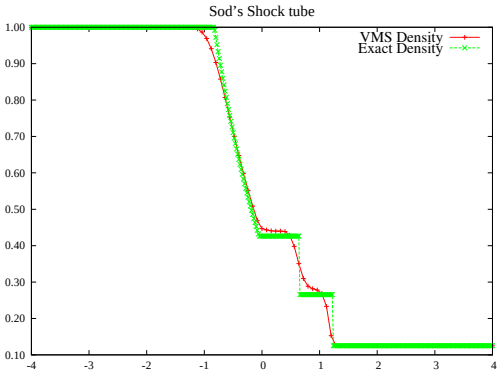

FIGURE 2.2: Sod's shock tube. Comparison of the density analytical result (green line) and the corresponding solution of the simulation (red line) using the diagonal τ subscale and two different configurations of the Fourier subscale. We use 4 integration Gauss points. The solution is advanced to $t = 0.7$.

(A) 4 Gauss points, $M_{\text{freq}} = 0$

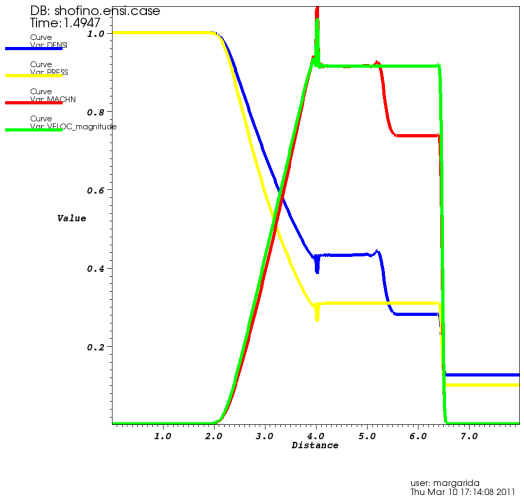

(B) 9 Gauss points, $M_{\text{freq}} = 0$

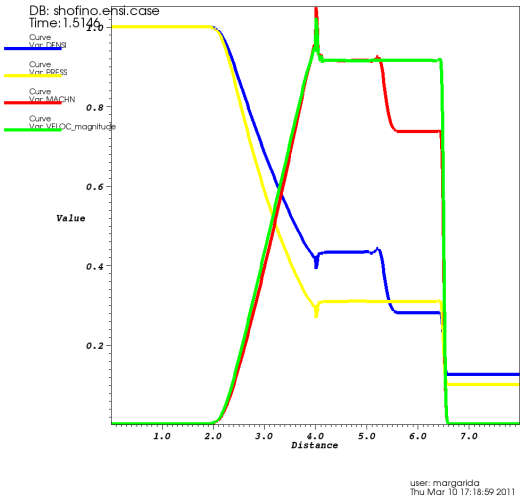

(C) 4 Gauss points, $M_{\text{freq}} = 1$

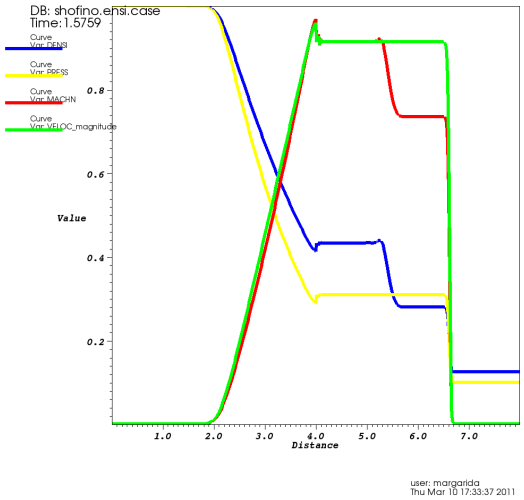

(D) 9 Gauss points, $M_{\text{freq}} = 1$

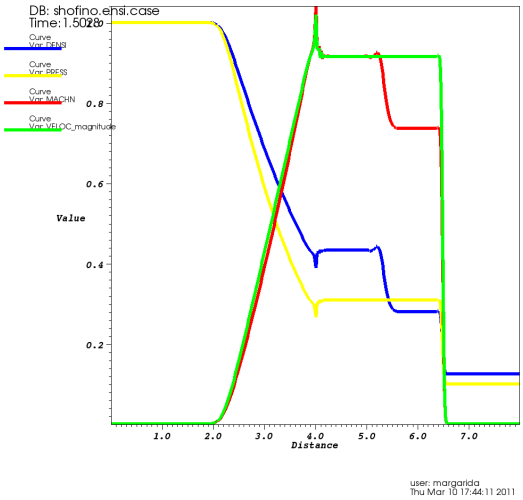

(E) 4 Gauss points, $M_{\text{freq}} = 2$

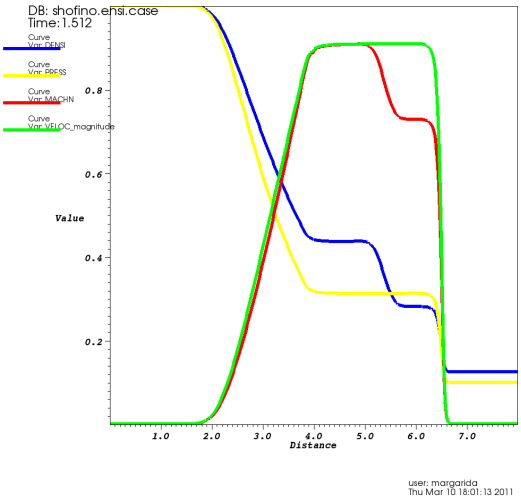

(F) 9 Gauss points, $M_{\text{freq}} = 2$

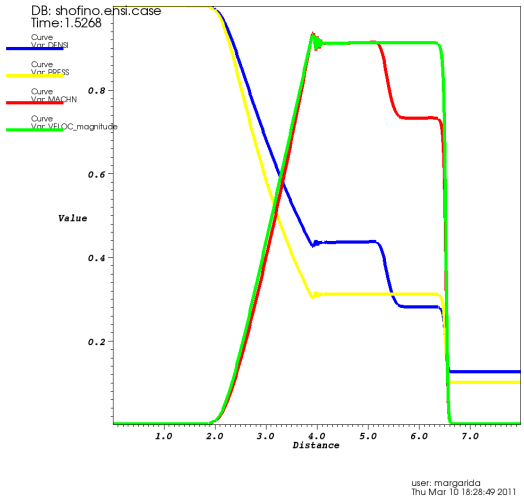

(G) 4 Gauss points, $M_{\text{freq}} = 3$

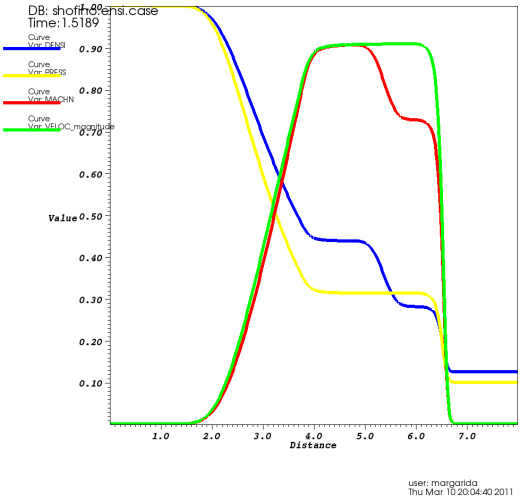

(H) 9 Gauss points, $M_{\text{freq}} = 3$

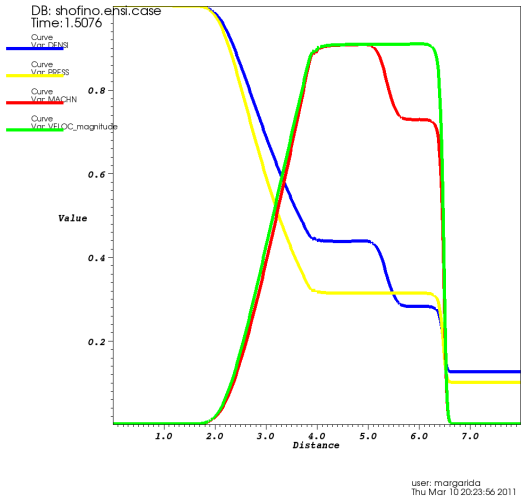

FIGURE 2.3: Sod's shock tube. Comparison of the solution of the density (blue line), pressure (yellow line), Mach number (red line), and velocity module (green line), using different number of frequencies and Gauss points for the Fourier subscale. The solution is advanced to $t \approx 1.5$.

(A) Diagonal τ subscale (B) Fourier subscale

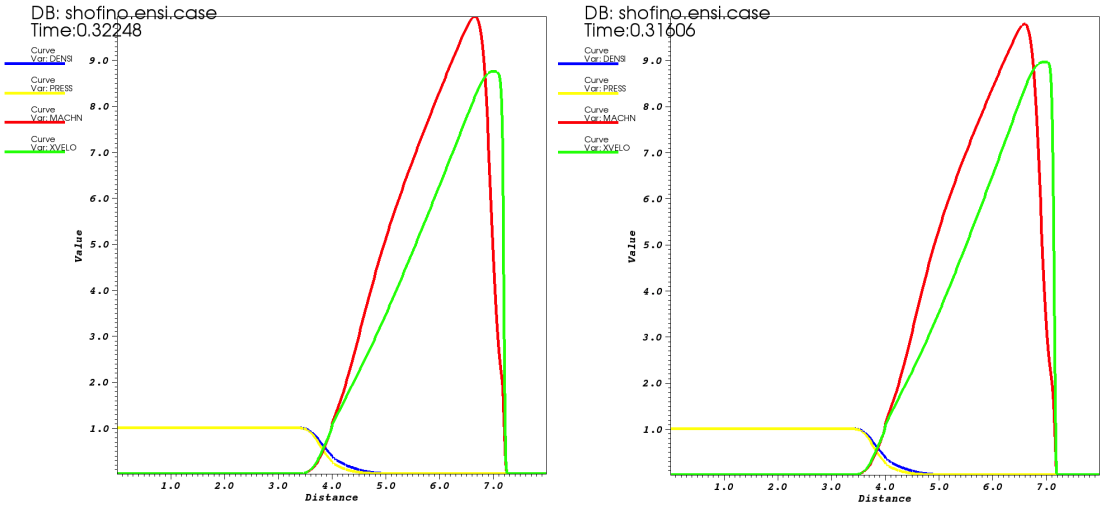

FIGURE 2.4: Sod's shock tube. We compare the diagonal τ and the Fourier subscale results of the density (blue line), pressure (yellow line), Mach number (red line), and velocity module (green line), for a supersonic case of the shock tube that reaches a maximum Mach number of around 10. We use a CFL number of 0.8, 4 Gauss integration points, and the Fourier subscale uses $M_{\text{freq}} = 1$.

(A) Density and pressure (B) Mach number and velocity module

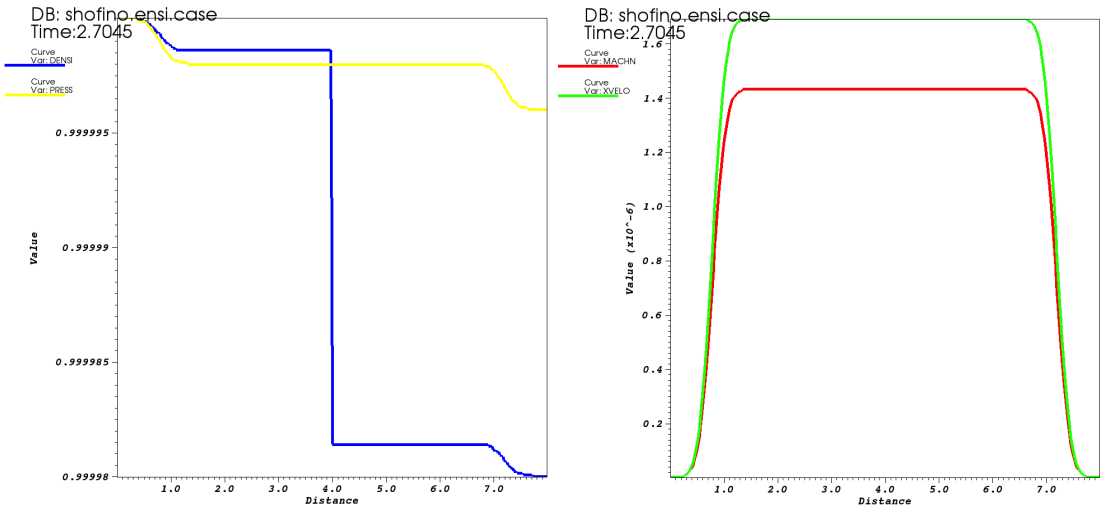

FIGURE 2.5: Sod's shock tube. Results for the diagonal τ subscale, of the density (blue line), pressure (yellow line), Mach number (red line), and velocity module (green line), for a very subsonic case of the shock tube that reaches a maximum Mach number of around 1.4×10^{-6}. We use a CFL number of 0.8 and 4 Gauss integration points. The corresponding results for the Fourier subscale using $M_{\text{freq}} = 1$, are not shown here because they are almost identical to the diagonal τ subscale ones.

2.4.2 Carter plate

We solve the flow over the Carter plate Shakib et al. [1991], Zienkiewicz et al. [1995] which is a two-dimensional supersonic viscous flow that enters a rectangular region from its left side at a Mach number of 3 and a Reynolds number of 1000. This problem reaches a steady state. The surface of the domain is divided in two parts, the first part from $x_1 = -1$ to $x_1 = -0.8$ is a slip wall and the rest of the surface from $x_1 = -0.8$ to $x_1 = 1$ is the so-called plate that is non-slip. The initial conditions are $M = 3$, $\rho = 1$, $\mathbf{u} = (1, 0)$, $T = 0.00028$, $\mu = 0.001$, and $Pr = 0.72$. c_{p}, c_{v}, and κ are determined to obtain the desired Mach and Prandtl numbers. We use in this problem the Sutherland viscosity law:

$$\frac{\mu}{\mu_{\mathrm{ref}}} = \frac{T_{\mathrm{ref}} + 110.3}{T + 110.3} \left(\frac{T}{T_{\mathrm{ref}}} \right)^{\frac{3}{2}} , \tag{2.67}$$

where μ_{ref} and T_{ref} are the inflow values of μ and T, respectively. We impose the following boundary conditions. The non-slip boundary condition on the plate consists of setting $\mathbf{u} = 0$ and a stagnation temperature of $T = 0.00078$. A slip boundary condition is imposed on the first section of the surface as well as on the top wall, that is we impose $u_2 = 0$. Velocity $\mathbf{u}$, density ρ, and temperature T are imposed on the inflow boundary at the same values as for the initial conditions and the outflow is left free of boundary conditions. We solve this problem using a structured mesh of 27000 rectangles and 27336 nodes. To avoid spurious oscillations around the shocks a discontinuity capturing diffusion is required. Isotropic shock capturing (2.61) is used in this problem. This case is solved using a CFL number of 0.6, 4 integration Gauss points, and $M_{\mathrm{freq}} = 2$ for the Fourier subscale. We consider that convergence is achieved when the total residual is of the order of 10^{-4}.

When the supersonic flow enters the region, a curved shock and a boundary layer are developed from the leading edge of the plate. The shock is formed due to the big inflow velocity and the changing boundary condition on the surface. This can be seen on the contours of the Mach number once the steady solution is reached, which are presented in Fig. 2.6. We observe that the diagonal τ subscale and the Fourier subscale give very similar result. This fact is also seen from Fig. 2.7, where we compare the Mach number result over a vertical line passing by $x_1 = 0$, for the two subscale options. It is observed that our results are in good agreement with those presented in the literature: Rispoli and Saavedra [2006], Shakib et al. [1991], Vázquez [1998].

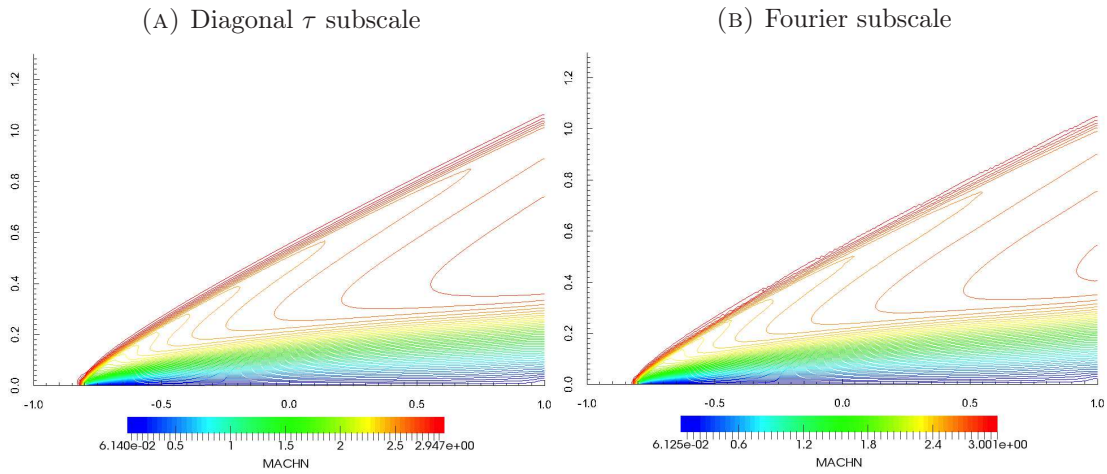

FIGURE 2.6: Carter's problem. Mach number contours corresponding to the diagonal τ subscale and the Fourier subscale. We use 4 Gauss points and the isotropic shock capturing for these simulations. The Fourier subscale uses $M_{\text{freq}} = 2$.

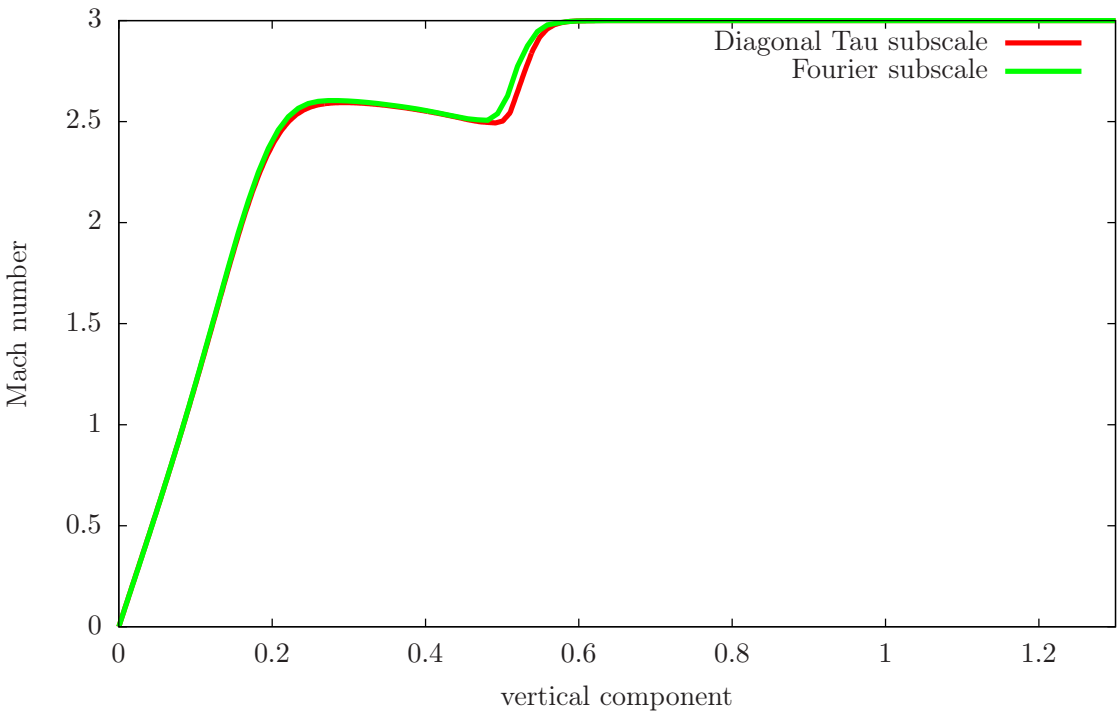

FIGURE 2.7: Carter's problem. Comparison of the diagonal τ subscale (red line) and the Fourier subscale (green line) results for the Mach number over a vertical line of the domain passing by $x_1 = 0$. We use 4 Gauss points and the isotropic shock capturing for these simulations. The Fourier subscale uses $M_{\text{freq}} = 2$.

2.4.3 Scramjet

We solve the two-dimensional inviscid flow past a supersonic scramjet inlet configuration having two struts Kumar [1981, 1982], Kumar and Tiwari [1982]. This problem reaches a steady state. The initial conditions are: the Mach number $M = 5$, the velocity $\mathbf{u} = (1, 0)$, the density $\rho = 1$, and the temperature $T = 1$. c_{p} and c_{v} are determined to obtain the desired Mach number. The boundary conditions consist of imposing the velocity, the density, and the temperature at the inflow and the outflow is set free. The normal velocity is imposed to be zero on the surface wall, the top wall, and the two struts boundaries. We use an unstructured mesh of 95103 triangles and 48535 nodal points. Anisotropic shock capturing (2.61) is required for this simulation, otherwise the solution blows-up. After numerical experiments, this case is solved using CFL numbers of 0.7 and 0.6 for the diagonal τ subscale and the Fourier subscale options, respectively, 3 integration Gauss points, and $M_{\mathrm{freq}} = 2$ for the Fourier subscale. The Fourier subscale scheme needs a smaller CFL, which makes us think that it is less robust than the diagonal τ subscale for this particular problem. We consider that convergence is achieved when the total residual is of the order of 10^{-5}.

In Fig. 2.8 we compare pressure and Mach number contours for the diagonal τ subscale and the Fourier subscale. We observe that the shocks are placed at the same location for both options, however the diagonal τ subscale option seems to better capture the shocks with less oscillations. In Fig. 2.9 we show for the diagonal τ subscale option the result of the Mach contours over two embedded meshes, the original one of 95103 elements and 48535 grid points, and a refined one having 380412 elements and 192200 grid points. We can appreciate that the shocks are sharper on the fine mesh but its placement is the same in both meshes. Compared with Kumar [1982] our results are less oscillatory and the shocks are more sharply captured.

(A) Pressure, Diagonal τ subscale

(B) Pressure, Fourier subscale

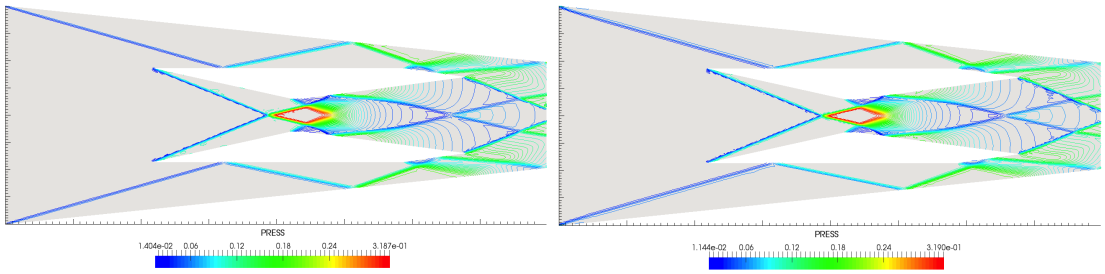

(C) Mach, Diagonal τ subscale

(D) Mach, Fourier subscale

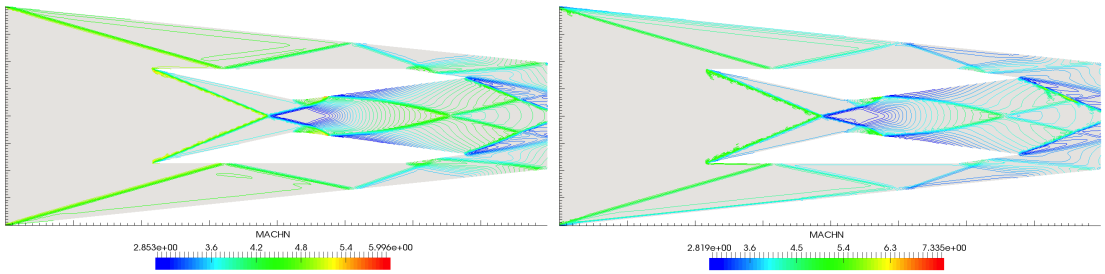

FIGURE 2.8: Scramjet problem. Scramjet contours for the pressure and the Mach number using anisotropic shock capturing and 3 Gauss points. The diagonal τ subscale and the Fourier subscale results are displayed for comparison. The Fourier subscale uses $M_{\text{freq}} = 2$.

(A) Original mesh

(B) Refined mesh

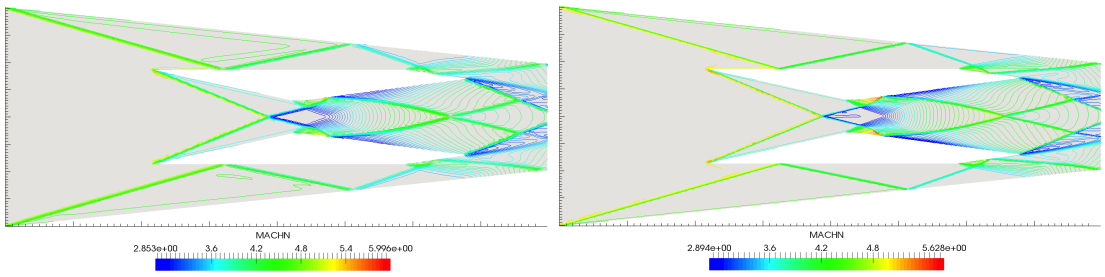

FIGURE 2.9: Scramjet problem. Contours of the Mach number for the diagonal τ subscale using the original mesh of 95103 elements and a refined embedded mesh of 380412 elements.

2.5 Summary and conclusions

We introduced a variational multiscale stabilization method for compressible flows. Two different options are considered concerning the modeling of the subscales: 1) the diagonal

τ subscale and 2) the Fourier subscale. Their results are compared on several test cases, for viscous and inviscid, steady and transient flows at different Mach numbers, from subsonic to supersonic regimes. The first option for the subscale presents a simpler structure, involves less computational cost, and gives similar or better results compared to the second option. For this reason, a variational multiscale stabilization based on the diagonal τ subscale is used in the rest of this work.

Chapter 3

VMS for dry and moist atmospheric flow

The compressible variational multiscale stabilization presented in Chapter 2 is here applied to the solution of the Euler equations for dry and moist nonhydrostatic stratified flows. This work is meant to verify how the algorithm performs when solving problems in the framework of nonhydrostatic atmospheric dynamics. This effort is justified by the previously observed good performance of VMS and by the advantages that a compact Galerkin formulation offers on massively parallel architectures —a paradigm for both computational fluid dynamics (CFD) and numerical weather prediction (NWP) practitioners. We also propose a simple technique to construct a well-balanced approximation of the dominant hydrostatics that, if not properly discretized, may cause unacceptable vertical oscillations. This is a relevant problem in NWP, especially in the proximity of steep topography. To evaluate the performance of the method for dry stratified environments standard 2D and 3D test cases are selected.

In the presence of moisture, the fully compressible Euler equations are coupled to a system of three advection equations that model the transport of water quantities in the atmosphere. A Kessler-type parametrization of microphysical processes of warm rain is used Kessler [1969]. Because analytical solutions for this problem are not available, the model is assessed by comparison with similar simulations presented in the literature. The metrics for evaluation are the intensity and spatial distribution of the storm, its duration, the location of precipitation, and water accumulation at different grid resolutions.

This work is done in collaboration with an expert in the meteorological field, Simone Marras. Taking profit of his expertise in the physics of the atmosphere, the contribution of the present thesis in this atmospheric flow simulation is on the stabilization and numerical treatment of the problem.

3.1 Equations of dry nonhydrostatic compressible flows

Let $d = 3$ be the space dimension. Given a bounded domain $\Omega \subset \mathbb{R}^d$ and a time interval $(0, T)$, $T \in \mathbb{R}^+$, we write the Euler equations of atmospheric flows Klemp et al. [2007] with no Coriolis effects as:

$$\frac{\partial \mathbf{q}}{\partial t} + \mathcal{L}(\mathbf{q}) = \mathbf{f}(\mathbf{q}) \,, \tag{3.1}$$

where $\mathbf{q}$ is the vector of the unknowns, $\mathcal{L}$ is the differential operator, and $\mathbf{f}$ is the source vector. We have:

$$\mathbf{q} = \begin{bmatrix} U \\ V \\ W \\ \rho \\ \theta \end{bmatrix}, \quad \mathcal{L}(\mathbf{q}) = \begin{bmatrix} \nabla \cdot \left(\frac{\mathbf{U}U}{\rho} + p\mathbf{e}_x \right) \\ \nabla \cdot \left(\frac{\mathbf{U}V}{\rho} + p\mathbf{e}_y \right) \\ \nabla \cdot \left(\frac{\mathbf{U}W}{\rho} + p\mathbf{e}_z \right) \\ \nabla \cdot \mathbf{U} \\ \frac{\mathbf{U}}{\rho} \cdot \nabla\theta \end{bmatrix}, \quad \mathbf{f}(\mathbf{q}) = \begin{bmatrix} 0 \\ 0 \\ -\rho\, g \\ 0 \\ 0 \end{bmatrix},$$

where $\nabla = \left(\frac{\partial}{\partial x}, \frac{\partial}{\partial y}, \frac{\partial}{\partial z} \right)$, and $\mathbf{e}_x = (1,0,0)^{\mathrm{T}}$, $\mathbf{e}_y = (0,1,0)^{\mathrm{T}}$, and $\mathbf{e}_z = (0,0,1)^{\mathrm{T}}$ are the unitary vectors in the space directions x, y, and z, respectively. Superscript T indicates the transpose operator. Density ρ, momentum $\mathbf{U} = (U, V, W)^{\mathrm{T}}$, and potential temperature θ are functions of space $\mathbf{x} = (x, y, z)$ and time t. We also define the velocity $\mathbf{u} = \mathbf{U}/\rho = (u, v, w)$. The acceleration of gravity, of modulus g, acts along the vertical direction. It is understood that in two dimensions, the y-direction disappears. System (3.1) is closed by the state law for pressure

$$p = p_0 \left(\frac{R\,\rho\theta}{p_0} \right)^{\gamma}, \tag{3.2}$$

where $p_0 = 10^5\, Pa$ is the surface pressure. The problem consists in finding $\mathbf{q}(\mathbf{x}, t)$ such that equation (3.1) with proper boundary and initial conditions is verified $\forall (\mathbf{x}, t) \in \Omega \times (0, T)$.

Hydrostatic balance Dynamics in the atmosphere is characterized by small variations of the thermodynamic quantities with respect to some background reference state Klein [2000], Marchuk [1974]. This is expressed by the splitting $\rho(\mathbf{x}, t) = \rho'(\mathbf{x}, t) + \bar{\rho}(z)$, $p(\mathbf{x}, t) = p'(\mathbf{x}, t) + \bar{p}(z)$, and $\theta(\mathbf{x}, t) = \theta'(\mathbf{x}, t) + \bar{\theta}(z)$, where the primed and barred quantities represent, respectively, the perturbation and the background state of ρ, p, and θ, and are such that $\rho' \ll \bar{\rho}$, $p' \ll \bar{p}$ and $\theta' \ll \bar{\theta}$. The barred quantities only depend on

the vertical direction z. When vertical acceleration is zero, the third of equations (3.1) simplifies to the equation for hydrostatic balance

$$\partial_z \bar{p} = -g\bar{\rho}. \tag{3.3}$$

Given the considerations above and the analysis of nearly-hydrostatic flows for well-balanced methods Botta et al. [2004], $\mathcal{L}$ and $\mathbf{f}$ in (3.1) change to

$$\mathcal{L}(\mathbf{q}) = \begin{bmatrix} \nabla \cdot \left(\frac{\mathbf{U}U}{\rho} + p' \mathbf{e}_x \right) \\ \nabla \cdot \left(\frac{\mathbf{U}V}{\rho} + p' \mathbf{e}_y \right) \\ \nabla \cdot \left(\frac{\mathbf{U}W}{\rho} + p' \mathbf{e}_z \right) \\ \nabla \cdot \mathbf{U} \\ \frac{\mathbf{U}}{\rho} \cdot \nabla \theta \end{bmatrix}, \quad \mathbf{f}(\mathbf{q}) = \begin{bmatrix} 0 \\ 0 \\ -\rho' g \\ 0 \\ 0 \end{bmatrix}. \tag{3.4}$$

System (3.1) with fluxes and source defined as (3.4) is used in this chapter.

3.2 Microphysics and definitions for moist atmospheres

Cloud microphysics includes all the thermo-physical processes at the scales of the particles that form the cloud. Examples are the phase change of water quantities or the agglomeration of particles into larger ones. The most common representation of cloud microphysics was designed by Kessler [1969]. Kessler's model is a microphysical parametrization, meaning that it relies on the physical knowledge of certain processes without the need for a full computation of all the microscale processes that are involved. Kessler's model only considers three forms of water: water vapor, cloud water, and rain water. Ice or drizzle for example, are not considered. Then water substances in the atmosphere are treated in terms of density of water vapor, ρ_v, density of cloud water, ρ_c, and density of rain, ρ_r. The notation and the thermodynamics of water quantities is briefly introduced. The details of moist convection are found in Bannon [2002], Emanuel [1994], Iribarne and Godson [1981]. Given the density of dry air, ρ_d, the mixing ratios of vapor, cloud, and rain are

$$q_i = \frac{\rho_i}{\rho_d} \qquad i = v, c, r \ . \tag{3.5}$$

Pressure of moist air, p, is the sum of the partial pressure of dry air and the partial pressure of vapor, we have:

$$p = \rho_d \, R_d \, T \left(1 + \frac{q_v}{\varepsilon} \right), \tag{3.6}$$

where T indicates temperature, $R_d = 287\, J\, kg^{-1}\, K^{-1}$ is the gas constant of dry air, $\varepsilon = R_d/R_v$, and $R_v = 461\, J\, kg^{-1}\, K^{-1}$ is the gas constant of water vapor. Density

temperature is defined as

$$T_\rho = T\frac{1+q_v/\varepsilon}{1+q_t}\,, \tag{3.7}$$

where $q_t = q_v + q_c + q_r$. From (3.7), density potential temperature is

$$\theta_\rho = T_\rho\left(\frac{p_0}{p}\right)^{R_d/c_{pd}}\,, \tag{3.8}$$

where $p_0 = 10^5\,Pa$ and $c_{pd} = 1004\,J\,kg^{-1}\,K^{-1}$ is the specific heat of dry air at constant pressure. In terms of θ_ρ, the equation of state becomes

$$p = p_0\left(\frac{R_d\,\rho_d\theta_\rho}{p_0}\right)^{c_{pd}/c_{vd}}\,, \tag{3.9}$$

where $c_{vd} = 717\,J\,kg^{-1}\,K^{-1}$ is the specific heat of dry air at constant volume.

3.3 Equations of moist nonhydrsotatic compressible flows

Moist dynamics can be modeled through the coupling of the Euler equations of non-viscous compressible flows (3.1) that are used to model the environmental motion, and three transport equations for water species being transported by the atmosphere. The Euler equations of atmospheric flows without rotation (3.1) with the presence of moisture can be expressed in two dimensions as

$$\frac{\partial \mathbf{q}}{\partial t} + \mathcal{L}(\mathbf{q}) = \mathbf{f}(\mathbf{q})\,, \tag{3.10}$$

where

$$\mathbf{q} = \begin{bmatrix} U \\ W \\ \rho_d \\ \theta_\rho \end{bmatrix}, \quad \mathcal{L}(\mathbf{q}) = \begin{bmatrix} \nabla\cdot\left(\frac{\mathbf{U}U}{\rho_d} + p'\mathbf{e}_x\right) \\ \nabla\cdot\left(\frac{\mathbf{U}W}{\rho_d} + p'\mathbf{e}_z\right) \\ \nabla\cdot\mathbf{U} \\ \frac{\mathbf{U}}{\rho_d}\cdot\nabla\theta_\rho \end{bmatrix}, \quad \mathbf{f}(\mathbf{q}) = \begin{bmatrix} 0 \\ -\rho_d' g\,(1+q_v'+q_c+q_r) \\ 0 \\ S_{\theta_\rho} \end{bmatrix}. \tag{3.11}$$

We use the same notation as in section 3.1. Buoyancy of moist air in the momentum equation is due to the term $-\rho_d' g\,(q_v' + q_c + q_r)$. The source or sink term S_{θ_ρ} includes the latent heat release or gain that occurs during the phase changes of moisture variables.

In (3.11), q_v', q_c, and q_r come from the solution of the following transport equation:

$$\frac{\partial \varphi}{\partial t} + \mathcal{M}(\varphi) = \mathbf{m}(\varphi)\,, \tag{3.12}$$

where

$$\varphi = \begin{bmatrix} q_v' \\ q_c \\ q_r \end{bmatrix}, \quad \mathcal{M}(\varphi) = \mathbf{u} \cdot \nabla \begin{bmatrix} q_v' \\ q_c \\ q_r \end{bmatrix}, \quad \mathbf{m}(\varphi) = \begin{bmatrix} S_{q_v} \\ S_{q_c} \\ S_{q_r} \end{bmatrix}. \tag{3.13}$$

The quantities $S_{q_v}, S_{q_c}, S_{q_r}$ above, and S_{θ_ρ} in the energy equation, include the micro-physical processes of condensation, coalescence, and evaporation that are described in what follows. How the source terms of the previous equations are defined and how they affect the dynamics of the simulation is determined by these processes. The illustrations reported in this section are not exhaustive. The reader is referred to the literature for a more thorough analysis (e.g. see Houze [1993] and references therein).

Given the approximated Teten's formula for saturation vapor pressure, suggested in Bolton [1980] as

$$e^* = 611.2\exp\left(\frac{17.67\,T}{T + 243.5}\right),$$

the saturation mixing ratio is

$$q_{vs} = \frac{\varepsilon e^*}{p - e^*}. \tag{3.14}$$

From Klemp and Wilhelmson [1978], the S-terms in (3.13) are

$$\begin{aligned} S_{\theta_\rho} &= -\tfrac{L_v}{c_p T}\left(\dot{q}_{vs} + E_r\right), \\ S_{q_v} &= \dot{q}_{vs} + E_r, \\ S_{q_c} &= -\dot{q}_{vs} - A_r - C_r, \\ S_{q_r} &= \tfrac{1}{\rho}\tfrac{\partial}{\partial z}(\rho V_r q_r) - E_r + A_r + C_r, \end{aligned} \tag{3.15}$$

where $L_v = L_{v0} - (c_{pl} - c_{pv})(T - T_0)$ is the latent heat of vaporization with reference value $L_{v0} = 2.5e{+}6\,J\,kg^{-1}$, c_{pl} and c_{pv} are the heat coefficients of liquid water and water vapor, respectively, at constant pressure, T_0 is a reference temperature, V_r is the terminal fall speed of raindrops (taken positive in the downward direction), and $\dot{q_{vs}}$ is the rate of condensation or evaporation (the dot symbol indicates time derivative). A_r, C_r, and E_r are the rates of auto-conversion, collection, and evaporation, respectively, of rain. They are computed using the formulas:

$$A_r = \texttt{MAX}\left(0, k_1(q_c - a_T)\right), \tag{3.16a}$$

$$C_r = k_2 \rho^{0.375}\, q_c\, q_r^{0.875}, \tag{3.16b}$$

$$E_r = -\frac{1}{\rho}\frac{(q_v/q_{vs}-1)k(\rho\, q_r)^{0.525}}{5.4\times 10^5 + 2.55\times 10^6 (p\, q_{vs})}\ , \tag{3.16c}$$

where Kessler's parameters are $k_1 = 0.001\, s^{-1}$, $k_2 = 2.2\, s^{-1}$, $a_T = 0.001\, kg\, kg^{-1}$, and k is the ventilation factor that is a function of the terminal fall speed.

Method of solution At every time step, systems (3.10) and (3.12) are solved separately. Phase changes are applied using the saturation adjustment technique of Soong and Ogura [1973]. This consists in solving the problem in two steps. First, the equations are solved by the finite element method with an explicit time integration scheme and without considering phase change. The equations without the terms of phase change are:

$$\frac{\partial q}{\partial t} + \mathcal{L}(q) = \mathbf{h}(q)\ , \tag{3.17}$$

where

$$\mathbf{h}(q) = \begin{bmatrix} 0 \\ 0 \\ -\rho_d' g\,(1 + q_v' + q_c + q_r) \\ 0 \end{bmatrix}, \tag{3.18}$$

and

$$\frac{\partial \varphi}{\partial t} + \mathcal{M}(\varphi) = 0\ . \tag{3.19}$$

Second, the solution variables are corrected using Kessler microphysics. See algorithm 1.

Algorithm 1 Steps to add microphysical processes using saturation adjustment.

Initialize $\mathbf{q}^0$ and φ^0
for all time-step n **do**
1. **Dry atmosphere and transport solution:**
   Compute $\mathbf{q}^n$, the n solution of (3.17) using explicit FE.
   Compute φ^n, the n solution of (3.19) using explicit FE.
2. **Phase change variables:**
   Compute S_{θ_v} and $\mathbf{m}$ from Kessler microphysics.
3. **Moist solution:**
   Update $\mathbf{q}^n$ and φ^n using S_{θ_ρ} and $\mathbf{m}$.

end do

3.4 Numerical formulation

We present in this section the discretization of the dry and moist atmospheric equations. The space discretization is done by finite elements stabilized by the variational multiscale method, while discretization in time is done by explicit finite differences. In the case of dry atmospheric flow we consider set (3.1) for discretization, and with the presence of moisture we discretize systems (3.17) and (3.19).

3.4.1 Compressible VMS for dry atmospheres

We proceed in analogous way to section 2.3 and do the same assumptions. In the framework of VMS we write

$$\mathbf{q} = \mathbf{q}^h + \tilde{\mathbf{q}}\,, \tag{3.20}$$

and obtain the weak stabilized form of (3.1) as

$$\begin{aligned} &\textstyle\int_{\Omega^h} \psi^h \frac{\partial \mathbf{q}^h}{\partial t}\, d\Omega^h + \int_{\Omega^h} \psi^h \mathcal{L}(\mathbf{q}^h)\, d\Omega^h - \int_{\Omega^h} \psi^h\, \mathbf{f}(\mathbf{q}^h) d\Omega^h \\ &+ \textstyle\int_{\Omega^h} \psi^h \mathcal{L}(\mathbf{q}^h, \tilde{\mathbf{q}})\, d\Omega^h - \int_{\Omega^h} \psi^h \mathbf{f}(\tilde{\mathbf{q}})\, d\Omega^h = 0 \qquad \forall\, \psi^h \in W^h\,, \end{aligned} \tag{3.21}$$

where the linearization for the $\mathcal{L}$ operator is chosen as

$$\mathcal{L}(\mathbf{q}, \tilde{\mathbf{q}}) = \begin{bmatrix} \nabla \cdot \tilde{\mathbf{U}} \\ \nabla \cdot \left(\frac{\mathbf{U}\tilde{U}}{\rho} + \frac{c_o}{2} (\rho\theta)^{\gamma-1} (\theta\tilde{\rho} + \rho\tilde{\theta}) \mathbf{e}_x \right) \\ \nabla \cdot \left(\frac{\mathbf{U}\tilde{V}}{\rho} + \frac{c_o}{2} (\rho\theta)^{\gamma-1} (\theta\tilde{\rho} + \rho\tilde{\theta}) \mathbf{e}_y \right) \\ \nabla \cdot \left(\frac{\mathbf{U}\tilde{W}}{\rho} + \frac{c_o}{2} (\rho\theta)^{\gamma-1} (\theta\tilde{\rho} + \rho\tilde{\theta}) \mathbf{e}_z \right) \\ \frac{\mathbf{U}}{\rho} \cdot \nabla\tilde{\theta} \end{bmatrix}\,,$$

where $c_0 = p_0\,(R/p_0)^{\gamma}$. To eliminate the $\tilde{\mathbf{q}}$ derivatives in $\mathcal{L}(\mathbf{q}^h, \tilde{\mathbf{q}})$, we integrate by parts the corresponding term in (3.21) and assume the resulting boundary term equal to zero, obtaining:

$$\begin{aligned} &\textstyle\int_{\Omega^h} \psi_p^h \frac{\partial \mathbf{q}^h}{\partial t}\, d\Omega^h + \underbrace{\int_{\Omega^h} \psi_p^h \mathcal{L}(\mathbf{q}^h)\, d\Omega^h - \int_{\Omega^h} \psi_p^h\, \mathbf{f}(\mathbf{q}^h)\, d\Omega^h}_{\text{Galerkin term}} \\ &\underbrace{- \int_{\Omega^h} \mathbf{s}(\psi_p^h, \mathbf{q}^h, \tilde{\mathbf{q}})\, d\Omega^h - \int_{\Omega^h} \psi_p^h \mathbf{f}(\tilde{\mathbf{q}})\, d\Omega^h}_{\text{Stabilization term}} = 0\,, \end{aligned} \tag{3.22}$$

holding for all $p \in \{1, \dots, N\}$, where

$$\mathbf{s}(\psi_p^h, \mathbf{q}^h, \tilde{\mathbf{q}}) = \nabla\psi_p^h \cdot \begin{bmatrix} \tilde{\mathbf{U}} \\ \frac{\mathbf{U}_h\tilde{U}}{\rho_h} + \frac{c_o}{2}(\rho_h\theta_h)^{\gamma-1}(\theta_h\tilde{\rho} + \rho_h\tilde{\theta})\mathbf{e}_x \\ \frac{\mathbf{U}_h\tilde{V}}{\rho_h} + \frac{c_o}{2}(\rho_h\theta_h)^{\gamma-1}(\theta_h\tilde{\rho} + \rho_h\tilde{\theta})\mathbf{e}_y \\ \frac{\mathbf{U}_h\tilde{W}}{\rho_h} + \frac{c_o}{2}(\rho_h\theta_h)^{\gamma-1}(\theta_h\tilde{\rho} + \rho_h\tilde{\theta})\mathbf{e}_z \\ \frac{\mathbf{U}_h}{\rho_h}\tilde{\theta} \end{bmatrix} + \psi_p^h \begin{bmatrix} 0 \\ 0 \\ 0 \\ 0 \\ \nabla \cdot \left(\frac{\mathbf{U}_h}{\rho_h}\right)\tilde{\theta} \end{bmatrix} .$$

Equation (3.26) is the weak stabilized form of equation (3.1).

The subscales are approximated in every element $K \in \mathcal{P}^h$ as described in equation (2.24). We repeat this expression here for the sake of completeness:

$$\tilde{\mathbf{q}} = \tau\ \mathbf{r}(\mathbf{q}^h)\ , \tag{3.23}$$

where

$$\mathbf{r}(\mathbf{q}^h) = -\mathcal{L}(\mathbf{q}^h) + \mathbf{f}(\mathbf{q}^h) \tag{3.24}$$

is the residual of the governing equation and $\tau = \text{diag}(\tau_\rho, \tau_\text{U}, \tau_\text{V}, \tau_\text{W}, \tau_\theta)$ is the stabilization diagonal matrix. We define τ element-wise as follows

$$\tau_\rho = \tau_U = \tau_V = \tau_W = \frac{1}{4}\frac{h}{||\mathbf{u}|| + c} \qquad \text{and} \qquad \tau_\theta = \frac{1}{4}\frac{\text{h}}{||\mathbf{u}||}\ . \tag{3.25}$$

Above, h is the element characteristic length that, in this work, is taken as the shortest edge of the element. The expression for τ_ρ, τ_U, τ_V, and τ_W meet expression (2.25) when $\mu = 0$, except for the factor $\frac{1}{4}$ which is used in the Euler equations of atmospheric flows case because is seen to perform better for the examples that we solve, otherwise the results become too diffusive. We think that this is due to the fact that we are dealing with very low Mach problems. Concerning τ_θ, we observe better stabilization if it does not depend on c, because $||\mathbf{u}||$ is the characteristic speed of the last equation of system (3.1). It is important to see the local nature of the sub-scales that are meant to exist only where residuals are important. This, with non-constant values, marks the major difference with respect to artificial diffusion. This fact is illustrated in Figs. 3.2 and 3.4, where the physical structure and the values of $\tilde{\mathbf{q}}$ (normalized with respect to the corresponding maximum value of $\mathbf{q}$) are shown, for two of the benchmarks solved in Section 3.5.

VMS can not be seen as a physical viscosity. Considering equations (3.4.1) and (3.31), we see that the VMS stabilization is not only made of diffusion-like terms, but by terms that can not be classified as viscous contributions. VMS stabilization is a result of their interaction.

3.4.2 Compressible VMS for moist atmospheres

Compressible VMS is here applied to systems (3.17) and (3.19). We proceed as is subsection 3.4.1 and use the same notation. Then we obtain the stabilized weak form of the Euler equation (3.17) as

$$\begin{aligned}&\int_{\Omega^h} \psi_p^h \tfrac{\partial \mathbf{q}^h}{\partial t}\, d\Omega^h + \underbrace{\int_{\Omega^h} \psi_p^h \mathcal{L}(\mathbf{q}^h)\, d\Omega^h - \int_{\Omega^h} \psi_p^h\, \mathbf{h}(\mathbf{q}^h)\, d\Omega^h}_{\text{Galerkin term}} \\ &\underbrace{- \sum_{K\in\mathcal{P}_h} \int_K \left(\mathbf{s}_{\mathrm{E}}(\psi_p^h, \mathbf{q}^h, \tilde{\mathbf{q}}) - \psi_p^h\, \mathbf{h}(\tilde{\mathbf{q}})\right) dK}_{\text{Stabilization term}} = 0\,,\end{aligned} \tag{3.26}$$

holding for all $p \in \{1, \dots, N\}$, where

$$\mathbf{s}_{\mathrm{E}}(\psi_p^h, \mathbf{q}^h, \tilde{\mathbf{q}}) = \nabla\psi_p^h \cdot \begin{bmatrix} \tilde{\mathbf{U}} \\ \frac{\mathbf{U}^h \tilde{U}}{\rho^h} + \frac{c_o}{2}(\rho^h\theta_\rho^h)^{\gamma-1}(\theta_\rho^h\tilde{\rho} + \rho^h\tilde{\theta}_\rho)\mathbf{e}_x \\ \frac{\mathbf{U}^h \tilde{W}}{\rho^h} + \frac{c_o}{2}(\rho^h\theta_\rho^h)^{\gamma-1}(\theta_\rho^h\tilde{\rho} + \rho^h\tilde{\theta}_\rho)\mathbf{e}_z \\ \frac{\mathbf{U}^h}{\rho^h}\tilde{\theta}_\rho \end{bmatrix} + \psi_p^h \begin{bmatrix} 0 \\ 0 \\ 0 \\ \nabla\cdot\left(\frac{\mathbf{U}^h}{\rho^h}\right)\tilde{\theta}_\rho \end{bmatrix}. \tag{3.27}$$

We note that the stabilization term of equation (3.26) is computed using the fluxes and source terms defined in (3.1) instead of (3.4).

With analogous reasoning, the splitting $\varphi = \varphi^h + \tilde{\varphi}$ yields the stabilized weak form of equation the transport equation (3.19) as

$$\int_{\Omega^h} \psi_p^h\, \tfrac{\partial \varphi^h}{\partial t}\, d\Omega^h + \underbrace{\int_{\Omega^h} \psi_p^h\, \mathcal{M}(\varphi^h)\, d\Omega^h}_{\text{Galerkin term}} \underbrace{- \sum_{K\in\mathcal{P}_h} \int_K \mathbf{s}_{\mathrm{T}}(\psi_p^h, \tilde{\varphi})\, dK}_{\text{Stabilization term}} = 0\,, \tag{3.28}$$

holding for all $p \in \{1, \dots, N\}$, where $\mathcal{M}(\varphi^h) = \mathbf{u}^h \cdot \nabla\varphi^h$ and

$$\mathbf{s}_{\mathrm{T}}(\psi_p^h, \tilde{\varphi}) = (\nabla\psi_p^h \cdot \mathbf{u}^h + \psi_p^h\, \nabla\cdot\mathbf{u}^h)\,\tilde{\varphi}\,. \tag{3.29}$$

We define φ^h as the projection of φ onto W^h and expand it as

$$\varphi^h(\mathbf{x}, t) = \sum_{p=1}^{N} \psi_p^h(\mathbf{x})\, \varphi_p^h(t)\,, \tag{3.30}$$

where $\xi \in \Omega^h$ and $\varphi_p^h(t)$ is the value of φ^h at node $\mathbf{x}^p$ and time t.

The subgrid scales are approximated in every element $K \in \mathcal{P}^h$ by the corresponding residual-based expressions

$$\tilde{\mathbf{q}} = \tau_{\mathrm{E}}\, \mathbf{r}_{\mathrm{E}}(\mathbf{q}^h) \qquad \text{and} \qquad \tilde{\varphi} = \tau_{\mathrm{T}}\, \mathbf{r}_{\mathrm{T}}(\varphi^h)\ , \tag{3.31}$$

where τ_{E} and τ_{T} are the stabilization parameter matrices of the Euler and transport equations, respectively; and $\mathbf{r}_{\mathrm{E}}(\mathbf{q}^h) = -\mathcal{L}(\mathbf{q}^h) + \mathbf{h}(\mathbf{q}^h)$ and $\mathbf{r}_{\mathrm{T}}(\varphi^h) = -\mathcal{M}(\varphi^h)$ are the residuals of equations (3.17) and (3.19), respectively. For the compressible Euler equations (3.17), the stabilization parameter τ_{E} is that of equation (3.25). Concerning the transport equations (3.19), we use the classical stabilization parameter of Hughes and Mallet [1986a]:

$$\tau_{\mathrm{T}} = \frac{1}{2}\frac{h}{||\mathbf{u}||}\ . \tag{3.32}$$

Turbulent mixing is an important ingredient in the simulation of moist atmospheres. Because in this work turbulence is not accounted for, the limitations of the model that we present are obvious. In the absence of a proper turbulence closure scheme, many research codes represent subgrid-scale mixing with an artificial viscous term. The amount of diffusivity that VMS introduces is localized and limited to the regions of important gradients, as it will be seen in the numerical results of this chapter. In the current formulation, it cannot be considered as a type of turbulence model. Research is indeed being carried out in this direction and the reader is referred to, e.g., Bazilevs et al. [2007], Koobus and Charbel [2004], Wasberg et al. [2009], where a large eddy simulation (LES) system based on the ideas behind VMS is described. The main difference between VMS described in this article and VMS defined for LES, lies in the additional viscous stresses that are necessary for a proper turbulence modeling and that are considered in the three referenced articles. This topic represents an open field of research that, however, goes beyond the scope of this work.

3.4.3 Time discretization for dry atmospheres

Although we are fully aware of its limits when applied to atmospheric simulations, in this work we simply apply a linear explicit Euler time integration scheme. Time discretization

of (3.26) gives

$$\begin{aligned}\int_{\Omega^h} \psi_p^h \tfrac{\mathbf{q}^{h,n+1}-\mathbf{q}^{h,n}}{\Delta t}\, d\Omega^h &= -\int_{\Omega^h} \psi_p^h \mathcal{L}(\mathbf{q}^{h,n})\, d\Omega^h + \int_{\Omega^h} \psi_p^h\, \mathbf{f}(\mathbf{q}^{h,n})\, d\Omega^h \\ &+ \int_{\Omega^h} \mathbf{s}(\psi_p^h, \mathbf{q}^{h,n}, \tilde{\mathbf{q}}^{n+1})\, d\Omega^h + \int_{\Omega^h} \psi_p^h \mathbf{f}(\tilde{\mathbf{q}}^{n+1})\, d\Omega^h\ .\end{aligned} \tag{3.33}$$

holding for all $p \in \{1, \ldots, N\}$, where we define $\tilde{\mathbf{q}}^{n+1} = \tau\ \mathbf{r}(\mathbf{q}^{h,n})$. As done in subsection 2.3.5, an elementary time step is defined as

$$\Delta t^{\,el} = C\ \frac{1}{4}\frac{h}{||\mathbf{u}|| + c}\ , \tag{3.34}$$

where $C \in (0, 1)$ is the CFL number and h is the smallest edge length of the element. Expression (3.34) is recovered as well from (2.47) when the particular case of the Euler equations is considered. $\Delta t^{\,el}$ is interpolated on the nodes of the grid, obtaining a local time step $\Delta t^{\,p}$, $p = 1, \ldots, N$, at each node $\mathbf{x}^p$ of the grid. As it is expressed in (2.48), the global time step is computed as the minimum time step of the domain:

$$\Delta t = \min_{p=1,\ldots,N} \{\Delta t^{\,p}\}\ . \tag{3.35}$$

As it is analogously done in subsection 2.3.5, the value of $\mathbf{q}^{h,n+1}$ at each node of the computational grid is

$$\mathbf{q}^{h,n+1} = \mathbf{q}^{h,n} + \Delta t\ \mathbf{M}^{-1}\left(\mathbf{G}(\mathbf{q}^{h,n}) + \mathbf{S}(\mathbf{q}^{h,n}, \tilde{\mathbf{q}}^{n+1})\right)\ , \tag{3.36}$$

In (3.38), $\mathbf{M}$ is the global mass matrix, defined in (2.50), which is diagonalized by lumping techniques Hughes [2000]. $\mathbf{G}$ and $\mathbf{S}$ are the Galerkin and stabilization vectors, respectively, which are constructed by assembly of

$$\mathbf{G}^p(\mathbf{q}^{h,n}) = -\int_{\Omega^h} \psi_p^h \mathcal{L}(\mathbf{q}^{h,n})\, d\Omega^h + \int_{\Omega^h} \psi_p^h\, \mathbf{f}(\mathbf{q}^{h,n})\, d\Omega^h$$

$$\mathbf{S}^p(\mathbf{q}^{h,n}, \tilde{\mathbf{q}}^{n+1}) = \int_{\Omega^h} \mathbf{s}(\psi_p^h, \mathbf{q}^{h,n}, \tilde{\mathbf{q}}^{n+1})\, d\Omega^h + \int_{\Omega^h} \psi_p^h \mathbf{f}(\tilde{\mathbf{q}}^{n+1})\, d\Omega^h\ ,$$

respectively, for $p = 1, \ldots, N$. We define $\tilde{\mathbf{q}}^{n+1} = \tau\, \mathbf{r}(\mathbf{q}^{h,n})$ and $\mathbf{q}^{h,n}$ is computed using equality (2.12). All the integrals above are approximated by Gauss quadrature (2.53).

Well-balanced atmosphere and interpolation error Numerical integration by the Gauss quadrature rule demands a linear interpolation of the integrand from the grid nodes to the Gauss points placed inside the element. In a problem where small perturbations from a reference state are the quantities of interest, if the interpolation step of the

reference state values is not done properly the hydrostatic balance can not be assured. This is because the error of interpolation of the reference state would be orders of magnitude larger than the approximated values of the perturbation variables. To maintain a balanced state up to machine precision, we opt for a simple technique that consists of explicitly computing the reference quantities at the Gauss points, while interpolating only the deviation variables. We test this equilibrium preserving methodology by the two-dimensional equilibrium test presented in Botta et al. [2004] and Gassmann [2010], a resting atmosphere over a steep mountain that must remain still at all times. We observe that equilibrium is indeed preserved with this simple technique; the same does not apply if the same exercise is solved without the explicit computation of the reference state at the Gauss nodes. For more detail on this test refer to Marras [2012], Marras et al. [2013a].

No special numerical treatment or special assumption on the governing equations are considered for the low Mach regime typical of atmospheric dynamics. Nevertheless, this algorithm can treat a widespread range of flow regimes including very low Mach number flows.

No dimensional splitting is used in that both the horizontal and vertical directions are not distinguished in the discretization process. In other words, the Euler equations are solved by the same numerical method in all space dimensions. The great advantage of this is that the code becomes totally free from the geometry of the grid. This approach is classical in CFD and was first applied in NWP by Bacon et al. [2000], Bonaventura [2000], Giraldo and Restelli [2008] using finite volumes, finite differences, and high order spectral elements, respectively.

3.4.4 Time discretization for moist atmospheres

As it is analogously presented in subsection 3.4.3, time discretization of (3.26) by a forward Euler method gives

$$\begin{aligned}&\int_{\Omega^h} \psi_p^h \, \tfrac{\mathbf{q}^{h,n+1}-\mathbf{q}^{h,n}}{\Delta t} \, d\Omega^h = -\int_{\Omega^h} \psi_p^h \, \mathcal{L}(\mathbf{q}^{h,n}) \, d\Omega^h + \int_{\Omega^h} \psi_p^h \, \mathbf{h}(\mathbf{q}^{h,n}) \, d\Omega^h \\ &+ \textstyle\sum_{K\in\mathcal{P}_h} \int_K \left(\mathbf{s}_{\mathrm{E}}(\psi_p^h, \mathbf{q}^{h,n}, \tilde{\mathbf{q}}^{n+1}) + \psi_p^h \, \mathbf{h}(\tilde{\mathbf{q}}^{n+1}) \right) dK \, ,\end{aligned} \tag{3.37}$$

holding for all $p \in \{1, \ldots, N\}$. Then the value of $\mathbf{q}^{h,n+1}$ at each node of the computational grid is obtained as

$$\mathbf{q}^{h,n+1} = \mathbf{q}^{h,n} + \Delta t \, \mathbf{M}^{-1} \left(\mathbf{G}_{\mathrm{E}}(\mathbf{q}^{h,n}) + \mathbf{S}_{\mathrm{E}}(\mathbf{q}^{h,n}, \tilde{\mathbf{q}}^{n+1}) \right) \, , \tag{3.38}$$

where $\mathbf{G}$ and $\mathbf{S}$ are the Galerkin and stabilization vectors, respectively, which are constructed by assembly of

$$\mathbf{G}_{\mathrm{E}}^{p}(\mathbf{q}^{h,n}) = -\int_{\Omega^h} \psi_p^h \, \mathcal{L}(\mathbf{q}^{h,n}) \, d\Omega^h + \int_{\Omega^h} \psi_p^h \, \mathbf{f}(\mathbf{q}^{h,n}) \, d\Omega^h$$

$$\mathbf{S}_{\mathrm{E}}^{p}(\mathbf{q}^{h,n}, \tilde{\mathbf{q}}^{n+1}) = \sum_{K \in \mathcal{P}_h} \int_K \left(\mathbf{s}_{\mathrm{E}}(\psi_p^h, \mathbf{q}^{h,n}, \tilde{\mathbf{q}}^{n+1}) + \psi_p^h \, \mathbf{h}(\tilde{\mathbf{q}}^{n+1}) \right) dK \, ,$$

respectively, for $p = 1, \ldots, N$. We define $\tilde{\mathbf{q}}^{n+1} = \tau_{\mathrm{E}} \, \mathbf{r}_{\mathrm{E}}(\mathbf{q}^{h,n})$ and $\mathbf{q}^{h,n}$ is computed using equality (2.12).

For the transport equation (3.28) we proceed analogously and obtain the corresponding discretized expression

$$\varphi^{h,n+1} = \varphi^{h,n} + \Delta t \, \mathbf{M}^{-1} \left(\mathbf{G}_{\mathrm{T}}(\varphi^{h,n}) + \mathbf{S}_{\mathrm{T}}(\varphi^{h,n}, \tilde{\varphi}^{n+1}) \right), \tag{3.39}$$

where

$$\mathbf{G}_{\mathrm{T}}^{p}(\varphi^{h,n}) = -\int_{\Omega^h} \psi_p^h \, \mathcal{M}(\varphi^{h,n}) \, d\Omega^h$$

$$\mathbf{S}_{\mathrm{T}}^{p}(\varphi^{h,n}, \tilde{\varphi}^{n+1}) = \sum_{K \in \mathcal{P}_h} \int_K \mathbf{s}_{\mathrm{T}}(\psi_p^h, \tilde{\varphi}^{n+1}) \, dK \, ,$$

for $p = 1, \ldots, N$.

In the presence of moisture, a safety factor $C = 0.5$ is used in the computation of the time step Δt from (3.34)-(3.35) in all the solved examples. Once $\mathbf{q}^{h,n+1}$ and $\varphi^{h,n+1}$ are computed from (3.38) and (3.39), we update their values using the microphysics constants from Kessler [1969].

3.5 Numerical results

In this section, the compressible VMS algorithm for atmospheric flow presented in Section 3.4 is tested against a suite of five standard tests in a low Mach environment. Four test cases in a dry atmosphere (three two-dimensional tests and a three-dimensional one) and one test case of moist atmospheric flow in two dimension. The first two tests are a rising thermal bubble and a density current, in Subsections 3.5.1 and 3.5.2, respectively. They are two-dimensional tests. The idea is that we perturb the background atmosphere with thermal anomalies that vary in definition and size. These tests do not have analytic solution and the metrics that we use are based on comparison with the literature using symmetry considerations, front velocity of the moving thermal perturbation, and the magnitude of extrema. In Subsection 3.5.3, we solve a two-dimensional mountain problem that have semi-analytic solution based on the linear theory of small perturbations. The last case in a dry atmosphere, in Subsection 3.5.4, is a three-dimensional rising thermal

bubble. Finally, in Subsection 3.5.5 we solve a two-dimensional convective storm and precipitation of warm rain. The numerical results presented in this section, have been included in Marras [2012], Marras et al. [2013a,b, 2015]. Here we concentrate on the numerical discussion of the problems which represents the major contribution of this thesis to this work.

In the two-dimensional mountain case and the two-dimensional storm problem, the top and lateral boundaries are treated with the Rayleigh-type non-reflecting boundary conditions described in Durran and Klemp [1983], Klemp and Lilly [1978], Marras [2012], Restelli [2007]. The use of a Rayleigh-type absorbing layer avoids reflection of internal gravity waves and high-frequency acoustic waves by damping of the solution inside the absorbing layer. It is worth to remark that within the absorbing layer the numerical method remains the same. In the area occupied by the absorbing layer, the solution variables $\mathbf{q}$ are corrected as $\mathbf{q}_{\text{corrected}} = \mathbf{q} + \mathcal{D}\,(\mathbf{q} - \mathbf{q}_b)$, where $\mathbf{q}_b$ indicates the value of the unknown at the nodes on the physical boundary and $\mathcal{D} \in [0, 1]$ is the damping coefficient which depends on the distance from the base of the absorbing layer, in a way that $\mathcal{D} = 0$ at the base of the absorbing layer and $\mathcal{D} = 1$ at the physical boundary. The upper boundary is more critical than the lateral boundaries and, following Restelli's experience, we use different damping coefficients for the two cases (see Restelli [2007] for details). Refer for example to Marras [2012] for an explicit definition of $\mathcal{D}$.

3.5.1 Warm bubble

A large bubble of radius $r_o = 50\,m$ and centered in $(x_c, z_c) = (500, 260)\,m$ is initially at rest and used to perturb the atmosphere at uniform $\bar{\theta} = \theta_0 = 300\,K$. The thermal perturbation is defined by a Gaussian as in the original problem of Robert [1993], where the domain extends within $[0, 1000] \times [0, 1500]\,m^2$. The thermal perturbation with amplitude $A = 0.5\,K$ and $\sigma = 100\,m$ is defined by the law:

$$\theta' = \begin{cases} A & \text{if } R \leq r_o \\ \\ A\,e^{-(R-r_o)^2/\sigma^2} & \text{if } R > r_o \end{cases} \tag{3.40}$$

where the perturbation boundary is $R = \sqrt{(x - x_c)^2 + (z - z_c)^2}$. Zero normal velocity is imposed at the four boundaries to impose no flux boundary conditions.

The background state is characterized by a neutral atmosphere with uniform potential temperature $\bar{\theta}$ and background pressure $\bar{p}$ in hydrostatic equilibrium satisfying equation

(3.3) such that

$$\bar{p} = p_0 \left(1 - \frac{g}{c_p \theta_0} z\right)^{c_p/R} , \tag{3.41}$$

where the surface potential temperature and surface pressure are $\theta_0 = 300\,K$ and $p_0 = 10^5\,Pa$. The equation of state (3.2) is used to derive $\bar{\rho}$:

$$\bar{\rho} = \frac{p_0^{R/c_p}}{R\theta_0}\, \bar{p}^{c_v/c_p} . \tag{3.42}$$

For comparison against Robert [1993], the final time is set to $T = 1080\,s$. The computational grid resolution is $\Delta x = \Delta z = 2.5\,m$. The plots of θ', p', u, and w are shown in Fig. 3.1. The solution presents rotating structures qualitatively comparable to the result of the reference. Fig. 3.2 shows the normalized values and distribution of the subscales $\tilde{\mathbf{q}}$ on the domain. As expected from equation (3.31), their values are more important where residuals are bigger. Table 3.1 shows $\tilde{\mathbf{q}}$ and $\mathbf{q}^h$ extrema.

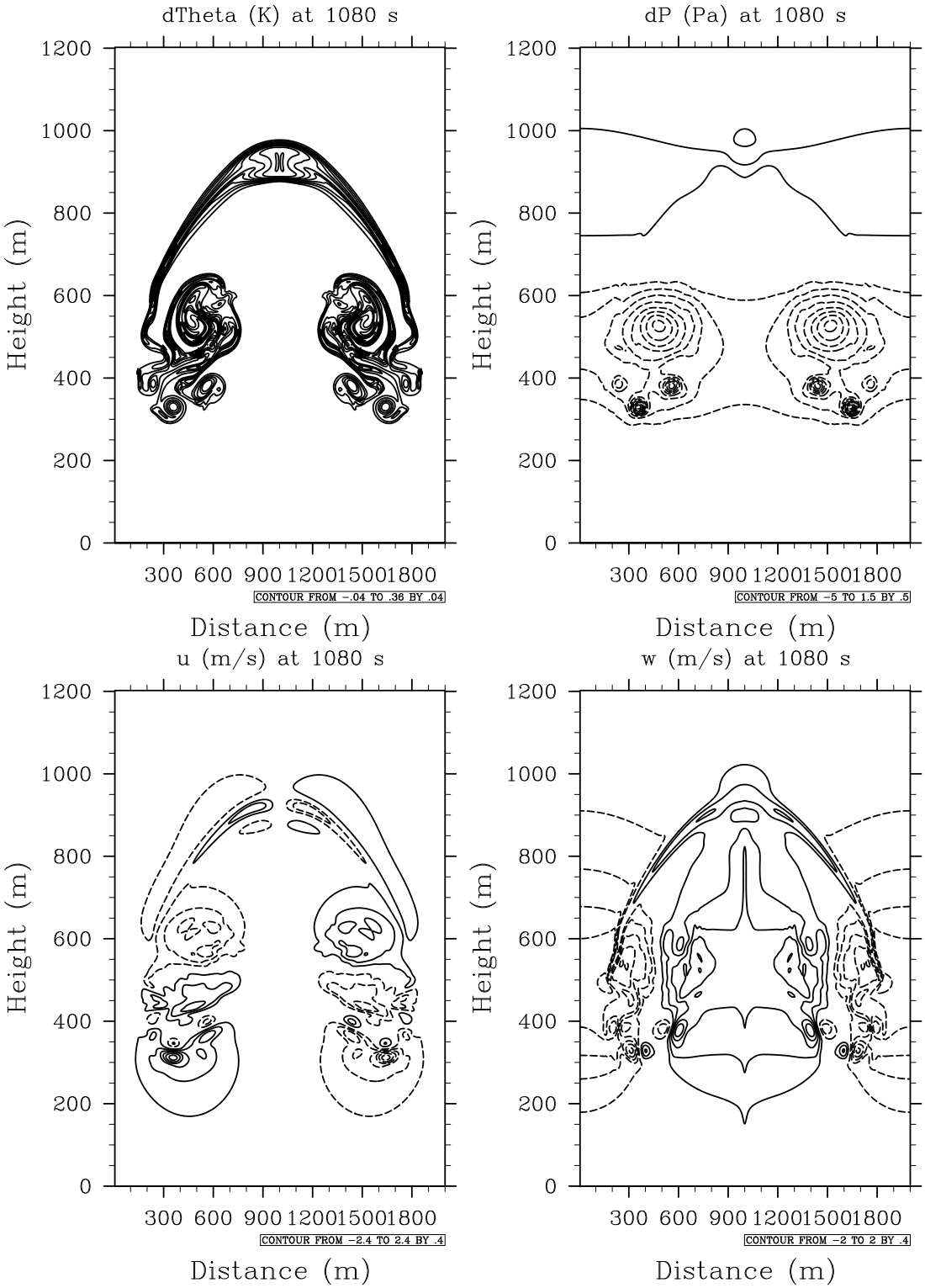

FIGURE 3.1: Warm bubble. Solution at $T = 1080\,s$ for grid resolution $\Delta x = \Delta z = 2.5\,m$. Top row: θ' and p' contours. Bottom row: u and w contours.

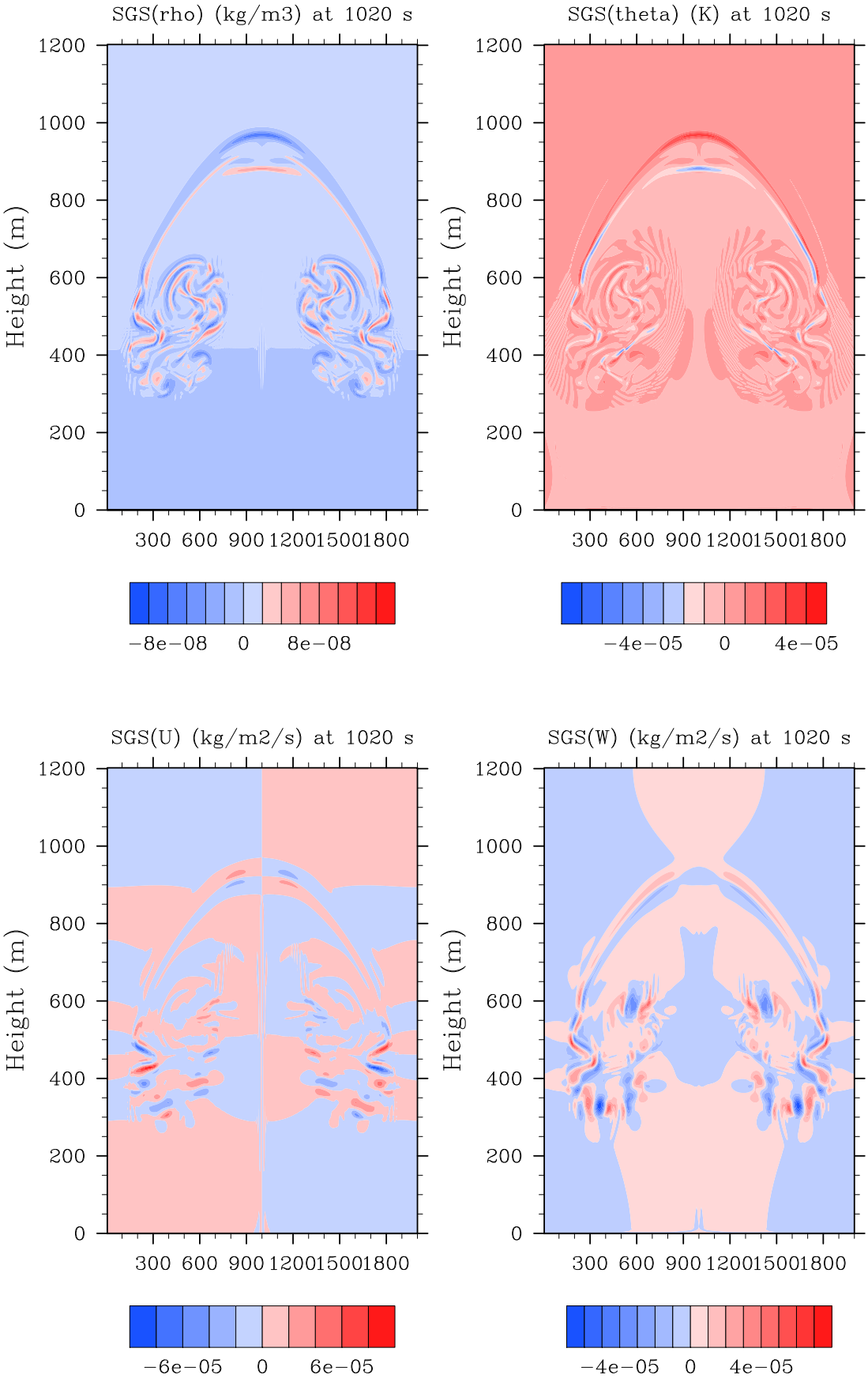

FIGURE 3.2: Warm bubble. Filled contours of the normalized subscales at $T = 1080\,s$ and $\Delta x = \Delta z = 2.5\,m$ resolution. Top row: $\tilde{\rho}/\rho_{max}$, $\tilde{\theta}/\theta_{max}$. Bottom row: $\tilde{U}/U_{max}$, $\tilde{W}/W_{max}$

.

TABLE 3.1: Warm bubble. $\tilde{\mathbf{q}}$ and $\mathbf{q}^h$ extrema at $T = 1080s$ and $\Delta x = \Delta z = 2.5\,m$ resolution.

	ρ^h	$\tilde{\rho}$	U^h	$\tilde{U}$	W^h	$\tilde{W}$	θ^h	$\tilde{\theta}$
max.	1.149	1.676e-7	2.906	2.656e-4	2.610	1.844e-4	303.5	1.464e-2
min.	1.015	-1.170e-7	-2.906	-2.656e-4	-2.576	-1.771e-4	303.1	-2.331e-2

3.5.2 Density current

After its introduction in different numerical Carpenter et al. [1990] and experimental Droegemeier and Wilhelmson [1987] studies, Straka et al. [1993] documented in detail the density current problem as a standard benchmark in NWP. In this work, like in Ahmad and Lindeman [2007], Straka's test is modified and run without the artificial diffusion with diffusivity constant $K = 75\,m^2\,s^{-1}$. The initial base-state atmosphere is characterized by a uniform potential temperature $\bar{\theta} = \theta_0 = 300\,K$ within the domain $[-25600, 25600] \times [0, 6400]\,m^2$. A perturbation of θ centered in $(x_c, z_c) = (0, 3000)\,m$ and with radii $(r_x, r_z) = (4000, 2000)\,m$ is given by the cosine distribution

$$\theta' = \begin{cases} 0 & \text{if } R > 1 \\ A\left[\frac{1+\cos(\pi_c R)}{2}\right] & \text{if } R \leq 1 \end{cases} \tag{3.43}$$

where $A = -15$ K is the perturbation amplitude, and R the analytical definition of the perturbation that goes as

$$R = \sqrt{\left(\frac{x - x_c}{r_x}\right)^2 + \left(\frac{z - z_c}{r_z}\right)^2}.$$

The same background state from Subsection 3.5.1 is used here. The four boundaries are defined as no-flux permitting walls. The initial velocity is zero.

Fig. 3.3 shows the contours of θ' at $T = 900\,s$ for four different resolutions: 1) $\Delta x = \Delta z = 25\,m$, 2) $\Delta x = \Delta z = 50\,m$, 3) $\Delta x = \Delta z = 75\,m$, and 4) $\Delta x = \Delta z = 100\,m$. The cold perturbation introduces a heavier pool of air whose downward motion is responsible for the development of the propagating front. Inertia causes the top layers of the front to pull back giving rise to Kelvin-Helmholtz structures.

Being inviscid, the result should be comparable to that presented by Ahmad and Lindeman [2007], where the solution is computed on a grid of size $\Delta x = \Delta z = 50\,m$. At the same resolution, we observe the same number rotating structures (see Fig. 3.3) and measure a difference of the front position normalized by the domain half-length equal

to 0.0135. We consider the front position defined as the last node on the ground where $\theta' = -1\,K$. The front position is at $14629\,m$ at $900\,s$ for the $50\,m$ resolution, giving a front speed of $16.25\,m\,s^{-1}$. The front is slower on a coarser grid as it is also observed in Fig. 5 of Straka et al. [1993]. Concerning θ', a peak appears close to the ground. On the finest grid, $\theta'_{max} = 7.81\,K$ at $(x, z) = (11802, 0)\,m$ at $900\,s$. Through extensive numerical experiments we observed that the peak remains bounded and does not propagate in its neighborhood. However, this should be analyzed in detail in the future.

As the resolution is increased, the amount of structures that are resolved increases as well. The solution is inviscid, non-linear, and non-steady. Without viscosity that could homogenize the solution by diffusive effects, we do not expect to reach space-convergence to a common solution. Rather, we expect more and more structures to be resolved until the smallest refinement of the order of the subgrid scales is reached. This goes way beyond the resolutions of interest in NWP and its analysis falls out of the scope of this work. In Fig. 3.3, oscillations in potential temperature appear in the wake of the density current. They are a consequence of the large inertia of the falling pool that, once it has reached the ground, abruptly changes direction of motion. The oscillations are partially dragged by the wake of the flow and stand still in the proximity of the lower layers of the domain. The small numerical dissipation that is added by VMS is not enough to suppress them. A localized discontinuity capturing method may be a viable solution.

Fig. 3.4 shows the normalized values and distribution of the subscales on the domain. As expected from equation (3.31), their values are more important where residuals are bigger. Table 3.2 shows $\tilde{\mathbf{q}}$ and $\mathbf{q}^h$ extrema.

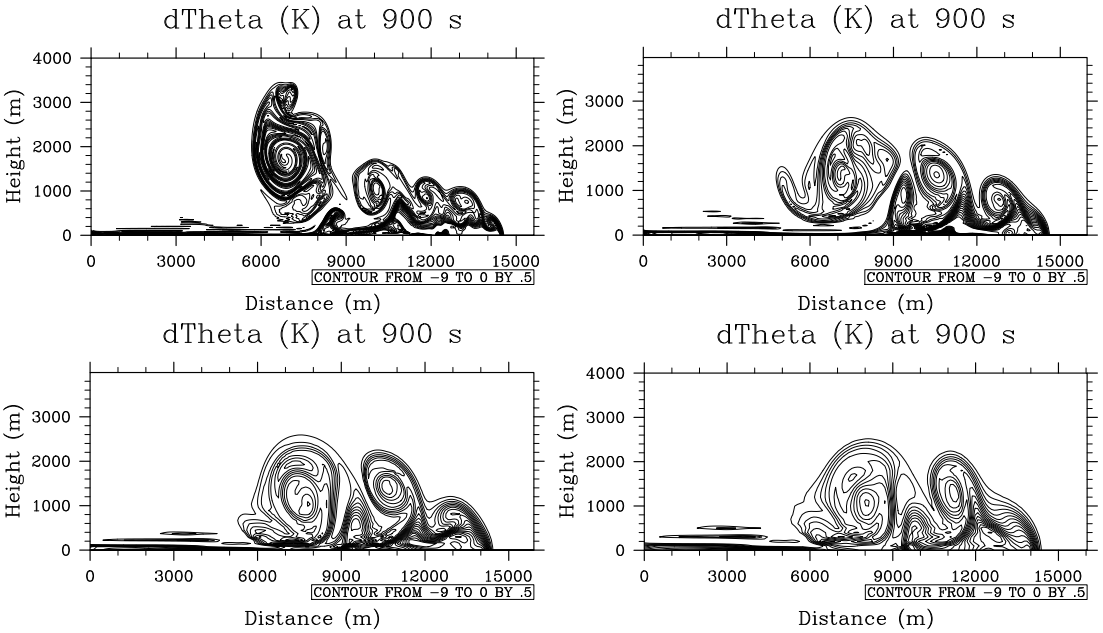

FIGURE 3.3: Density current. Contours of θ' at $T = 900\,s$ for four different grid resolutions. Top row: $\Delta x = \Delta z = 25\,m$ and $\Delta x = \Delta z = 50\,m$ resolution. Bottom row: $\Delta x = \Delta z = 75\,m$ and $\Delta x = \Delta z = 100\,m$ resolution.

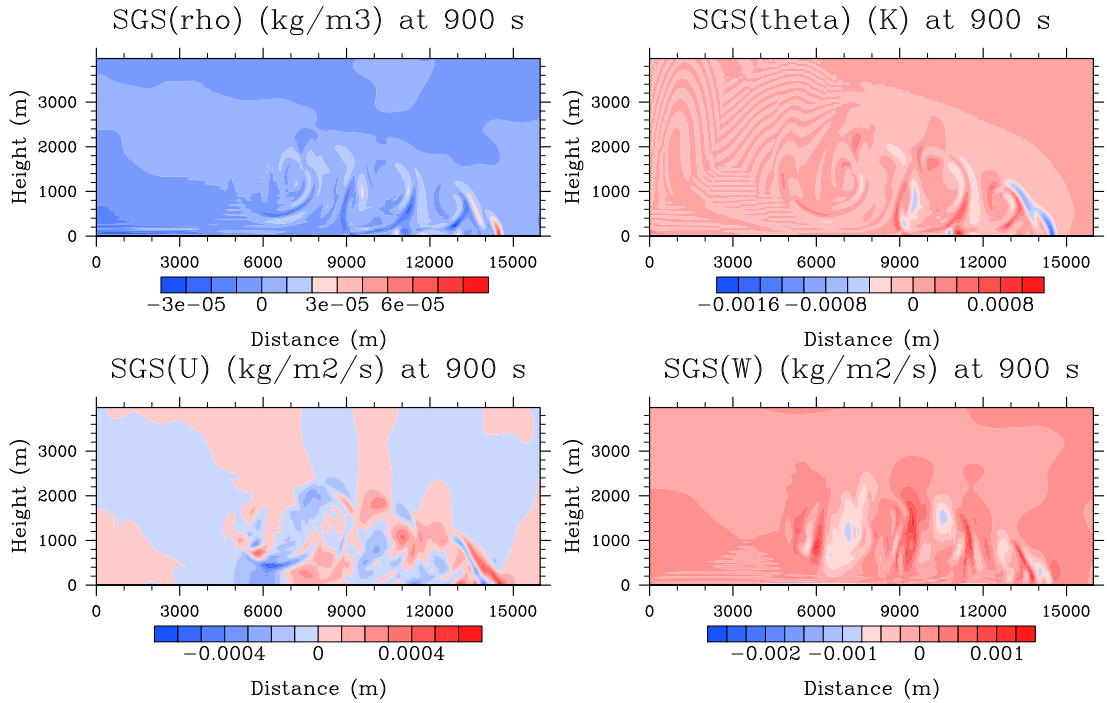

FIGURE 3.4: Density current. Filled contours of the normalized subscales at $T = 900\,s$ and $\Delta x = \Delta z = 50\,m$ resolution. Top row: $\tilde{\rho}/\rho_{max}$, $\tilde{\theta}/\theta_{max}$. Bottom row: $\tilde{U}/U_{max}$, $\tilde{W}/W_{max}$.

TABLE 3.2: Density current. $\tilde{\mathbf{q}}$ and $\mathbf{q}^h$ extrema at $T = 900s$ and $\Delta x = \Delta z = 50\,m$ resolution.

	ρ^h	$\tilde{\rho}$	U^h	$\tilde{U}$	W^h	$\tilde{W}$	θ^h	$\tilde{\theta}$
max.	1.206	1.038e-4	40.76	2.606e-2	18.60	2.448e-2	348.8	0.3932
min.	0.6472	-4.739e-5	-40.76	-2.606e-2	-25.97	-4.748e-2	194.2	-0.5834

3.5.3 Linear hydrostatic mountain waves

We are solving the flow passing through a mountain Smith [1979]. The mountain is the *Witch of Agnesi*

$$h(x,z) = \frac{h_c}{1 + \left(\frac{x-x_c}{a_c}\right)^2}, \tag{3.44}$$

with height $h_c = 1\,m$, semi-width $a_c = 10000\,m$ and center $x_c = 120000\,m$ within the domain $[0, 240000] \times [0, 24000]\,m^2$ Durran and Klemp [1983], Smith [1979]. The initial flow has uniform velocity $(\bar{u}, \bar{w}) = (20, 0)\,m\,s^{-1}$. The $Brunt-Väisälä$ frequency, defined as

$$N^2 = g\frac{\partial}{\partial z}\ln\bar{\theta}\,, \tag{3.45}$$

is $N = 0.0195\,s^{-1}$ in this case. The described values of N, h_c, a_c lead to a flow of strong stability over a wide mountain. These conditions are such that a gravity wave propagates only vertically, with negligible vertical accelerations. The steady state solution is expected at $T > 10\,hrs$ approximately. The correct simulation of vertically propagating linear hydrostatic mountain waves is a classical test to verify a model's robustness and efficiency.

We use a computational grid with 400×200 bilinear elements in x and z, giving a resolution of $600\,m$ in x and $120\,m$ in z. No-flux boundary conditions are used on the bottom boundary while the top and lateral boundaries are treated with the non-reflecting boundary conditions described in the begining of Section 3.5. The absorbing layer is built at $z \geq 12000\,m$ and for $x \leq -80000\,m$ and $x \geq 80000\,m$.

By integration of (3.45) along z, we obtain the background potential temperature as

$$\bar{\theta} = \theta_0\, e^{\frac{N^2}{g}z}, \tag{3.46}$$

where θ_0 is the potential temperature measured at the surface. In the case of linear hydrostatic flows, an isothermal atmosphere with $\theta_0 = 250\,K$ flows above a single-peaked mountain. Hydrostatic balance is verified for $\bar{p}$. From equations (3.3) and (3.2) and under

the hypothesis of isothermal atmosphere, the background pressure is found as:

$$\bar{p} = p_0 e^{-\frac{g}{R\theta_0}z} \,. \tag{3.47}$$

In Fig. 3.5 the numerical solution of u', w', and θ' is plotted on top of the analytic solution. Convergence to the stationary condition is measured by the time variation of vertical momentum flux. The momentum flux for hydrostatic mountains is defined as

$$m(z) = \bar{\rho}(z) \int_{-\infty}^{\infty} u'(x,z)\, w'(x,z)\, dx. \tag{3.48}$$

For analysis, $m(z)$ is normalized by the analytic hydrostatic momentum flux $m_{HS}(z) = -0.25\pi\, \rho_0 \bar{u} N h_c^2$, where ρ_0 is the density on the ground. From the normalized momentum flux, $m(z)/m_{HS}(z)$, represented in Fig. 3.6 we deduce that the simulation has reached steady-state after $T = 12\, hrs$.

The deviation errors are quantified by the root-mean-square error (RMS) and normalized L_2 norm given by

$$\text{RMS} = \sqrt{\sum_{k=1}^{n_{nodes}} (\mathbf{q}_k^h - \mathbf{q}_k^{analytic})^2 \,/\, n_{nodes}}$$

and

$$\|\mathbf{q}^h - \mathbf{q}^{analytic}\|_{L_2} = \sqrt{\frac{\sum_{p=1}^{N} (\mathbf{q}_p^h - \mathbf{q}_p^{analytic})^2}{\sum_{p}^{N} (\mathbf{q}_p^{analytic})^2}} \,,$$

where $\mathbf{q}^{analytic}$ is the analytic solution, N is the number of nodes of the grid, and $\mathbf{q}_p$ is the value of $\mathbf{q}$ at node p. RMS and the normalized L_2-norm of $\mathbf{q}^h - \mathbf{q}^{analytic}$ are computed inside the portion of domain that is not affected by the Rayleigh-type boundary conditions and reported in Table 3.3. It emerges that the vertical perturbed velocity approximates the analytic solution best. This is expected from the hydrostatic regime of the problem, where vertical acceleration should be sufficiently small. The discrepancy of u' and θ' with respect to the analytic solution appears within the acceptable values from previous studies using element-based methods (e.g., Giraldo and Restelli [2008]).

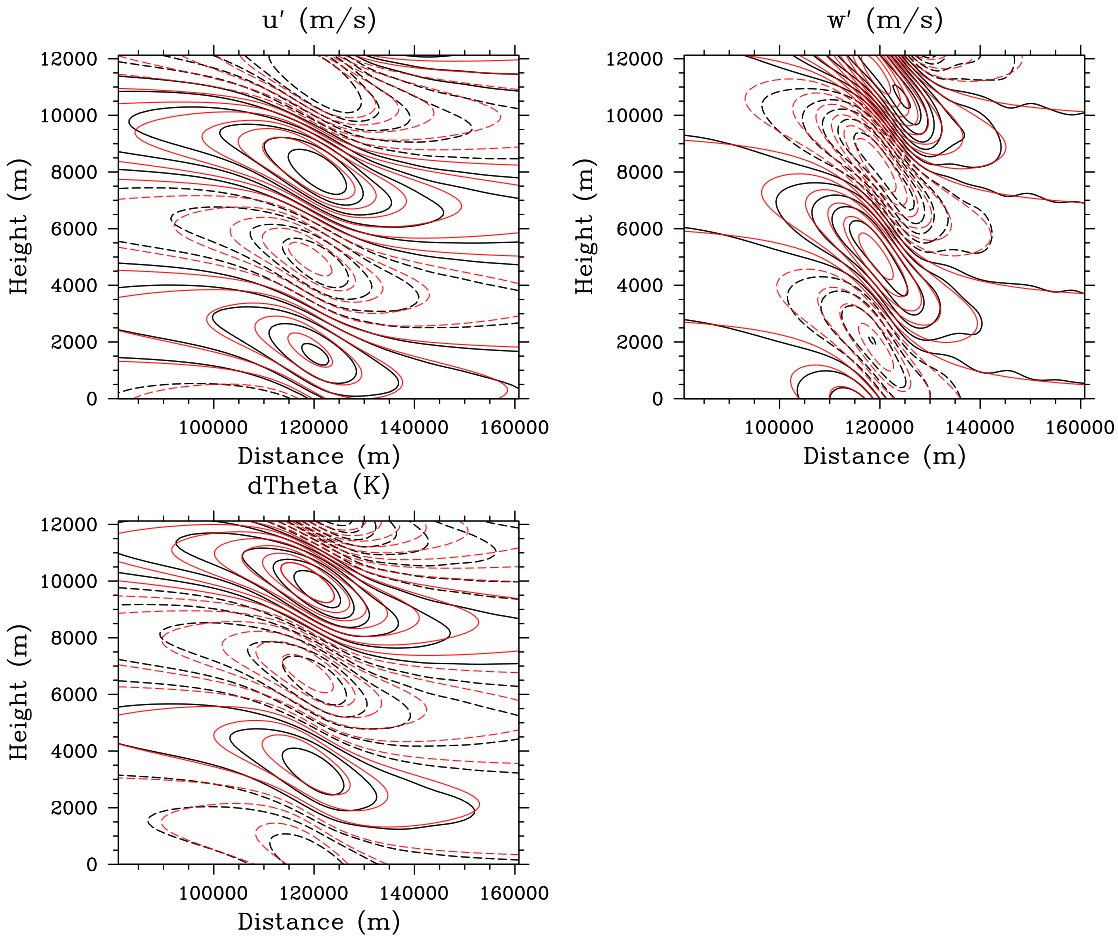

FIGURE 3.5: Linear hydrostatic mountain waves. From top left, in clockwise direction: u', w', and θ' contours at $T = 12\,hrs$ computed on a grid of 400×200 bilinear elements. The numerical and analytic solutions are black and red, respectively. The negative values are dashed. The contours are plotted as: $-0.025 \leq u' \leq 0.025$ with contour interval of 0.005; $-0.005 \leq w' \leq 0.005$ with contour interval of 0.0005; $-0.025 \leq \theta' \leq 0.025$ with contour interval of 0.00357.

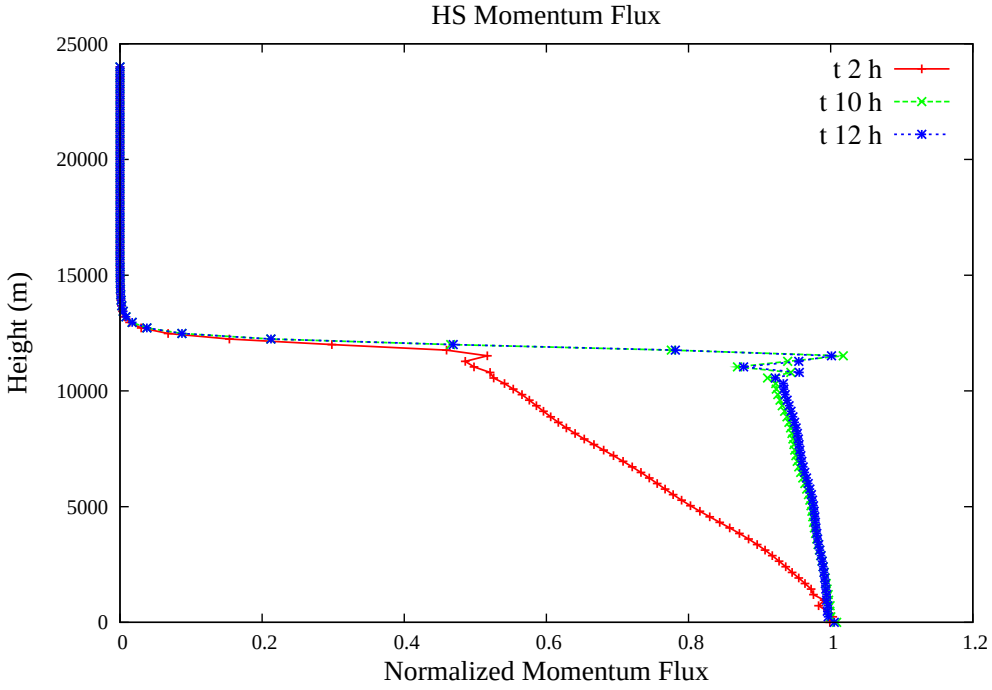

FIGURE 3.6: Linear hydrostatic mountain waves. Normalized momentum flux at $T = 2\,hrs, 10\,hrs, 12\,hrs$.

TABLE 3.3: Linear hydrostatic mountain waves. RMS and normalized L_2 norm of $\mathbf{q}^h - \mathbf{q}^{analytic}$ for 400×200 elements.

	θ'	u	w
RMS	1.519e-3	2.294e-3	2.784e-4
L_2	1.972e-2	2.350e-2	1.127e-2

3.5.4 3D warm bubble

The problem of a 3D rising thermal bubble is taken from Ahmad [2008]. The domain is the volume $[0, 3200] \times [0, 3200] \times [0, 4000]\, m^3$, The initial atmosphere is neutrally stratified with $\bar{\theta} = \theta_0 = 300\, K$. Its perturbation, θ', is now spherical and is centered in $(x_c, y_c, z_c) = (1600, 1600, 500)\, m$. It is a linear function of space and defined as

$$\theta' = A\left(1 - \frac{R}{r_0}\right), \tag{3.49}$$

where $R = \sqrt{(x - x_c)^2 + (y - y_c)^2 + (z - z_c)^2}$, $r_0 = 250\, m$, and $A = 2\, K$. The initial velocity field is zero everywhere. Solid boundaries are prescribed.

As for two-dimensional advective thermals, the warm perturbation generates acceleration in the inner region of the bubble where temperature is higher, with subsequent downdrafts originating at the boundaries of the perturbation. A classical mushroom shape generates because of the faster, vertically moving, center of the thermal. The mesh resolution is uniform and set to $40\,m$ using $80 \times 80 \times 100$ hexahedra. Symmetry considerations and direct comparison against Ahmad [2008] are used to evaluate the results.

Fig. 3.7 display the xz and yz cross-sections of θ' and p' at $T = 480\,s$. Due to the symmetric nature of the problem and the initial spherical shape of θ', the evolution of the perturbation of potential temperature is expected to remain axisymmetric at all times. The same consideration applies to the perturbation of density (ρ', not shown), and hence pressure. By observing Fig. 3.7, this is indeed verified. At $T = 480\,s$ the front is at $z = 2400\,m$ approximately.

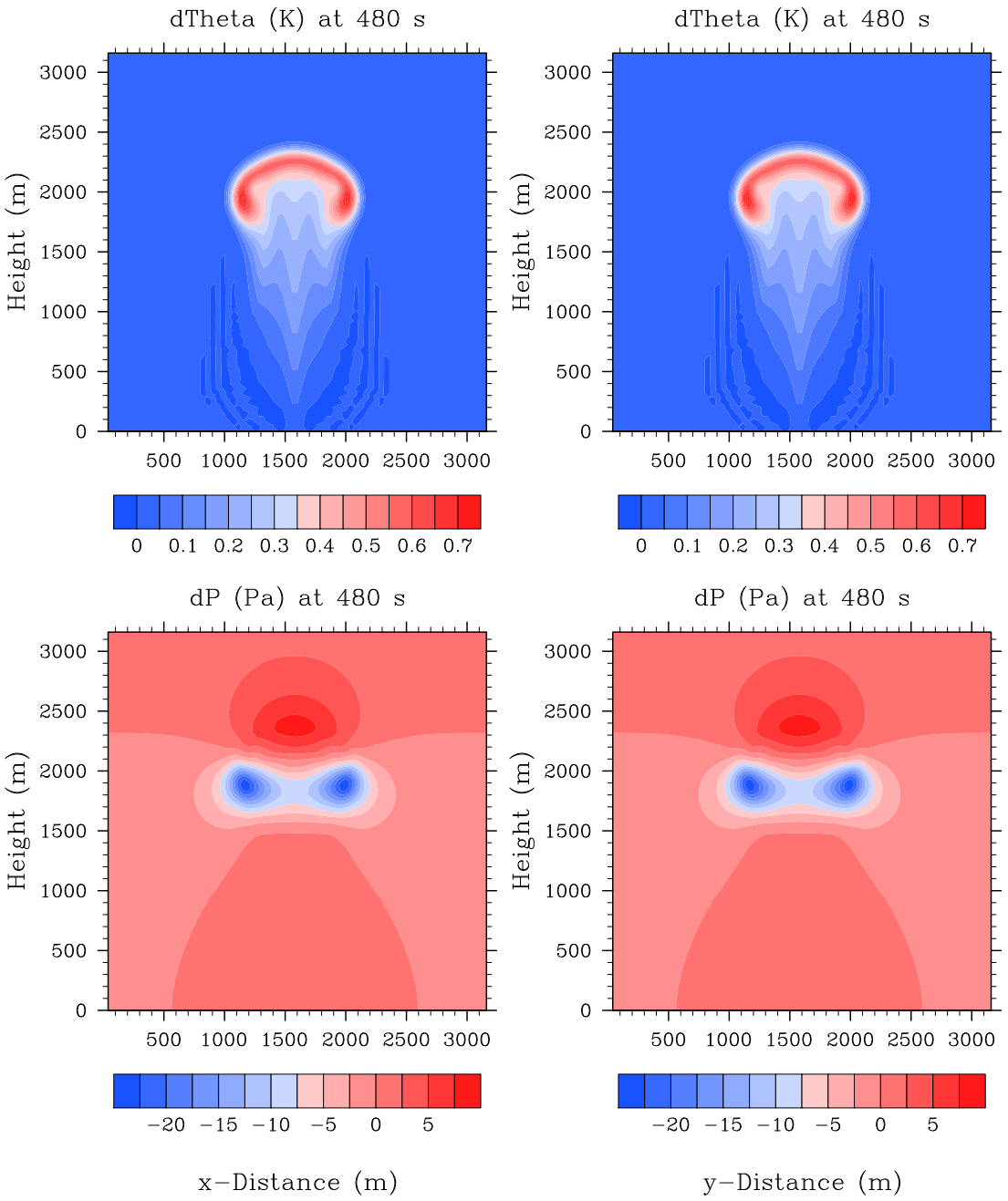

FIGURE 3.7: 3D warm bubble. Filled contours of θ' (top row) and p' (bottom row) are computed on a grid of $80 \times 80 \times 100$ elements. The left and right columns represent, respectively, the xz and yz planes. For plotting reasons, the plotted domain is shorter than the computational domain. Values are shown at $t = 480\,s$.

3.5.5 Storm-GGD12

We simulate the two-dimensional convective storm and precipitation of warm rain presented in Gaberšek et al. [2012]. A layer of unsaturated water vapor characterizes the lower troposphere. The amount of moisture decreases with height and the flow is forced by a vertical wind shear. Condensation starts in a volume that contains water vapor

and is raised to regions of lower temperature and pressure. These conditions allow the expansion of the wet volume and hence vapor condensation. Buoyancy is excited by an elliptical warm bubble whose characteristics are described in equation (3.50) below. Once the rising air parcels reach the level of free convection, lifting continues as long as the parcels are less dense than the surroundings. At saturation, rain begins to form and precipitate.

An atmospheric sounding is a measurement of vertical distribution of physical properties of the atmospheric column. The vertical wind shear, as well as the initial background temperature, water vapor, and horizontal velocity come from the sounding of Gaberšek et al. [2012], Rotunno et al. [1988]. The domain extends along $240\,km$ in the horizontal and $24\,km$ in the vertical directions. The thermal perturbation of potential temperature θ' is centered at $(x_c, z_c) = (120, 2)\,km$ and defined by

$$\theta' = \theta_c \cos^2 \frac{\pi r}{2} \qquad \text{if } r \leq 1, \tag{3.50}$$

with amplitude $\theta_c = 5.0\,K$ and $r = \sqrt{(x - x_c)/x_r^2 + (z - z_c)/z_r^2}$. The radii of the ellipse are $(x_r, z_r) = (10, 1.5)\,km$. The weak stability of the atmosphere changes from a Brunt-Väisälä frequency $N = 0.01\,s^{-1}$ below the tropopause (at approximately $12\,km$) to a more stable condition with $N = 0.02\,s^{-1}$ above $12\,km$.

The simulation is performed on a computational grid with horizontal resolution $\Delta x = 580\,m$ and vertical spacing $\Delta z = 290\,m$ (414×83 quadrilateral elements). The grid spacing is chosen to reproduce, as faithfully as possible, the nominal grid used by Gaberšek et al. [2012] with high-order spectral elements of unevenly spaced nodes.

The boundaries are modeled as follows. The top and bottom boundaries are rigid walls that allow free-slip. Given a domain sufficiently large compared to the extension of the cloud, periodic boundary conditions in the x direction are a suitable choice. The formation of a lifting convective cloud is the cause of upward-propagating gravity-waves which reflect back to the computational domain. For this reason the absorbing layer condition described in the begining of Section 3.5 is implemented on the top boundary. The Rayleigh layer is introduced at $z \geq 11.7\,km$. The effect of the absorbing layer is evident in the upper region of the domain where the contour lines of θ are oscillation-free. Reflecting gravity waves could affect the thermodynamic fields by unwanted oscillations that eventually could either quench or boost unphysically the development of the storm.

The storm evolution is presented in Figures 3.8 and 3.9. The cloud starts to form at approximately $t = 900\,s$ (not shown) with precipitating water reaching the ground at $t = 1800\,s$ (Fig. 3.8, bottom). The vertical motion of the cloud top stops at the tropopause, where the stability of the background state increases. The cold pool that

forms on the surface due to evaporation and consequent air cooling is visible in Fig. 3.9. Fig. 3.10 shows the velocity vector field of the developing storm. We observe the important vertical motion through the core of the developing cloud which splits left and right as the cloud top approaches the tropopause. The numerical values of the maxima are collected in Table 3.4. The results remain quantitatively and qualitatively comparable to those in Gaberšek et al. [2012].

In Fig. 3.11, the spatial distribution of the subscales is shown. We observe that the subscales are more important within the regions of highest convection, precipitation, and highest gradients of density potential temperature. The locality of VMS, and hence the value of the subscales, could be used as an error estimator if grid refinement were to be used.

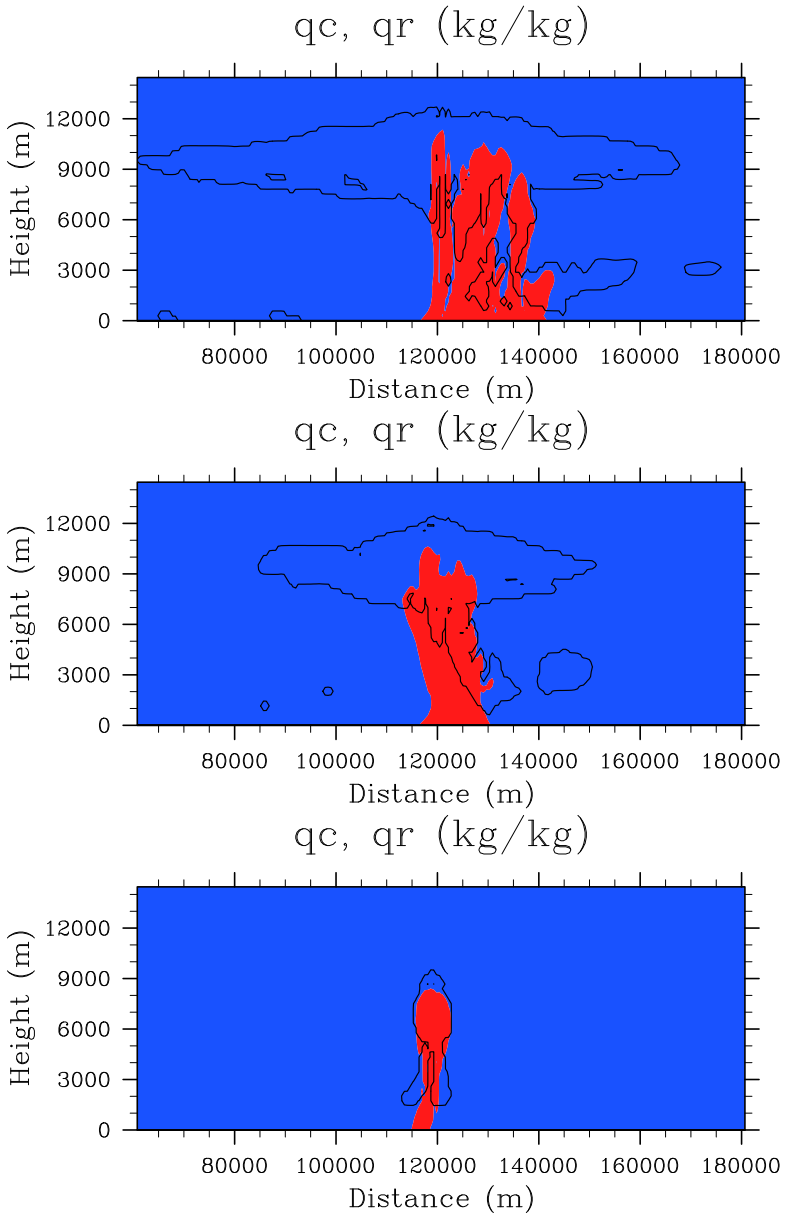

FIGURE 3.8: Storm-GGD12. Storm evolution at $1800\,s$ (bottom), $6000\,s$ (middle), and $9000\,s$ (top), solved on uniform grid with $\Delta x = 580\,m$ and $\Delta z = 290\,m$ (414×83 quadrilaterals). The thick black contour represents the outline of the cloud where $q_c = 10^{-5}\,kg\,kg^{-1}$. Precipitating water $q_r \geq 10^{-4}\,kg\,kg^{-1}$ is plotted in solid red color.

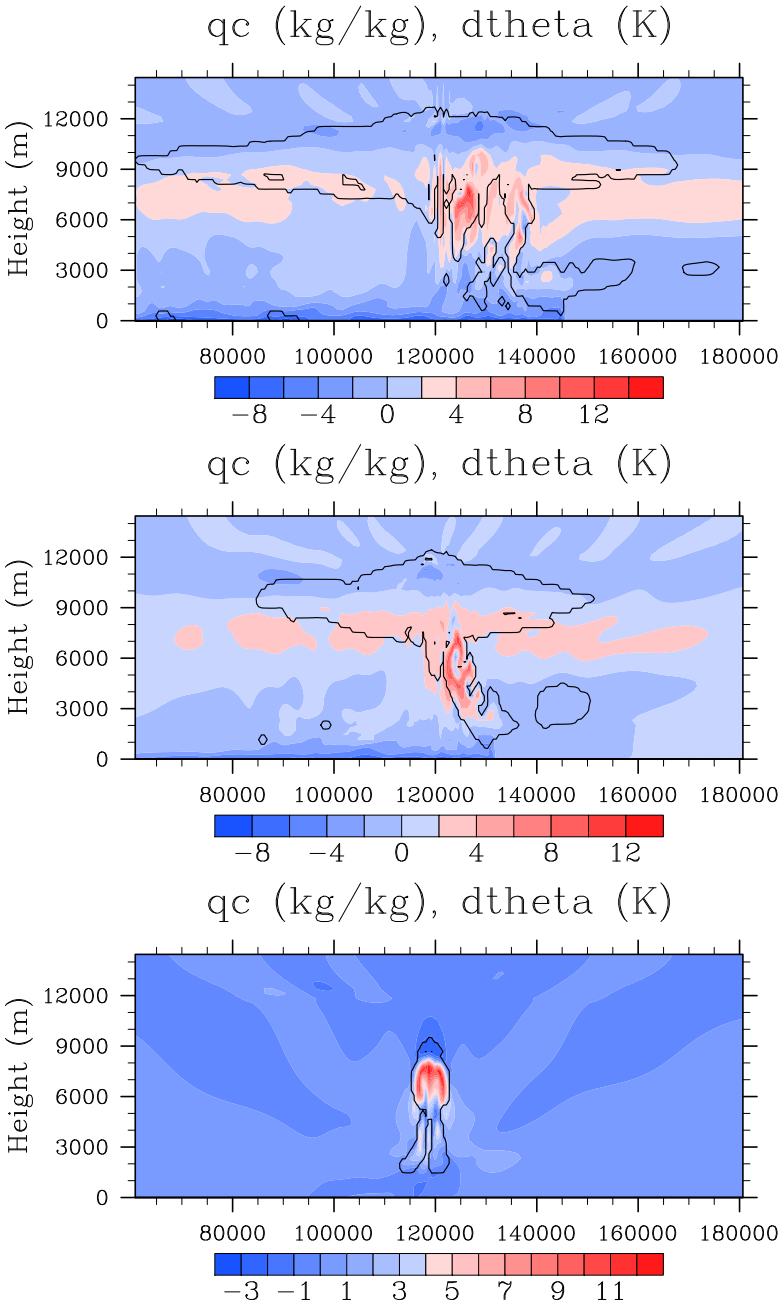

FIGURE 3.9: Storm-GGD12. As in Fig. 3.8, but with filled contours of θ'_ρ. At 1800 s (bottom), 6000 s (middle), and 9000 s (top). The color scales are left free to show the absolute extrema of θ'_ρ.

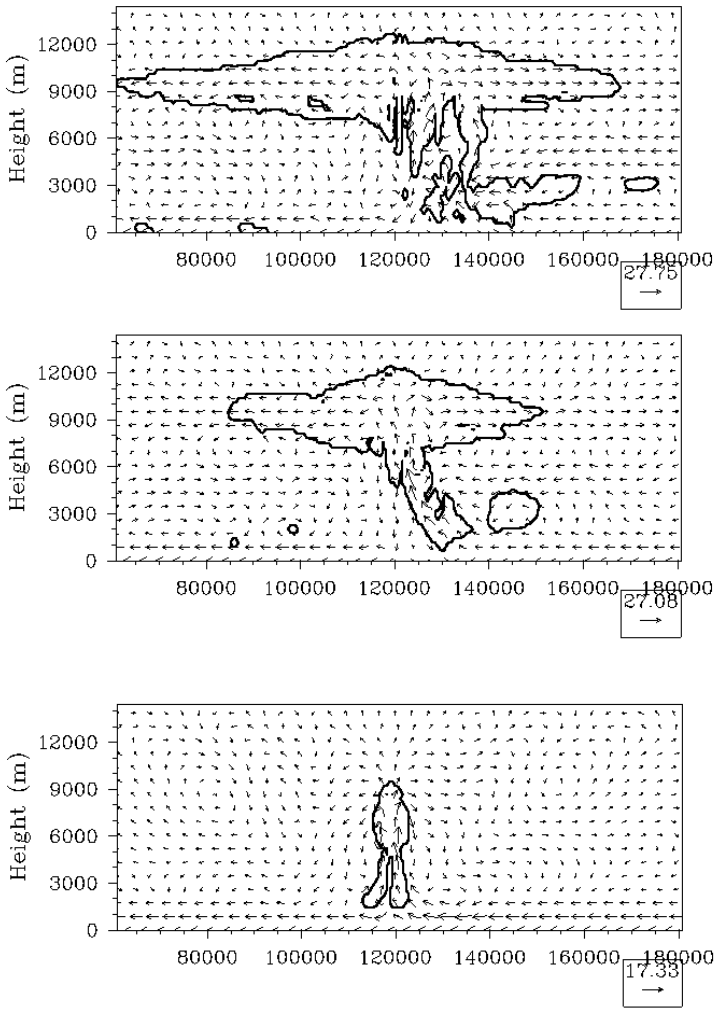

FIGURE 3.10: Storm-GGD12. Velocity vectors and cloud water contour ($q_c = 10^{-5}\, kg\, kg^{-1}$) for the storm simulation on the grid of $\Delta x = 580\, m$ and $\Delta z = 290\, m$ (414×83 quadrilaterals). At $1800\, s$ (bottom), $6000\, s$ (middle), and $9000\, s$ (top).

TABLE 3.4: Storm-GGD12. Results of the extrema of $\theta'_\rho, q_c, q_r, w$. t_{q_c} and t_{q_r} indicate the time when q_c and q_r first form.

$\theta'_{\rho,min}$ (K)	$\theta'_{\rho,max}$ (K)	$q_{c,max}$ $(g\, kg^{-1})$	$q_{r,max}$ $(g\, kg^{-1})$	w_{max} $(m\, s^{-1})$	t_{q_c} (s)	t_{q_r} (s)
-9.97	16.15	4.10	8.54	24.70	369	811

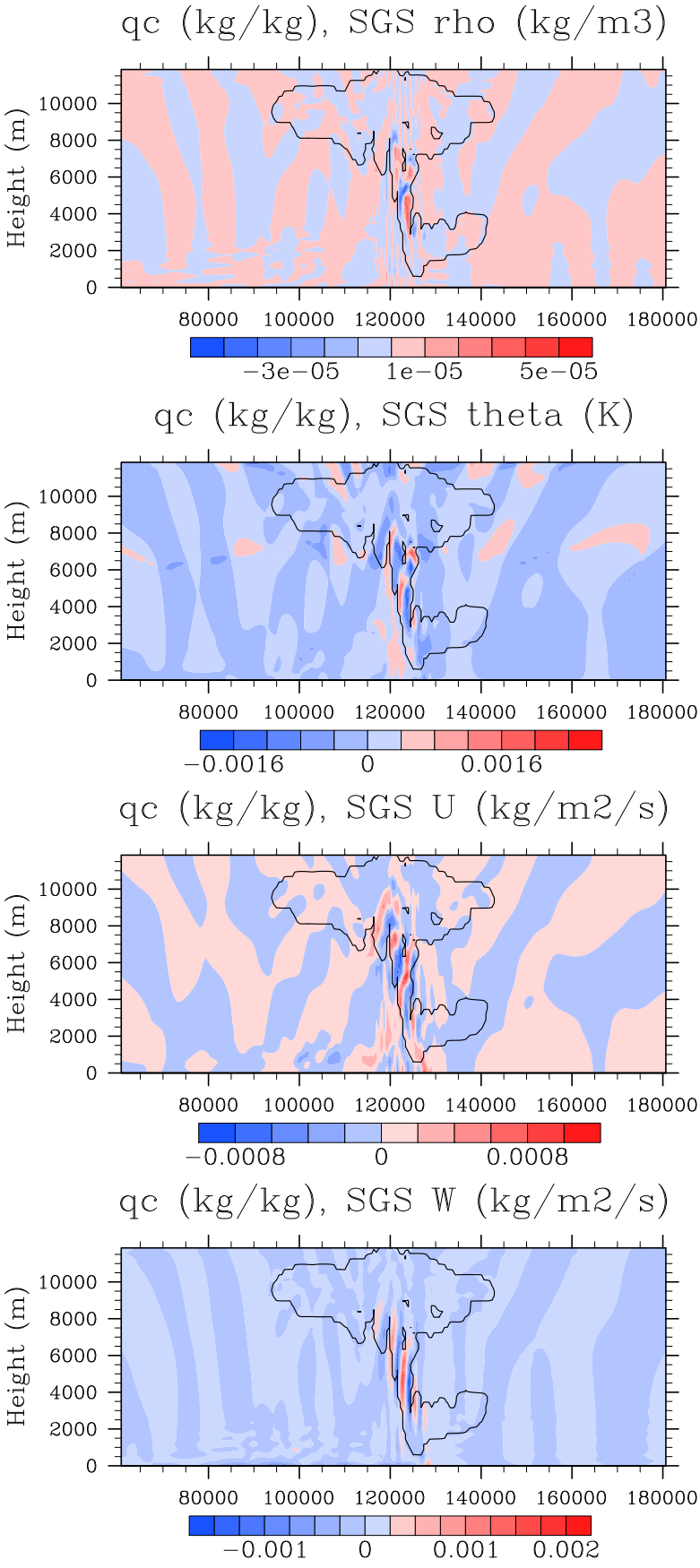

FIGURE 3.11: Storm-GGD12. Filled contours of the normalized subscales at 5000 s. Top row, from left: $\tilde{\rho}/\rho_{max}$, $\tilde{\theta}_\rho/\theta_{\rho,max}$. Bottom row, from left: $\tilde{U}/U_{max}$, and $\tilde{W}/W_{max}$.

3.6 Summary and conclusions

In this chapter we proposed the use of Finite Elements with Variational Multiscale Stabilization for the solution of the compressible Euler equations for dry and moist stratified flows at low Mach numbers typical of atmospheric dynamics. The extension of VMS to compressible flows presented in Chapter 2 is adapted to the treatment of thermally perturbed stratified atmospheres modeled through the fully compressible Euler equations. With the presence of moisture, the Euler equations are coupled to a set of three transport equations that model advection of water tracers in the atmosphere. A Kessler microphysics parametrization is used to model phase changes during the formation and development of a convective storm.

Performance and accuracy are measured by means of standard benchmarks adopted by atmospheric modelers for dry and wet dynamics. In this respect, the algorithm proved to be successful. Two and three-dimensional tests are performed in the case of dry atmospheric flow and two-dimensional tests in the case of moist atmospheres. However the results are encouraging to suggest further analysis of the algorithm for fully three-dimensional moist simulations. In terms of stability, the compressible VMS technique introduced in this work stabilizes the solution of low-Mach number compressible flows. For moist dynamics, the solution of the two coupled systems of hyperbolic equations with phase change preserves stability during the long-lasting simulations. The main features of the storm such as spatial distribution, time evolution, and rain accumulation are in good agreement with those of other authors.

Because the algorithm and its implementation are fully unstructured, it can be extended for mesh adaptivity and for the treatment of complex topographies. In terms of algorithm complexity, the overhead that is added by VMS is minimal because the construction of the stabilizing operator is carried out within the same element and node loops already defined for the finite element computation of the original operators of the Euler equations.

We also introduced a simple methodology that limits the truncation errors introduced in the solution of the hydrostatic states that, otherwise, would cause the generation of unphysical vertical accelerations. With this strategy, only the deviations from the background state in hydrostatic balance are considered in the evaluation of the element integrals, while the background state is explicitly computed at the Gauss points.

Chapter 4

Local preconditioning and VMS for compressible flow: P-VMS

In this chapter we introduce a preconditioned variational multiscale stabilization (P-VMS) method for compressible flows. The compressible VMS method presented in Chapter 2 is here adapted to the preconditioned Navier-Stokes equations. Local preconditioning of both steady and transient flow is considered in this chapter. The Navier-Stokes equations are solved on fully unstructured grids and discretized using the finite element method. The P-VMS method can be decomposed in three parts. First, a local preconditioner is applied to the continuous equations to reduce the stiffness while covering a wide range of Mach numbers. Then, the resulting preconditioned system is discretized in space using finite elements and stabilized with a variational multiscale stabilization method adapted for the preconditioned equations. Finally, a certain finite differences time discretization is chosen, resulting in explicit or implicit schemes. In this chapter, the solution is advanced in time using a fully explicit time discretization, although P-VMS is general and can be applied to fully implicit solvers. The proposed method is assessed by comparing convergence and accuracy of the solutions between the non-preconditioned and preconditioned cases, in particular for *van Leer-Lee-Roe*'s van Leer et al. [1991] and *Choi-Merkle*'s Choi and Merkle [1993] preconditioners, in some selected examples for viscous and inviscid, transient and steady flow, covering a large range of Mach numbers.

4.1 Stiffness of the Euler equations

In this section we explain the stiffness problem present in the flow equations. Thus we concentrate here on the Euler equations (2.8). As a measure for the stiffness we define

the condition number.

4.1.1 One-dimensional case

In order to fully understand the effect of local preconditioning, let us first analyze the one-dimensional case. A system of the form

$$\frac{\partial \mathbf{\Phi}}{\partial t} + \mathbf{A}(\mathbf{\Phi}) \frac{\partial \mathbf{\Phi}}{\partial x} = 0 \,, \tag{4.1}$$

is called *hyperbolic* if the matrix $\mathbf{A}$ is diagonalizable with real eigenvalues. These eigenvalues are called the *characteristic propagation speeds* of the system. It is widely known that marching in time an hyperbolic system containing different propagation speeds presents some problems. By the CFL condition Courant et al. [1967] the time step should be $\Delta t \leq \frac{h}{|\lambda|_{\max}}$, where h is a characteristic length of the grid and $|\lambda|_{\max}$ the largest absolute value of the eigenvalues of the matrix $\mathbf{A}$. A common time step for all the equations means that some eigenmodes would use a time step that is not the best not only in terms of accuracy but also in terms of efficiency; this is because the fast waves impose their small time steps to the slow ones. In the one-dimensional case, the propagation speeds are the eigenvalues of the convective jacobian: $\lambda(\mathbf{A}) = \{|u|-c\,,\ |u|+c\,,\ |u|\} = c\,\{M-1,\ M+1,\ M\}$. When $M \to 0$ or $M \to 1$ a large disparity occurs between the eigenvalues, resulting in a non efficient time marching of the equations.

Although this happens regardless of the time-space discretization that is utilized, its effect is blatantly observed in the discretized form, because any discretization of the system would be more robust if all the modes traveled at the same speed. A system of hyperbolic equations is said to be *stiff* or *ill-conditioned* when it exists a big disparity between its eigenvalues or characterisc speeds. In that case, convergence problems arise regardless of the discretization method that is used. The stiffness of a system is measured by the so-called condition number or characteristic condition number, defined in the following.

Let us recall that the *condition number* of a matrix $\mathbf{A}$ is defined as

$$\kappa(\mathbf{A}) = \frac{|\lambda(\mathbf{A})|_{\max}}{|\lambda(\mathbf{A})|_{\min}} \,, \tag{4.2}$$

where $|\lambda(\mathbf{A})|_{\max}$ and $|\lambda(\mathbf{A})|_{\min}$ are respectively the maximum and the minimum absolute values of the eigenvalues of $\mathbf{A}$. In one dimension, the *characteristic condition number*, κ, of the Euler system of equations (4.1) corresponds to the condition number of its

jacobian matrix, $\kappa(\mathbf{A})$, that is

$$\kappa = \begin{cases} \frac{M+1}{M} & M < \frac{1}{2} \\ \frac{M+1}{1-M} & \frac{1}{2} \leq M \leq 1 \\ \frac{M+1}{M-1} & 1 < M \ . \end{cases} \tag{4.3}$$

4.1.2 Multi-dimensional case

In the multi-dimensional case (2.8), there is one Jacobian $\mathbf{A}^i$ for each space direction $i = 1, \ldots, d$. Therefore, the definition of the condition number is not as obvious as it is for the one dimensional case and wave analysis becomes a necessary mathematical tool to evaluate the stiffness of 2D and 3D hyperbolic equations as the Euler equations (2.8). Examples of its use can be found in Darmofal and van Leer [1998, 1999], Lee [1996, 1991], van Leer et al. [1991]. The idea is to compute the condition number by analyzing the wave propagation speed (or wave speed) of plane waves. The basic rationale is the following. A plane wave of the form $\mathbf{\Phi}(\mathbf{n} \cdot \mathbf{x} - \lambda t)$ is plugged into (2.8), where $\mathbf{n}$ is a unit vector defining the direction of propagation and λ is the propagation speed of the plane wave. Thus the eigenvalue problem

$$(\mathbf{A_n} - \lambda \, \mathrm{Id}) \, \mathbf{\Phi}' = 0 \ , \tag{4.4}$$

where $\mathbf{A_n} = \sum_{i=1}^{d} \mathbf{A}^i \, n_i$, is found.

Then, the wave speeds in the propagation direction $\mathbf{n}$ are the eigenvalues $\lambda_j(\mathbf{A_n})$, $j = 1, \ldots, d+2$. As in the one-dimensional case, to respect the CFL condition the time step should be

$$\Delta t \leq \frac{h}{|\lambda|_{\max}} \ , \tag{4.5}$$

where h is a characteristic length of the grid and

$$|\lambda|_{\max} = \max_{j,\mathbf{n}} \, |\lambda_j(\mathbf{A_n})| \ , \tag{4.6}$$

is the maximum absolute value of the eigenvalues of the problem. The characteristic propagation speeds of the Euler equations in the reference coordinates are:

$$\begin{aligned} \lambda_{1,\ldots,d} &= \mathbf{u} \cdot \mathbf{n} \\ \lambda_{d+1,d+2} &= \mathbf{u} \cdot \mathbf{n} \pm c \ . \end{aligned} \tag{4.7}$$

In streamline coordinates (in Appendix B.2) they write:

$$\begin{aligned} \lambda_{1,\dots,d} &= cMn_1 \\ \lambda_{d+1,d+2} &= c(Mn_1 \pm 1) \ . \end{aligned} \tag{4.8}$$

As we consider all the unit vectors $\mathbf{n}$, the ensembles (4.7) and (4.8) turn to be the same. In fact, the reference coordinates and the streamline coordinates always give the same ensemble of eigenvalues. The largest absolute value of the eigenvalues is

$$|\lambda|_{\max} = c(M+1) \ , \tag{4.9}$$

defining the time steps for the marching scheme. The goal of preconditioning is therefore to cluster the eigenvalues (4.8) as much as possible.

The natural extension of expression (4.2) to the multi-dimensional case is

$$\frac{\max_{i,\mathbf{n}} |\lambda_i(\mathbf{A_n})|}{\min_{i,\mathbf{n}} |\lambda_i(\mathbf{A_n})|} \ . \tag{4.10}$$

However this is not a good measure of the problem stiffness. This is because the values $\lambda_{1,\dots,d}(\mathbf{A_n})$ are zero when $\mathbf{n}$ is orthogonal to the velocity $\mathbf{u}$, so the denominator $min_{i,\mathbf{n}}|\lambda_i(\mathbf{A_n})|$ is always zero regardless of the local Mach number. The same problem is encountered when analyzing the preconditioned system. Therefore, the group velocity is instead used in preconditioning analysis Darmofal and van Leer [1998], Lee [1991] to define the condition number. The group velocity is the propagation speed of the envelope of a plane wave defined as

$$\mathbf{g}_i(\mathbf{n}) = \nabla_{\mathbf{n}}(\|\mathbf{n}\| \, \lambda_i(\mathbf{n})) \ . \tag{4.11}$$

In this work $\|\cdot\|$ represents the L^2 norm. For an equivalent way of computing the group velocity, refer to Appendix D. The condition number is defined as the ratio of the largest and the smallest magnitude of the group velocities

$$\kappa = \frac{\max_{i,\mathbf{n}} \|\mathbf{g}_i(\mathbf{n})\|}{\min_{i,\mathbf{n}} \|\mathbf{g}_i(\mathbf{n})\|} \ . \tag{4.12}$$

Regardless of the space dimension, by plugging (4.8) into (4.11) (or equivalently, into euqations (D.1)-(D.4) of Appendix D), the group velocities, $\mathbf{g}(\mathbf{n})$, for the Euler system (2.8) are

$$\begin{aligned} \mathbf{g}_{1,\dots,d} &= (cM, 0, \dots, 0)^{\mathrm{T}} \\ \mathbf{g}_{d+1,d+2} &= (M \pm n_1, n_2, \dots, n_d)^{\mathrm{T}} \ , \end{aligned} \tag{4.13}$$

and their magnitudes are

$$\begin{aligned} \|\mathbf{g}_{1,\dots,d}\| &= cM \\ \|\mathbf{g}_{d+1,d+2}\| &= c\sqrt{M^2+1\pm 2Mn_1}\ . \end{aligned} \tag{4.14}$$

Therefore the condition number of the multidimensional system (2.8) is (4.3), that is, we obtain the same condition number as in the one-dimensional case.

4.2 Local preconditioning

We firstly apply local preconditioning to the Euler equations (2.8) for steady problems. Afterwards, we consider the Navier-Stokes equations (2.7) as well as transient problems. In this work, *van Leer-Lee-Roe*'s (VLR) and *Choi-Merkle*'s (CM) preconditioners are used. In this section they are described and briefly analyzed. VLR preconditioner is here used for the Euler equations and steady flow problems, as originally introduced in Lee [1991], van Leer et al. [1991]. Its extension to steady Navier-Stokes flow can be found in Lee [1996]. No applications of the VLR preconditioner to transient problems are found in the literature. CM preconditioner is here used in its original form for the Euler and Navier-Stokes equations of steady flow Choi and Merkle [1993]. We use CM preconditioner for transient problems as well López et al. [2012].

4.2.1 Euler equations

The three-dimensional preconditioned Euler equations in conservative variables and non-conservative form are written as follows:

$$\frac{\partial \mathbf{\Phi}}{\partial t} + \mathbf{P}\mathbf{A}^i(\mathbf{\Phi})\,\frac{\partial \mathbf{\Phi}}{\partial x_i} = 0\ , \tag{4.15}$$

where $\mathbf{P}$ is the local preconditioner and $i = 1,\dots,3$ labels the space dimension. The unpreconditioned Euler equations (2.8) are found when $\mathbf{P} = \mathrm{Id}$, where Id is the identity matrix. Given a bounded domain $\Omega \subset \mathbb{R}^3$, and a time interval $(0,T)$, $T \in \mathbb{R}$, $T > 0$, the problem is to find $\mathbf{\Phi}(\mathbf{x},t)$ verifying equation (4.15) with proper initial and boundary conditions, for all $(\mathbf{x},t) \in \Omega \times (0,T)$. As noted in Darmofal and van Leer [1998], Lee [1996], assuming that $\mathbf{P}$ has non-zero determinant and (4.15) converges to a steady state solution, the time derivatives go to zero and (2.8) and (4.15) will share the same steady solution.

A preconditioner is said to be optimal if it reduces the stiffness of the system to the minimum attainable. Optimality is, in fact, the main goal of preconditioning. However,

some essential considerations have to be taken into account Darmofal and van Leer [1998], Lee [1996]:

- Positivity. The preconditioner should not reverse the direction of the propagation speeds of the system. Otherwise incoming and outgoing waves would inverse roles and cause problems for the imposed boundary conditions. This requirement is satisfied if $\mathbf{P}$ is a positive-definite matrix.
- Symmetrizability. In order to guarantee that the energy of the system remains bounded, the system of equations should remain symmetrizable after preconditioning. This means that it exists a symmetric, positive definite matrix $\mathbf{S}$, such that $\mathbf{S}\,\mathbf{P}\mathbf{A}^i$ is a symmetric matrix for all $i = 1, \ldots, d$.
- Continuity. The preconditioner should verify some continuity conditions through all Mach number regimes. This is especially sensitive at the sonic point (i.e.: when $M = 1$) where a smooth transition between the subsonic and the supersonic preconditioners is required.

Although the original equations (4.15) are expressed and solved with respect to the conservative variables, $\mathbf{\Phi} = (U_1\ U_2\ U_3\ \rho\ E)^{\mathrm{T}}$, different sets are used in the literature to design and to introduce in a clearer way the preconditioners. These sets are the so-called symmetrizing, symmetrizing with streamline coordinates, and primitive sets of variables, which are described in the Appendices B.1, B.2, and C, respectively. For instance, the VLR preconditioner is constructed and usually expressed using the symmetrizing variables with streamline coordinates, $\mathrm{d}\mathbf{\Phi}_{\mathrm{SS}} = \left(\mathrm{d}q_1\ \mathrm{d}q_2\ \mathrm{d}q_3\ \frac{\mathrm{d}p}{\rho c}\ \mathrm{d}s\right)^{\mathrm{T}}$, defined in Appendix B.2. On the other hand, the CM preconditioner is constructed using the primitive variables, $\mathbf{\Phi}_{\mathrm{P}} = (u_1\ u_2\ u_3\ p\ T)^{\mathrm{T}}$, whose change of variables matrices with the conservative variables are defined in Appendix C.

As explained in Lee [1991], van Leer et al. [1991], in the one-dimensional case, the optimal condition number we can obtain when preconditioning is 1, in two dimensions it is 1 for supersonic flow and $\frac{1}{\sqrt{1-M^2}}$ for subsonic flow, and in three dimensions it is $\frac{1}{\sqrt{1-M^2}}$ for subsonic and $\frac{M}{\sqrt{M^2-1}}$ for supersonic flow. This is summarized in Table 4.1.

	No preco	Optimal preco		
		1D	2D	3D
Subsonic	$\frac{M+1}{\min\{M,1-M\}}$	1	$\frac{1}{\sqrt{1-M^2}}$	$\frac{1}{\sqrt{1-M^2}}$
Supersonic	$\frac{M+1}{M-1}$	1	1	$\frac{M}{\sqrt{M^2-1}}$

TABLE 4.1: Condition number of the non-preconditioned Euler equations and optimal condition number of the preconditioned Euler equations.

Condition number In the same way as it is done in Section 4.1 for the non-preconditioned Euler equations (2.8), wave analysis is used for the preconditioned case (4.15). The characteristic propagation speeds, group velocities, and condition number of (4.15) are defined in this paragraph, and its value for the VLR and CM preconditioners is computed in Subsections 4.2.4 and 4.2.5, respectively.

The characteristic propagation speeds or eigenvalues of system (4.15) are the propagation speeds of a plane wave solution of the system, which are the eigenvalues of $\mathbf{PA_n} = \sum_{i=1}^{d} \mathbf{PA}^i n_i$, that is: $\lambda_j(\mathbf{PA_n})$, $j = 1, \ldots, d+2$, where $\mathbf{n}$ is a unit vector defining the direction of propagation of the plane wave. The largest eigenvalues absolute value of the preconditioned problem (4.15), defined by

$$|\lambda|_{\max} = \max_{j,\mathbf{n}} |\lambda_j(\mathbf{PA_n})| \,, \tag{4.16}$$

is the one expected to determine the time step for this problem. This subject is discussed in more detail in Subsection 3.4.4.

In an analogous fashion as it is defined in Subsection 4.1.2, the group velocities of the preconditioned Euler system (4.15) are defined by

$$\mathbf{g}_i(\mathbf{n}) = \nabla_{\mathbf{n}}(\|\mathbf{n}\| \, \lambda_i(\mathbf{n})) \,, \tag{4.17}$$

where $\lambda_i(\mathbf{n})) = \lambda_i(\mathbf{PA_n})$, for $i = 1, \ldots, d$. An equivalent way to compute the group velocities is found in Appendix D. The condition number is defined by equation (4.12) that we repeat here for the sake of clarity:

$$\kappa = \frac{\max_{i,\mathbf{n}} \|\mathbf{g}_i(\mathbf{n})\|}{\min_{i,\mathbf{n}} \|\mathbf{g}_i(\mathbf{n})\|} \,. \tag{4.18}$$

In (4.18), the group velocities of the preconditioned Euler system (4.17) are used.

The expressions of the eigenvalues, the maximum absolute value of the eigenvalues, and the condition number for the three preconditioning options are summarized in Tables 4.2 and 4.3 for the two and three dimensional cases, respectively.

4.2.2 Navier-Stokes equations

As it is done in the previous section, the three-dimensional preconditioned Navier-Stokes equations in conservative variables and non-conservative form can be written as follows:

$$\frac{\partial \mathbf{\Phi}}{\partial t} + \mathbf{PA}^i(\mathbf{\Phi}) \, \frac{\partial \mathbf{\Phi}}{\partial x_i} - \frac{\partial}{\partial x_i} \left(\mathbf{PK}^{ir}(\mathbf{\Phi}) \, \frac{\partial \mathbf{\Phi}}{\partial x_r} \right) = 0 \,, \tag{4.19}$$

We consider here that $\frac{\partial \mathbf{P}}{\partial x_i}$ can be neglected. Under this assumption, if (4.19) converges to a steady solution, its time derivatives go to zero and (2.7) and (4.19) will share the same steady solution (as noted in Darmofal and van Leer [1998], Lee [1996]).

4.2.3 Transient problems

Local preconditioning modifies the transient evolution of the problem, and then it can only be directly applied to steady flow problems. For this reason, when transient problems are considered, a pseudo-time technique should be applied Jameson [1991], Merkle and Athavale [1987]. A pseudo-time derivative, $\frac{\partial \mathbf{\Phi}}{\partial \mathcal{T}}$, is added to the original equations (2.7). Then we have the physical time step and the pseudo-time step, and the local preconditioner is applied to the pseudo-time in order to accelerate its convergence to a pseudo steady state at each physical time-step. Thus the preconditioned Navier-Stokes equations for transient flow problems read

$$\frac{\partial \mathbf{\Phi}}{\partial \mathcal{T}} + \mathbf{P}\frac{\partial \mathbf{\Phi}}{\partial t} + \mathbf{P}\mathbf{A}^i(\mathbf{\Phi})\,\frac{\partial \mathbf{\Phi}}{\partial x_i} - \frac{\partial}{\partial x_i}\left(\mathbf{P}\mathbf{K}^{ir}(\mathbf{\Phi})\,\frac{\partial \mathbf{\Phi}}{\partial x_r}\right) = 0\,, \tag{4.20}$$

and at each physical time step we iterate in pseudo-time until a pseudo steady state is reached. In the context of time implicit solvers, this is called pseudo-transient continuation, see for example Knoll and Keyes [2004].

4.2.4 VLR preconditioner

The VLR preconditioner for the Euler equations Lee [1996, 1991] gives optimal condition number and applies to subsonic, transonic, and supersonic regimes. It is obtained by imposing a general preconditioning matrix that verifies a number of properties such as: optimality, accuracy, continuity at the sonic point, preservation of the decoupled entropy equation, positivity and symmetrizability. For the details of its derivation refer to Lee [1996, 1991]. The analysis of local preconditioning for the Euler equations is simplified when using the symmetrizing variables and streamline coordinates which are defined in Appendix B.2. The VLR preconditioner, originally expressed in these variables is given by

$$\mathbf{P}^{\text{ss}}_{\text{VLR}} = \begin{pmatrix} \frac{\tau}{\beta^2}+1 & 0 & 0 & -\frac{\tau M}{\beta^2} & 0 \\ 0 & \tau & 0 & 0 & 0 \\ 0 & 0 & \tau & 0 & 0 \\ -\frac{\tau M}{\beta^2} & 0 & 0 & \frac{\tau M^2}{\beta^2} & 0 \\ 0 & 0 & 0 & 0 & 1 \end{pmatrix}, \tag{4.21}$$

where

$$\tau = \min\left\{\beta, \frac{\beta}{M}\right\} = \begin{cases} \beta & M < 1 \\ \frac{\beta}{M} & M \geq 1 \end{cases} \tag{4.22}$$

and $\beta = \sqrt{|1 - M^{*2}|}$. In order to avoid division by zero in (4.21), M^* is defined as

$$M^* = \begin{cases} M & M \in (0, 1-\epsilon) \cup (1+\epsilon, +\infty) \\ 1-\epsilon & M \in (1-\epsilon, 1) \\ 1+\epsilon & M \in [1, 1+\epsilon)\ , \end{cases} \tag{4.23}$$

where $\epsilon = 0.01$. For the cases tested so far, (4.23) has proven to be fine. However a more sophisticated way of avoiding the sonic-point discontinuity is found in Lynn [1995]. From (4.21)-(4.22), the VLR preconditioner in the subsonic regime reads

$$\mathbf{P}^{\text{ss}}_{\text{VLR,sub}} = \begin{pmatrix} 1+\frac{1}{\beta} & 0 & 0 & \frac{-M}{\beta} & 0 \\ 0 & \beta & 0 & 0 & 0 \\ 0 & 0 & \beta & 0 & 0 \\ \frac{-M}{\beta} & 0 & 0 & \frac{M^2}{\beta} & 0 \\ 0 & 0 & 0 & 0 & 1 \end{pmatrix}, \tag{4.24}$$

whereas in the supersonic regime it reads

$$\mathbf{P}^{\text{ss}}_{\text{VLR,super}} = \begin{pmatrix} \frac{1+\beta}{M\beta} & 0 & 0 & \frac{-1}{\beta} & 0 \\ 0 & \frac{\beta}{M} & 0 & 0 & 0 \\ 0 & 0 & \frac{\beta}{M} & 0 & 0 \\ \frac{-1}{\beta} & 0 & 0 & \frac{M}{\beta} & 0 \\ 0 & 0 & 0 & 0 & 1 \end{pmatrix}. \tag{4.25}$$

We remark that (4.24) and (4.25) match continuously at the sonic point (i.e., when $M = 1$). Other articles of reference for the VLR preconditioner are Darmofal and van Leer [1998, 1999], Godfrey et al. [1993], Lee [1996, 1998a]. The importance of the eigenvectors structure of the preconditioned system is explained in Darmofal and Schmid [1996]. An extension of the Euler VLR preconditioner to the Navier-Stokes equations is found in Lee [1996], Lee and van Leer [1993], Lee et al. [1997], Lee [1998b]. The VLR preconditioner in the conservative variables set is

$$\mathbf{P}_{\text{VLR}} = \frac{\partial \mathbf{\Phi}}{\partial \mathbf{\Phi}_{\text{ss}}} \mathbf{P}^{\text{ss}}_{\text{VLR}} \frac{\partial \mathbf{\Phi}_{\text{ss}}}{\partial \mathbf{\Phi}}\ , \tag{4.26}$$

that is,

$$\mathbf{P}_{\text{VLR}} = \begin{pmatrix} a\,u_1u_1+\tau & a\,u_1u_2 & a\,u_1u_3 & b\,u_1 & c\,u_1 \\ a\,u_1u_2 & a\,u_2u_2+\tau & a\,u_2u_3 & b\,u_2 & c\,u_2 \\ a\,u_3u_1 & a\,u_3u_2 & a\,u_3u_3+\tau & b\,u_3 & c\,u_3 \\ d\,u_1 & d\,u_2 & d\,u_3 & e & f \\ g\,u_1 & g\,u_2 & g\,u_3 & h & i \end{pmatrix} , \tag{4.27}$$

where

$$\begin{aligned}
a &= \tfrac{1}{\|\mathbf{u}\|^2}\left(1+\tfrac{\tau}{\beta^2}-\tau\right)+\tfrac{1}{c^2}\left(\tfrac{R}{c_v}\tfrac{\tau(1-M^2)}{\beta^2}-\tfrac{\tau}{\beta^2}+\tfrac{R}{c_v}\right) , \\
b &= \tfrac{\tau(M^2-1)}{\beta^2}\left(1+\tfrac{1}{2}\tfrac{R}{c_v}M^2\right)-\tfrac{1}{2}\tfrac{R}{c_v}M^2 , \\
c &= \tfrac{R}{c_v}\tfrac{1}{c^2}\left(\tfrac{\tau(M^2-1)}{\beta^2}-1\right) , \\
d &= \tfrac{R}{c_v}\tfrac{1}{c^2}\left(1-\tfrac{\tau M^2}{\beta^2}\right)-\tfrac{\tau}{c^2\beta^2} , \\
e &= 1+\tfrac{\tau M^2}{\beta^2}+\tfrac{1}{2}\tfrac{R}{c_v}M^2\left(\tfrac{\tau M^2}{\beta^2}-1\right) , \\
f &= \tfrac{R}{c_v}\tfrac{1}{c^2}\left(\tfrac{\tau M^2}{\beta^2}-1\right) , \\
g &= 1+\left(1-\tfrac{c_v}{R}\right)\tfrac{\tau}{\beta^2}+\left(\tfrac{R}{c_v}-\tfrac{3}{2}\right)\tfrac{\tau M^2}{\beta^2}+\tfrac{1}{2}\tfrac{R}{c_v}M^2\left(1-\tfrac{\tau M^2}{\beta^2}\right) , \\
h &= \|\mathbf{u}\|^2\left[\left(\tfrac{c_v}{R}-1+M^2\left(1-\tfrac{1}{2}\tfrac{R}{c_v}\right)\right)\tfrac{\tau}{\beta^2}+\tfrac{1}{4}\tfrac{R}{c_v}M^2\left(\tfrac{\tau M^2}{\beta^2}-1\right)-\tfrac{1}{2}\right] , \\
i &= \left(1-\tfrac{R}{c_v}\right)\tfrac{\tau M^2}{\beta^2}+\tfrac{1}{2}\tfrac{R}{c_v}M^2\left(\tfrac{\tau M^2}{\beta^2}-1\right) , \\
\tau &= \min\left\{\beta,\tfrac{\beta}{M}\right\}=\begin{cases}\beta & M<1\\ \tfrac{\beta}{M} & M\geq 1\end{cases} , \\
\beta &= \sqrt{|1-M^{*2}|} .
\end{aligned} \tag{4.28}$$

2D condition number In two dimensions, the characteristic propagation speeds or eigenvalues for the VLR preconditioned system are

$$\begin{aligned}
\lambda_{1,2} &= cMn_1 \\
\lambda_{3,4} &= \tfrac{1}{2}cM\tau\left[(1+\tfrac{M^2-1}{\beta^2})n_1 \pm \sqrt{(1+\tfrac{M^2-1}{\beta^2})^2n_1^2+4\tfrac{1-M^2n_1^2}{\beta^2}}\right] .
\end{aligned} \tag{4.29}$$

Using (4.29) in (4.17) (or equivalently, in equation (D.1) of Appendix D), the group velocities of the VLR preconditioned system are

$$\begin{aligned}
\mathbf{g}_{1,2} &= (cM,0)^{\mathrm{T}} \\
\mathbf{g}_{3,4} &= \begin{cases} \pm\tfrac{cM}{\sqrt{1-M^2n_1^2}}((1-M^2)n_1,n_2)^{\mathrm{T}} & M<1 \\ c(\sqrt{M^2-1},\pm 1)^{\mathrm{T}} & M>1 , \end{cases}
\end{aligned} \tag{4.30}$$

and their norms are

$$\begin{aligned}\|\mathbf{g}_{1,2}\| &= cM \\ \|\mathbf{g}_{3,4}\| &= \begin{cases} cM\sqrt{\frac{1-M^2(2-M^2)n_1^2}{1-M^2n_1^2}} & M<1 \\ cM & M>1\,. \end{cases}\end{aligned} \tag{4.31}$$

By equations (4.31) and (4.12) the condition number is

$$\kappa = \begin{cases} \frac{1}{\sqrt{1-M^2}} & M<1 \\ 1 & M>1\,. \end{cases} \tag{4.32}$$

3D condition number Using the same definitions and following the path of the two-dimensional case, we proceed here in three dimensions. The eigenvalues of the system are

$$\begin{aligned}\lambda_{1,2} &= cMn_1 \\ \lambda_3 &= cM\tau n_1 \\ \lambda_{4,5} &= \tfrac{1}{2}cM\tau\left[(1+\tfrac{M^2-1}{\beta^2})n_1 \pm \sqrt{(1+\tfrac{M^2-1}{\beta^2})^2n_1^2 + 4\tfrac{1-M^2n_1^2}{\beta^2}}\right]\,,\end{aligned} \tag{4.33}$$

the group velocities $\mathbf{g}(\mathbf{n})$ are

$$\begin{aligned}\mathbf{g}_{1,2} &= (cM,0,0)^{\mathrm{T}} \\ \mathbf{g}_3 &= \begin{cases} (cM\sqrt{1-M^2},0,0)^{\mathrm{T}} & M<1 \\ (c\sqrt{M^2-1},0,0)^{\mathrm{T}} & M>1 \end{cases} \\ \mathbf{g}_{4,5} &= \begin{cases} \pm\frac{cM}{\sqrt{1-M^2n_1^2}}((1-M^2)n_1,n_2,n_3)^{\mathrm{T}} & M<1 \\ (\sqrt{M^2-1},\pm\frac{n_2}{\sqrt{1-n_1^2}},\pm\frac{n_3}{\sqrt{1-n_1^2}})^{\mathrm{T}} & M>1\,, \end{cases}\end{aligned} \tag{4.34}$$

and their norms are

$$\begin{aligned}\|\mathbf{g}_{1,2}\| &= cM \\ \|\mathbf{g}_3\| &= \begin{cases} cM\sqrt{1-M^2} & M<1 \\ c\sqrt{M^2-1} & M>1 \end{cases} \\ \|\mathbf{g}_{4,5}\| &= \begin{cases} cM\sqrt{\frac{1-M^2(2-M^2)n_1^2}{1-M^2n_1^2}} & M<1 \\ cM & M>1\,. \end{cases}\end{aligned} \tag{4.35}$$

The condition number of the VLR preconditioned system is then

$$\kappa = \frac{1}{\sqrt{1 - \min\{M^2, M^{-2}\}}} \,. \tag{4.36}$$

For both the two and three-dimensional cases, the largest eigenvalues absolute value of the VLR preconditioned system in all regimes is

$$|\lambda|_{\max} = cM = \|u\| \,. \tag{4.37}$$

4.2.5 CM preconditioner

The CM preconditioner is introduced in Choi and Merkle [1993] for steady Euler and Navier-Stokes flow. A simple parameter change permits to apply CM preconditioner to inviscid and viscous flow. CM steady preconditioner is easily adapted for transient problems in López et al. [2012], Vigneron et al. [2006]. CM preconditioner is not optimal as the VLR is, and its benefits only exist for low Mach numbers, however it has the advantage to be easily adapted for viscous and transient flows.

If we write the preconditioned Navier-Stokes equations as

$$\frac{\partial \mathbf{\Phi}_{\mathrm{P}}}{\partial t} + \mathbf{\Gamma}^{-1}\,\mathbf{A}^i\,\frac{\partial \mathbf{\Phi}}{\partial x_i} - \frac{\partial}{\partial x_i}\left(\mathbf{\Gamma}^{-1}\,\mathbf{K}^{ir}(\mathbf{\Phi})\,\frac{\partial \mathbf{\Phi}}{\partial x_r}\right) = 0 \,, \tag{4.38}$$

the CM preconditioner (as presented in Choi and Merkle [1993]) reads

$$\mathbf{\Gamma}^{-1} = \begin{pmatrix} \frac{1}{\rho} & 0 & 0 & \frac{-u_1}{\rho} & 0 \\ 0 & \frac{1}{\rho} & 0 & \frac{-u_2}{\rho} & 0 \\ 0 & 0 & \frac{1}{\rho} & \frac{-u_3}{\rho} & 0 \\ 0 & 0 & 0 & \beta M_r^2 & 0 \\ \frac{-u_1}{c_p\rho} & \frac{-u_2}{c_p\rho} & \frac{-u_3}{c_p\rho} & \frac{1}{c_p\rho}\left(\frac{1}{2}\|\mathbf{u}\|^2 - c_pT + \beta M_r^2\right) & \frac{1}{c_p\rho} \end{pmatrix} ; \tag{4.39}$$

its inverse is

$$\mathbf{\Gamma} = \begin{pmatrix} \rho & 0 & 0 & \frac{u_1}{\beta M_r^2} & 0 \\ 0 & \rho & 0 & \frac{u_2}{\beta M_r^2} & 0 \\ 0 & 0 & \rho & \frac{u_3}{\beta M_r^2} & 0 \\ 0 & 0 & 0 & \frac{1}{\beta M_r^2} & 0 \\ \rho u_1 & \rho u_2 & \rho u_3 & \frac{1}{\beta M_r^2}\frac{E+p}{\rho} & c_p\rho \end{pmatrix} , \tag{4.40}$$

where $\beta = k_\beta c^2$, with $k_\beta = 1$ for inviscid problems and $k_\beta = max\left\{1, \frac{Re_h^{-1}(Re_h^{-1}-1)}{M_r^2(Re_h^{-1}-1+M^{-2})}\right\}$ for viscous problems, where $Re_h = \frac{\rho\|\mathbf{u}\|h}{\mu}$ is the cell Reynolds number and h the characteristic element length that is here taken as the minimum element length. In (4.39)-(4.40), the reference Mach number for steady problems is:

$$M_r = \begin{cases} \epsilon & M < \epsilon \\ M & \epsilon < M < 1 \\ 1 & 1 < M \end{cases}, \tag{4.41}$$

with $\epsilon = 10^{-5}$, and, as computed by Vigneron et al. [2006], for transient problems it is:

$$M_r = \begin{cases} \epsilon & M' < \epsilon \\ M' & \epsilon < M' < 1 \\ 1 & 1 < M' \end{cases}, \tag{4.42}$$

where $M' = \sqrt{M^2 + CFL_c^{-2}}$, $CFL_c = \frac{c\Delta t}{h}$. In the CFL_c definition, Δt is the used time step, and h the characteristic length used for its computation, which is the shortest element length in this work. In conservative variables, the CM preconditioner is $\mathbf{P}_{\text{CM}} = \frac{\partial \mathbf{\Phi}}{\partial \mathbf{\Phi}_{\text{P}}}\mathbf{\Gamma}^{-1}$, that is,

$$\mathbf{P}_{\text{CM}} = \begin{pmatrix} 1+\frac{u_1u_1}{c_pT} & \frac{u_1u_2}{c_pT} & \frac{u_1u_3}{c_pT} & \frac{u_1}{c_pT}\,a & -\frac{u_1}{c_pT} \\ \frac{u_2u_1}{c_pT} & 1+\frac{u_2u_2}{c_pT} & \frac{u_2u_3}{c_pT} & \frac{u_2}{c_pT}\,a & -\frac{u_2}{c_pT} \\ \frac{u_3u_1}{c_pT} & \frac{u_3u_2}{c_pT} & 1+\frac{u_3u_3}{c_pT} & \frac{u_3}{c_pT}\,a & -\frac{u_3}{c_pT} \\ \frac{u_1}{c_pT} & \frac{u_2}{c_pT} & \frac{u_3}{c_pT} & 1+\frac{1}{c_pT}\,a & -\frac{1}{c_pT} \\ u_1\,b & u_2\,b & u_3\,b & a\,b & -\frac{1}{2}\frac{\|\mathbf{u}\|^2}{c_pT} \end{pmatrix}, \tag{4.43}$$

where $a = \frac{c_v}{R}\beta M_r^2 - \frac{1}{2}\|\mathbf{u}\|^2$ and $b = 1 + \frac{1}{2}\frac{\|\mathbf{u}\|^2}{c_pT}$. The CM preconditioner in symmetrizing variables and streamline coordinates is $\mathbf{P}^{\text{ss}}_{\text{CM}} = \frac{\partial \mathbf{\Phi}_{\text{ss}}}{\partial \mathbf{\Phi}}\,\mathbf{P}_{\text{CM}}\,\frac{\partial \mathbf{\Phi}}{\partial \mathbf{\Phi}_{\text{ss}}}$, which gives

$$\mathbf{P}^{\text{ss}}_{\text{CM}} = \begin{pmatrix} 1 & 0 & 0 & 0 & 0 \\ 0 & 1 & 0 & 0 & 0 \\ 0 & 0 & 1 & 0 & 0 \\ 0 & 0 & 0 & \mathcal{E} & -\frac{\mathcal{E}}{\rho c} \\ 0 & 0 & 0 & 0 & 1 \end{pmatrix}, \tag{4.44}$$

where $\mathcal{E} = \frac{\beta M_r^2}{c^2}$.

2D and 3D condition numbers We compute here the eigenvalues and condition number of the CM preconditioned Euler system for steady problems. Afterwards we

compute the eigenvalues for Euler transient problems. The eigenvalues for transient viscous flow are computed in López et al. [2012]. In the Euler steady case the eigenvalues are

$$\begin{aligned} \lambda_{1,\dots,d} &= cMn_1 \\ \lambda_{d+1,d+2} &= \tfrac{1}{2}c\left(Mn_1(1+M_r^2) \pm \sqrt{M^2n_1^2(1+M_r^2)^2 + 4M_r^2(1-M^2n_1^2)}\right) . \end{aligned} \tag{4.45}$$

where $\mathbf{n}$ is a unit vector defining the wave propagation direction. CM is a preconditioner for low Mach number regimes. When $M > 1$ we have $M_r = 1$ and we found the same eigenvalues as for the non-preconditioned case. As it is pointed out in Darmofal and van Leer [1998], above Mach numbers of approximately 0.4, the CM preconditioner has worse condition number than the unpreconditioned Euler equations and it could be switched off. The maximum eigenvalue in absolute value in all regimes is

$$|\lambda|_{\max} = \frac{1}{2}c\left(M(1+M_r^2) + \sqrt{M^2(1+M_r^2)^2 + 4M_r^2(1-M^2)}\right) . \tag{4.46}$$

Taking definition (4.17) (or equivalently, expressions (D.1)-(D.4)) and using the values of (4.45), the group velocities of the Euler steady case are

$$\mathbf{g}_{1,\dots,d} = (cM, 0, \dots, 0)^{\mathrm{T}}$$

$$\mathbf{g}_{d+1,d+2} = \begin{cases} \tfrac{1}{2}c\left(M(1+M_r^2) \pm n_1 \frac{M^2(1-M_r^2)^2+4M_r^2}{\sqrt{M^2n_1^2(1-M_r^2)^2+4M_r^2}}, \pm n_2 \frac{4M_r^2}{\sqrt{M^2n_1^2(1-M_r^2)^2+4M_r^2}}, \dots, \right. & \\ \left. \pm n_d \frac{4M_r^2}{\sqrt{M^2n_1^2(1-M_r^2)^2+4M_r^2}}\right)^{\mathrm{T}} & M < 1 \\ (M \pm n_1, n_2, \dots, n_d)^{\mathrm{T}} & M > 1 , \end{cases} \tag{4.47}$$

and their norms are

$$\|\mathbf{g}_{1,\dots,d}\| = cM$$

$$\|\mathbf{g}_{d+1,d+2}\| = \begin{cases} \tfrac{1}{2}c\left[\left(M(1+M_r^2) \pm \frac{(M^2(1-M_r^2)^2+4M_r^2)n_1}{\sqrt{M^2n_1^2(1-M_r^2)^2+4M_r^2}}\right)^2 + \right. & \\ \left. \left(\frac{4M_r^2(1-n_1^2)}{\sqrt{M^2n_1^2(1-M_r^2)^2+4M_r^2}}\right)^2\right]^{\frac{1}{2}} & M < 1 \\ c\sqrt{M^2+1\pm 2Mn_1} & M > 1 . \end{cases} \tag{4.48}$$

Then, from (4.48) and definition (4.12), the condition number of the CM preconditioned Euler system for steady flow is

$$\kappa = \begin{cases} \dfrac{M(1+M_r^2)+\sqrt{M^2(1-M_r^2)^2+4M_r^2}}{\left|M(1+M_r^2)-\sqrt{M^2(1-M_r^2)^2+4M_r^2}\right|} & M<1 \\ \\ \dfrac{M+1}{M-1} & M>1\,. \end{cases} \tag{4.49}$$

In the CM preconditioned Euler transient case, a pseudo-time is added to the original equations, as explained in Subsection 4.2.3. In this case the eigenvalues become

$$\begin{aligned} \lambda_{1,\dots,d} &= cM(1-in_1CFL_{\mathbf{u}}^{-1}) \\ \lambda_{d+1,d+2} &= \tfrac{1}{2}cM(1-in_1CFL_{\mathbf{u}}^{-1})\left((1+M_r^2)\pm\sqrt{(1-M_r^2)^2-4M_r(iM+CFL_c^{-1})^{-2}}\right)\,, \end{aligned} \tag{4.50}$$

and the maximum eigenvalue in absolute value is

$$|\lambda|_{\max} = cM\sqrt{1+CFL_{\mathbf{u}}^{-2}}\,, \tag{4.51}$$

where $CFL_{\mathbf{u}} = \frac{\|\mathbf{u}\|\Delta t}{h}$. In the $CFL_{\mathbf{u}}$ definition, Δt is the used time step, and h the characteristic length used for its computation.

Eigenvalues	NP		$\{cMn_1, cMn_1, c(Mn_1\pm 1)\}$
	VLR	$M<1$	$\{cMn_1, cMn_1, \pm cM\sqrt{1-M^2n_1^2})\}$
		$M>1$	$\{cMn_1, cMn_1, c(\sqrt{M^2-1}n_1 \pm \sqrt{1-n_1^2})\}$
	CM	$M<1$	$\{cMn_1, cMn_1, \frac{1}{2}c\left(Mn_1(1+M_r^2)\pm\sqrt{M^2n_1^2(1+M_r^2)^2+4M_r^2(1-M^2n_1^2)}\right)\}$
		$M>1$	$\{cMn_1, cMn_1, c(Mn_1\pm 1)\}$
Max. eigenvalue	NP		$c(M+1)$
	VLR		cM
	CM	$M<1$	$\frac{1}{2}c\left(M(1+M_r^2)+\sqrt{M^2(1+M_r^2)^2+4M_r^2(1-M^2)}\right)$
		$M>1$	$c(M+1)$
Condition number	NP		$\frac{M+1}{\min\{M,\lvert M-1\rvert\}}$
	VLR	$M<1$	$\frac{1}{\sqrt{1-M^2}}$
		$M>1$	1
	CM	$M<1$	$\frac{\sqrt{M^2(1+M_r^2)^2+4M_r^2(1-M^2)}+M(1+M_r^2)}{\sqrt{M^2(1+M_r^2)^2+4M_r^2(1-M^2)}-M(1+M_r^2)}$
		$M>1$	$\frac{M+1}{M-1}$

TABLE 4.2: 2D eigenvalues, their maximum, and the condition number of the NP (non preconditioned), VLR, and CM preconditioning options, for the Euler equations and steady flow.

Eigenvalues	NP		$\{cMn_1, cMn_1, cMn_1, c(Mn_1 \pm 1)\}$
	VLR	$M<1$	$\{cMn_1, cMn_1, cM\sqrt{1-M^2}n_1, \pm cM\sqrt{1-M^2n_1^2}\}$
		$M>1$	$\{cMn_1, cMn_1, c\sqrt{M^2-1}n_1, c(\sqrt{M^2-1}n_1 \pm \sqrt{1-n_1^2})\}$
	CM	$M<1$	$\{cMn_1, cMn_1, cMn_1, \frac{1}{2}c\left(Mn_1(1+M_r^2) \pm \sqrt{M^2n_1^2(1+M_r^2)^2 + 4M_r^2(1-M^2n_1^2)}\right)\}$
		$M>1$	$\{cMn_1, cMn_1, cMn_1, c(Mn_1 \pm 1)\}$
Max. eigenvalue	NP		$c(M+1)$
	VLR		cM
	CM	$M<1$	$\frac{1}{2}c\left(M(1+M_r^2) + \sqrt{M^2(1+M_r^2)^2 + 4M_r^2(1-M^2)}\right)$
		$M>1$	$c(M+1)$
Condition number	NP		$\frac{M+1}{\min\{M, \lvert M-1\rvert\}}$
	VLR	$M<1$	$\frac{1}{\sqrt{1-M^2}}$
		$M>1$	$\frac{M}{\sqrt{M^2-1}}$
	CM	$M<1$	$\frac{\sqrt{M^2(1+M_r^2)^2+4M_r^2(1-M^2)}+M(1+M_r^2)}{\sqrt{M^2(1+M_r^2)^2+4M_r^2(1-M^2)}-M(1+M_r^2)}$
		$M>1$	$\frac{M+1}{M-1}$

TABLE 4.3: 3D eigenvalues, its maximum and the condition number of the NP (non preconditioned), VLR, and CM preconditioning options, for the Euler equations and steady flow.

4.3 Numerical formulation of P-VMS

In this section we set the bases for the P-VMS method to solve the compressible Navier-Stokes equations. The space discretization is done using finite elements with VMS stabilization, we proceed in analogous way as in Section 2.3. Time is discretized using a first order forward finite difference scheme.

The stabilized space discretized weak form of the preconditioned Navier-Stokes equations (4.19) is

$$\int_{\Omega^h} \psi_p^h \frac{\partial \mathbf{\Phi}^h}{\partial t}\, d\Omega^h + \int_{\Omega^h} \psi_p^h\, \mathbf{PA}^i(\mathbf{\Phi}^h)\, \frac{\partial \mathbf{\Phi}^h}{\partial x_i}\, d\Omega^h + \int_{\Omega^h} \frac{\partial \psi_p^h}{\partial x_i}\, \mathbf{PK}^{ir}(\mathbf{\Phi}^h)\, \frac{\partial \mathbf{\Phi}^h}{\partial x_r}\, d\Omega^h + \sum_{K\in\mathcal{P}_h} \int_K \mathcal{L}^*_{\mathbf{P}}(\mathbf{\Phi}^h)\psi_p^h\, \tilde{\mathbf{\Phi}}\, dK = 0\,, \quad (4.52)$$

holding for all $p \in \{1, \dots, N\}$, where

$$\begin{aligned}\mathcal{L}^*_{\mathbf{P}}(\mathbf{\Phi})\psi &= -\frac{\partial}{\partial x_i}\left(\psi\, \mathbf{PA}^i(\mathbf{\Phi})\right) - \frac{\partial}{\partial x_r}\left(\frac{\partial \psi}{\partial x_i}\, \mathbf{PK}^{ir}(\mathbf{\Phi})\right) \\ &= -\frac{\partial \psi}{\partial x_i}\, \mathbf{PA}^i(\mathbf{\Phi}) - \psi\, \frac{\partial(\mathbf{PA}^i(\mathbf{\Phi}))}{\partial x_i} - \frac{\partial^2 \psi}{\partial x_r \partial x_i}\, \mathbf{PK}^{ir}(\mathbf{\Phi}) - \frac{\partial \psi}{\partial x_i}\, \frac{\partial(\mathbf{PK}^{ir}(\mathbf{\Phi}))}{\partial x_r}\,. \end{aligned} \quad (4.53)$$

The subscales $\tilde{\boldsymbol{\Phi}}$ are approximated in every element $K \in \mathcal{P}^h$ as described in equation (2.24) from subsection 2.3.4.1, as the product of a parameter matrix τ by the residual of the governing equation. We repeat this expression here for the sake of completeness:

$$\tilde{\boldsymbol{\Phi}} = \tau\, \mathbf{r}(\boldsymbol{\Phi}^h)\ . \tag{4.54}$$

For the preconditioned Navier-Stokes equations (4.19), the residual reads

$$\mathbf{r}(\boldsymbol{\Phi}^h) = -\,\mathbf{P}\mathbf{A}^i(\boldsymbol{\Phi}^h)\frac{\partial \boldsymbol{\Phi}^h}{\partial x_i} + \frac{\partial}{\partial x_i}\left(\mathbf{P}\mathbf{K}^{ir}(\boldsymbol{\Phi}^h)\frac{\partial \boldsymbol{\Phi}^h}{\partial x_r}\right)\ . \tag{4.55}$$

The stabilization parameter τ for the Euler preconditioned problem for steady flow is defined inside each element as

$$\tau = \frac{h}{|\lambda|_{max}}\ , \tag{4.56}$$

where h is chosen as the smallest edge length of the element and $|\lambda|_{max}$ is the largest characteristic propagation speed of system (4.15), as defined in (4.16) (in (4.6) for the non-preconditioned case). Using expression (4.37) for the VLR case, (4.56) becomes

$$\tau = \frac{h}{\|\mathbf{u}\|}\ , \tag{4.57}$$

where a lower bound is used when $\mathbf{u} = 0$. The same parameter τ will be used for the CM preconditioned case, as it will be shown later to perform better than the one using its own $|\lambda|_{\max}$ (in (4.46)). In (4.57), if $\mathbf{u} = 0$ a lower bound is used. Using expression (4.9), in the unpreconditioned case (i.e. when $P = \mathrm{Id}$) we get

$$\tau = \frac{h}{\|\mathbf{u}\| + c}\ , \tag{4.58}$$

where c is the speed of sound. Expression (4.58) for τ is also meet with expression (2.25), when we consider the particular case of the Euler equations. Now expression (4.54) is plugged into equation (4.52) to find an approximate solution of problem (4.15).

The stabilization parameter τ for the Navier-Stokes CM preconditioned problem for steady flow is

$$\tau = \left(\frac{\|\mathbf{u}\|}{h} + \frac{4\,\mu}{\rho\, h^2}\right)^{-1}\ , \tag{4.59}$$

and for the Navier-Stokes CM preconditioned problem for transient flow it is

$$\tau = \left(\frac{1}{2}\frac{\|\mathbf{u}\|\sqrt{1 + CFL_{\mathbf{u}}^{-2}}}{h} + \frac{4\,\mu}{\rho\, h^2}\right)^{-1}\ . \tag{4.60}$$

In (4.60) we used the maximum eigenvalue in absolute value (4.51). The stabilization parameter τ for the Navier-Stokes unpreconditioned case is defined by expression (2.25) that we reproduce here for the sake of clarity:

$$\tau = \left(\frac{\|\mathbf{u}\| + c}{h} + \frac{4\,\mu}{\rho\, h^2} \right)^{-1} . \tag{4.61}$$

Equation (4.52) is discretized in time by a first order explicit scheme and obtain the full discretized weak form:

$$\begin{aligned} &\int_{\Omega^h} \psi_p^h \, \frac{\mathbf{\Phi}^{h,n+1} - \mathbf{\Phi}^{h,n}}{\Delta t} \, d\Omega^h + \int_{\Omega^h} \psi_p^h \, \mathbf{PA}^i(\mathbf{\Phi}^{h,n}) \, \frac{\partial \mathbf{\Phi}^{h,n}}{\partial x_i} \, d\Omega^h \\ &\quad + \int_{\Omega^h} \frac{\partial \psi_p^h}{\partial x_i} \, \mathbf{PK}^{ir}(\mathbf{\Phi}^{h,n}) \, \frac{\partial \mathbf{\Phi}^{h,n}}{\partial x_r} \, d\Omega^h + \sum_{K \in \mathcal{P}_h} \int_K \mathcal{L}^*_{\mathbf{P}}(\mathbf{\Phi}^{h,n}) \psi_p^h \, \tilde{\mathbf{\Phi}}^{n+1} \, dK \; = 0 \, , \end{aligned} \tag{4.62}$$

holding for all $p \in \{1, \ldots, N\}$. The superscripts $n+1$ and n indicate the current and the previous time steps, respectively. The value of $\tilde{\mathbf{\Phi}}^{n+1}$ is computed from the information of the previous time step, i.e. $\tilde{\mathbf{\Phi}}^{n+1} = \tau^n \, \mathbf{r}(\mathbf{\Phi}^{h,n})$, and $\mathbf{\Phi}^{h,n}$ is computed using equality (2.12).

In this work, two ways of time stepping are considered: local and global time stepping. For the preconditioned Euler steady problem a time step inside each element is defined as

$$\Delta t^{\,el} = C \, \frac{h}{|\lambda|_{\max}} \, , \tag{4.63}$$

where $C \in (0, 1)$ is the CFL number, h is the smallest edge length of the element, and $|\lambda|_{max}$ is the maximum eigenvalue in absolute value, defined in (4.16) (in (4.6) for the non-preconditioned case). As done in subsection 2.3.5, the elementary time step (4.63) is interpolated on the nodes of the grid, obtaining the local time step $\Delta t^{\,p}$, $p = 1, \ldots, N$, at each node $\mathbf{x}^p$ of the grid. The global time step is computed as the minimum time step of the domain as it is expressed in (2.48). We repeat this expression here for the sake of completeness:

$$\Delta t = \min_{p=1,\ldots,N} \{\Delta t^{\,p}\} \, . \tag{4.64}$$

For the VLR preconditioner $|\lambda|_{\max} = \|\mathbf{u}\|$, so that the elementary time step becomes

$$\Delta t^{\,el} = C \, \frac{h}{\|\mathbf{u}\|} \, . \tag{4.65}$$

As it is done for (4.57), we impose in (4.65) a lower bound on $\mathbf{u}$ to avoid division by zero. The same time step is used for the CM preconditioned case, as it will be shown later to perform better than the one using its own $|\lambda|_{\max}$. When no preconditioner is used, the

time step inside each element is computed as

$$\Delta t^{el} = C \, \frac{h}{\|\mathbf{u}\| + c} \, , \tag{4.66}$$

and local and global time steps are defined from (4.66). Expression (4.66) is recovered as well from (2.47) when the particular case of the Euler equations is considered. From definitions (4.65) and (4.66), it can be observed that, especially in low-Mach regimes, the time step for the preconditioned case could be orders of magnitude larger than the non-preconditioned one. As it will be shown later, this entails a speed up of the convergence for the preconditioned system.

As it is done in the computation of the stabilization parameter τ, for the CM preconditioned Navier-Stokes steady problem, the time step is

$$\Delta t^{el} = C \, \left(\frac{\|\mathbf{u}\|}{h} + \frac{4\,\mu}{\rho\, h^2} \right)^{-1} \, , \tag{4.67}$$

and for the CM preconditioned Navier-Stokes equations of transient flow the pseudo-time step is

$$\Delta \mathcal{T}^{el} = C_{\mathcal{T}} \, \left(\frac{1}{2} \frac{\|\mathbf{u}\| \sqrt{1 + CFL_{\mathbf{u}}^{-2}}}{h} + \frac{4\,\mu}{\rho\, h^2} \right)^{-1} \, , \tag{4.68}$$

where $C_{\mathcal{T}} \in (0, 1)$ is a safety factor for the pseudo-time. The pseudo-time step for the Navier-Stokes unpreconditioned case is defined by expression (2.47), that is:

$$\Delta \mathcal{T}^{el} = C_{\mathcal{T}} \, \left(\frac{\|\mathbf{u}\| + c}{h} + \frac{4\,\mu}{\rho\, h^2} \right)^{-1} \, . \tag{4.69}$$

The physical time step for preconditioned transient problems is always computed as usually done, by expression (2.47), that we reproduce here for the sake of clarity:

$$\Delta t^{el} = C \, \left(\frac{\|\mathbf{u}\| + c}{h} + \frac{4\,\mu}{\rho\, h^2} \right)^{-1} \, . \tag{4.70}$$

As it is explained in subsection 2.3.5, the value of $\mathbf{\Phi}^{h,n+1}$ is found at each node of the computational grid through equation (2.54), that we reproduced here for the sake of completeness:

$$\mathbf{\Phi}^{h,n+1} = \mathbf{\Phi}^{h,n} + \Delta t \, \mathbf{M}^{-1} \left(\mathbf{G}(\mathbf{\Phi}^{h,n}) + \mathbf{S}(\mathbf{\Phi}^{h,n}, \tilde{\mathbf{\Phi}}^{n+1}) \right) \, . \tag{4.71}$$

In (4.71), $\mathbf{M}$ is the global Mass matrix, defined in (2.50), which is diagonalized by lumping techniques Hughes [2000]. $\mathbf{G}$ and $\mathbf{S}$ are the Galerkin and stabilization vectors,

respectively, which are constructed by assembly of

$$\mathbf{G}^p = -\int_{\Omega^h} \psi_p^h \, \mathbf{PA}^i(\mathbf{\Phi}^{h,n}) \, \frac{\partial \mathbf{\Phi}^{h,n}}{\partial x_i} \, d\Omega^h - \int_{\Omega^h} \frac{\partial \psi_p^h}{\partial x_i} \, \mathbf{PK}^{ir}(\mathbf{\Phi}^{h,n}) \, \frac{\partial \mathbf{\Phi}^{h,n}}{\partial x_r} \, d\Omega^h \tag{4.72}$$

and

$$\mathbf{S}^p = -\sum_{K \in \mathcal{P}_h} \int_K \left(-\frac{\partial \psi_p^h}{\partial x_i} \, \mathbf{PA}^i(\mathbf{\Phi}^{h,n}) - \psi_p^h \, \frac{\partial (\mathbf{PA}^i(\mathbf{\Phi}^{h,n}))}{\partial x_i} \right.$$
$$\left. -\frac{\partial^2 \psi_p^h}{\partial x_r \partial x_i} \, \mathbf{PK}^{ir}(\mathbf{\Phi}^{h,n}) - \frac{\partial \psi_p^h}{\partial x_i} \, \frac{\partial (\mathbf{PK}^{ir}(\mathbf{\Phi}^{h,n}))}{\partial x_r} \right) \, \tau^n \, \mathbf{r}(\mathbf{\Phi}^{h,n}) \, dK \, , \tag{4.73}$$

respectively, for $p = 1, \ldots, N$. In the current implementation of this method, terms $\frac{\partial (\mathbf{PA}^i(\mathbf{\Phi}^{h,n}))}{\partial x_i}$ and $\frac{\partial (\mathbf{PK}^{ir}(\mathbf{\Phi}^{h,n}))}{\partial x_r}$ are neglected, however they should be taken into account in the future. It is important to notice that local preconditioning comes before any discretization method is applied to the equations; once discretized, the resulting algebraic system could eventually present disparities in its eigenvalues, related for example to different element sizes on the mesh, different values of velocity, density, etc. over the domain. Therefore, local preconditioning convergence could even improve if additional algebraic preconditioners are applied as well.

4.4 Numerical results

P-VMS performance for Euler steady flow is assessed through two well-known benchmarks. The first example is the flow past a two dimensional NACA 0012 airfoil at zero angle of attack and different Mach numbers, from subsonic flows at very low Mach number, up to supersonic regimes. The second one is the three dimensional ONERA M6 wing test case at 3.06° angle of attack and a Mach number of 0.8395. In order to test P-VMS for viscous flow as well as transient problems, a viscous NACA 0012 at 0.0001 Mach number and 10000 Reynolds number and a shock tube at Mach 0.00184 are also solved. A first order explicit time integration scheme is used for the time integration.

In the Euler steady case, VLR and CM preconditioners are used and compared to the non preconditioned (NP) case. For these three preconditioning options (NP, VMS, and CM), both global and local time stepping are tested, giving the following options:

- No preconditioning with global time step (NP-globalTS)
- No preconditioning with local time step (NP-localTS)
- VLR preconditioning with global time step (VLR-globalTS)

- VLR preconditioning with local time step (VLR-localTS)
- CM preconditioning with global time step (CM-globalTS)
- CM preconditioning with local time step (CM-localTS)

In what follows, when we want to specify the time stepping that is used, we will refer to the different cases by using the above abbreviations in brackets. In the Navier-Stokes and transient cases, only CM preconditioner is used and compared to the unpreconditioned method.

At the continuous stage the unpreconditioned and the preconditioned equations, share the same solution. However, both systems are different and have different condition numbers, so that they can react differently to the numerical discretization. Consequently they can give slightly different solutions, or one of them can converge while the other diverges. As noted in Darmofal and van Leer [1998], local preconditioning "[...] has the benefit of increasing the accuracy of the discretization". This fact would be seen through the following test cases.

Convergence rates are here represented as the base ten logarithm of a normalized residual, Res, i.e. the residual Res with logarithmic scale, on the vertical axis, over the iteration number on the horizontal axis, where

$$
\begin{aligned}
Res &= \frac{\|\Delta \mathbf{U}\|}{\|\mathbf{U}\|} + \frac{\|\Delta \rho\|}{\|\rho\|} + \frac{\|\Delta E\|}{\|E\|} \ , \\
\frac{\|\Delta \mathbf{U}\|}{\|\mathbf{U}\|} &= \frac{\sqrt{\sum\limits_{\substack{p=1,\dots,N \\ i=1,\dots,d}} (U_i^{n+1}(\mathbf{x}^p) - U_i^n(\mathbf{x}^p))^2}}{\sqrt{\sum\limits_{\substack{p=1,\dots,N \\ i=1,\dots,d}} (U_i^{n+1}(\mathbf{x}^p))^2}} \ , \\
\frac{\|\Delta \rho\|}{\|\rho\|} &= \frac{\sqrt{\sum\limits_{p=1,\dots,N} (\rho^{n+1}(\mathbf{x}^p) - \rho^n(\mathbf{x}^p))^2}}{\sqrt{\sum\limits_{p=1,\dots,N} (\rho^{n+1}(\mathbf{x}^p))^2}} \ , \\
\frac{\|\Delta E\|}{\|E\|} &= \frac{\sqrt{\sum\limits_{p=1,\dots,N} (E^{n+1}(\mathbf{x}^p) - E^n(\mathbf{x}^p))^2}}{\sqrt{\sum\limits_{p=1,\dots,N} (E^{n+1}(\mathbf{x}^p))^2}} \ .
\end{aligned}
\tag{4.74}
$$

4.4.1 NACA 0012 airfoil

Inviscid flow past a two-dimensional NACA 0012 airfoil is solved at zero angle of attack and inflow Mach numbers: 0.001, 0.01, 0.1, 0.3, 0.5, 0.7, 0.9, 1.0, 1.2, 1.8, 2.0. The rest of the initial conditions being: $\rho = 1$, $\mathbf{u} = (1, 0)$, $T = 1$, and c_{p} and c_{v} are determined

to obtain the desired inflow Mach numbers. An unstructured grid of 4522 triangles and 2315 grid nodes is used. The CFL number values used for these simulations are in Table 4.5. It corresponds to the maximum CFL number that can be used for each simulation, obtained through numerical experiments. Slip boundary conditions are used on the airfoil and on the upper and lower walls of the domain. A constant velocity and temperature are prescribed at the inflow and a constant density at the outflow. A prudential distance is taken from the airfoil to the inflow and outflow boundaries in order to avoid the numerical instabilities of reflecting waves.

The same problem for a Mach number of 0.0001 is solved in the original paper by Choi and Merkle [1993] using central differencing in space. In van Leer et al. [1991], they solve it by finite volumes, using the VLR preconditioner and different Mach numbers ranging between 0.01 tand 1.8.

Results of pressure contours for the different inflow Mach numbers are displayed in Figs. 4.1 to 4.11. They show the final steady state solution corresponding to the NP and VLR options using local time stepping. The results using the CM preconditioner are not shown here, they are very similar to the VLR ones for low Mach numbers ($M \leq 0.3$) and to the NP ones otherwise. CM is in fact a preconditioner for low Mach number regimes, otherwise it does not remove the stiffness of the non-preconditioned Euler equations. The CM preconditioned system is worse conditioned than the non-preconditioned case when $0.4 < M < 1$. When $M > 1$ the characteristic speeds of the CM preconditioned system are indeed the same of the NP case (see Subsection 4.2.5 for more detail). For all Mach numbers, VLR using global and local time stepping give identical steady result. NP-globalTS and NP-localTS options give very similar but not identical results, the same happens between CM-globalTS and CM-localTS options.

For Mach numbers 0.001, 0.01, and 0.1, the non-preconditioned VMS gives a very unstable result, shown in Figs. 4.1-4.3, while P-VMS using both VLR or CM converges rapidly to a smooth solution. This fact shows that the use of VLR or CM preconditioners gives enough stability to VMS to handle low Mach number flows accurately and robustly.

As expected, non-preconditioned VMS becomes more stable as the Mach number increases. When $M = 0.3$ the non-preconditioned VMS pressure contours still present some error at the surface of the airfoil (Fig. 4.4), which is not at all the case for the P-VMS in either VLR or CM. With a more refined grid the non-preconditioned VMS could give a good result, however the object of this study is to compare the convergence and stability properties of non-preconditioned and preconditioned options, under the same conditions. For Mach numbers 0.5 and 0.7 (Figs. 4.5 and 4.6) all the options give very similar results.

To better compare, no shock-capturing diffusion is used for the supersonic cases. Then the result presents some oscillations near the shocks in the supersonic regions. When $M = 0.9$ (Fig. 4.7) VLR option seems to capture the sharp shock that appears in the tail of the airfoil more accurately than NP and CM options. We Observe in Fig. 4.9 that for $M = 1.2$ the results of NP and CM options are different from VLR one. The front shock is formed at $x = 0.5$ in VLR case and slightly before in NP and CM ones. The VLR pressure contours and position of the front shock compare better with the result from Arias et al. [2007] than the NP and CM ones. Similar discrepancy between NP/CM and VLR options concerning the front shock position appears for Mach numbers 1.8 and 2.0 (Figs. 4.10 and 4.11).

The maximum and minimum values of the Mach number of the steady solution for the different preconditioning and time stepping options are displayed in Table 4.4 for comparison. The minimum value of the Mach number is reached at the leading edge where M should be zero. This value represents the main disagreement between NP, VLR and CM options. The NP and CM cases always have larger minimum values than the VLR option. In the CM case those values are at most one order of magnitude larger than the VLR case. However, in the NP case they are most of the times one or two orders of magnitude larger than in the VLR case. This shows the improved accuracy properties of the P-VMS, especially in the case of the VLR preconditioner, for which the Mach number at the leading edge approaches zero the most. When $M = 1.2$, the Mach number result for the NP-localTS option presents an overshot on a point of the outflow boundary, which is reflected in Table 4.4 in the Mach number maximum value for this case. The use of local time stepping is not as robust for the unpreconditioned case as it is when preconditioning is used.

Even if the CFL number has to be reduced when local time stepping is used (see Table 4.5), local time stepping improves the convergence rate compared to global time stepping (not shown). This improvement is less significant when $M \to 0$, where both time stepping options give similar convergence, as well as for the CM option when $M \to 1$.

Results of convergence rates are displayed in Fig. 4.12. The benefits of VLR-localTS for all Mach numbers and CM-localTS for low Mach number regimes in terms of convergence acceleration and stability of the solution for the Euler equations is clearly demonstrated in these examples. VLR-localTS gives the best convergence rate in all cases. CM-localTS compared to NP-localTS performs better for low Mach numbers. However when $0.3 < M < 1$, it is seen to give similar convergence rates to the NP-localTS case, and worse convergence rates when $M > 1$. This is the expected behavior from what is said in Subsection 4.2.5.

When $M = 1.0$ at the inflow, the convergence obtained with the VLR preconditioner is very sensitive to the definition of the reference Mach number M^* (equation (4.23)) around the sonic point. This definition depends on the value of the bound parameter ϵ that is set to 0.01 in this work. If ϵ is set to 0.1, the VLR-localTS convergence stalls at approximately 10^{-6} (not shown). If it is set to 0.001, the problem diverges.

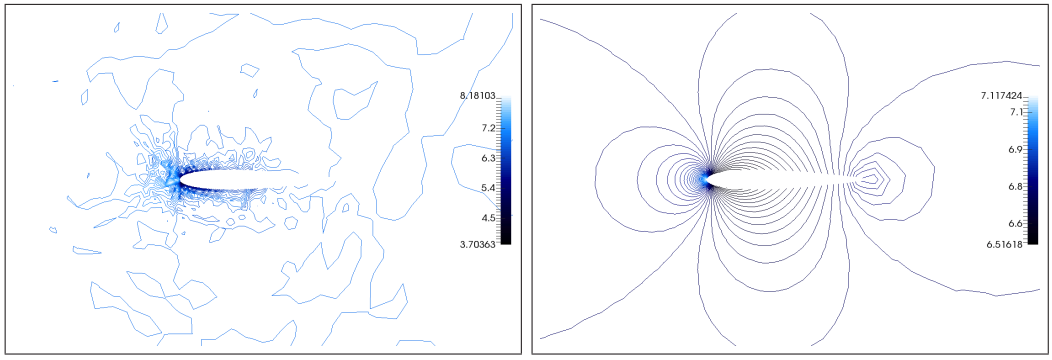

FIGURE 4.1: NACA 0012 test case. Pressure contours for an inflow Mach number of 0.001 for the NP (left) and VLR (right) cases with local time step. Due to the very small change in pressure at this Mach number, the contours of $p - p_{\text{ref}}$, that is the change in pressure in relation to a reference, $p_{\text{ref}} = 714279$, are plotted.

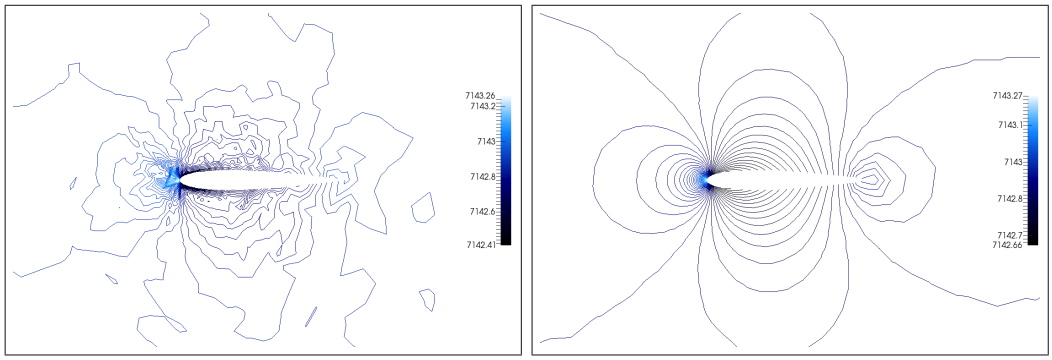

FIGURE 4.2: NACA 0012 test case. Pressure contours for an inflow Mach number of 0.01 for the NP (left) and VLR (right) cases with local time step.

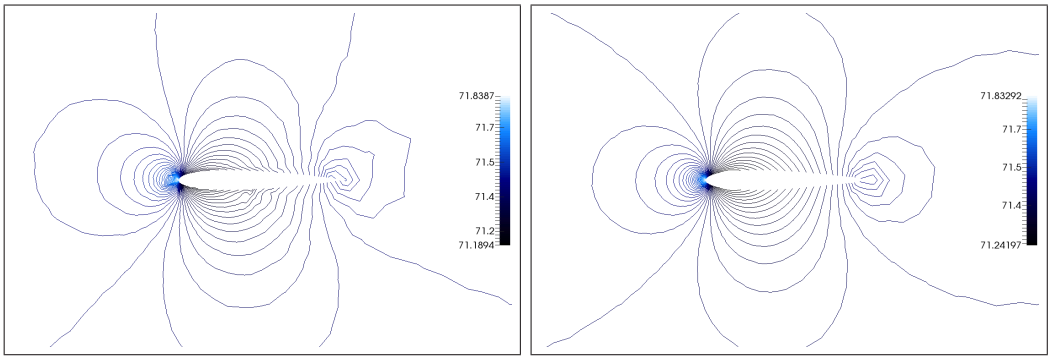

FIGURE 4.3: NACA 0012 test case. Pressure contours for an inflow Mach number of 0.1 for the NP (left) and VLR (right) cases with local time step.

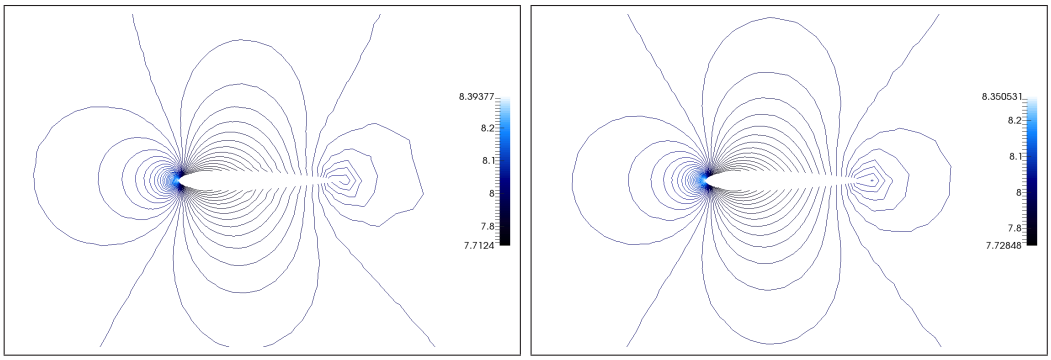

FIGURE 4.4: NACA 0012 test case. Pressure contours for an inflow Mach number of 0.3 for the NP (left) and VLR (right) cases with local time step.

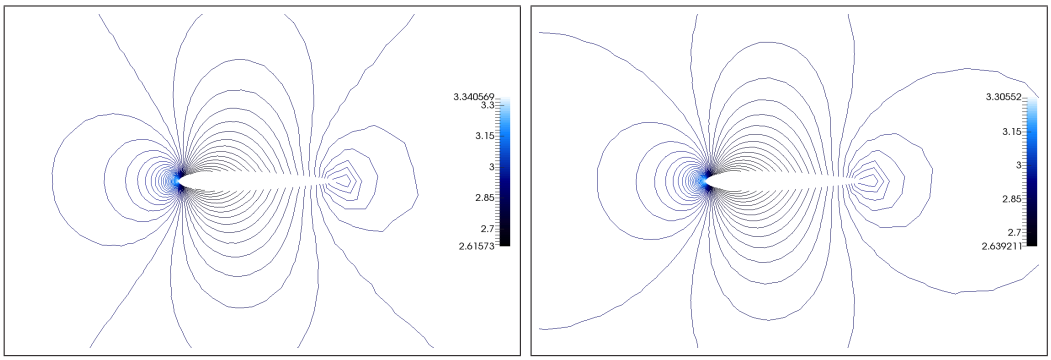

FIGURE 4.5: NACA 0012 test case. Pressure contours for an inflow Mach number of 0.5 for the NP (left) and VLR (right) cases with local time step.

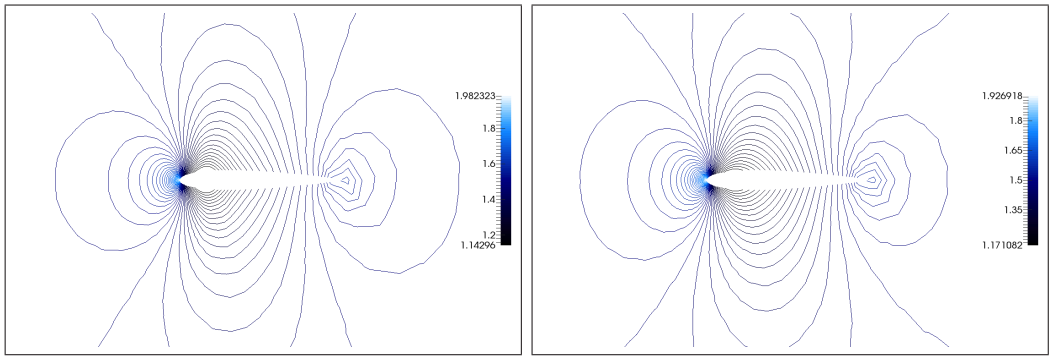

FIGURE 4.6: NACA 0012 test case. Pressure contours for an inflow Mach number of 0.7 for the NP (left) and VLR (right) cases with local time step.

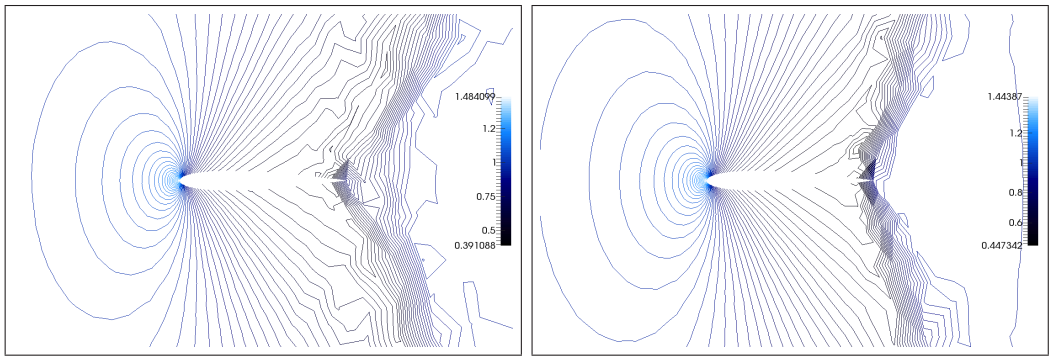

FIGURE 4.7: NACA 0012 test case. Pressure contours for an inflow Mach number of 0.9 for the NP (left) and VLR (right) cases with local time step.

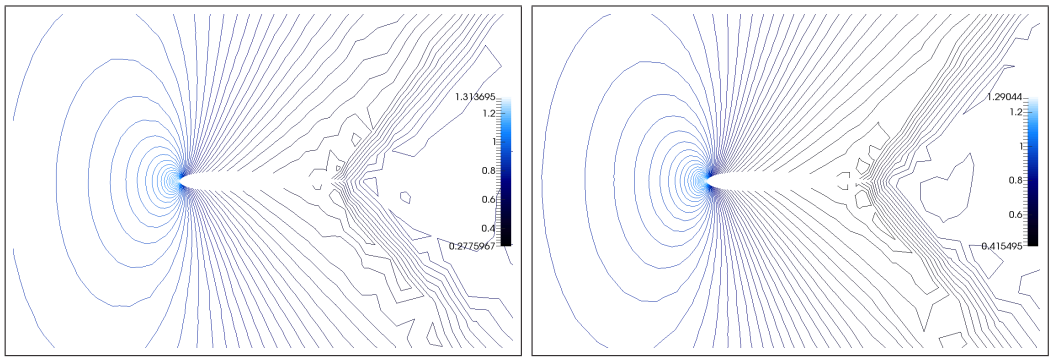

FIGURE 4.8: NACA 0012 test case. Pressure contours for an inflow Mach number of 1.0 for the NP (left) and VLR (right) cases with local time step.

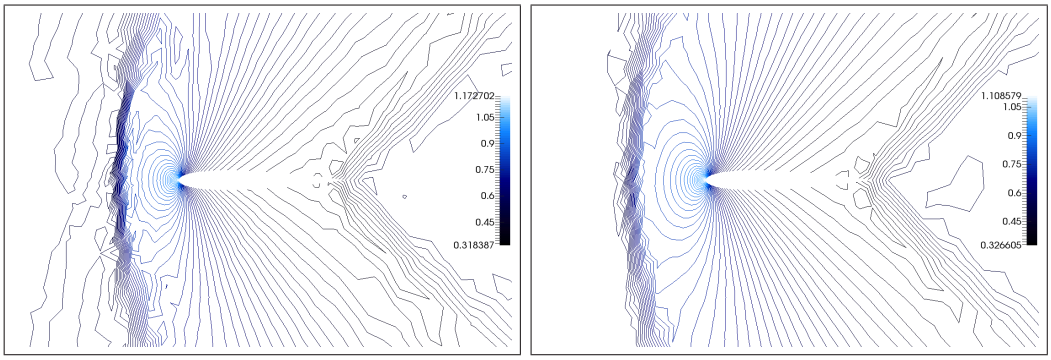

FIGURE 4.9: NACA 0012 test case. Pressure contours for an inflow Mach number of 1.2 for the NP (left) and VLR (right) cases with local time step.

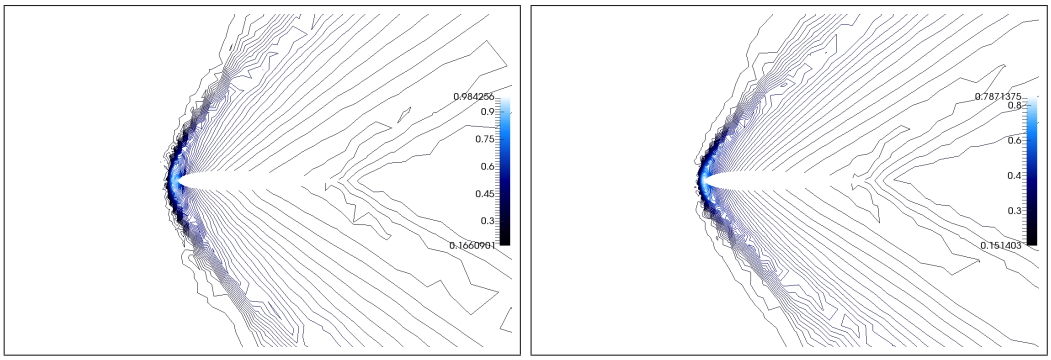

FIGURE 4.10: NACA 0012 test case. Pressure contours for an inflow Mach number of 1.8 for the NP (left) and VLR (right) cases with local time step.

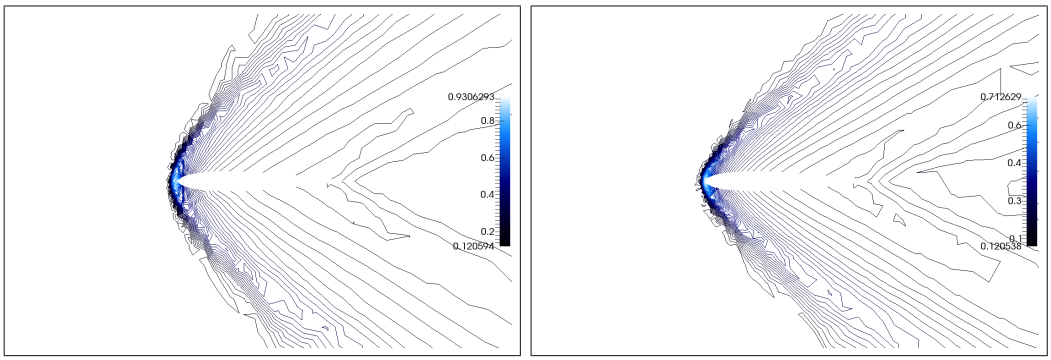

FIGURE 4.11: NACA 0012 test case. Pressure contours for an inflow Mach number of 2.0 for the NP (left) and VLR (right) cases with local time step.

Mach	NP-globalTS	NP-localTS	VLR	CM-globalTS	CM-localTS
0.001	-	-	3.22×10^{-6}/0.001182	1.36×10^{-5}/0.001181	1.00×10^{-5}/0.001182
0.01	-	-	3.22×10^{-5}/0.01182	1.36×10^{-4}/0.01181	1.02×10^{-4}/0.01182
0.1	0.00397/0.1179	0.00375/0.1179	3.19×10^{-4}/0.1183	0.001347/0.1182	0.001271/0.1183
0.3	0.0141/0.366	0.0141/0.366	8.90×10^{-4}/0.359	0.00371/0.359	0.00374/0.359
0.5	0.0178/0.628	0.0178/0.628	0.00119/0.614	0.00511/0.615	0.00511/0.615
0.7	0.0174/0.945	0.0173/0.949	0.00109/0.927	0.00521/0.932	0.00519/0.933
0.9	0.0189/1.53	0.0189/1.53	0.001439/1.44	0.00719/1.50	0.00720/1.50
1.0	0.0146/1.79	0.0146/1.79	4.37×10^{-4}/1.45	0.00219/1.80	0.00219/1.80
1.2	0.0214/1.53	0.0223/4.77	0.00726/1.49	0.00830/1.75	0.00835/1.92
1.8	0.0545/2.09	0.0545/2.09	0.0166/1.97	0.0378/2.53	0.0378/2.53
2.0	0.0233/2.40	0.0233/2.40	0.0476/2.20	0.0377/2.88	0.0377/2.88

TABLE 4.4: NACA 0012 test case. Comparative minimum/maximum Mach numbers over the domain once reached the steady state. The different preconditioning options using global and local time stepping are compared for the NACA0012 test case at different inflow Mach numbers. VLR-globalTS and VLR-localTS values are shown in the same column (VLR) as they give identical results. The dash symbol "-" indicates that the result didn't converge.

Mach	0.001	0.01	0.1	0.3	0.5	0.7	0.9	1.0	1.2	1.8	2.0
NP-globalTS	0.4	0.4	0.4	0.5	0.6	0.6	0.6	0.6	0.6	0.6	0.7
NP-localTS	0.3	0.3	0.3	0.4	0.4	0.4	0.3	0.4	0.4	0.4	0.4
VLR-globalTS	0.5	0.5	0.5	0.5	0.6	0.6	0.6	0.6	0.6	0.8	0.7
VLR-localTS	0.3	0.3	0.3	0.3	0.3	0.3	0.3	0.3	0.3	0.3	0.2
CM-globalTS	0.2	0.2	0.2	0.2	0.2	0.1	0.2	0.3	0.3	0.4	0.4
CM-localTS	0.1	0.1	0.1	0.1	0.1	0.1	0.1	0.1	0.1	0.1	0.1

TABLE 4.5: NACA 0012 test case. Comparison of the CFL numbers used for the different preconditioning options at different inflow Mach numbers.

(A) $M = 0.001$

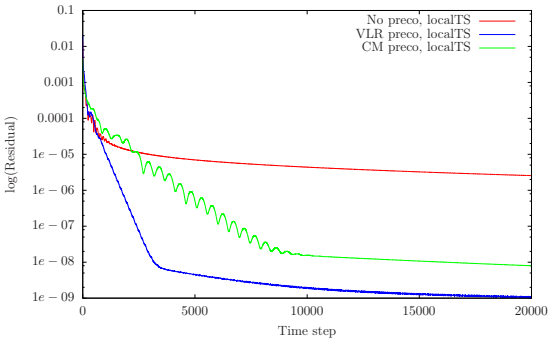

(B) $M = 0.01$

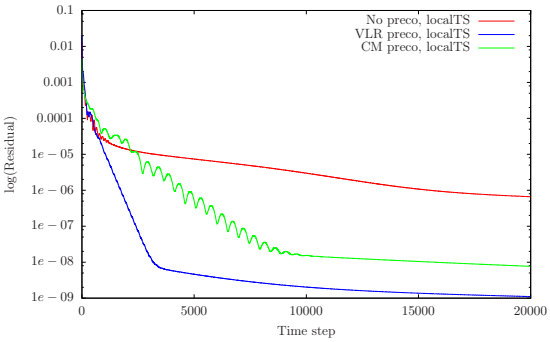

(C) $M = 0.1$

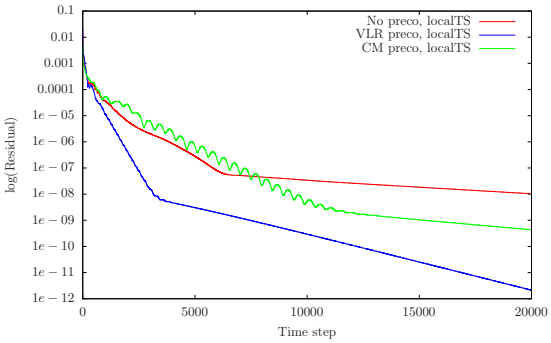

(D) $M = 0.3$

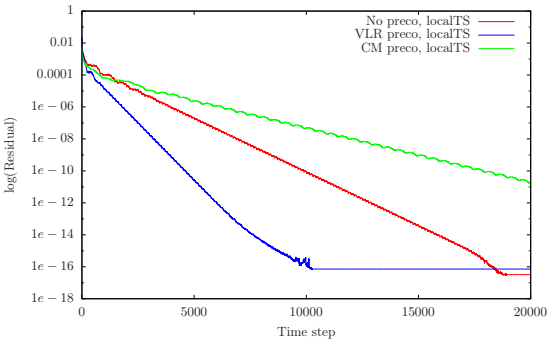

(E) $M = 0.5$

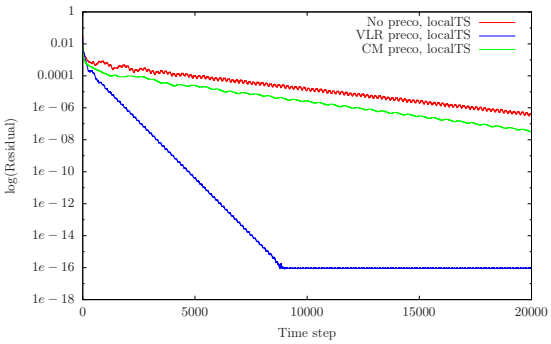

(F) $M = 0.7$

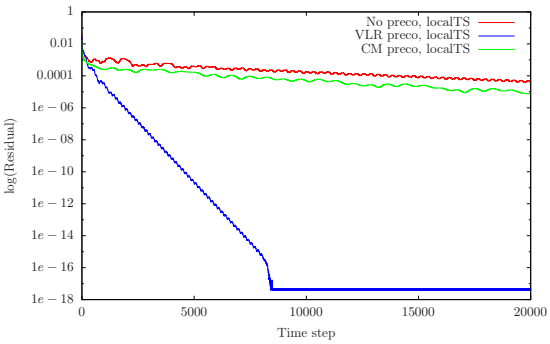

(G) $M = 0.9$

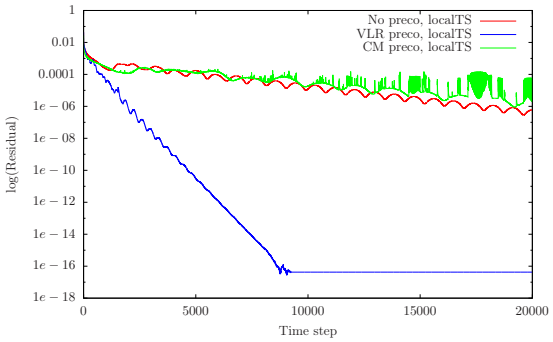

(H) $M = 1.0$

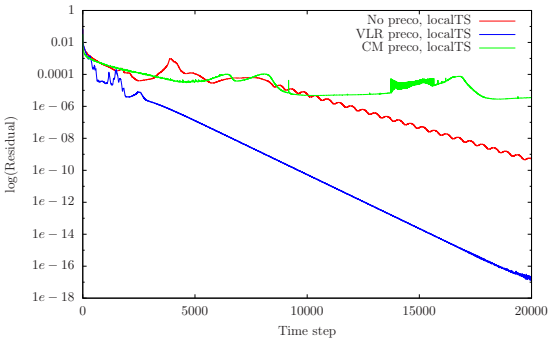

(I) $M = 1.2$

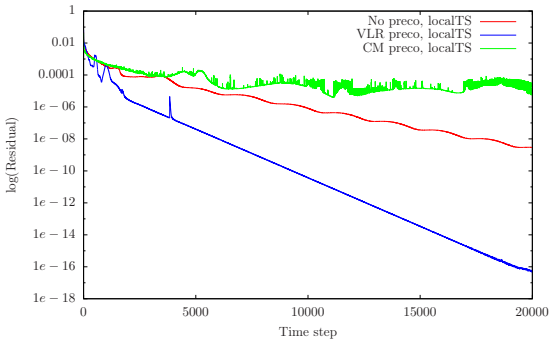

(J) $M = 1.8$

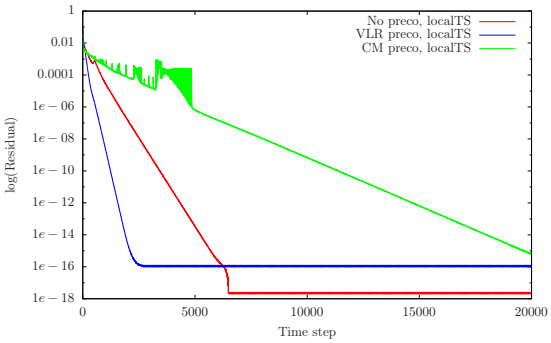

(K) $M = 2.0$

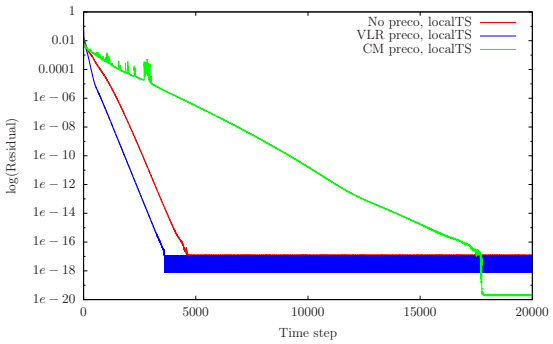

FIGURE 4.12: NACA 0012 test case. Residual-convergence rates over the time step using the three preconditioning options (NP, VLR, and CM) with local time at different inflow Mach numbers.

4.4.2 ONERA M6 wing

The ONERA M6 wing configuration details and experimental results are found in Schmitt and Charpin [1979]. The results presented here correspond to inviscid transonic flow at a Mach number of 0.8395 and an angle of attack of 3.06°. As in the NACA 0012 test case, the rest of the initial conditions are $\rho = 1$, $\|\mathbf{u}\| = 1$, $T = 1$, and c_p and c_v are determined to obtain the desired inflow Mach numbers. An unstructured tetrahedral mesh is used on this simulation consisting of 472026 elements and 94481 grid points. VLR and NP options are tested for this case. The CM option improving only the performance for low Mach number regimes, is not considered in this problem. The NP-localTS option does not converge for this problem. A constant velocity and temperature are prescribed at the inflow and a constant density at the outflow. A prudential distance is taken from the airfoil to the inflow and outflow boundaries in order to avoid the numerical instabilities of reflecting waves. Slip boundary conditions are used on the rest of the walls of the domain as well as on the airfoil.

Convergence for the NP-globalTS and VLR-localTS cases are compared in Fig. 4.13. We observe that the VLR-localTS configuration considerably accelerates the convergence compared to the NP-globalTS one.

The pressure contours on the upper and lower surface of the wing for the VLR-localTS case with $CFL = 0.2$ are shown in Fig. 4.14. In the upper surface contours we can identify the complex sharp shock structure that is formed.

The pressure coefficient values of the VLR-localTS simulation at seven spanwise orthogonal sections of the wing are compared to the experimental results in Schmitt and Charpin [1979] in Fig. 4.15. The seven sections are at 20% ($y = 0.23926\,m$), 44% ($y = 0.526372\,m$), 65% ($y = 0.777595\,m$), 80% ($y = 0.95704\,m$), 90% ($y = 1.07667\,m$), 95% ($y = 1.136485\,m$), and 99% ($y = 1.184337\,m$) of the semi-span that goes from $y = 0$ to $y = 1.1963\,m$, where y is the span-wise coordinate. We observe some differences of these results near the shock located at $x = 0.6$ on the horizontal axis and on the trailing edge for all cases, whether preconditioned or not. Considering that we are comparing the experimental results with an Euler solution, the obtained pressure coefficient values at the different sections are reasonable (see for instance Luo et al. [1998]).

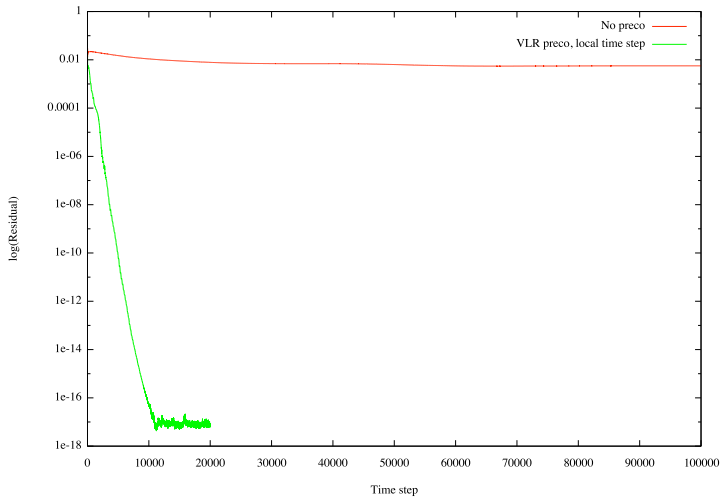

FIGURE 4.13: ONERA M6 test case. Convergence rate comparison between the non preconditioned case using a global time stepping (red line) and the VLR preconditioned case using a local time stepping (green line).

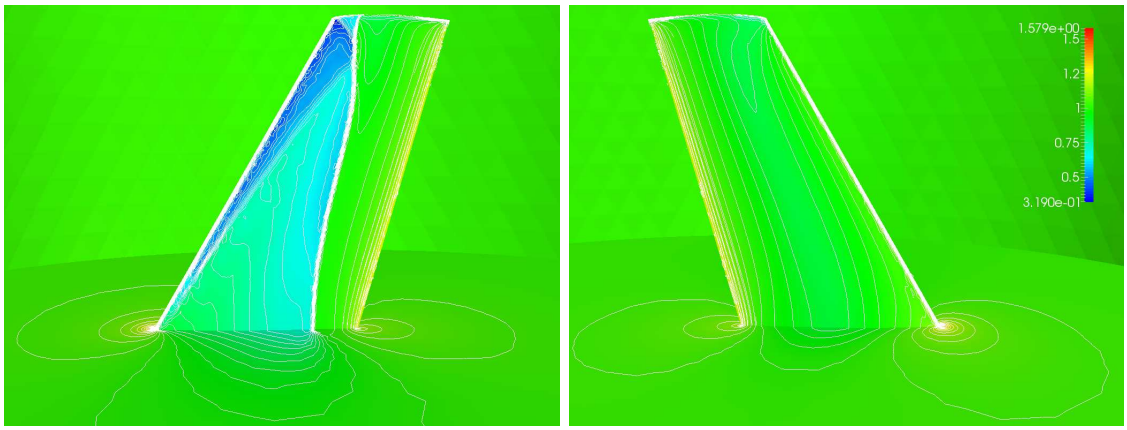

FIGURE 4.14: ONERA M6 test case. Pressure contours on the upper (left figure) and lower (right figure) surfaces for the VLR preconditioned case with local time step.

(A) 20% of the semi-span

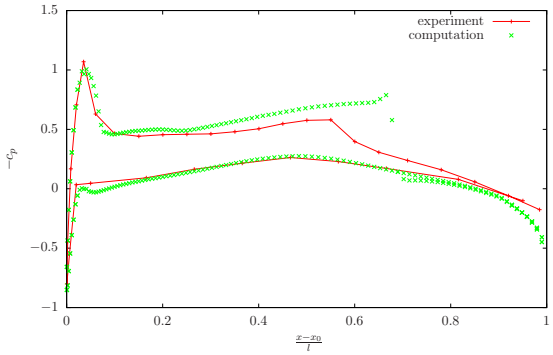

(B) 44% of the semi-span

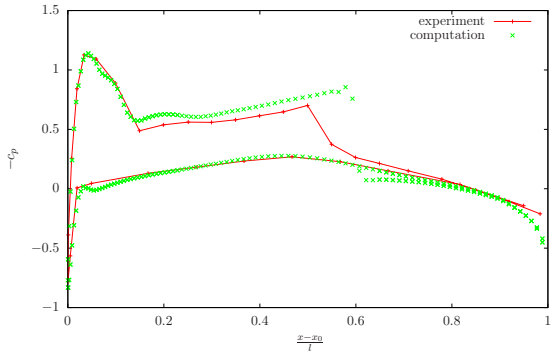

(C) 65% of the semi-span

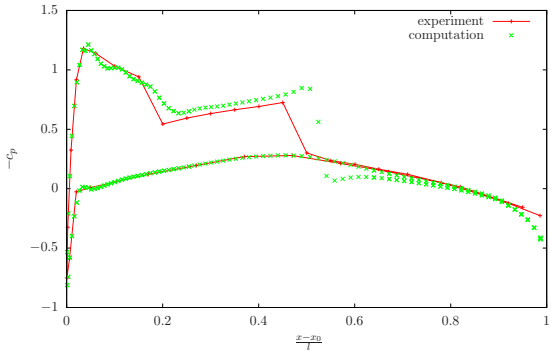

(D) 80% of the semi-span

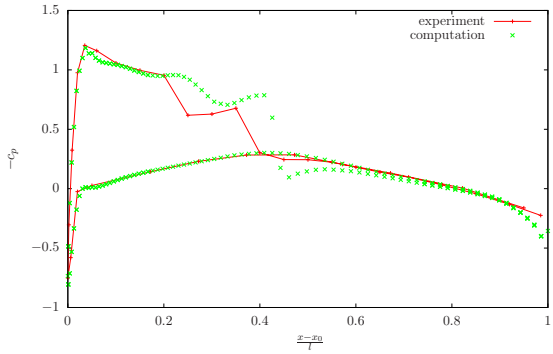

(E) 90% of the semi-span

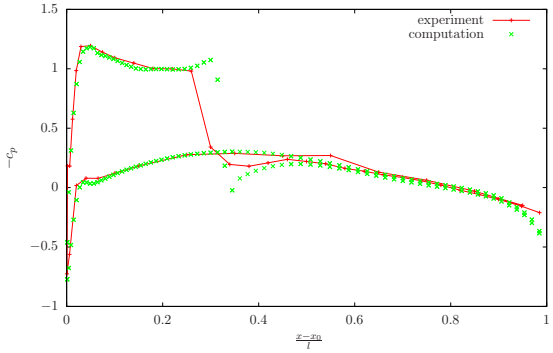

(F) 95% of the semi-span

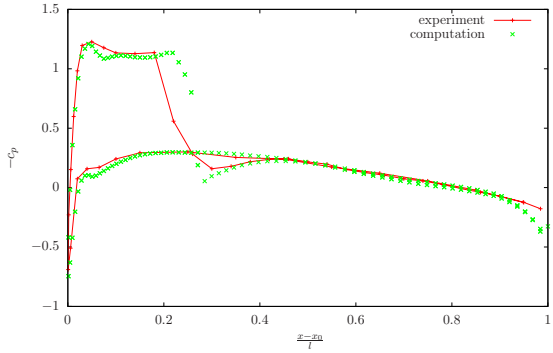

(G) 99% of the semi-span

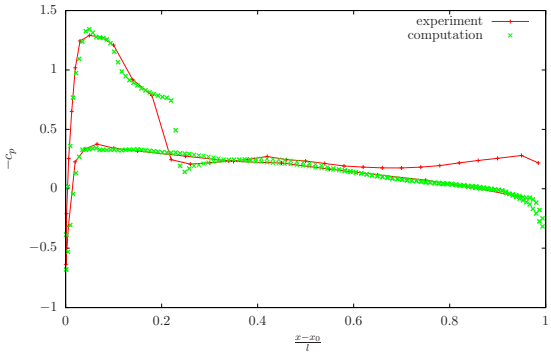

FIGURE 4.15: ONERA M6 test case. The c_p values for the experimental and VLR-localTS's results are compared on seven span-wise sections of the wing.

4.4.3 Viscous NACA 0012 airfoil

Viscous flow past a two-dimensional NACA 0012 airfoil is solved at zero angle of attack, inflow Mach number 0.0001 and Reynolds number 10000. The rest of the initial conditions are $\rho = 1$, $\mathbf{u} = (1, 0)$, $T = 1$, $\mu = 0.0001$, and $Pr = 0.8$. c_{p}, c_{v}, and κ are determined to obtain the desired Mach and Prandtl numbers. This problem reaches a steady state. We impose the following boundary conditions. Non-slip boundary conditions are set over the airfoil, it consists of setting $\mathbf{u} = 0$. Slip boundary conditions are imposed on the top and bottom walls, that is, we impose $u_2 = 0$. Velocity $\mathbf{u}$ and temperature T are imposed at the inflow boundary, and density ρ is imposed at the outflow boundary. The unstructured grid of 6042 elements (rectangles and triangles) and 4317 grid nodes shown in Fig. 4.16 is used for this simulation. For both the NP and CM preconditioned cases, we use a global time step with a CFL number of $C = 1.0$. The local time stepping seems to be more sensitive to the reflecting waves. The non-preconditioned case with local time step does not converge. The CM preconditioned case with local time step, with a CFL number of $C = 0.1$, seems to converge during the first 10000 steps, reaching a residual of around 10^{-6}, however it ends up to diverge.

Results of the Mach number contours for the NP and the CM preconditioned cases are displayed in Fig. 4.17 after 90000 time steps. We observe that the CM preconditioned case presents a better result than the NP case with smoother contours, especially in the boundary layer. Also the convergence is significantly improved when using CM preconditioner as it is shown in Fig. 4.18. The NP case seems to converge after 90000 simulation steps, however we observe that the solution is not stable and it ends-up to diverge if we continue the simulation. This fact shows once more time that the preconditioned problem is more robust than the non-preconditioned one. We notice that the residual convergence of the CM preconditioned case stalls at around 10^{-8}. We find

a similar behaviour in the CM preconditioned convergence of the inviscid NACA 0012 at low Mach numbers (see Figs. 4.12a and 4.12b in Subsection 4.4.1). We think that this could be due to the threshold $\epsilon = 10^{-5}$ that is present in the definition of the CM preconditioner, in the reference Mach number (4.41) and (4.42).

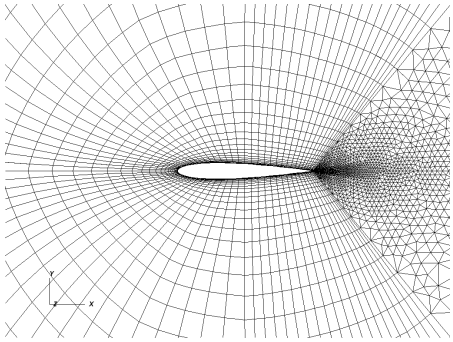

FIGURE 4.16: Viscous NACA 00012 test case. Plot of the computational grid.

(A) Unpreconditioned case (B) CM preconditioned case

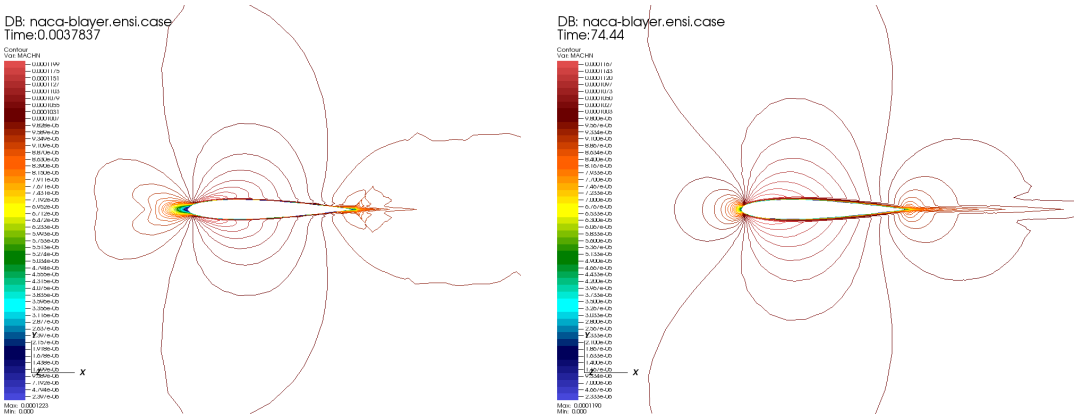

FIGURE 4.17: Viscous NACA 00012 test case. Mach number contours after 90000 time steps, for the unpreconditioned and the CM preconditioned cases, for an inflow Mach number of 0.0001 and a Reynolds number of 10000. A global time stepping is used for both simulations with CFL number of $C = 1.0$.

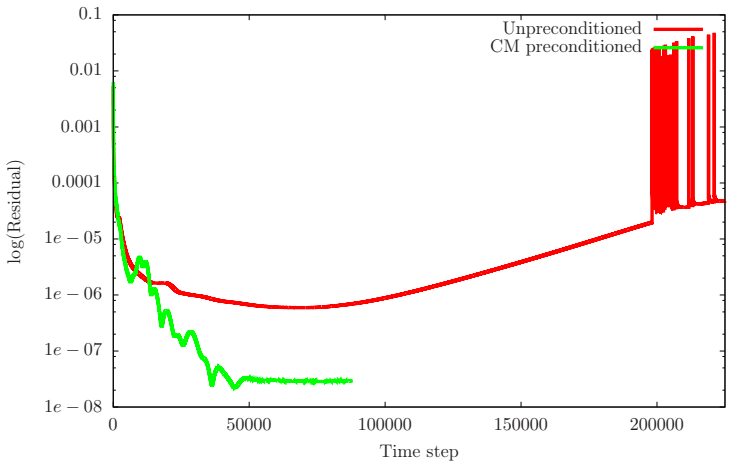

FIGURE 4.18: Viscous NACA 00012 test case. Convergence rate comparison between the unpreconditioned (red line) and the CM preconditioned (green line) cases, for an inflow Mach number of 0.0001 and a Reynolds number of 10000. A global time stepping is used for both simulations with CFL number of $C = 1.0$.

4.4.4 Shock tube

Here we assess the performance of P-VMS for a transient problem. The Sod's shock tube originally proposed by Sod [1978] and already solved in Subsection 2.4.1, is here solved with a different initial setting which gives a maximum Mach number of 0.00184 approximately. The problem description, mesh configuration, and boundary conditions for this problem can be found in Subsection 2.4.1. The difference here is that the initial conditions are: the left density is set to 1 and the right density is set to 0.999, the left total energy is set to 2.5 and the right total energy is set to 2.499, and the initial velocity is set to 0.002. Global physical time and pseudo-time steps are used for both the NP and CM cases. The physical time is fixed and prescribed to $\Delta t = 0.006\,s$. The pseudo-time uses a safety factor $C_{\mathcal{T}} = 1.0$ and six pseudo-time iterations are performed at each physical time step, for both the NP and the CM preconditioned cases.

The goal of local preconditioning is the uniformization of the characteristic propagation speeds of the system which entails a gain in convergence speed. The preconditioner is here applied to accelerate the convergence of the pseudo-time to a pseudo steady state at each physical time-step. This is shown in Fig. 4.19a where the convergences in pseudo-time of the NP and the CM preconditioned cases are compared. The agreement between the NP and the CM preconditioned cases with pseudo-time, and the NP case with no pseudo-time is shown in Fig. 4.19b representing the convergence in physical time. Density and pressure results corresponding to the CM preconditioned case with pseudo-time are given in Fig. 4.20.

The classical Sod's shock tube, whose configuration is described in Subsection 2.4.1, is also solved here to analyse the effect of the pseudo-time iterations on this problem. The pseudo-time uses a safety factor $C_{\mathcal{T}} = 0.9$ and four pseudo-time iterations are performed at each physical time step, for both the NP and the CM preconditioned cases. As it is shown in Fig. 4.21b, when a straight compressible VMS is used, numerical oscillations appear near the shocks. We observe from Fig. 4.21a that this oscillations are considerably reduced with the use of pseudo-time iterations. We conclude that pseudo-time iterations involve a gain in accuracy and robustness to the numerical method. The solution of the CM preconditioned case, in Fig. 4.21c, is very similar to the solution of the NP case, both of them using a pseudo-time stepping.

(A) Pseudo-time convergence

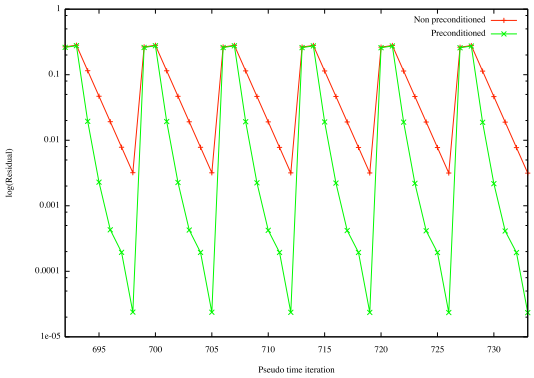

(B) Physical time convergence

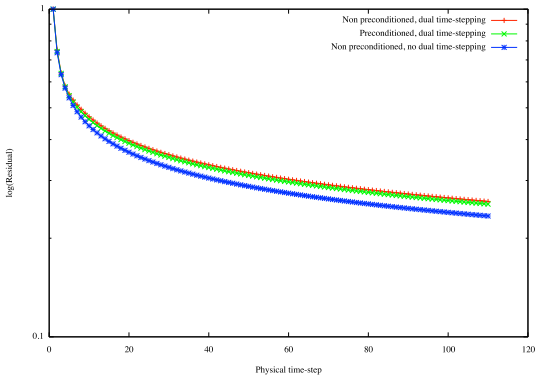

FIGURE 4.19: Shock tube test case reaching a Mach number of 0.00184 approximately. (A) Convergence history within pseudo-time of the NP (red color) and the CM preconditioned (green color) cases, both using 6 iterations of pseudo-time. (B) Convergence history within physical time of the NP case with six pseudo-time iterations (red color), the CM preconditioned case with six pseudo-time iterations (green color), and the NP case without pseudo-time iterations (blue color), showing the agreement of the solution on the three cases.

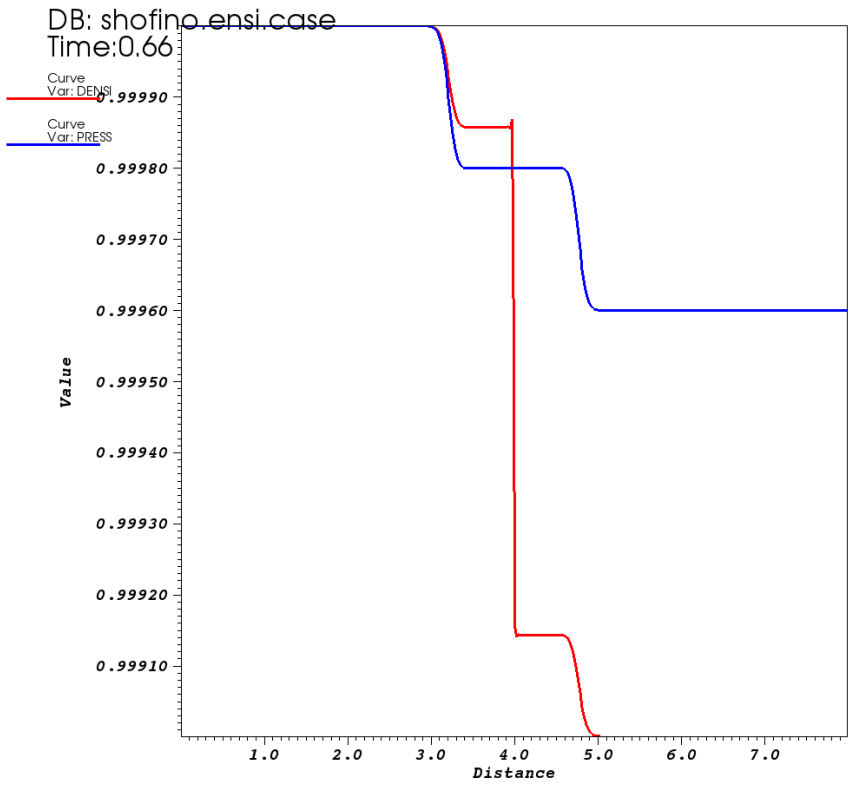

FIGURE 4.20: Shock tube test case reaching a Mach number of 0.00184 approximately. Density and pressure results at 0.66 seconds for the CM preconditioned case using six pseudo-time iterations.

(A) NP, pseudo-time

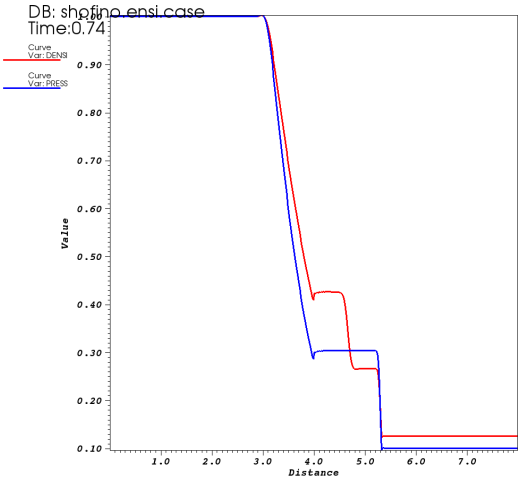

(B) NP

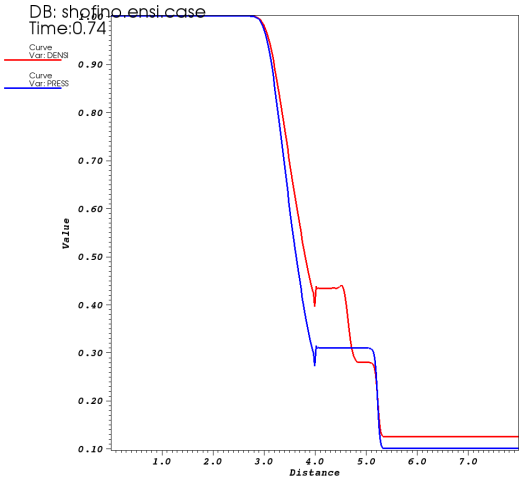

(C) CM, pseudo-time

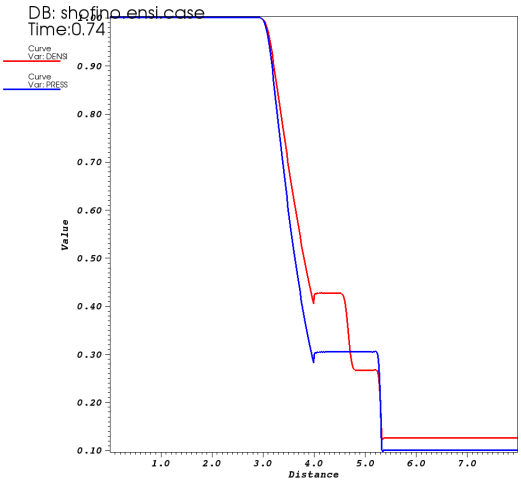

FIGURE 4.21: Shock tube classical test case reaching a Mach number of 0.828 approximately. Density and pressure results at 0.74 seconds for the NP case (A) with and (B) without pseudo-time, and (C) the CM preconditioned case with pseudo-time. We are using four pseudo-time iterations.

4.5 Summary and conclusions

In this chapter a variational multiscale stabilization for the locally preconditioned Navier-Stokes equations is introduced. Both steady and transient flows are considered. This stabilization method, that we call P-VMS, is applied to the finite element discretization of compressible flows. Time discretization is approached by a linear explicit scheme in

order to present and assess P-VMS in the most simple and direct way possible. The local and global time stepping are compared.

Due to the effect of local preconditioning on the equations, the preconditioned system is better suited for the computation of the VMS for a wide-range of Mach numbers. The combined action of local preconditioning and VMS results in a robust and precise numerical method. As local preconditioning is applied before any discretization is done, it does not necessarily add extra computational cost compared to the non-preconditioned option. Indeed, the products $\mathbf{PA}^i$ and $\mathbf{PK}^{ir}$ can be computed analytically and the corresponding expressions introduced into the code.

VLR and CM preconditioners are tested over two and a three-dimensional benchmarks for viscous and inviscid, transient and steady flow, comprising an ample range of Mach numbers. We observed that preconditioning gives improvement in terms of convergence acceleration, stability, and smoothness of the solution even for very low Mach numbers. The use of a local time stepping compared to a global one, accelerates the convergence to the steady solution as well. In the Euler steady case, VLR preconditioning gives better improvement than CM one on the convergence rate and applies from subsonic to supersonic regimes. CM preconditioning improves the convergence for low Mach number flows, but it can be easily applied to viscous flow and transient problems.

Chapter 5

Fourier stability analysis and local Courant number for P-VMS

In this chapter we present the results of a Fourier stability analysis of the preconditioned variational multiscale stabilization (P-VMS) method introduced in Chapter 4. P-VMS combines a variational multiscale stabilized finite elements discretization together with local preconditioning. We consider P-VMS using *van Leer-Lee-Roe*'s van Leer et al. [1991] and *Choi-Merkle*'s Choi and Merkle [1993] local preconditioners for the Euler equations of compressible steady flow. VLR preconditioner applies for low Mach, transonic and supersonic regimes, while CM preconditioner only gives improvement at low Mach. In this chapter we concentrate on explicit time integration schemes. The stability analysis is performed on a two dimensional simplified problem with a structured mesh and its conclusions are applied to two and three dimensional general problems with unstructured meshes. As a result of this analysis a local Courant-Friedrichs-Lewy number is defined for the computation of the time step. Its performance in convergence rate is evaluated by comparison with the traditional constant Courant-Friedrichs-Lewy number, in some test cases including a large range of Mach numbers.

5.1 Fourier analysis

The motivation of the Fourier analysis Vichnevetsky and Bowles [1982] is to analyze the behavior of the numerical scheme in terms of error propagation and damping of all the Fourier modes. On the one hand, the Fourier footprint (FFP) technique analyzes the configuration of the eigenvalues of the discrete spatial operator for all the Fourier modes, in particular it allows to verify the eigenvalues clustering after a space discretization is

done. On the other hand, the von Neumann analysis studies the convergence behavior of the full (space and time) discretized scheme.

Here we enumerate some examples of the use of Fourier analysis to evaluate the smoothing properties of local preconditioning in the context of the Euler and Navier-Stokes equations. In Godfrey [1994], Lee [1996, 1998a,b, 1991], Lynn and van Leer [1993], van Leer et al. [1991] the FFP is computed for the Euler and Navier-Stokes equations using VLR preconditioning for steady flow and a first-order finite volumes upwind discretization in space. In Lee [1996, 1991], Lynn and van Leer [1993], van Leer et al. [1991] a von Neumann stability analysis for a multi-stage explicit time-marching method is additionally done. In Darmofal and van Leer [1998] a complete stability analysis is done for the Euler equations using VLR and block-Jacobi preconditioners for steady flow, an upwind finite differences discretization in space, and an optimal two-stage explicit discretization in time. In Choi and Merkle [1993] the von Neumann stability analysis for the Navier-Stokes equations of steady flow is done using CM preconditioning, introduced in the same article. Euler implicit discretization in time and central differencing in space is used. In Allmaras [1993, 1995] the FFP is computed for the block-Jacobi preconditioned case. In Pierce and B. [1996] a full stability analysis is performed for the Euler and Navier-Stokes equations using a block-Jacobi preconditioner for steady flow, a finite volume discretization in space, and a 5-stage Runge-Kutta time stepping scheme. In Sheng [2010], Wang [2005] the FFP is analyzed for the finite volume upwind discrete operator of the unsteady Navier-Stokes equations using Briley et al. preconditioning Briley et al. [2003]. As it is the case of the precedent examples, Fourier stability analysis for the preconditioned Euler and Navier-Stokes equations has been done since now in the context of finite volumes and finite differences schemes.

In the following subsections we perform a Fourier stability analysis of the P-VMS method and compare it to the unpreconditioned VMS. To this purpose the preconditioned system (4.15) is discretized in space using P-VMS and, in time, using a first order forward finite differences scheme (see Subsection 4.3). In this chapter, a local time stepping is considered (see Subsection 2.3.5). VLR and CM preconditioners are considered in the P-VMS scheme when computing the FFP in Subsection 5.1.1. After performing the von Neumann analysis in Subsection 5.1.2, unexpected improvement of the numerical scheme has come as well, which is explained in Subsection 5.1.3.

5.1.1 Fourier footprint

The FFP is the locus of the discrete spatial operator's eigenvalues in the complex plane. We expect the preconditioner to reduce the spread of these eigenvalues as well as re-arrange its disposition in the complex plane in such a way that the stability condition defined in Subsection 5.1.2 is more easily verified.

The FFP is computed as follows. As an analytical expression for the eigenvalues of fifth (or higher) order matrices does not exist Stewart [1994], the FFP of the three-dimensional problem can not be analytically formulated. The FFP is computed from the discretized spatial operator for a simplified two-dimensional case and the consequences of its analysis will be considered on general two and three-dimensional cases. We consider a two-dimensional structured mesh with identical rectangles of dimension $\Delta x_1 \times \Delta x_2$. We apply the variational multiscale stabilized finite element space discretization and obtain equation (4.52). We note $\mathbf{\Phi}_{kl}$ the value of $\mathbf{\Phi}$ at node $\mathbf{x}^{kl}$ and suppose that the jacobians $\mathbf{A}^i$, $i = 1, 2$, are constant in a neighborhood of $\mathbf{\Phi}_{kl}$, for each node $\mathbf{x}^{kl}$ of the grid. We use equality (2.12) in the Euler version of equation (4.52) and compute the integrals by a nodal integration rule, that for a function f writes

$$\int_K f(\mathbf{x})\, dK \approx \sum_{p=1}^{N} f(\mathbf{x}^p)\, \omega^p \,, \tag{5.1}$$

where K is an element of the grid, N is the number of nodes $\mathbf{x}^p$ of the element K, and ω^p its weight that is $\frac{1}{N}|K|$. In this case $N = 4$ and $\omega^p = \frac{1}{4}\Delta x_1 \Delta x_2$. Then we obtain

$$\frac{\partial \mathbf{\Phi}_{k,l}}{\partial t} = \mathbf{R}(\mathbf{\Phi}) \,, \tag{5.2}$$

where

$$\begin{aligned}
\mathbf{R}(\mathbf{\Phi}) = -\Big\{ & \tfrac{1}{2\,\Delta x_1}\mathbf{A}^1(\mathbf{\Phi}_{k+1,l} - \mathbf{\Phi}_{k-1,l}) + \tfrac{1}{2\,\Delta x_2}\mathbf{A}^2(\mathbf{\Phi}_{k,l+1} - \mathbf{\Phi}_{k,l-1}) \\
& + \tfrac{1}{\Delta x_1\,\Delta x_1}\mathbf{A}^1\tau\mathbf{A}^1(-\mathbf{\Phi}_{k+1,l} + 2\mathbf{\Phi}_{k,l} - \mathbf{\Phi}_{k-1,l}) + \tfrac{1}{\Delta x_2\,\Delta x_2}\mathbf{A}^2\tau\mathbf{A}^2(-\mathbf{\Phi}_{k,l+1} + 2\mathbf{\Phi}_{k,l} - \mathbf{\Phi}_{k,l-1}) \\
& + \tfrac{1}{4\,\Delta x_1\,\Delta x_2}\left(\mathbf{A}^1\tau\mathbf{A}^2 + \mathbf{A}^2\tau\mathbf{A}^1\right)(\mathbf{\Phi}_{k-1,l+1} - \mathbf{\Phi}_{k+1,l+1} + \mathbf{\Phi}_{k+1,l-1} - \mathbf{\Phi}_{k-1,l-1})\Big\} \,.
\end{aligned} \tag{5.3}$$

We introduce in (5.2) a discrete Fourier mode

$$\mathbf{\Phi}_{k,l} = \hat{\mathbf{\Phi}}(\omega)\, e^{i(k\omega_1 + l\omega_2)} \,, \tag{5.4}$$

for $\omega \in [-\pi, \pi] \times [-\pi, \pi]$ and obtain

$$\frac{\partial \mathbf{\Phi}_{k,l}}{\partial t} = \hat{\mathcal{F}}(\omega)\, \mathbf{\Phi}_{k,l} \,, \tag{5.5}$$

where

$$\hat{\mathcal{F}}(\omega) = -\Big\{ \tfrac{i \sin\omega_1}{\Delta x_1}\mathbf{A}^1 + \tfrac{i \sin\omega_2}{\Delta x_2}\mathbf{A}^2 + \tfrac{2(1-\cos\omega_1)}{\Delta x_1 \Delta x_1}\mathbf{A}^1\tau\mathbf{A}^1 + \tfrac{2(1-\cos\omega_2)}{\Delta x_2 \Delta x_2}\mathbf{A}^2\tau\mathbf{A}^2 + \tfrac{\sin\omega_1 \sin\omega_2}{\Delta x_1 \Delta x_2}\left(\mathbf{A}^1\tau\mathbf{A}^2 + \mathbf{A}^2\tau\mathbf{A}^1\right)\Big\} \tag{5.6}$$

is the Fourier symbol. The ensemble of its eigenvalues, $\{\lambda_i(\hat{\mathcal{F}}(\omega))\}_{i,\omega}$, for $i = 1, \ldots, 4$ and $\omega \in [-\pi, \pi] \times [-\pi, \pi]$, define the FFP, simply noted here as $\lambda(\hat{\mathcal{F}})$. The ensemble of the four eigenvalues generated by each frequency combination, $\omega = (\omega_1, \omega_2)$, is noted as $\lambda(\hat{\mathcal{F}}(\omega))$. The FFP does not depend on the system of unknowns in equation (5.2). The effect of the grid element aspect ratio to the FFP is excluded in this work by supposing $AR = \frac{\Delta x_2}{\Delta x_1} = 1$. We call h the element length in both directions: $h = \Delta x_1 = \Delta x_2$. If we express the problem in symmetrizing variables (in B.1) it is easy to see that the FFP exclusively depends on h, c, M, and the angle α of the velocity in relation to the coordinate axes.

In Figs. 5.1-5.6 the FFP of the non-preconditioned VMS stabilized finite elements discretization is compared to the P-VMS one, where both VLR and CM preconditioners are used. The scaled FFP, $\frac{h}{c}\lambda(\hat{\mathcal{F}})$, which only depends on M and α, is shown. Different Mach numbers are displayed: $M = 0.01$, 0.1, 0.5, 0.7, 0.9, 2.0. The flow speed is considered to be aligned with the grid, that is, we suppose $\alpha = 0$. When $\alpha = 0$, $\hat{\mathcal{F}}(-\omega)$ and $\hat{\mathcal{F}}(\omega)$ are symmetric about the real axis, in other words they are conjugate complex numbers. For this reason only positive Fourier angles, $\omega \in [0, \pi] \times [0, \pi]$, are plotted. High frequencies, which are those in $I_{\text{high}} = [\frac{\pi}{2}, \pi] \times [\frac{\pi}{2}, \pi]$, are represented in red color; low frequencies, which are those in $I_{\text{low}} = [0, \frac{\pi}{2}] \times [0, \frac{\pi}{2}]$, in blue color; and medium frequencies, which are the rest of the frequencies, in green color.

It is seen from Figs. 5.4-5.6 that the FFP for the CM preconditioned case is very similar to the NP one when M approaches one and $M > 1$. CM is in fact a preconditioner for low Mach number regimes, otherwise it does not remove the stiffness of the non-preconditioned Euler equations. The CM preconditioned system compared to the NP one is indeed worse conditioned when $0.4 < M < 1$ and has the same characteristic speeds when $M > 1$ (see Section 4.2.5 or Darmofal and van Leer [1998] for the details).

We observe that for low Mach numbers the FFP that corresponds to a first order upwind finite volumes discretization (used for example in Lee [1996], Lynn and van Leer [1993], Wang [2005]) is very similar to the one corresponding to the VMS stabilized finite element discretization used in this work, for both the unpreconditioned and the VLR preconditioned cases. The precedent conclusion is done by comparing: Fig. 5.1 of this chapter with Fig. 4.1(a) in Wang [2005] for the non-preconditioned FFP when $M = 0.01$, as well as Fig. 5.2 of this chapter with Fig. 2.9 in Lee [1996] for both the non-preconditioned

and the VLR preconditioned cases when $M = 0.1$. When $M = 0.5$, 0.9, and 2.0, Figs. 5.3, 5.5, and 5.6 of this chapter are compared to Figs. 6-8 and 10-12 in Lynn and van Leer [1993]. We conclude that differences in the shape of the FFP between the finite volumes and the finite elements semi-discretizations appear for moderate to high Mach numbers, for both non-preconditioned and VLR preconditioned cases. Details on the Fourier symbol, $\hat{\mathcal{F}}(\omega)$, for the first order upwind finite volumes semi-discrete operator can be found in Wang [2005]. No FFP of the CM preconditioned case has been found in the literature to compare.

In comparison with the unpreconditioned case, VLR preconditioning reduces the locus of the FFP. To a lesser degree, the same effect is seen with the CM preconditioning for low Mach numbers. Before preconditioning many different scales are present in the FFP. VLR preconditioner as well as CM one for low Mach numbers, clear up the FFP of the non-preconditioned equations and give a more orderly spread of the eigenvalues. A group of eigenvalues is seen to cluster near the origin in the FFP of the NP case for all Mach numbers. A clustering on the real axis appears as well for low Mach numbers. This fact is a consequence of the disparity on the propagation speeds of the Euler equations Darmofal and van Leer [1998]. VLR preconditioner as well as CM one for low Mach numbers, displace most of these eigenvalues from the real axis and the origin, then a better clustering of the eigenvalues is obtained. As it is understood in the next subsection, the reduction of the spread as well as a better clustering of the eigenvalues that is obtained when preconditioning, help to the damping of the error and a better convergence of the numerical scheme.

(A) NP

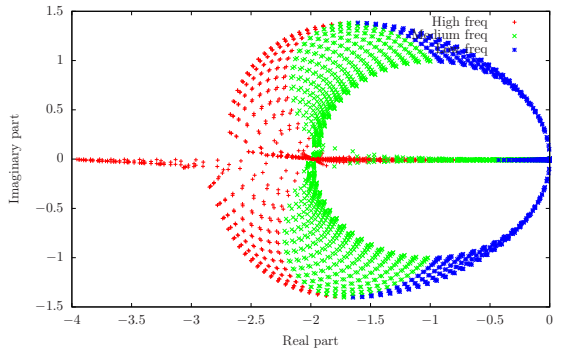

(B) VLR

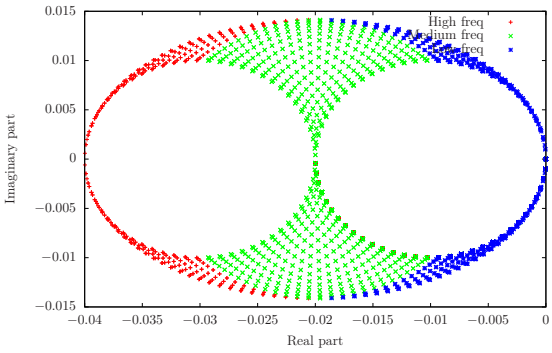

(C) CM

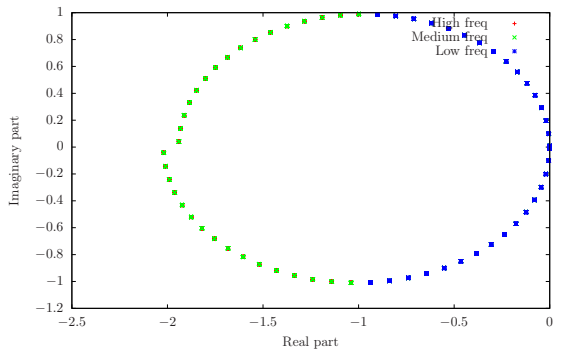

FIGURE 5.1: The scaled FFP, $\frac{h}{c}\lambda(\hat{\mathcal{F}}(\omega))$, for $\omega \in [0,\pi] \times [0,\pi]$, $M = 0.01$, $\alpha = 0$, and $AR = 1$, is plotted for the NP, VLR, and CM preconditioning options. High frequencies are plotted in red, medium frequencies in green and low frequencies in blue.

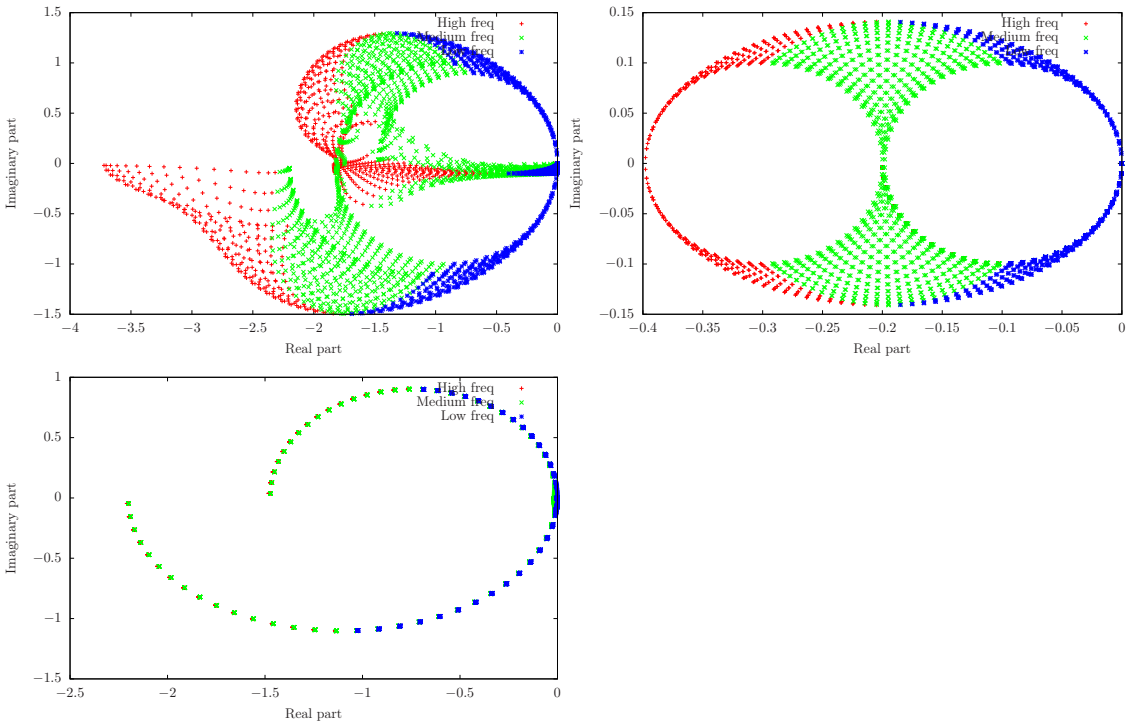

FIGURE 5.2: Same as in Fig. 5.1 but for a Mach number of 0.1.

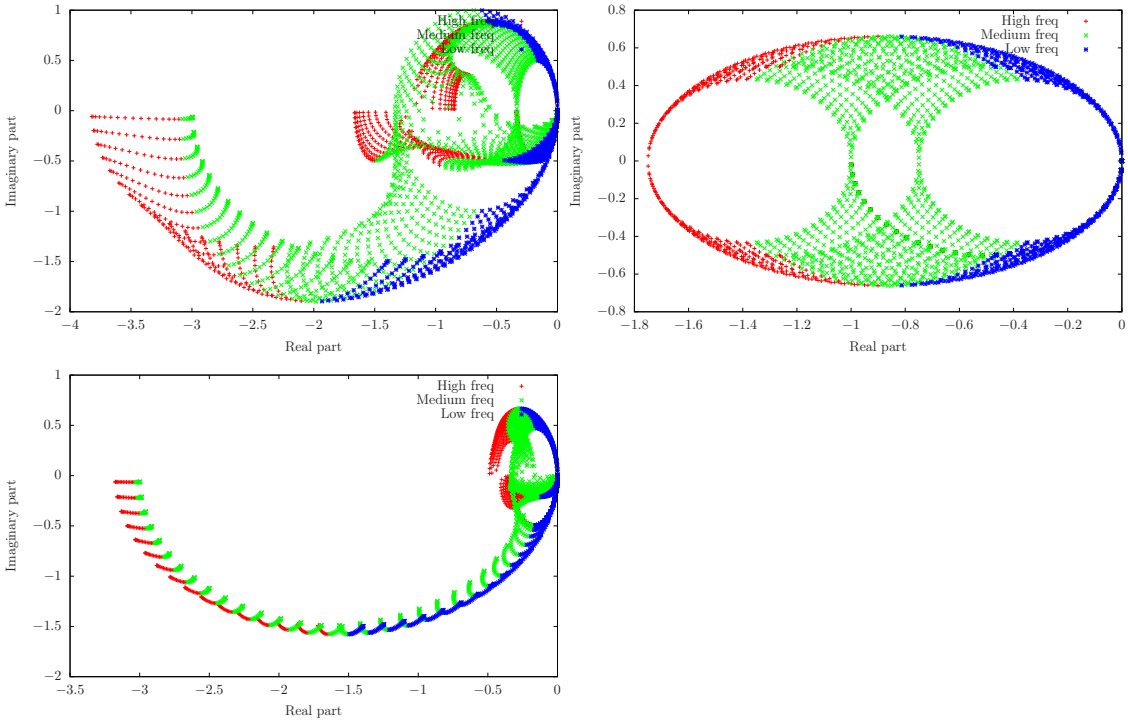

FIGURE 5.3: Same as in Fig. 5.1 but for a Mach number of 0.5.

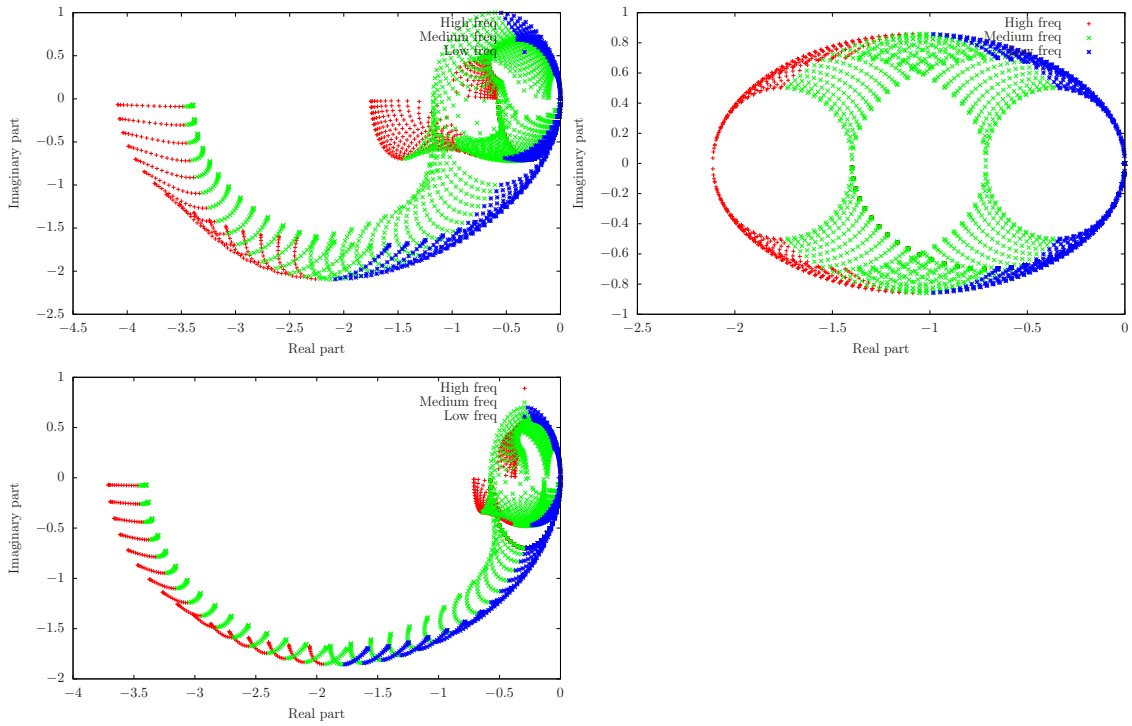

FIGURE 5.4: Same as in Fig. 5.1 but for a Mach number of 0.7.

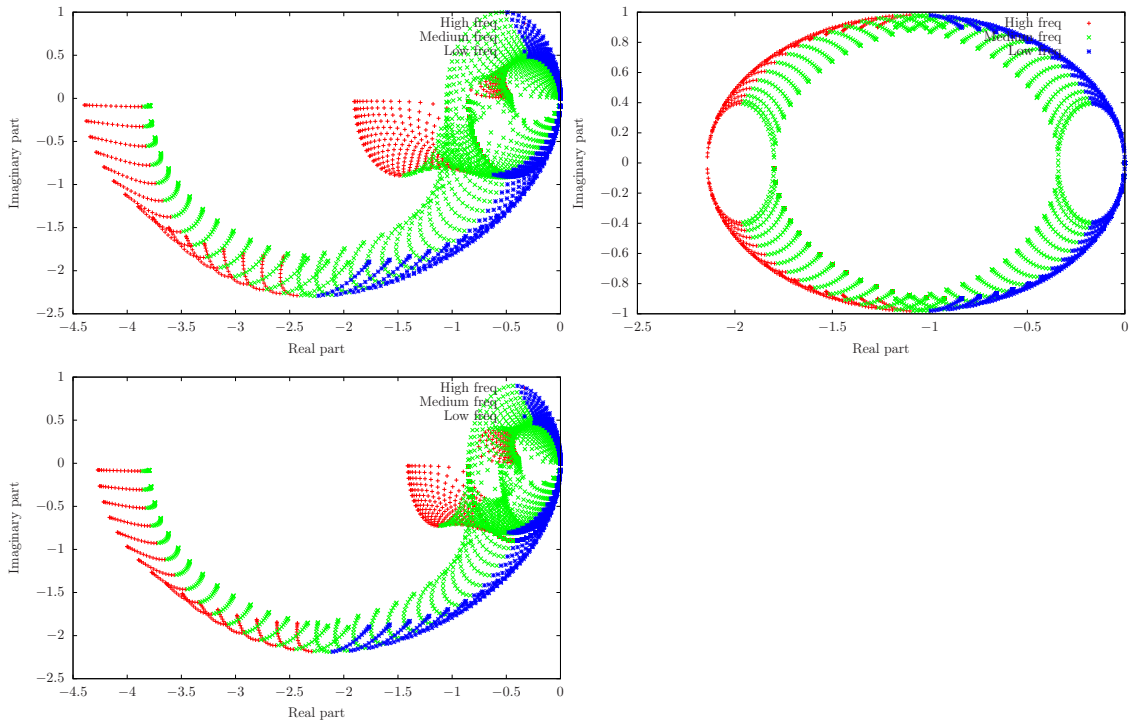

FIGURE 5.5: Same as in Fig. 5.1 but for a Mach number of 0.9.

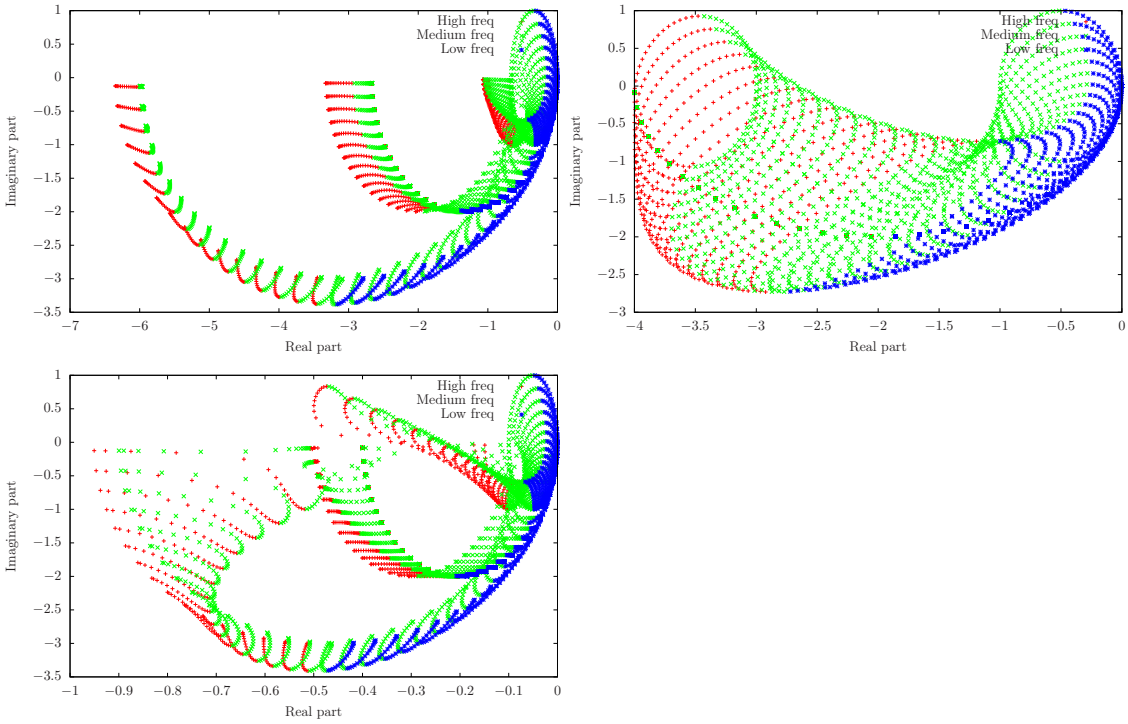

FIGURE 5.6: Same as in Fig. 5.1 but for a Mach number of 2.0.

5.1.2 Von Neumann stability analysis

Von Neumann stability analysis O'Brien et al. [1950] is used to determine the behavior of the full-discretized equations in terms of convergence of the solution. It gives information on the error propagation over the time iterations and the damping behavior of the scheme. A necessary condition for the convergence of the problem is determined with von Neumann analysis: the FFP scaled by the time step should remain inside a defined stability region that depends on the time discretization scheme.

The von Neumann stability analysis is applied to the full (i.e. space and time) discretized operator and is performed as follows. The space-discretized equation of a simplified two-dimensional case (5.2) is discretized in time using a first order explicit (or forward Euler) time integration, obtaining

$$\frac{\mathbf{\Phi}_{k,l}^{n+1} - \mathbf{\Phi}_{k,l}^{n}}{\Delta t} = \mathbf{R}(\mathbf{\Phi}_{k,l}^{n}) \; . \tag{5.7}$$

Similarly to what is done with (5.4), the analysis is obtained by looking at the time evolution of numerical solutions of the form

$$\mathbf{\Phi}_{k,l}^{n+1} = \hat{\mathbf{\Phi}}^{n+1}(\omega) \; e^{i(k\omega_1 + l\omega_2)} \; , \tag{5.8}$$

for $\omega = (\omega_1, \omega_2) \in [-\pi, \pi] \times [-\pi, \pi]$. Inserting (5.8) into the time-discretized equation (5.7), we have

$$\frac{\mathbf{\Phi}_{k,l}^{n+1} - \mathbf{\Phi}_{k,l}^{n}}{\Delta t} = \hat{\mathcal{F}}(\omega) \; \mathbf{\Phi}_{k,l}^{n} \; , \tag{5.9}$$

where $\hat{\mathcal{F}}(\omega)$ is the Fourier symbol defined in (5.6), we suppose $AR = 1$ as well. Isolating the unknown of the current time in (5.9) we obtain:

$$\mathbf{\Phi}_{k,l}^{n+1} = \Big[\mathrm{Id} + \Delta t \, \hat{\mathcal{F}}(\omega) \Big] \; \mathbf{\Phi}_{k,l}^{n} \; . \tag{5.10}$$

From (5.10) the amplification matrix of our problem is defined as

$$G(\omega) = \mathrm{Id} + \Delta t \, \hat{\mathcal{F}}(\omega) \; , \tag{5.11}$$

and its eigenvalues are

$$\lambda_i(G) = 1 + \Delta t \, \lambda_i(\hat{\mathcal{F}}(\omega)) \; . \tag{5.12}$$

To assure numerical stability, the spectral radius of the amplification matrix should not exceed unity, thus none of its eigenvalues' absolute value should, that is:

$$|\lambda_i(G)| = |1 + \Delta t \, \lambda_i(\hat{\mathcal{F}}(\omega))| \leq 1 \; , \tag{5.13}$$

for $i = 1, \ldots, 4$. The region defined by (5.13) in the complex plane $\Delta t\, \hat{\mathcal{F}}(\omega)$, which is

$$S = \{z \in \quad | \ |1 + z| \leq 1\} \ , \tag{5.14}$$

is the stability region of a first order explicit time integration scheme, that is the unit disc centered at $(-1, 0)$. For this algorithm to be stable, the FFP scaled by the time step, $\Delta t\, \lambda(\hat{\mathcal{F}}(\omega))$ for all values of $\omega \in [-\pi, \pi] \times [-\pi, \pi]$, should be inside the region S.

As explained in subsection 5.1.1, the FFP depends on h, c, M, and α. From the expression of the time step (equations (4.65) and (4.66) for the preconditioned and the unpreconditioned problems, respectively) we can see that the dependence of the FFP on h and c is canceled when it is scaled by the time step, thus $\Delta t\, \lambda(\hat{\mathcal{F}})$ depends on C, M, and α. The CFL number, C, is a constant factor of $\Delta t\, \lambda(\hat{\mathcal{F}})$ so it does not change its shape but only its size. This number should be such that $\Delta t\, \lambda(\hat{\mathcal{F}})$ is inside the stability region S. For each problem that we are solving, the choice of the CFL number is done through numerical testing. In the next Subsection we present a non-constant CFL number which depends on the Mach number at each point of the domain.

The FFP scaled by the time step for both the NP and VLR options and for a Mach number of 0.01 are displayed in Fig. 5.7. The CFL numbers in order to fit inside the stability region are $C = 0.495$ and $C = 0.505$ for the NP and VLR cases, respectively. Although the required CFL numbers are very similar for both cases, the time step of the preconditioned case is larger, of some orders of magnitude for low Mach numbers. This is because, contrary to the NP case, when preconditioning the speed of the sound is not present in the computation of the time step (see equations (4.65) and (4.66)).

As observed in subsection 5.1.1 from Figs. 5.1-5.6, VLR preconditioning, and CM for low Mach numbers, reduce the spread of the eigenvalues, making it easier for them to be contained within the stability region of any particular method and allowing larger time steps. In contrast, the spread of the eigenvalues of the NP case, restricts the possible time step. We also observe that preconditioning removes considerably the clustering of the FFP near the origin, where the spectral radius of the amplification matrix approaches one. This improves the error damping properties of the method.

(A) NP case, $C = 0.505$ (B) VLR case, $C = 0.495$

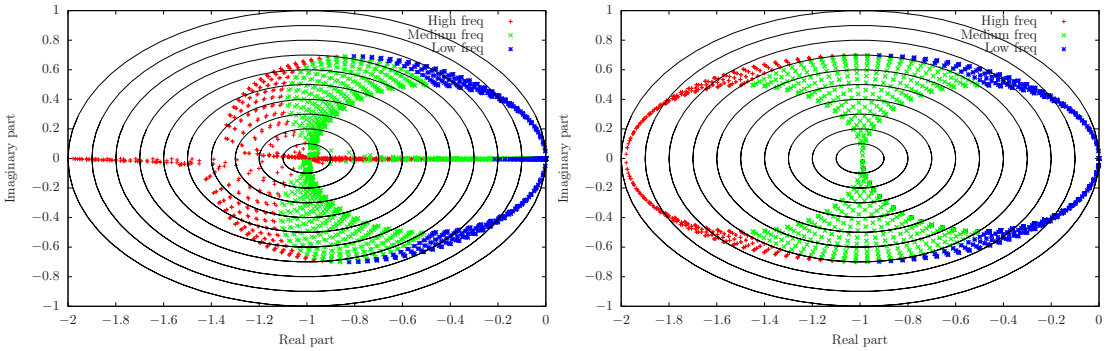

FIGURE 5.7: The FFP scaled by the time step, $\Delta t\,\lambda(\hat{\mathcal{F}}(\omega))$, for $\omega \in [0,\pi] \times [0,\pi]$, $M = 0.01$, $\alpha = 0$, and $AR = 1$, is plotted for (a) the NP case with CFL number $C = 0.505$ and (b) the VLR case with $C = 0.495$. Contours of the complex polynomial $|1+z|$ which defines the stability region for a first order explicit time integration scheme are overlaid, up to level 1 with increments of 0.1.

5.1.3 Local CFL number

The CFL number C, $0 < C < 1$, in the time step equation (4.63), is constant all over the domain and depends on the problem that it is solved. We chose it for each problem through numerical experiments to be as big as possible but small enough to permit the problem to converge.

Based on the von Neumann analysis of the previous subsection we propose an alternative and systematic way of computing the CFL number. This results in a local CFL number in the sense that it is variable over the domain and computed at each point of the grid using local parameters. Given a Mach number M, we can compute the maximum CFL number, $C_{\max}$, assuring that $\Delta t\,\lambda(\hat{\mathcal{F}})$ is inside the stability region (5.14), in other words, assuring that the stability condition (5.13) is verified. It writes

$$C_{\max}(M) := \max\{\, C \;\mid\; |\lambda_i(G(\omega, C, M, \alpha))| \leq 1\,,\;\; \forall i, \omega, \alpha\,\}\,, \tag{5.15}$$

where $i = 1, \ldots, 4$, $\omega \in [-\pi, \pi] \times [-\pi, \pi]$, $\alpha \in [0, 2\pi]$, and $\lambda_i(G)$ are the eigenvalues of the amplification matrix (5.12). As in the two previous subsections the element aspect ratio of the grid is supposed to be $AR = 1$. The CFL number, inside the time step, scales the value of $\Delta t\,\lambda(\hat{\mathcal{F}})$ without changing its shape but only its size. Different placements of $\Delta t\,\lambda(\hat{\mathcal{F}})$ inside the stability region (5.14) are found through the choice of the CFL number. The modes of $\Delta t\,\lambda(\hat{\mathcal{F}})$ placed near the center of the stability region, are more strongly damped. This fact makes us realize that the maximum CFL number defined in (5.15) is not necessarily the most efficient in terms of convergence of the solution. For

this reason, we define three other local CFL numbers, C_{high}, C_{low}, and C_{all}, maximizing the damping of high frequencies, low frequencies and all the frequencies, respectively. They write:

$$C_{\text{high}}(M) = \underset{0<C\leq C_{\max}(M)}{\arg\min} \left\{ \underset{\substack{i=1,\dots,4 \\ \omega\in I_{\text{high}} \\ \alpha\in[0,2\pi]}}{\text{mean}} |\lambda_i(G(\omega, C, M, \alpha))| \right\}, \tag{5.16}$$

$$C_{\text{low}}(M) = \underset{0<C\leq C_{\max}(M)}{\arg\min} \left\{ \underset{\substack{i=1,\dots,4 \\ \omega\in I_{\text{low}} \\ \alpha\in[0,2\pi]}}{\text{mean}} |\lambda_i(G(\omega, C, M, \alpha))| \right\}, \tag{5.17}$$

$$C_{\text{all}}(M) = \underset{0<C\leq C_{\max}(M)}{\arg\min} \left\{ \underset{\substack{i=1,\dots,4 \\ \omega\in [-\pi,\pi]^2 \\ \alpha\in[0,2\pi]}}{\text{mean}} |\lambda_i(G(\omega, C, M, \alpha))| \right\}. \tag{5.18}$$

As defined in subsection 5.1.1, high and low frequencies are those in $I_{\text{high}} = [\frac{\pi}{2}, \pi] \times [\frac{\pi}{2}, \pi]$ and $I_{\text{low}} = [0, \frac{\pi}{2}] \times [0, \frac{\pi}{2}]$, respectively. Now we define the precedent local CFL numbers (equations (5.15)-(5.18)) but only considering $\alpha = 0$ flow angle

$$C_{\max,0}(M) = \max \{ C \;\mid\; |\lambda_i(G(\omega, C, M, \alpha))| \leq 1, \;\; \forall i, \omega, \; \alpha = 0 \}. \tag{5.19}$$

$$C_{\text{high},0}(M) = \underset{0<C\leq C_{\max}(M)}{\arg\min} \left\{ \underset{\substack{i=1,\dots,4 \\ \omega\in I_{\text{high}} \\ \alpha=0}}{\text{mean}} |\lambda_i(G(\omega, C, M, \alpha))| \right\}, \tag{5.20}$$

$$C_{\text{low},0}(M) = \underset{0<C\leq C_{\max}(M)}{\arg\min} \left\{ \underset{\substack{i=1,\dots,4 \\ \omega\in I_{\text{low}} \\ \alpha=0}}{\text{mean}} |\lambda_i(G(\omega, C, M, \alpha))| \right\}, \tag{5.21}$$

$$C_{\text{all},0}(M) = \underset{0<C\leq C_{\max}(M)}{\arg\min} \left\{ \underset{\substack{i=1,\dots,4 \\ \omega\in [-\pi,\pi]^2 \\ \alpha=0}}{\text{mean}} |\lambda_i(G(\omega, C, M, \alpha))| \right\}. \tag{5.22}$$

As all the precedent analysis is done for a two-dimensional simplified case but we are using it for two and three-dimensional general problems, when a local CFL is used, we should multiply the time step (4.63) by a constant, that we call safety factor, $SF \in (0, 1]$, obtaining

$$\Delta t^{\,el} = SF \; C(M) \; \frac{h}{|\lambda|_{\max}}. \tag{5.23}$$

In (5.23), $C(M)$ is any of the previously defined local CFL numbers (equations (5.15)-(5.18) and (5.19)-(5.22)) and SF is chosen according to each problem needs. Then the elementary time step becomes

$$\Delta t^{\,el} = SF \; C(M) \; \frac{h}{\|\mathbf{u}\|}, \tag{5.24}$$

for the VLR preconditioned case and

$$\Delta t^{\,el} = SF \; C(M) \; \frac{h}{\|\mathbf{u}\| + c}, \tag{5.25}$$

when no preconditioner is used. The local time step Δt is obtained at each node of the grid by interpolating the elementary one Δt^{el}.

The different local CFL number options are computed for a finite list of Mach numbers and plotted in Fig. 5.8 for the NP and VLR cases. A close-up of this plots for $0 \leq M \leq 2$ is presented in Fig. 5.9. Higher resolution is given between 0 and 1 Mach number because bigger gradients are found in this interval. The local CFL number is especially interesting for problems that contain a wide range of Mach numbers. Because CM preconditioner is only designed for low Mach regimes, the study of the local CFL is here focused on the NP and VLR cases. We can see that in the VLR case $C_{\text{high},0}$ and C_{high} are the most restrictive, giving the lowest CFL numbers when $M < 1$. The same happens in the NP case for very low Mach numbers, otherwise $C_{\text{low},0}$ and C_{low} are the most restrictive ones. Being the most restrictive does not necessarily mean that it gives the smallest time step, because a safety factor, SF, multiplies the time step (see equation (5.23)). This fact is exemplified for the NACA 0012 test case in Fig. 5.12 of Subsection 5.2.1. In the VLR case $C_{\text{high},0}$, $C_{\text{low},0}$, and $C_{\text{all},0}$ present very similar values than C_{high}, C_{low}, and C_{all}, respectively, showing that the consideration of all flow angles does not make a difference in this case. For the VLR case as well, $C_{\text{max},0}$ and C_{max} give very similar result for $M < 2$ and out of the sonic point neighborhood, otherwise they present a big difference. In the NP case, $C_{\text{low},0}$ and C_{low} have very similar values for all Mach numbers. $C_{\text{high},0}$ and C_{high} as well as $C_{\text{all},0}$ and C_{all} give very similar results when $M < 0.2$ and different results otherwise. Finally, $C_{\text{max},0}$ and C_{max} are very similar for low Mach numbers and very different otherwise. We conclude that the VLR case is less sensitive than the NP case to flow angle changing for all Mach numbers and local CFL definitions. Then for the VLR preconditioned case, the extension of $\Delta t\, \lambda(\hat{\mathcal{F}})$ as well as its distribution of the frequencies, experiment very little change when modifying the flow angle α.

The use of the local CFL number finds all its power in problems where a large range of Mach numbers exists. For this reason, being CM preconditioner only useful for low Mach regimes, the local CFL is only considered for the non-preconditioned (NP) and for the VLR preconditioned systems.

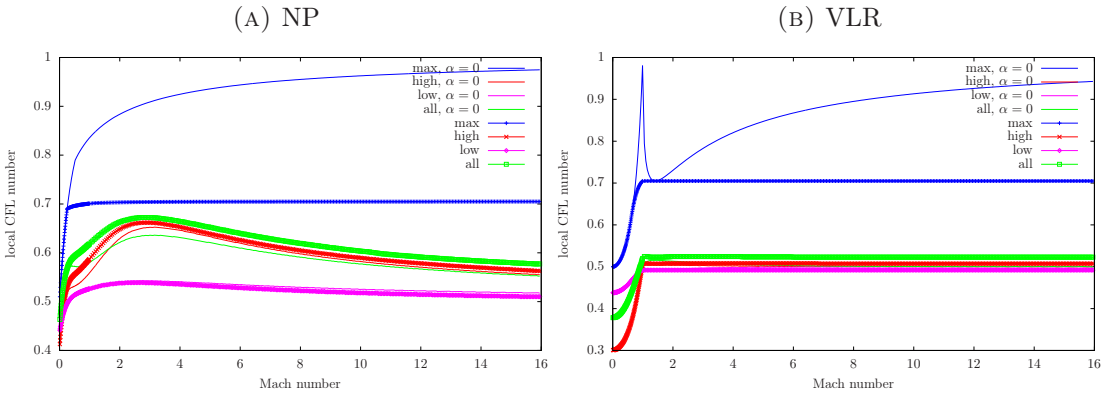

FIGURE 5.8: The different local CFL numbers: $C_{\max,0}(M)$, $C_{\text{high},0}(M)$, $C_{\text{low},0}(M)$, $C_{\text{all},0}(M)$, $C_{\max}(M)$, $C_{\text{high}}(M)$, $C_{\text{low}}(M)$, and $C_{\text{all}}(M)$, from equations (5.19)-(5.22) and (5.15)-(5.18), respectively, are plotted for the unpreconditioned and the VLR preconditioned cases. Higher resolution is given between 0 and 1 Mach number where bigger gradients are found.

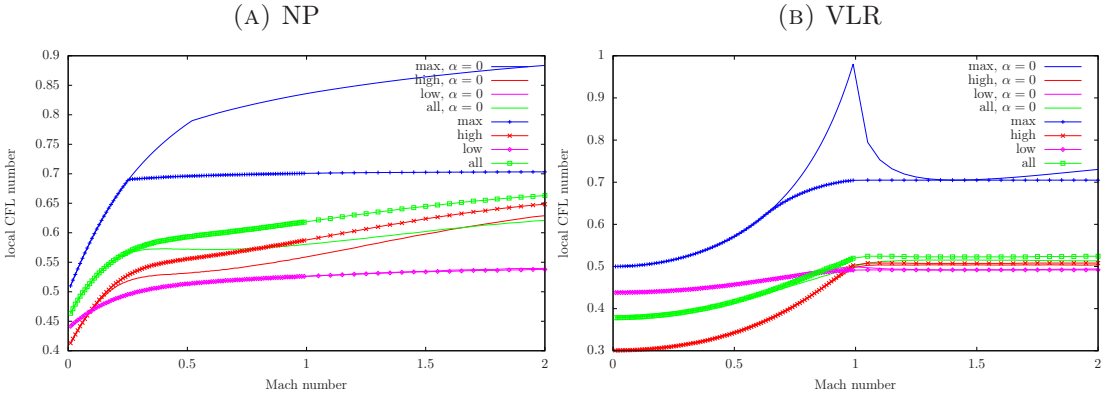

FIGURE 5.9: Close-up of Fig. 5.8, for Mach numbers between 0 and 2.

The FFPs scaled by the time step, $\Delta t\,\lambda(\hat{\mathcal{F}})$, using the local CFL values $C_{\max,0}$, $C_{\text{high},0}$, $C_{\text{low},0}$, and $C_{\text{all},0}$ for $M = 0.7$, are plotted in Fig. 5.10. The safety factor SF is set to 1 in this case. We can see for the high and low cases how the FFP is scaled in a way that the corresponding areas are placed around the center of the stability region, where the damping of the Fourier modes is stronger.

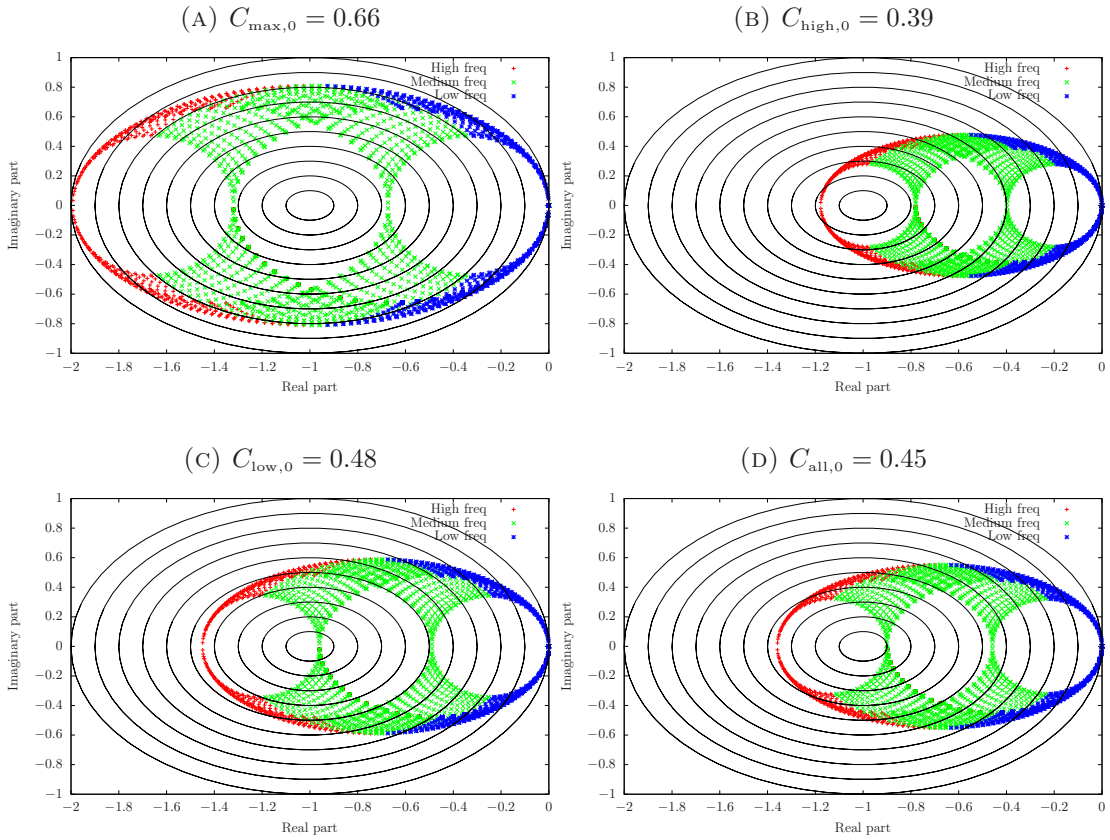

FIGURE 5.10: The VLR preconditioned FFPs scaled by the time step, $\Delta t\,\lambda(\hat{\mathcal{F}}(\omega))$, $\omega \in [0,\pi] \times [0,\pi]$, for $M = 0.7$, $\alpha = 0$, and $AR = 1$. Four different local CFL numbers are used: $C_{\max,0}$, $C_{\text{high},0}$, $C_{\text{low},0}$, and $C_{\text{all},0}$. Contours of the complex polynomial $|1 + z|$ which defines the stability region for a first order explicit time integration scheme are overlaid, up to level 1 with increments of 0.1.

5.2 Numerical results

We assess the performance of the different local CFL definitions, for the VLR preconditioned system, using P-VMS and an explicit time scheme, through two test cases. The first one is the two-dimensional flow past a NACA 0012 profile at different Mach numbers, from Mach 0.001 to 2.0, and zero angle of attack. The second one, a three-dimensional case, is the flow past an ONERA M6 wing at Mach numbers 0.8395 and 2.0, and 3.06° angle of attack. No difference in the steady solution is found in these problems when using a constant CFL number or the different local CFL options. Some of these cases have been already analyzed in Chapter 4 to asses the performance of P-VMS; a constant CFL has been used in that case.

For both test cases, we impose slip boundary condition on the airfoil as well as in the walls of the three dimensional ONERA M6 wing. We prescribe a constant velocity and

temperature at the inflow and a constant density at the outflow. We take a prudential distance from the airfoil to the inflow and outflow boundaries in order to avoid the numerical instabilities of reflecting waves. We suppose a diatomic ideal gas then $\gamma = 1.4$ in all the following simulations.

Convergence rates are here represented as a normalized residual, *Res* from equation (4.74), on the vertical axis, over the iteration number on the horizontal axis.

5.2.1 NACA 0012 airfoil

We solve the NACA 0012 airfoil test case for inviscid flow at zero angle of attack and different inflow Mach numbers: 0.001, 0.01, 0.1, 0.3, 0.5, 0.7, 0.9, 1.0, 1.2, 1.8, and 2.0. The rest of the initial conditions being: $\rho = 1$, $\mathbf{u} = (1, 0)$, $T = 1$, and c_{p} and c_{v} are determined to obtain the desired inflow Mach numbers. We use an unstructured grid of 4522 triangles and 2315 grid nodes. The NACA 0012 test case with identical configuration and for the same inflow Mach numbers is solved in Subsection 4.4.1.

Here we test the different definitions of the local CFL number (equations (5.15)-(5.18) and (5.19)-(5.22)) for the VLR preconditioned system, and compare them to the constant CFL number for the NP and VLR cases. All the simulations use a local time stepping. When a local CFL is used, the local time step defined from (5.24) with the safety factors in Table 5.2 are used for the differently configured simulations of the NACA 0012 problem. Otherwise, the values that we use for the constant CFL numbers (in equation (4.63)) are displayed in Table 5.1 for both the NP and VLR cases.

Pressure contours of the VLR preconditioned steady solution for the different Mach number configurations are found in Figs. 4.1 to 4.11. It is worth to remark that for the cases where $M > 1$, we did not use any additional shock capturing diffusion. Although this fact introduces some localized over and undershoots, we preferred to use this strategy to better compare the local CFL action throughout a large range of Mach numbers with no additional ingredients.

For the different inflow Mach numbers, we compare in Figure 5.11 the convergence rates of: the constant CFL number simulations for the NP and VLR cases and the different local CFL options for the VLR case. First of all we observe the improvement in convergence of the VLR case compared to the NP one, for all Mach numbers. Then we see that, in the supersonic cases, where a wider range of Mach numbers is found, the benefits in convergence of using the local CFL are notable compared to the traditional constant one. For low Mach numbers, both the constant and the local CFL options for the VLR case

give very similar convergence rates. As expected from Figure 5.9b, the obtained convergences with $C_{\max}$ and $C_{\max,0}$ are different for $M = 0.7$, 0.9, 1.0, and 1.2 and very similar otherwise. For all Mach numbers, the convergence rates that we obtain with C_{high}, C_{low}, and C_{all} are very similar to those obtained using $C_{\text{high},0}$, $C_{\text{low},0}$, and $C_{\text{all},0}$, respectively, showing that these options are not very sensitive to the consideration of the flow angle. In general we observe that the traditional constant CFL gives the worst convergence rate while the local CFL maximizing the damping of the high frequencies gives the best one. Furthermore, we can observe from Table 5.1 that when using the local CFL maximizing the damping of the high frequencies, the required safety factor is 0.9 or 1.0, while the other options require a grater correction to the time step: SF going from 0.4 to 0.8. This fact shows that C_{high} and $C_{\text{high},0}$ are the best defined local CFL options for this case. We conclude that for the NACA 0012 test case using VLR preconditioner, C_{high} and $C_{\text{high},0}$ are the best local CFL options.

Concerning the VLR case, in Fig. 5.12 the value of the constant CFL, C in equation (4.65), is compared to the values of the different local CFL options times the corresponding safety factor, $SF\,C_{\max}$, $SF\,C_{\text{high}}$, $SF\,C_{\text{low}}$, and $SF\,C_{\text{all}}$, in equation (5.24), for all the considered inflow Mach number configurations of the NACA 0012 test case. We represent $C = 0.3$ for the constant CFL, which is the used value for almost all Mach numbers (see the VLR row in Table 5.1). Concerning the safety factors, which are displayed in Table 5.2, we chose to represent for each local CFL option, the lowest safety factor along all the Mach number configurations. That is, we take $SF = 0.5$ for $C_{\max}$, $SF = 0.9$ for C_{high}, $SF = 0.6$ for C_{low}, and $SF = 0.7$ for C_{all}. The represented values multiply the critical time step, that is $\frac{h}{\|\mathbf{u}\|}$ for the VLR case, and they are needed because of the difficulty to compute the proper critical time step. We observe that even if C_{high} present the lowest value among the local CFL options (see Fig. 5.9b), once multiplied by the corresponding safety factor, it gives the highest value for this test case.

(A) $M = 0.001$

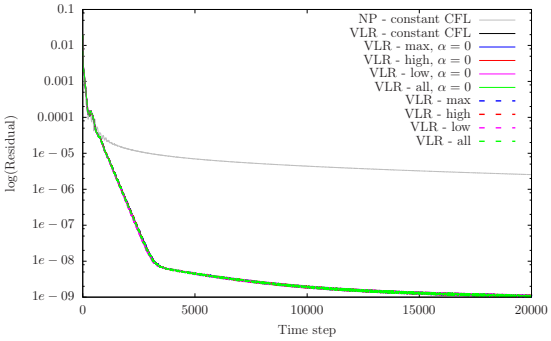

(B) $M = 0.01$

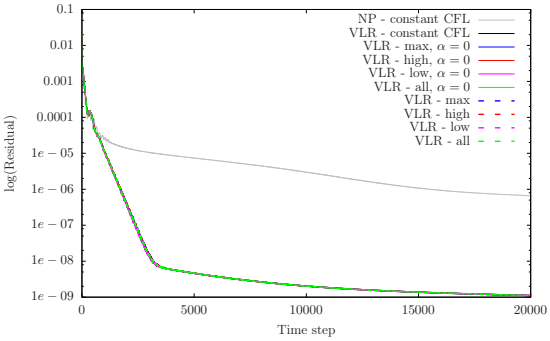

(C) $M = 0.1$

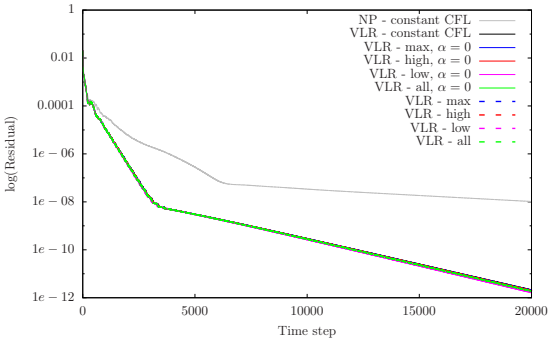

(D) $M = 0.3$

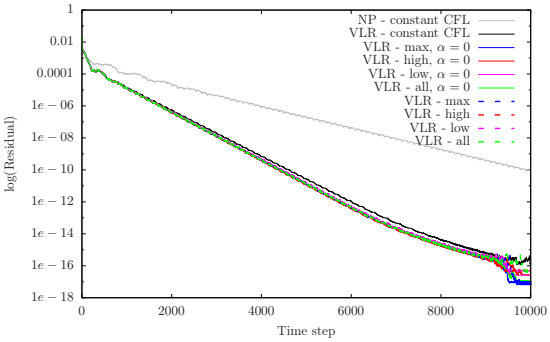

(E) $M = 0.5$

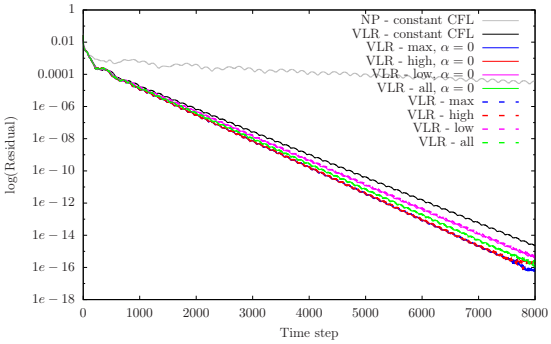

(F) $M = 0.7$

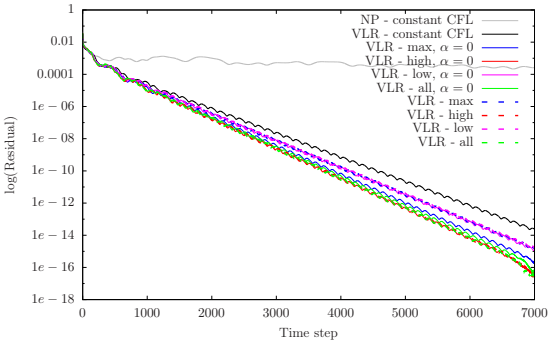

(G) $M = 0.9$

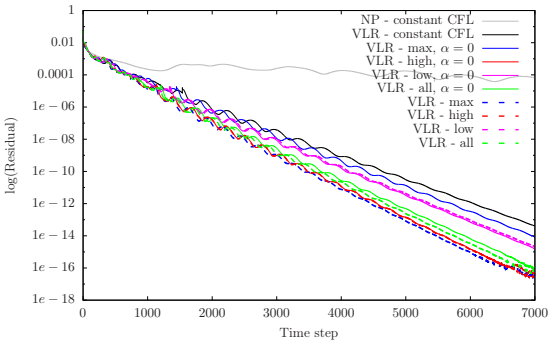

(H) $M = 1.0$

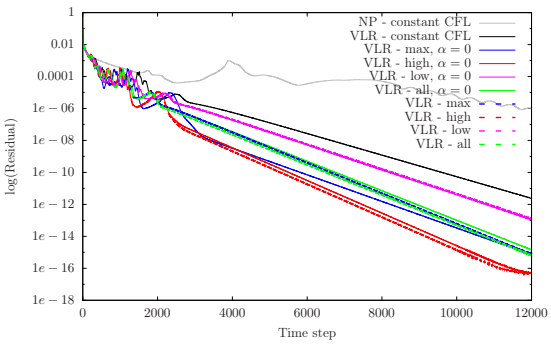

(I) $M = 1.2$

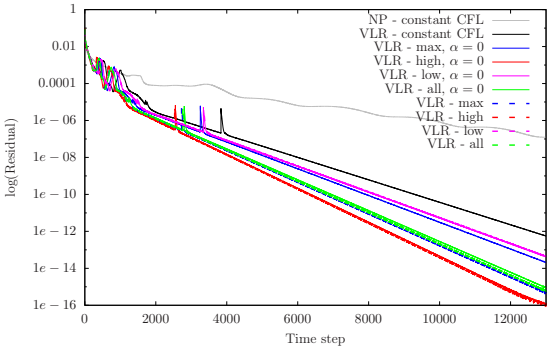

(J) $M = 1.8$

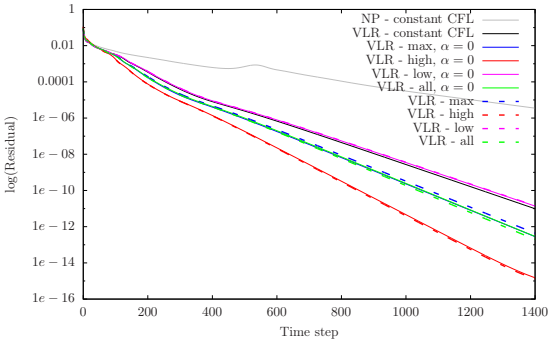

(κ) $M = 2.0$

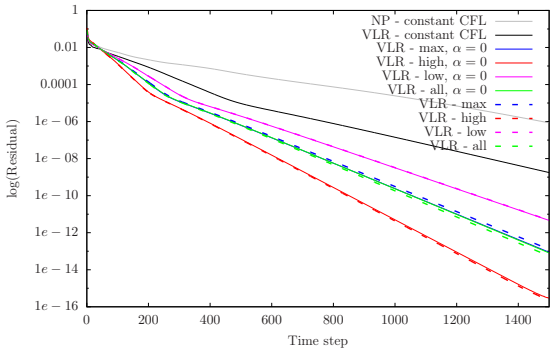

FIGURE 5.11: NACA 0012 test case. Comparison of the residual-convergence rates over the time step of the NP case with a constant CFL, the VLR case with a constant CFL, and the VLR case with the different local CFL options: $C_{\max,0}$, $C_{\text{high},0}$, $C_{\text{low},0}$, $C_{\text{all},0}$, $C_{\max}$, C_{high}, C_{low}, and C_{all}, for the solution of flow past the NACA 0012 airfoil at different inflow Mach numbers and zero angle of attack. All the simulations use a local time stepping.

Inflow Mach	0.001	0.01	0.1	0.3	0.5	0.7	0.9	1.0	1.2	1.8	2.0
NP - constant CFL	0.3	0.3	0.3	0.4	0.4	0.4	0.3	0.4	0.4	0.4	0.4
VLR - constant CFL	0.3	0.3	0.3	0.3	0.3	0.3	0.3	0.3	0.3	0.3	0.2

TABLE 5.1: NACA 0012 test case. Constant CFL number values, C in the time step equation (4.63), for the NP and VLR cases and for the different inflow Mach number configurations. All the simulations use a local time stepping.

Inflow Mach	0.001	0.01	0.1	0.3	0.5	0.7	0.9	1.0	1.2	1.8	2.0
VLR - maximum CFL, $\alpha = 0$	0.6	0.6	0.6	0.6	0.6	0.5	0.4	0.5	0.5	0.5	0.5
VLR - maximum CFL	0.6	0.6	0.6	0.6	0.6	0.5	0.6	0.6	0.6	0.5	0.5
VLR - high freq. CFL, $\alpha = 0$	1.0	1.0	1.0	1.0	1.0	0.9	0.9	0.9	0.9	0.9	0.9
VLR - high freq. CFL	1.0	1.0	1.0	1.0	1.0	0.9	0.9	0.9	0.9	0.9	0.9
VLR - low freq. CFL, $\alpha = 0$	0.7	0.7	0.7	0.7	0.7	0.7	0.7	0.7	0.7	0.6	0.6
VLR - low freq. CFL	0.7	0.7	0.7	0.7	0.7	0.7	0.7	0.7	0.7	0.6	0.6
VLR - all freq. CFL, $\alpha = 0$	0.8	0.8	0.8	0.8	0.8	0.8	0.8	0.8	0.8	0.7	0.7
VLR - all freq. CFL	0.8	0.8	0.8	0.8	0.8	0.8	0.8	0.8	0.8	0.7	0.7

TABLE 5.2: NACA 0012 test case. Comparative of the constant safety factors, SF in the time step equation (5.24), for the VLR case and the different local CFL options, for the different inflow Mach number configurations. All the simulations use a local time stepping.

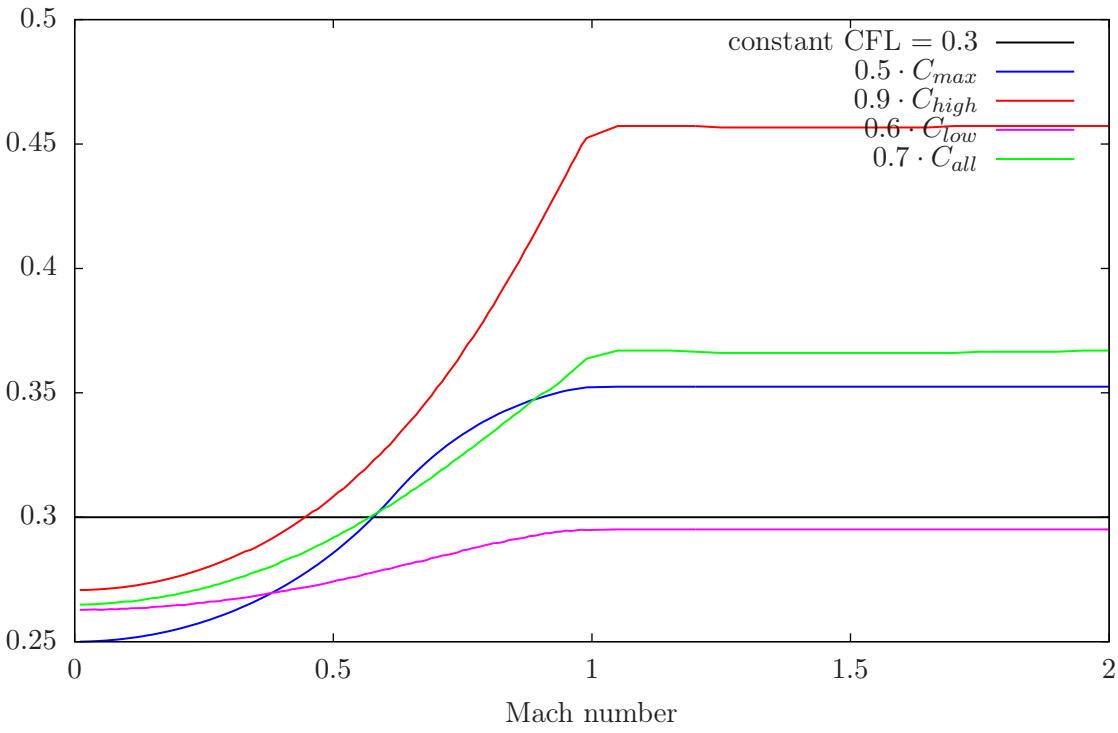

FIGURE 5.12: NACA 0012 test case. The value of the constant CFL, $C = 0.3$, that is used for almost all the Mach number configurations of the NACA 0012 test case (see the constant CFL values for the VLR case in Table 5.1), is here compared to the values of $SF\,C(M)$, that is, the different local CFL number options multiplied by the corresponding safety factors. In this plot we take into account from Table 5.2 the lowest safety factors along all Mach numbers. All the plots correspond to the VLR case with a local time stepping.

5.2.2 ONERA M6 wing

The well-known ONERA M6 wing test case Schmitt and Charpin [1979] is solved here for inviscid flow, at an angle of attack of 3.06°, and two different inflow Mach numbers: 0.8395 and 2.0. As in the NACA 0012 test case, the rest of the initial conditions are $\rho = 1$, $\|\mathbf{u}\| = 1$, $T = 1$, and c_{p} and c_{v} are determined to obtain the desired inflow Mach numbers. An unstructured tetrahedral mesh is used here consisting of 472026 elements and 94481 grid points.

For this problem, the different local CFL options (equations (5.15)-(5.18) and (5.19)-(5.22)) for the VLR case are assessed and compared to the traditional constant CFL number for both the NP and VLR cases. The 0.8395 Mach number configuration is reported in the original paper for the ONERA M6 wing Schmitt and Charpin [1979] and already solved in Subsection 4.4.2 for the assessment of P-VMS. The 2.0 Mach number configuration which is not in the original paper of the ONERA M6, is solved here in order to test the local CFL number on a supersonic three-dimensional case. A local time

stepping is used in all the VLR simulations. A global time stepping is used in the NP simulation of the 0.8395 Mach number configuration, as the local time stepping does not converge for this case unless an additional shock capturing diffusion is used. The NP case for the 2.0 Mach number configuration does not converge as well regardless a global or a local time step is used. This fact shows how the P-VMS method using VLR preconditioner is more robust than the unpreconditioned VMS. By global time step we mean the minimum of the local time steps all over the computational domain. The constant CFL numbers (see equation (4.63)) for this test case are reported in Table 5.3. When the different local CFL numbers are used in the VLR case (see equation (5.24)), the safety factors in Table 5.4 are needed for the different configurations of the ONERA M6 test case.

Convergence rates of the 0.8395 inflow Mach number configuration, for the NP and VLR cases using a constant CFL and the VLR case using the different local CFL options, are shown and compared in Fig. 5.13. As seen in the previous NACA 0012 test case, in Subsection 5.2.1, the constant CFL gives the worst convergence while the two local CFL numbers maximizing the damping of the high frequencies, $C_{\text{high},0}$ and C_{high}, from equations (5.20) and (5.16), respectively, are seen to perform the best. Both $C_{\text{high},0}$ and C_{high} give almost identical convergence rates as well. From Table 5.4 we see that they have the highest safety factor, $SF = 0.6$, meaning that these two local CFL definitions require the lowest correction, then they are the best defined options. Concerning the 2.0 inflow Mach number configuration, $C_{\text{high},0}$ and C_{high} local CFL options for the VLR case are tested and compared to the constant CFL option for the VLR case as well. The corresponding convergence rates are presented in Fig. 5.15 showing once again the improvement of the local CFL compared to the constant one. We observe that the residual convergence stalls at around 10^{-6}, we think that this is due to the presence of shocks, to the fact that no shock capturing is added, and because of the coarse mesh used.

Pressure contours on the upper and lower surface of the wing are displayed in Figs. 4.14 and 5.14, for Mach numbers 0.8395 and 2.0, respectively, and for the VLR case. In the upper surface contours of the inflow Mach number 0.8395 configuration, we see the complex sharp shock structure that is formed. As for the NACA 0012 case, no shock-capturing diffusion is used for a better comparison, thus the result presents some oscillations localized near the shocks in the supersonic case. However, it is worth to mention that while in the VLR preconditioned cases the shock over and undershoots remain localized, with almost no influence in the rest of the domain, in the NP case it is not possible to solve the problem unless additional shock capturing diffusion is used. This fact tends to confirm the preconditioner beneficial effect in terms of stabilization, accuracy and robustness.

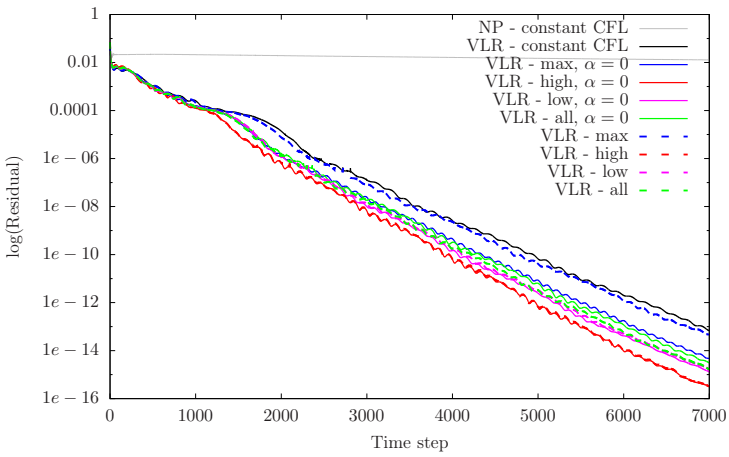

FIGURE 5.13: ONERA M6 test case. Comparison of the residual-convergence rates over the time step of the NP case with a constant CFL, the VLR case with a constant CFL, and the VLR case with the different local CFL options: $C_{\max,0}$, $C_{\text{high},0}$, $C_{\text{low},0}$, $C_{\text{all},0}$, $C_{\max}$, C_{high}, C_{low}, and C_{all}, for the solution of flow past the ONERA M6 wing at 0.8395 inflow Mach number and 3.06 angle of attack.

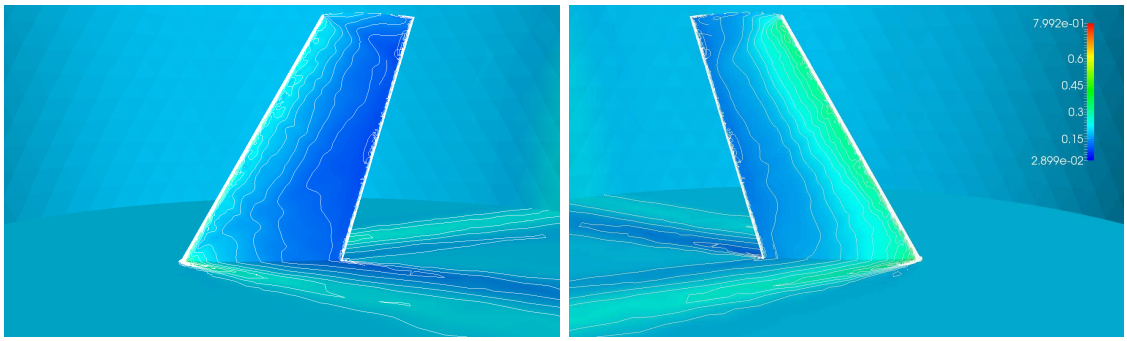

FIGURE 5.14: ONERA M6 test case. Pressure contours on the upper (left figure) and lower (right figure) surfaces of the M6 wing at 2.0 inflow Mach number and 3.06° of angle of attack for the VLR preconditioned case with local time step.

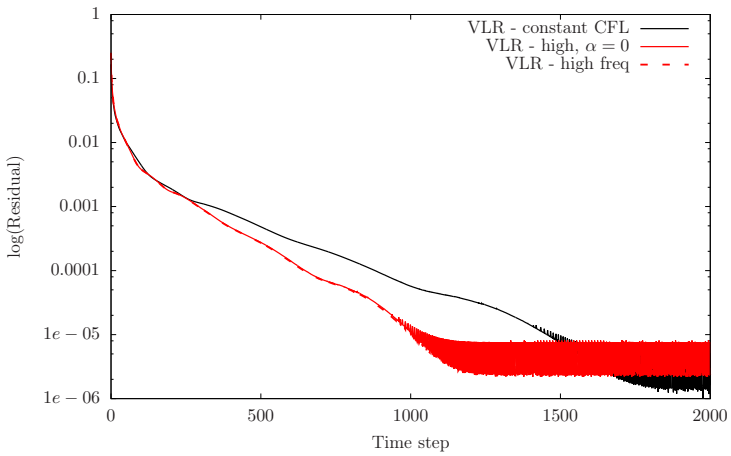

FIGURE 5.15: ONERA M6 test case. Comparison of the residual-convergence rates over the time step of the constant CFL option and $C_{\text{high},0}$ and C_{high} local CFL options, for the VLR case, for the solution of flow past the ONERA M6 wing at 2.0 inflow Mach number and 3.06° angle of attack.

Inflow Mach	0.8395	2.0
NP - constant CFL	0.8	–
VLR - constant CFL	0.2	0.2

TABLE 5.3: ONERA M6 test case. Constant CFL number values, C in the time step equation (4.63), for the NP and VLR cases and for the 0.8395 and 2.0 inflow Mach number configurations at 3.06° angle of attack. The VLR case uses a local time stepping and the NP case uses a global time stepping because it does not converge with a local one. The NP case for $M = 2.0$ does not converge.

Inflow Mach	0.8395	2.0
VLR - maximum CFL, $\alpha = 0$	0.3	–
VLR - maximum CFL	0.3	–
VLR - high freq. CFL, $\alpha = 0$	0.6	0.6
VLR - high freq. CFL	0.6	0.6
VLR - low freq. CFL, $\alpha = 0$	0.5	–
VLR - low freq. CFL	0.5	–
VLR - all freq. CFL, $\alpha = 0$	0.5	–
VLR - all freq. CFL	0.5	–

TABLE 5.4: ONERA M6 test case. Comparative of the constant safety factors, *SF* in the time step equation (5.24), for the VLR case. The safety factors for the different local CFL options are displayed for the 0.8395 inflow Mach number configuration. The safety factors corresponding to $C_{\text{high},0}$ and C_{high} local CFL options are displayed for the 2.0 inflow Mach number configuration. All these simulations use a local time stepping.

5.3 Summary and conclusions

A Fourier stability analysis of the P-VMS method for the Euler equations of steady flow are performed in this chapter. Time discretization is done here by a linear explicit scheme using local time stepping. The benefits of P-VMS compared to the original VMS, in terms of eigenvalues clustering and damping of the error, are theoretically seen through Fourier analysis. P-VMS with VLR preconditioning, and CM for low Mach numbers, is seen to reduce the spread of the eigenvalues, making it easier for them to be contained within the stability region of any particular method and allowing larger time steps. The FFP of the finite elements VMS used in this work is found to be very similar to the FFP of a first order upwind finite volumes scheme, for low Mach numbers, for both the unpreconditioned and the VLR preconditioned cases. This is not the case for moderate to high Mach numbers, where both methods give different FFP configurations. No comparison with the finite volumes CM preconditioned case is possible because of the lack of results in the literature.

We defined a local CFL number that is computed systematically and improves the convergence of the constant CFL number. The local CFL is here computed for the P-VMS

scheme, however the same technique can be applied to any numerical scheme, independently of the preconditioning choice, after a Fourier stability analysis is done. The improvement in convergence of the local CFL is visible in problems where a large range of Mach numbers is present. For this reason, the NP and the VLR preconditioned systems take advantage of the use of the local CFL number, but not the CM case that only applies for low Mach numbers. The improvement of the local CFL number in terms of acceleration of the convergence rate is seen through two numerical examples covering a large range of Mach numbers. Different options for the local CFL number are considered and compared to the traditional constant CFL number. The local CFL that is defined to provide a maximum damping of the high frequencies is seen to perform the best in terms of convergence acceleration, for all the performed test cases.

Chapter 6

Conclusions and future work

We presented a variational multiscale stabilization method for the Euler and Navier-Stokes equations of compressible flow. Two versions of the method are presented in this work. The first version, that we call *diagonal τ subscale*, uses the classical structure of the stabilization subscale, that is the product of a parameter τ times the residual of the equation. The second version, that we call *Fourier subscale*, presents a more complex structure for the subscale that is modeled using a Fourier transform approximation. These two versions are tested and compared through a batch of test cases for viscous and inviscid, transient and steady flow, at different Mach number regimes. We conclude that the diagonal τ subscale is more convenient than the Fourier subscale because it is simpler, it involves less calculations, and gives similar or better results. The Fourier subscale is a valid and powerful method which can eventually lead to better numerical methods if further carried on. The diagonal τ subscale has been used in the rest of this work.

The developed method is applied to atmospheric flow simulations. In order to be adapted for atmospheric simulations, these equations present little modification compared to the classical Euler equations of compressible flow. To evaluate the performance of the method, two and three dimensional test cases are solved. The method is also applied to moist atmospheric flow, where the Euler equations are coupled to a set of prognostic equations for water species that, by means of the Kessler microphysics scheme, are allowed to change phase and trigger a long-lasting two-dimensional convective storm.

In order to improve our method we develop P-VMS, where the originally presented VMS is combined to local preconditioning. We adapt the original method to solve the preconditioned Navier-Stokes equations of compressible flow, for steady and transient problems. We consider P-VMS using two different local preconditioners: VLR and CM. Both of them are applied to the Euler equations of steady flow, and only CM preconditioner is

applied to viscous flow as well as transient problems. Local preconditioning is applied to the set of equations before any discretization is done. In this way, P-VMS takes the benefits of local preconditioning which substantially reduces the stiffness of the original equations. P-VMS is assessed through different fluid dynamics test cases for viscous and inviscid, transient and steady flow, covering a wide range of Mach numbers. A significant improvement in the rate of convergence, robustness and accuracy of the method is seen in the presented examples. VLR brings the best improvement for all Mach numbers and CM is only good for low Mach numbers however it could be interesting for future work as it is easily adapted to viscous flow and transient problems.

Finally the behavior of P-VMS for the Euler equations of steady flow problems is theoretically studied through Fourier stability analysis. After this analysis we find a new improvement to the method by means of the definition of a local CFL number in the computation of the time step. The technique that we use to compute a local CFL number for the P-VMS method could be applied to any other numerical scheme and preconditioning option. The stability analysis is performed on a two dimensional simplified problem with a structured mesh and its conclusions are applied to two and three dimensional general problems with unstructured meshes. The benefits of the local CFL is significant in problems where a large range of Mach numbers is present. Because of this, the local CFL is computed for the unpreconditioned and the VLR preconditioned cases. The improvement in convergence rate of the local CFL is seen with several test cases of steady flow covering a large range of Mach numbers.

The potential of this work remains in the fact that we developed a method that could be applied to any physical problem. Future work should be oriented towards the application of P-VMS to coupled multi-physics large-scale problems as for example combustion problems, turbulent flow problems, fluid-structure interaction, using high-order elements, etc. To this end P-VMS must be additionally tested for viscous flow and transient problems.

Appendix A

Jacobian and diffusion matrices

The jacobian matrices $\mathbf{A}^i(\mathbf{\Phi})$, for $i = 1, \ldots, 3$, read

$$\mathbf{A}^1(\mathbf{\Phi}) = \begin{pmatrix} (2-\frac{R}{c_v})\frac{U_1}{\rho} & -\frac{R}{c_v}\frac{U_2}{\rho} & -\frac{R}{c_v}\frac{U_3}{\rho} & -\frac{U_1^2}{\rho^2}+\frac{1}{2}\frac{R}{c_v}\frac{U_kU_k}{\rho^2} & \frac{R}{c_v} \\ \frac{U_2}{\rho} & \frac{U_1}{\rho} & 0 & -\frac{U_1U_2}{\rho^2} & 0 \\ \frac{U_3}{\rho} & 0 & \frac{U_1}{\rho} & -\frac{U_1U_3}{\rho^2} & 0 \\ 1 & 0 & 0 & 0 & 0 \\ \frac{1}{\rho}(E+p-\frac{R}{c_v}\frac{U_1^2}{\rho}) & \frac{-R}{c_v}\frac{U_1U_2}{\rho^2} & \frac{-R}{c_v}\frac{U_1U_3}{\rho^2} & \frac{-U_1}{\rho^2}(E+p-\frac{1}{2}\frac{R}{c_v}\frac{U_kU_k}{\rho}) & (1+\frac{R}{c_v})\frac{U_1}{\rho} \end{pmatrix}, \quad \text{(A.1)}$$

$$\mathbf{A}^2(\mathbf{\Phi}) = \begin{pmatrix} \frac{U_2}{\rho} & \frac{U_1}{\rho} & 0 & -\frac{U_2U_1}{\rho^2} & 0 \\ -\frac{R}{c_v}\frac{U_1}{\rho} & (2-\frac{R}{c_v})\frac{U_2}{\rho} & -\frac{R}{c_v}\frac{U_3}{\rho} & -\frac{U_2^2}{\rho^2}+\frac{1}{2}\frac{R}{c_v}\frac{U_kU_k}{\rho^2} & \frac{R}{c_v} \\ 0 & \frac{U_3}{\rho} & \frac{U_2}{\rho} & -\frac{U_2U_3}{\rho^2} & 0 \\ 0 & 1 & 0 & 0 & 0 \\ \frac{-R}{c_v}\frac{U_2U_1}{\rho^2} & \frac{1}{\rho}(E+p-\frac{R}{c_v}\frac{U_2^2}{\rho}) & \frac{-R}{c_v}\frac{U_2U_3}{\rho^2} & \frac{-U_2}{\rho^2}(E+p-\frac{1}{2}\frac{R}{c_v}\frac{U_kU_k}{\rho}) & (1+\frac{R}{c_v})\frac{U_2}{\rho} \end{pmatrix}, \quad \text{(A.2)}$$

$$\mathbf{A}^3(\mathbf{\Phi}) = \begin{pmatrix} \frac{U_3}{\rho} & 0 & \frac{U_1}{\rho} & -\frac{U_3U_1}{\rho^2} & 0 \\ 0 & \frac{U_3}{\rho} & \frac{U_2}{\rho} & -\frac{U_3U_2}{\rho^2} & 0 \\ -\frac{R}{c_v}\frac{U_1}{\rho} & -\frac{R}{c_v}\frac{U_2}{\rho} & (2-\frac{R}{c_v})\frac{U_3}{\rho} & -\frac{U_3^2}{\rho^2}+\frac{1}{2}\frac{R}{c_v}\frac{U_kU_k}{\rho^2} & \frac{R}{c_v} \\ 0 & 0 & 1 & 0 & 0 \\ \frac{-R}{c_v}\frac{U_3U_1}{\rho^2} & \frac{-R}{c_v}\frac{U_3U_2}{\rho^2} & \frac{1}{\rho}(E+p-\frac{R}{c_v}\frac{U_3^2}{\rho}) & \frac{-U_3}{\rho^2}(E+p-\frac{1}{2}\frac{R}{c_v}\frac{U_kU_k}{\rho}) & (1+\frac{R}{c_v})\frac{U_3}{\rho} \end{pmatrix}. \quad \text{(A.3)}$$

The diffusion matrices $\mathbf{K}^{ir}$, for $i, r = 1, \ldots, 3$, read

$$\mathbf{K}^{ir}(\mathbf{\Phi})_{kl} = \begin{cases} (\delta_{kl}\delta_{ir} + \delta_{il}\delta_{kr} - \frac{2}{3}\delta_{ki}\delta_{rl})\frac{\mu}{\rho} & k,\, l = 1, \ldots, 3 \\ -\delta_{kr}\frac{\mu U_i}{\rho^2} - \delta_{ri}\frac{\mu U_k}{\rho^2} + \frac{2}{3}\delta_{ki}\frac{\mu U_r}{\rho^2} & k = 1, \ldots, 3,\, l = 4 \\ 0 & k = 1, \ldots, 3,\, l = 5 \\ 0 & k = 4,\, l = 1, \ldots, 5 \\ \delta_{ir}\frac{(\mu - \frac{\kappa}{c_\mathrm{v}})U_l}{\rho^2} + \delta_{il}\frac{\mu U_r}{\rho^2} - \frac{2}{3}\delta_{rl}\frac{\mu U_i}{\rho^2} & k = 5,\, l = 1, \ldots, 3 \\ \frac{1}{2}\frac{\mu U_i U_r}{\rho^3} - \delta_{ir}\big(\frac{(\mu - \frac{k}{c_\mathrm{v}})\|\mathbf{U}\|^2}{\rho^3} + \frac{\kappa}{c_\mathrm{v}}\frac{E}{\rho^2}\big) & k = 5,\, l = 4 \\ \delta_{ir}\frac{1}{\rho}\frac{\kappa}{c_\mathrm{v}} & k = 5,\, l = 5 \end{cases} \tag{A.4}$$

Appendix B

Symmetrizing variables

B.1 Euler equations in symmetrizing variables

We introduce the symmetrization of the Euler equations proposed by Turkel [1973]. The symmetrizing variables are

$$\mathrm{d}\boldsymbol{\Phi}_{\mathrm{s}} = \begin{pmatrix} \mathrm{d}u_1 & \mathrm{d}u_2 & \mathrm{d}u_3 & \dfrac{\mathrm{d}p}{\rho c} & \mathrm{d}p - c^2\mathrm{d}\rho \end{pmatrix}^{\mathrm{T}} , \tag{B.1}$$

where $\mathrm{d}p - c^2\mathrm{d}\rho = \frac{p}{c_{\mathrm{v}}}\mathrm{d}s$. They are related to the conservative variables through the expression $\mathrm{d}\boldsymbol{\Phi}_{\mathrm{s}} = \frac{\partial \boldsymbol{\Phi}_{\mathrm{s}}}{\partial \boldsymbol{\Phi}}\,\mathrm{d}\boldsymbol{\Phi}$, where

$$\frac{\partial \boldsymbol{\Phi}_{\mathrm{s}}}{\partial \boldsymbol{\Phi}} = \begin{pmatrix} \frac{1}{\rho} & 0 & 0 & -\frac{u_1}{\rho} & 0 \\ 0 & \frac{1}{\rho} & 0 & -\frac{u_2}{\rho} & 0 \\ 0 & 0 & \frac{1}{\rho} & -\frac{u_3}{\rho} & 0 \\ -\frac{R}{c_{\mathrm{v}}}\frac{u_1}{\rho c} & -\frac{R}{c_{\mathrm{v}}}\frac{u_2}{\rho c} & -\frac{R}{c_{\mathrm{v}}}\frac{u_3}{\rho c} & \frac{1}{2}\frac{R}{c_{\mathrm{v}}}\frac{u_k u_k}{\rho c} & \frac{R}{c_{\mathrm{v}}}\frac{1}{\rho c} \\ -\frac{R}{c_{\mathrm{v}}}u_1 & -\frac{R}{c_{\mathrm{v}}}u_2 & -\frac{R}{c_{\mathrm{v}}}u_3 & \frac{1}{2}\frac{R}{c_{\mathrm{v}}}u_k u_k - c^2 & \frac{R}{c_{\mathrm{v}}} \end{pmatrix} , \tag{B.2}$$

and its inverse

$$\frac{\partial \boldsymbol{\Phi}}{\partial \boldsymbol{\Phi}_{\mathrm{s}}} = \begin{pmatrix} \rho & 0 & 0 & \frac{\rho u_1}{c} & -\frac{u_1}{c^2} \\ 0 & \rho & 0 & \frac{\rho u_2}{c} & -\frac{u_2}{c^2} \\ 0 & 0 & \rho & \frac{\rho u_3}{c} & -\frac{u_3}{c^2} \\ 0 & 0 & 0 & \frac{\rho}{c} & -\frac{1}{c^2} \\ \rho u_1 & \rho u_2 & \rho u_3 & \frac{c_{\mathrm{v}}}{R}\rho c + \frac{1}{2}\frac{\rho u_k u_k}{c} & -\frac{1}{2}\frac{u_k u_k}{c^2} \end{pmatrix} . \tag{B.3}$$

We then obtain the symmetric jacobian matrices in the symmetrizing variables, $\mathbf{A}_{\mathrm{s}}^{i} = \frac{\partial \mathbf{\Phi}_{\mathrm{s}}}{\partial \mathbf{\Phi}} \mathbf{A}^{i} \frac{\partial \mathbf{\Phi}}{\partial \mathbf{\Phi}_{\mathrm{s}}}$, $i = 1, \ldots, 3$, which are explicitly written as:

$$\mathbf{A}_{\mathrm{s}}^{1} = \begin{pmatrix} u_1 & 0 & 0 & c & 0 \\ 0 & u_1 & 0 & 0 & 0 \\ 0 & 0 & u_1 & 0 & 0 \\ c & 0 & 0 & u_1 & 0 \\ 0 & 0 & 0 & 0 & u_1 \end{pmatrix}, \quad \mathbf{A}_{\mathrm{s}}^{2} = \begin{pmatrix} u_2 & 0 & 0 & 0 & 0 \\ 0 & u_2 & 0 & c & 0 \\ 0 & 0 & u_2 & 0 & 0 \\ 0 & c & 0 & u_2 & 0 \\ 0 & 0 & 0 & 0 & u_2 \end{pmatrix}, \quad \mathbf{A}_{\mathrm{s}}^{3} = \begin{pmatrix} u_3 & 0 & 0 & 0 & 0 \\ 0 & u_3 & 0 & 0 & 0 \\ 0 & 0 & u_3 & c & 0 \\ 0 & 0 & c & u_3 & 0 \\ 0 & 0 & 0 & 0 & u_3 \end{pmatrix}. \tag{B.4}$$

Then, (2.8) is equivalent to the symmetric system

$$\frac{\partial \mathbf{\Phi}_{\mathrm{s}}}{\partial t} + \mathbf{A}_{\mathrm{s}}^{i} \frac{\partial \mathbf{\Phi}_{\mathrm{s}}}{\partial x_i} = 0 \,. \tag{B.5}$$

B.2 Euler equations in symmetrizing variables and streamline coordinates

System (B.5) can be simplified even more by rotating the reference coordinates, $\mathbf{x} = (x_1, x_2, x_3)$, to obtain a coordinate system $\xi = (\xi_1, \xi_2, \xi_3)$, in which the flow is in the positive ξ_1-direction. They are called streamline coordinates. We write $\xi = \mathbf{R}\,\mathbf{x}$, where $\mathbf{R} = \mathbf{R}_{x_2}\mathbf{R}_{x_3}$,

$$\mathbf{R}_{x_2} = \begin{pmatrix} \cos\alpha & 0 & \sin\alpha \\ 0 & 1 & 0 \\ -\sin\alpha & 0 & \cos\alpha \end{pmatrix}, \quad \mathbf{R}_{x_3} = \begin{pmatrix} \cos\theta & \sin\theta & 0 \\ -\sin\theta & \cos\theta & 0 \\ 0 & 0 & 1 \end{pmatrix}. \tag{B.6}$$

$\mathbf{R}_{x_2}$ rotates the x_1x_3-plane counter-clockwise (when the x_2-axis points toward the observer, and the coordinate system is right-handed), and $\mathbf{R}_{x_3}$ rotates the x_1x_2-plane clockwise (when the x_3-axis points toward the observer, and the coordinate system is right-handed). The product reads:

$$\mathbf{R} = \begin{pmatrix} \cos\alpha\cos\theta & \cos\alpha\sin\theta & \sin\alpha \\ -\sin\theta & \cos\theta & 0 \\ -\sin\alpha\cos\theta & -\sin\alpha\sin\theta & \cos\alpha \end{pmatrix}. \tag{B.7}$$

For the flow to be in the positive ξ_1-direction, the angles θ and α or the velocity should verify

$$\begin{cases} \sin\theta = \frac{u_2}{\sqrt{u_1^2+u_2^2}} \\ \cos\theta = \frac{u_1}{\sqrt{u_1^2+u_2^2}} \end{cases}, \quad \begin{cases} \sin\alpha = \frac{u_3}{\|\mathbf{u}\|} \\ \cos\alpha = \frac{\sqrt{u_1^2+u_2^2}}{\|\mathbf{u}\|} \end{cases}, \quad \begin{cases} u_1 = \|\mathbf{u}\|\cos\alpha\cos\theta \\ u_2 = \|\mathbf{u}\|\cos\alpha\sin\theta \\ u_3 = \|\mathbf{u}\|\sin\alpha \,. \end{cases} \tag{B.8}$$

The velocity in the streamline coordinates is $\mathbf{q} = R\,\mathbf{u}$, then $q_1 = \|\mathbf{u}\|$ and $q_2 = q_3 = 0$. Therefore the symmetrizing variables with streamwise coordinates are

$$\mathrm{d}\boldsymbol{\Phi}_{\mathrm{ss}} = (\mathrm{d}q_1 \quad \mathrm{d}q_2 \quad \mathrm{d}q_3 \quad \frac{\mathrm{d}p}{\rho c} \quad \mathrm{d}p - c^2\mathrm{d}\rho)^{\mathrm{T}} \,. \tag{B.9}$$

They are expressed in terms of the symmetrizing and conservative variables as $\mathrm{d}\boldsymbol{\Phi}_{\mathrm{ss}} = \frac{\partial \boldsymbol{\Phi}_{\mathrm{ss}}}{\partial \boldsymbol{\Phi}_{\mathrm{s}}}\,\mathrm{d}\boldsymbol{\Phi}_{\mathrm{s}}$ and $\mathrm{d}\boldsymbol{\Phi}_{\mathrm{ss}} = \frac{\partial \boldsymbol{\Phi}_{\mathrm{ss}}}{\partial \boldsymbol{\Phi}}\,\mathrm{d}\boldsymbol{\Phi}$, respectively, where

$$\frac{\partial \boldsymbol{\Phi}_{\mathrm{ss}}}{\partial \boldsymbol{\Phi}_{\mathrm{s}}} = \begin{pmatrix} \cos\alpha\cos\theta & \cos\alpha\sin\theta & \sin\alpha & 0 & 0 \\ -\sin\theta & \cos\theta & 0 & 0 & 0 \\ -\sin\alpha\cos\theta & -\sin\alpha\sin\theta & \cos\alpha & 0 & 0 \\ 0 & 0 & 0 & 1 & 0 \\ 0 & 0 & 0 & 0 & 1 \end{pmatrix}, \tag{B.10}$$

its inverse is

$$\frac{\partial \boldsymbol{\Phi}_{\mathrm{s}}}{\partial \boldsymbol{\Phi}_{\mathrm{ss}}} = \begin{pmatrix} \cos\alpha\cos\theta & -\sin\theta & -\sin\alpha\cos\theta & 0 & 0 \\ \cos\alpha\sin\theta & \cos\theta & -\sin\alpha\sin\theta & 0 & 0 \\ \sin\alpha & 0 & \cos\alpha & 0 & 0 \\ 0 & 0 & 0 & 1 & 0 \\ 0 & 0 & 0 & 0 & 1 \end{pmatrix}, \tag{B.11}$$

and where

$$\frac{\partial \boldsymbol{\Phi}}{\partial \boldsymbol{\Phi}_{\mathrm{ss}}} = \begin{pmatrix} \frac{\rho u_1}{\|\mathbf{u}\|} & \frac{-\rho u_2}{\sqrt{u_1^2+u_2^2}} & \frac{-\rho u_1 u_3}{\|\mathbf{u}\|\sqrt{u_1^2+u_2^2}} & \frac{\rho u_1}{c} & -\frac{u_1}{c^2} \\ \frac{\rho u_2}{\|\mathbf{u}\|} & \frac{\rho u_1}{\sqrt{u_1^2+u_2^2}} & \frac{-\rho u_2 u_3}{\|\mathbf{u}\|\sqrt{u_1^2+u_2^2}} & \frac{\rho u_2}{c} & -\frac{u_2}{c^2} \\ \frac{\rho u_3}{\|\mathbf{u}\|} & 0 & \frac{\rho\sqrt{u_1^2+u_2^2}}{\|\mathbf{u}\|} & \frac{\rho u_3}{c} & -\frac{u_3}{c^2} \\ 0 & 0 & 0 & \frac{\rho}{c} & -\frac{1}{c^2} \\ \rho\|\mathbf{u}\| & 0 & 0 & \rho c\left(\frac{c_v}{R} + \frac{M^2}{2}\right) & -\frac{1}{2}M^2 \end{pmatrix}, \tag{B.12}$$

and its inverse is

$$\frac{\partial \boldsymbol{\Phi}_{\mathrm{ss}}}{\partial \boldsymbol{\Phi}} = \begin{pmatrix} \frac{u_1}{\rho\|\mathbf{u}\|} & \frac{u_2}{\rho\|\mathbf{u}\|} & \frac{u_3}{\rho\|\mathbf{u}\|} & \frac{-\|\mathbf{u}\|}{\rho} & 0 \\ \frac{-u_2}{\rho\sqrt{u_1^2+u_2^2}} & \frac{u_1}{\rho\sqrt{u_1^2+u_2^2}} & 0 & 0 & 0 \\ \frac{-u_1 u_3}{\rho\|\mathbf{u}\|\sqrt{u_1^2+u_2^2}} & \frac{-u_2 u_3}{\rho\|\mathbf{u}\|\sqrt{u_1^2+u_2^2}} & \frac{\sqrt{u_1^2+u_2^2}}{\rho\|\mathbf{u}\|} & 0 & 0 \\ \frac{-R}{c_v}\frac{u_1}{\rho c} & \frac{-R}{c_v}\frac{u_2}{\rho c} & \frac{-R}{c_v}\frac{u_3}{\rho c} & \frac{1}{2}\frac{R}{c_v}\frac{\|\mathbf{u}\|^2}{\rho c} & \frac{R}{c_v}\frac{1}{\rho c} \\ -\frac{R}{c_v}u_1 & -\frac{R}{c_v}u_2 & -\frac{R}{c_v}u_3 & \frac{1}{2}\frac{R}{c_v}\|\mathbf{u}\|^2 - c^2 & \frac{R}{c_v} \end{pmatrix}. \tag{B.13}$$

As $\frac{\partial}{\partial x_i} = \frac{\partial \xi_k}{\partial x_i}\frac{\partial}{\partial \xi_k}$, let $\mathbf{A}^i_{\rm ss} = \frac{\partial \mathbf{\Phi}_{\rm ss}}{\partial \mathbf{\Phi}_{\rm s}}\mathbf{A}^k_{\rm s}\frac{\partial \mathbf{\Phi}_{\rm s}}{\partial \mathbf{\Phi}_{\rm ss}}\ \frac{\partial \xi_i}{\partial x_k}$, or equivalently $\mathbf{A}^i_{\rm ss} = \frac{\partial \mathbf{\Phi}_{\rm ss}}{\partial \mathbf{\Phi}}\mathbf{A}^k\frac{\partial \mathbf{\Phi}}{\partial \mathbf{\Phi}_{\rm ss}}\ \frac{\partial \xi_i}{\partial x_k}$, for $i = 1, \ldots, 3$. Then:

$$\mathbf{A}^1_{\rm ss} = \begin{pmatrix} q_1 & 0 & 0 & c & 0 \\ 0 & q_1 & 0 & 0 & 0 \\ 0 & 0 & q_1 & 0 & 0 \\ c & 0 & 0 & q_1 & 0 \\ 0 & 0 & 0 & 0 & q_1 \end{pmatrix}, \quad \mathbf{A}^2_{\rm ss} = \begin{pmatrix} 0 & 0 & 0 & 0 & 0 \\ 0 & 0 & 0 & c & 0 \\ 0 & 0 & 0 & 0 & 0 \\ 0 & c & 0 & 0 & 0 \\ 0 & 0 & 0 & 0 & 0 \end{pmatrix}, \quad \mathbf{A}^3_{\rm ss} = \begin{pmatrix} 0 & 0 & 0 & 0 & 0 \\ 0 & 0 & 0 & 0 & 0 \\ 0 & 0 & 0 & c & 0 \\ 0 & 0 & c & 0 & 0 \\ 0 & 0 & 0 & 0 & 0 \end{pmatrix}. \tag{B.14}$$

which are very attractive to work with due to their sparseness and because $\mathbf{A}^i_{\rm ss}$ for $i = 2, 3$, are degenerated matrices. The Euler system of equations with symmetrizing variables and stream-wise coordinates is written as:

$$\frac{\partial \mathbf{\Phi}_{\rm ss}}{\partial t} + \mathbf{A}^i_{\rm ss}\frac{\partial \mathbf{\Phi}_{\rm ss}}{\partial \xi_i} = 0\,. \tag{B.15}$$

Systems (B.15), (2.8), and (B.5) are equivalent.

Appendix C

Primitive variables

The primitive variables are

$$\mathbf{\Phi}_{\mathrm{P}} = (u_1\ u_2\ u_3\ p\ T)^{\mathrm{T}} \tag{C.1}$$

The Jacobians that are used to change from primitive to conservawtive variables are given as:

$$\frac{\partial \mathbf{\Phi}}{\partial \mathbf{\Phi}_{\mathrm{P}}} = \begin{pmatrix} \rho & 0 & 0 & \frac{U_1}{p} & -\frac{U_1}{T} \\ 0 & \rho & 0 & \frac{U_2}{p} & -\frac{U_2}{T} \\ 0 & 0 & \rho & \frac{U_3}{p} & -\frac{U_3}{T} \\ 0 & 0 & 0 & \frac{\rho}{p} & -\frac{\rho}{T} \\ U_1 & U_2 & U_3 & \frac{1}{R}\left(\frac{1}{2}\frac{\|\mathbf{u}\|^2}{T} + c_v\right) & -\frac{1}{2}\frac{\rho\|\mathbf{u}\|^2}{T} \end{pmatrix} \tag{C.2}$$

and

$$\frac{\partial \mathbf{\Phi}_{\mathrm{P}}}{\partial \mathbf{\Phi}} = \begin{pmatrix} \frac{1}{\rho} & 0 & 0 & \frac{u_1}{\rho} & 0 \\ 0 & \frac{1}{\rho} & 0 & \frac{u_2}{\rho} & 0 \\ 0 & 0 & \frac{1}{\rho} & \frac{u_3}{\rho} & 0 \\ \frac{R}{c_v}u_1 & \frac{R}{c_v}u_2 & \frac{R}{c_v}u_3 & \frac{1}{2}\frac{R}{c_v}\|\mathbf{u}\|^2 & \frac{R}{c_v} \\ -\frac{u_1}{c_v\rho} & -\frac{u_2}{c_v\rho} & -\frac{u_3}{c_v\rho} & \frac{1}{c_v\rho}\left(\|\mathbf{u}\|^2 - \frac{E}{\rho}\right) & \frac{1}{c_v\rho} \end{pmatrix}. \tag{C.3}$$

Appendix D

Group velocity of a plane wave

D.1 2D case

Let us consider $\mathbf{n} = (n_1, n_2) = \|\mathbf{n}\|(\cos\theta, \sin\theta)$ in the two dimensional case, where $\theta = \arctan\left(\frac{n_2}{n_1}\right)$ is the angle of the wave propagation direction, $\mathbf{n}$, relative to the x_1-axis. Then the wave speeds can be expressed as $\lambda_i(\theta(\mathbf{n}))$. Thus, the group velocities (equation (4.11)) can be expressed as

$$\mathbf{g}_i(\mathbf{n}) = \begin{pmatrix} \cos\theta & -\sin\theta \\ \sin\theta & \cos\theta \end{pmatrix} \begin{pmatrix} \lambda_i(\theta) \\ \lambda_i'(\theta) \end{pmatrix} , \tag{D.1}$$

where $\lambda_i'(\theta) = \frac{\partial \lambda_i}{\partial \theta}$.

D.2 3D case

Extended to the three dimensional case, let $\mathbf{n} = (n_1, n_2, n_3)$ be the wave propagation direction and θ and α the wave propagation angles such that

$$\begin{cases} \sin\theta &= \frac{n_2}{\sqrt{n_1^2+n_2^2}} \\ \cos\theta &= \frac{n_1}{\sqrt{n_1^2+n_2^2}} \\ \theta &= \arctan\left(\frac{n_2}{n_1}\right) \end{cases} \qquad \begin{cases} \sin\alpha &= \frac{n_3}{\|\mathbf{n}\|} \\ \cos\alpha &= \frac{\sqrt{n_1^2+n_2^2}}{\|\mathbf{n}\|} \\ \alpha &= \arctan\left(\frac{n_3}{\sqrt{n_1^2+n_2^2}}\right) , \end{cases} \tag{D.2}$$

or equivalently,

$$\begin{cases} n_1 &= \|\mathbf{n}\| \cos\alpha \cos\theta \\ n_2 &= \|\mathbf{n}\| \cos\alpha \sin\theta \\ n_3 &= \|\mathbf{n}\| \sin\alpha \, . \end{cases} \tag{D.3}$$

Then the group velocities (equation (4.11)) can be computed as

$$\mathbf{g}_i(\mathbf{n}) = \begin{pmatrix} \cos\theta\cos\alpha & -\frac{\sin\theta}{\cos\alpha} & -\cos\theta\sin\alpha \\ \sin\theta\cos\alpha & \frac{\cos\theta}{\cos\alpha} & -\sin\theta\sin\alpha \\ \sin\alpha & 0 & \cos\alpha \end{pmatrix} \begin{pmatrix} \lambda_i(\theta,\alpha) \\ \frac{\partial\lambda_i}{\partial\theta} \\ \frac{\partial\lambda_i}{\partial\alpha} \end{pmatrix}. \tag{D.4}$$

Bibliography

N. Ahmad. The f-wave Riemann solver for meso- and micro-scale flows. *AIAA Paper*, 2008-465, 2008.

N. Ahmad and J. Lindeman. Euler solutions using flux-based wave decomposition. *Int. J. Numer. Meth. Fluids*, 54:47–72, 2007.

S. R. Allmaras. Analysis of a local matrix preconditioner for the 2-D Navier-Stokes equations. *AIAA Paper 93-3330*, 1993.

S. R. Allmaras. Analysis of semi-implicit preconditioners for multigrid solution of the 2-D Navier-Stokes equations. *AIAA Paper 95-1651*, 1995.

O. Arias, O. Falcinelli, N. Fico, and S. Elaskar. Finite volume simulation of a flow over a naca 0012. *Mecánica Computacional, Asociación Argentina de Mecánica Computacional*, 26:3097–3116, 2007.

M. Avila, R. Codina, and J. Principe. Large eddy simulation of low mach number flows using dynamic and orthogonal subgrid scales. *Comput. Fluids*, 99:44–66, 2014.

D. Bacon, N. Ahmad, Z. Boybeyi, T. Dunn, M. Hall, C Lee, R. Sarma, and M. Turner. A dynamically adaptive weather and dispersion model: the operational multiscale environment model with grid adaptivity (OMEGA). *Mon. Wea. Rev.*, 128:2044–2075, 2000.

P. Bannon. Theoretical foundations for models of moist convection. *J. Atmos. Sci.*, 59: 1967–1982, 2002.

Y. Bazilevs, V. Calo, J. A. Cottrell, T. J. R. Hughes, A. Reali, and G. Scovazzi. Variational multiscale residual-based turbulence modeling for large eddy simulation of incompressible flows. *Comput. Methods Appl. Mech. Engrg.*, 197:173–201, 2007.

D. Bolton. The computation of equivalent potential temperature. *Mon Wea Rev*, 108: 1046–1053, 1980.

L. Bonaventura. A semi-implicit, semi-Lagrangian scheme using the height coordinate for a nonhydrostatic and fully elastic model of atmospheric flows. *J. Comput. Phys.*, 158:186–213, 2000.

N. Botta, R. Klein, S. Langenberg, and S. Lutzenkirchen. Well balanced finite volume methods for nearly hydrostatic flows. *Journal of Computational Physics*, 196:539–565, 2004.

W.R. Briley, L.K. Taylor, and D.L. Whitfield. High-resolution viscous flow simulations at arbitrary mach number. *Journal of Computational Physics*, 184(1):79 – 105, 2003. ISSN 0021-9991. doi: http://dx.doi.org/10.1016/S0021-9991(02)00018-9. URL http://www.sciencedirect.com/science/article/pii/S0021999102000189.

R. Carpenter, K. Droegemeier, P. Woodward, and C. Hane. Application of the piecewise parabolic method (PPM) to meteorological modeling. *Mon. Wea. Rev.*, 118:586–612, 1990.

E. Casoni, A. Jérusalem, C. Samaniego, B. Eguzkitza, P. Lafortune, D. Tjahjanto, X. Sáez, G. Houzeaux, and M. Vázquez. Alya: computational solid mechanics for supercomputers. *Arch. Comp. Meth. Eng.*, (In press), 2014.

Y.-H. Choi and C.L. Merkle. The application of preconditioning in viscous flows. *Journal of Computational Physics*, 105(2):207 – 223, 1993. ISSN 0021-9991. doi: http://dx.doi.org/10.1006/jcph.1993.1069. URL http://www.sciencedirect.com/science/article/pii/S0021999183710697.

A. Chorin. A numerical method for solving incompressible viscous flow problems. *Journal of Computational Physics*, 2(1):12–26, 1967.

R. Codina. A discontinuity-capturing crosswind-dissipation for the finite element solution of the convection-diffusion equation. *Comput. Methods Appl. Mech. and Engrg.*, 110: 325–342, 1993.

R. Codina. Stabilized finite element approximation of transient incompressible flows using orthogonal subscales. *Comput. Methods Appl. Mech. Engrg.*, 191:4295–4321, 2002.

R. Codina and J. Blasco. Analysis of a stabilized finite element approximation of the transient convection-diffusion-reaction equation using orthogonal subscales. *Comput. Visusl. Sci.*, 4:167–174, 2002.

S Scott Collis and Y Chang. The DG/VMS method for unified turbulence simulation. *AIAA paper*, 3124:24–27, 2002.

Alessandro Corsini, Franco Rispoli, and Andrea Santoriello. A variational multiscale higher-order finite element formulation for turbomachinery flow computations. *Computer Methods in Applied Mechanics and Engineering*, 194(45-47): 4797–4823, 2005. ISSN 0045-7825. doi: 10.1016/j.cma.2004.11.013. URL http://www.sciencedirect.com/science/article/pii/S004578250400564X.

R. Courant, K. Friedrichs, and H. Lewy. On the partial difference equations of mathematical physics. *IBM Journal Res. Dev.*, 11(2):215–234, 1967.

D. L. Darmofal and B. van Leer. Local Preconditioning: Manipulating Mother Nature to Fool Father Time. In D. A. Caughey and M. M. Hafez, editors, *Computing the Future II: Frontiers of Computational Fluid Dynamics 1998*, pages 211 – 240. World Scientific Publishing Co. Pte. Ltd., Singapore, 1998.

D. L. Darmofal and B. van Leer. Local preconditioning of the Euler equations: A characteristic interpretation. *Von Karman Institute Lecture Series 1999-03*, 1999.

D.L. Darmofal and P.J. Schmid. The importance of eigenvectors for local preconditioners of the euler equations. *Journal of Computational Physics*, 127(2):346 – 362, 1996. ISSN 0021-9991. doi: http://dx.doi.org/10.1006/jcph.1996.0180. URL http://www.sciencedirect.com/science/article/pii/S0021999196901801.

K. Droegemeier and R. Wilhelmson. Numerical simulation of thunderstorm outflow dynamics. part I: outflow sensitivity experiments and turbulence dynamics. *J. Atmos. Sci.*, 44:1180–1210, 1987.

D. Durran and J. Klemp. A compressible model for the simulation of moist mountain waves. *Mon. Wea. Rev.*, 111(12):2341–2361, 1983.

K A. Emanuel. *Atmospheric Convection*. Oxford University Press, 1994.

Charbel Farhat, Ajay Kumar Rajasekharan, and Bruno Koobus. A dynamic variational multiscale method for large eddy simulations on unstructured meshes. *Computer Methods in Applied Mechanics and Engineering*, 195(13-16):1667 – 1691, 2006. ISSN 0045-7825. doi: http://dx.doi.org/10.1016/j.cma.2005.05.045. URL http://www.sciencedirect.com/science/article/pii/S0045782505003014. A Tribute to Thomas J.R. Hughes on the Occasion of his 60th Birthday.

S. Gaberšek, F. X. Giraldo, and J. Doyle. Dry and moist idealized experiments with a two-dimensional spectral element model. *Mon. Wea. Rev.*, 140:3163–3182, 2012.

A. Gassmann. Non-hydrostatic modelling with the icon model. ECMWF Workshop on non-hydrostatic modelling, 2010.

F. X. Giraldo and M. Restelli. A study of spectral element and discontinuous Galerkin methods for the Navier-Stokes equations in nonhydrostatic mesoscale atmospheric modeling: Equation sets and test cases. *Journal of Computational Physics*, 227:3849–3877, 2008.

A. Godfrey. Steps toward a robust preconditioning. *AIAA Paper 94-0520*, 1994.

A. G. Godfrey, R. W. Walters, and B. van Leer. Preconditioning for the navier-stokes equations with finite-rate chemistry. *AIAA Paper 93-0535*, 1993.

S. Gövert, D. Mira, J.B.W. Kok, M. Vázquez, and G. Houzeaux. Turbulent combustion modeling of a confined premixed methane/air jet flame using tabulated chemistry. *Applied Energy*, Accepted, 2015.

V. Gravemeier. *The variational multiscale method for laminar and turbulent incompressible flow*. PhD thesis, Universitat Stuttgart, 2003.

Guillermo Hauke and Thomas J.R. Hughes. A comparative study of different sets of variables for solving compressible and incompressible flows. *Computer Methods in Applied Mechanics and Engineering*, 153(1-2):1 – 44, 1998. ISSN 0045-7825. doi: http://dx.doi.org/10.1016/S0045-7825(97)00043-1. URL http://www.sciencedirect.com/science/article/pii/S0045782597000431.

I. Holmstrom. On a method for parametric representation of the state of the atmosphere. *Tellus*, 15:127–149, 1963.

R A. Houze. *Cloud Dynamics*. Academic Press, 1993.

G. Houzeaux, B. Eguzkitza, and M. Vázquez. A variational multiscale model for the advection-diffusion-reaction equation. *Comm. Numer. Meth. Engrg.*, 25:787–809, 2009.

G. Houzeaux, M. Vázquez, R. Aubry, and J.M. Cela. A massively parallel fractional step solver for incompressible flows. *J. Comput. Phys.*, 228(17):6316–6332, 2009. URL http://dx.doi.org/10.1016/j.jcp.2009.05.019.

G. Houzeaux, B. Eguzkitza, R. Aubry, H. Owen, and M. Vázquez. A Chimera method for the Navier-Stokes equations. *Int. J. Num. Meth. Fluids*, 75:155–183, 2014. doi: DOI:10.1002/fld.3886.

T. Hughes. Multiscale phenomena: Green's functions, the Dirichlet-to-Neumann formulation, subgrid scale models, bubbles and the origins of stabilized methods. *Comput. Methods Appl. Mech. and Engrg.*, 127:387–401, 1995.

T J R Hughes and M. Mallet. A new finite element formulation for computational fluid dynamics: IV. a discontinuity-capturing operator for multi-dimensional advective-diffusive systems. *Comp. Methods Appl. Mech. Engrg.*, 58:329–336, 1986a.

T J R Hughes and M. Mallet. A new finite element formulation for computational fluid dynamics: III. the generalized streamline operator for multidimensional advective-diffusive systems. *Comp. Methods Appl. Mech. Engrg.*, 58:305–328, 1986b.

T J R Hughes and T. Tezduyar. Finite element methods for first-order hyperbolic systems with particular emphasis pn the compressible Euler equations. *Comput. Methods Appl. Mech. Engrg.*, 45:217–284, 1984.

T J R Hughes, G. Feijoo, L. Mazzei, and J. Quincy. The variational multiscale method – A paradigm for computational mechanics. *Comput. Methods Appl. Mech. Engrg.*, 166: 3–24, 1998.

T J R. Hughes, L. Mazzei, and K E.. Jansen. Large Eddy Simulation and the variational multiscale method. *Comput. Visual. Sci.*, 3:47–59, 2000.

T.J. R. Hughes. *The finite element method: Linear static and dynamics finite element analysis*. Dover Publications Inc., 2nd edition, 2000.

T.J.R. Hughes, G. Scovazzi, and T E. Tezduyar. Stabilized methods for compressible flows. *J. Sci. Comput.*, 43:343–368, 2010.

J V. Iribarne and W L. Godson. *Atmospheric Thermodynamics*. Springer, 2nd edition, 1981.

A. Jameson. Time dependent calculations using multigrid with application to unsteady flows past airfoils and wings. *AIAA Paper 91-1596*, 1991.

V. John and P. Knobloch. On spurious oscillations at layers diminishing (*sold*) methods for convection-diffusion equations: Part I - *a* review. *Comput. Methods Appl. Mech. Engrg.*, 196:2197–2215, 2007.

E. Kessler. On the distribution and continuity of water substance in atmospheric circulation. *Meteorol. Monogr.*, 10:32, 1969.

R. Klein. Asymptotic analyses for atmospheric flows and the construction of asymptotically adaptive numerical methods. *ZAMM Z. Angew. Math. Mech.*, 80:765–777, 2000.

J. Klemp and D. Lilly. Numerical simulation of hydrostatic mountain waves. *J. Atmos. Sci.*, 35:78–107, 1978.

J. Klemp and R. Wilhelmson. The simulation of three-dimensional convective storm dynamics. *J. Atmos. Sci.*, 35:1070–1096, 1978.

J. Klemp, W. Skamarock, and J. Dudhia. Conservative split-explicit time integration methods for the compressible nonhydrostatic equations. *Mon. Wea. Rev.*, 135:2897–2913, 2007.

D.A. Knoll and D.E. Keyes. Jacobian-free Newton–Krylov methods: a survey of approaches and applications. *Journal of Computational Physics*, 193(2):357 – 397, 2004. ISSN 0021-9991. doi: http://dx.doi.org/10.1016/j.jcp.2003.08.010. URL http://www.sciencedirect.com/science/article/pii/S0021999103004340.

B. Koobus and F. Charbel. A variational multiscale method for the large eddy simulation of compressible turbulent flows on unstructured meshes - application to vortex shedding. *Comp. Methods Appl. Mech. Engr.*, 193:1367–1383, 2004.

A. Kumar. Numerical analysis of the scramjet inlet flow field using two-dimensional Navier-Stokes equations. In *Proceedings: 19th AIAA Aerospace Sciences Meeting, St. Louis, Missouri*, 1981.

A. Kumar. Two-dimensional analysis of a scramjet inlet flowfield. *AIAA Journal*, 20(1): 96–97, 1982.

A. Kumar and S. N. Tiwari. Analysis of the scramjet inlet flow field using two-dimensional Navier-Stokes equations. Technical Report 3562, NASA, 1982.

G J. Le Beau, S E. Ray, S K. Aliabadi, and T E. Tezduyar. SUPG finite element computation of compressible flows with the entropy and conservation variables formulations. *Comp. Methods Appl. Mech. Engrg.*, 104:397–422., 1993.

D. Lee. *Local Preconditioning of the Euler and Navier-Stokes Equations*. PhD thesis, University of Michigan, 1996.

D. Lee and B. van Leer. Progress in local preconditioning of the Euler and Navier-Stokes equations. *AIAA Paper 93-3328-CP*, 1993.

D. Lee, B. van Leer, and J. F. Lynn. A local Navier-Stokes preconditioner for all Mach and cell Reynolds number. *AIAA Paper 97-2024*, 1997.

Dohyung Lee. The Design of Local Navier-Stokes Preconditioning for Compressible Flow. *Journal of Computational Physics*, 144(2):460 – 483, 1998a. ISSN 0021-9991. doi: http://dx.doi.org/10.1006/jcph.1998.5994. URL http://www.sciencedirect.com/science/article/pii/S0021999198959940.

Dohyung Lee. Design Criteria for Local Euler Preconditioning. *Journal of Computational Physics*, 144(2):423 – 459, 1998b. ISSN 0021-9991. doi: http://dx.doi.org/10.1006/jcph.1998.5993. URL http://www.sciencedirect.com/science/article/pii/S0021999198959939.

W. T. Lee. *Local Preconditioning of the Euler Equations*. PhD thesis, University of Michigan, 1991.

V. Levasseur, P. Sagaut, F. Chalot, and A. Davroux. An entropy-variable-based VMS/GLS method for the simulation of compressible flows on unstructured grids. *Computer Methods in Applied Mechanics and Engineering*, 195(9-12):1154 – 1179, 2006. ISSN 0045-7825. doi: http://dx.doi.org/10.1016/j.cma.2005.04.009. URL http://www.sciencedirect.com/science/article/pii/S0045782505001568.

Ezequiel J. López, Norberto M. Nigro, Sofía S. Sarraf, and Santiago Márquez Damián. Stabilized finite element method based on local preconditioning for unsteady compressible flows in deformable domains with emphasis on the low mach number limit application. *International Journal for Numerical Methods in Fluids*, 69(1):124–145, 2012. ISSN 1097-0363. doi: 10.1002/fld.2547. URL http://dx.doi.org/10.1002/fld.2547.

Hong Luo, JosephD. Baum, and Rainald Löhner. A fast, matrix-free implicit method for compressible flows on unstructured grids. In Charles-Henri Bruneau, editor, *Sixteenth International Conference on Numerical Methods in Fluid Dynamics*, volume 515 of *Lecture Notes in Physics*, pages 73–78. Springer Berlin Heidelberg, 1998. ISBN 978-3-540-65153-6. doi: 10.1007/BFb0106564. URL http://dx.doi.org/10.1007/BFb0106564.

J. F. Lynn. *Multigrid solution of the Euler equations with local preconditioning*. PhD thesis, University of Michigan, 1995.

J. F. Lynn and B. van Leer. Multi-stage schemes for the Euler and Navier-Stokes equations with optimal smoothing. *AIAA Paper 93-3355-CP*, 1993.

G. I. Marchuk. *Numerical Methods in Weather Prediction*. Academic Press, 1974.

S. Marras. *Variational multiscale stabilization of finite and spectral elements for dry and moist atmospheric problems*. PhD thesis, Universitat Politècnica de Catalunya, Barcelona, Spain, 2012.

Simone Marras, Margarida Moragues, Mariano Vázquez, Oriol Jorba, and Guillaume Houzeaux. 3D simulations of convective storms using finite elements with variational multiscale stabilization. In *Proceedings: Solution of Partial Differential Equations on the Sphere Workshop (AMMW02), Newton Institute for Mathematical Science*, Cambridge, UK, 2012.

Simone Marras, Margarida Moragues, Mariano Vázquez, Oriol Jorba, and Guillaume Houzeaux. A variational multiscale stabilized finite element method for the solution of the Euler equations of nonhydrostatic stratified flows. *Journal of Computational Physics*, 236:380 – 407, 2013a. ISSN 0021-9991. doi: http://dx.doi.org/10.1016/j.jcp.2013.06.006.

Simone Marras, Margarida Moragues, Mariano Vázquez, Oriol Jorba, and Guillaume Houzeaux. Simulations of moist convection by a variational multiscale stabilized finite element method. *Journal of Computational Physics*, 252:195 – 218, 2013b. ISSN 0021-9991. doi: http://dx.doi.org/10.1016/j.jcp.2013.06.006.

Simone Marras, James F. Kelly, Margarida Moragues, Andreas Müller, Michal A. Kopera, Mariano Vázquez, Francis X. Giraldo, Guillaume Houzeaux, and Oriol Jorba. A review of element-based Galerkin methods for numerical weather prediction: Finite elements, spectral elements, and discontinuous Galerkin. *Archives of Computational Methods in Engineering*, pages 1–50, 2015. ISSN 1134-3060. doi: 10.1007/s11831-015-9152-1. URL http://dx.doi.org/10.1007/s11831-015-9152-1.

C. L. Merkle and M. Athavale. Time-accurate unsteady incompressible flow algorithms based on artificial compressibility. *AIAA Paper 87-1137*, 1987.

M. Moragues, M. Vázquez, and G. Houzeaux. Variational multiscale stabilization method for compressible flow. In *Proceedings: Argentinian Congress on Computational Mechanics*, Buenos Aires, Argentina, 2010a.

M. Moragues, M. Vázquez, G. Houzeaux, and R. Aubry. Variational multiscale stabilization of compressible flows in parallel architectures. In *Proceedings: Int. Conf. on Parallel CFD*, Kaoshiung, Taiwan, 2010b.

M. Moragues, M. Vázquez, and G. Houzeaux. Variational multiscale stabilization of compressible Navier-Stokes equations. In *Proceedings: Finite Elements in Flow Problems FEF*, Munich, Germany, 2011.

M. Moragues, M. Vázquez, and G. Houzeaux. Preconditioned VMS for compressible flow I: steady problems. In *Proceedings: ECCOMAS CFD Conference*, Barcelona, Spain, 2014a.

M. Moragues, M. Vázquez, and G. Houzeaux. Preconditioned VMS for compressible flow II: transient problems. In *Proceedings: ECCOMAS CFD Conference*, Barcelona, Spain, 2014b.

M. Moragues, G. Bernardino, M. Vázquez, and G. Houzeaux. Fourier stability analysis and local Courant number of the preconditioned variational multiscale stabilization (P-VMS) for Euler compressible flow. Accepted for publication at Computer Methods in Applied Mechanics and Engineering, 2015.

M. Moragues, M. Vázquez, G. Bernardino, and G. Houzeaux. Preconditioned VMS for compressible flow. In *Proceedings: Platform for advanced Scientific Computing Conference PASC*, Zurich, Switzerland, 2015.

M. Moragues, M. Vázquez, and G. Houzeaux. Local preconditioning and variational multiscale stabilization for Euler compressible steady flow. Submitted at Computer Methods in Applied Mechanics and Engineering, 2015.

Margarida Moragues, Simone Marras, Mariano Vázquez, and Guillaume Houzeaux. A variational multiscale stabilized finite element method to solve the Euler equations for nonhydrostatic stratified benchmarks. In *Proceedings: Solution of Partial Differential Equations on the Sphere Workshop (AMMW02), Newton Institute for Mathematical Science*, Cambridge, UK, 2012.

N. Nigro, M. Storti, S. Idelsohn, and T. Tezduyar. Physics based GMRES preconditioner for compressible and incompressible Navier-Stokes equations. *Computer Methods in Applied Mechanics and Engineering*, 154(3-4):203–228, 1998. ISSN 0045-7825. doi: http://dx.doi.org/10.1016/S0045-7825(97)00129-1. URL http://www.sciencedirect.com/science/article/pii/S0045782597001291.

Hilde Ouvrard, Bruno Koobus, Alain Dervieux, and Maria Vittoria Salvetti. Classical and variational multiscale LES of the flow around a circular cylinder on unstructured grids. *Computers & Fluids*, 39(7):1083 – 1094, 2010. ISSN 0045-7930. doi: http://dx.doi.org/10.1016/j.compfluid.2010.01.017. URL http://www.sciencedirect.com/science/article/pii/S0045793010000319.

G.G. O'Brien, M.A. Hyman, and S. Kaplan. A study of the numerical solution of partial differential equation. *Journal of Mathematics and Physics*, 29(4):223–249, 1950.

N. A. Pierce and GilesM. B. Preconditioning compressible flow calculations on stretched meshes. *AIAA Paper 96-0889*, 1996.

V. Puzyrev, J. Koldan, J. de la Puente, G. Houzeaux, M. Vázquez, and J.M. Cela. A parallel finite-element method for three-dimensional controlled-source electromagnetic forward modelling. *Geophysical J. Int.*, 193(2):678–693, 2013.

A. Quarteroni and A. Valli. *Numerical Approximation of Partial Differential Equations*. Springer, 1994.

M. Restelli. *Semi-Lagrangian and semi-implicit discontinuous Galerkin methods for atmospheric modeling applications*. PhD thesis, Politecnico di Milano, March 2007.

F. Rispoli and R. Saavedra. A stabilized finite element method based on SGS models for compressible flows. *Comput. Methods Appl. Mech. and Engrg.*, 196:652–664, 2006.

F. Rispoli, R. Saavedra, A. Corsini, and T. E. Tezduyar. Computation of inviscid compressible flow with V-SGS stabilization and $YZ\beta$ shock capturing. *Int. J. Numer. Methods Fluids*, 54:695–706, 2007.

A. Robert. Bubble convection experiments with a semi-implicit formulation of the euler equations. *J. Atmos. Sci.*, 50:1865–1873, 1993.

R. Rotunno, J B. Klemp, and M L. Weisman. A theory for strong, long-lived squall lines. *J. Atmos. Sci.*, 45:463–485, 1988.

C. Samaniego, G. Houzeaux, E. Samaniego, and M. Vázquez. Parallel embedded boundary methods for fluid and rigid-body interaction. *Comp. Meth. Appl. Mech. Eng.*, 290: 387–419, 2015.

V. Schmitt and F. Charpin. Pressure Distributions on the ONERA-M6-Wing at Transonic Mach Numbers. *AGARD Advisory Report No. 138, Experimental data base for computer program assessment by Fluid Dynamics Panel, Working Group 04*, 1979.

F Shakib, T J R Hughes, and Z Johan. A new finite element formulation for computational fluid dynamics: X. the compressible Euler and Navier-Stokes equations. *Comput. Methods Appl. Mech. Engrg.*, 89:141–291, 1991.

C. Sheng. A preconditioned arbitrary mach number scheme applied to rotating machinery. In Hyoung Woo Oh (Ed.), editor, *Computational Fluid Dynamics*, pages 363 – 390. InTech, Croatia, 2010.

T. Simons. A three-dimensional spectral prediction equation. *J. Atmos. Sci.*, 127:1–27, 1968.

R. B. Smith. The influence of mountains on the atmosphere. *Advances in Geophysics*, 21:87–230, 1979.

G. A. Sod. A survey of several finite difference methods for systems of nonlinear hyperbolic conservation laws. *Journal of Computational Physics*, 27(1):1–31, 1978.

S. Soong and Y. Ogura. A comparison between axisymmetric abd slab0symmetric cumulus cloud models. *J. Atmos. Sci.*, 30:879–893, 1973.

I. Stewart. *Galois Theory*. Chapman & Hall Mathematics, 3rd edition, 1994.

J. Straka, R. Wilhelmson, L. Wicker, J. Anderson, and K. Droegemeier. Numerical solution of a nonlinear density current: a benchmark solution and comparisons. *Int. J. Num. Meth. in Fluids*, 17:1–22, 1993.

Tayfun E. Tezduyar and Masayoshi Senga. Stabilization and shock-capturing parameters in SUPG formulation of compressible flows. *Computer Methods in Applied Mechanics and Engineering*, 195(13-16):1621 – 1632, 2006. ISSN 0045-7825. doi: http://dx.doi.org/10.1016/j.cma.2005.05.032. URL http://www.sciencedirect.com/science/article/pii/S0045782505002999. A Tribute to Thomas J.R. Hughes on the Occasion of his 60th Birthday.

E. Turkel. Symmetrization of the fluid dynamic matrices with applications. *Mathematics of Computation*, 27(124):729–736, 1973.

E. Turkel. Preconditioned methods for solving the incompressible and low speed compressible equations. *Journal of Computational Physics*, 72:277–298, 1987.

E. Turkel. Review of preconditioning methods for fluid dynamics. *Applied Numerical Mathematics*, 12(1–3):257 – 284, 1993. ISSN 0168-9274. doi: http://dx.doi.org/10.1016/0168-9274(93)90122-8. URL http://www.sciencedirect.com/science/article/pii/0168927493901228. Special Issue.

Eli Turkel and Veer N. Vatsa. Local preconditioners for steady and unsteady flow applications. *ESAIM: Mathematical Modelling and Numerical Analysis*, 39:515–535, 5 2005. ISSN 1290-3841. doi: 10.1051/m2an:2005021. URL http://www.esaim-m2an.org/article_S0764583X0500021X.

F. van der Bos, J. J. van der Vegt, and B. J. Geurts. A multiscale formulation for compressible turbulent flow suitable for general variational discretization techniques. *Comput. Methods Appl. Mech. Engrg.*, 196:2863–2875, 2007.

B. van Leer, W. Lee, and P. Roe. Characteristic time-stepping or local preconditioning of the Euler equations. *AIAA Paper*, 91-1552, 1991.

M. Vázquez. *Numerical modeling of compressible laminar and turbulent flow: the characteristic based split (CBS) finite element general algorithm.* PhD thesis, Universitat Politècnica de Catalunya, Barcelona, Spain, 1998.

M. Vázquez, M. Moragues, G. Houzeaux, R. Aubry, and S. Marras. Variational multiscale method for compressible flows. In *Proceedings: ECCOMAS CFD Conference*, Lisbon, Portugal, 2010.

M. Vázquez, G. Houzeaux, S. Koric, A. Artigues, J. Aguado-Sierra, R. Arís, D. Mira, H. Calmet, F. Cucchietti, H. Owen, A. Taha, E. Dering Burness, J. M. Cela, and M. Valero. Alya: Multiphysics engineering simulation towards exascale. *J. Computational Science*, Submitted, 2015a.

M. Vázquez, M. Pérez, M. Moragues, and G. Houzeaux. Parallel monolithic implicit solver for compressible flows. In *Proceedings: PANACM Conference*, Buenos Aires, Argentina, 2015b.

R. Vichnevetsky and J. B. Bowles. *Fourier Analysis of Numerical Approximations of Hyperbolic Equations.* SIAM Studies in Applied Mathematics 5, 1st edition, 1982.

D. Vigneron, G. Deliége, and J.-A. Essers. Low mach number local preconditioning for unsteday viscous finite volumes simulations on 3d unstructured grids. In E. Oñate P. Wesseling and J. Périaux (Eds), editors, *Proceedings of the European Conference on Computational Fluid Dynamics ECCOMAS CFD*, Delft, The Netherlands, 2006.

Mariano Vázquez, Simone Marras, Margarida Moragues, Oriol Jorba, Guillaume Houzeaux, and Romain Aubry. A massively parallel variational multiscale FEM scheme applied to nonhydrostatic atmospheric dynamics. In *Proceedings: EGU Annual Meeting, EGU-2010-9060*, Vienna, Austria, 2010.

X. Wang. *A Preconditioned Algorithm for Turbomachinery Viscous Flow Simulation.* PhD thesis, Mississippi State University, 2005.

C .E. Wasberg, T. Gjesdal, B. A. P. Reif, and Ø. Andreassen. Variational multiscale turbulence modelling in a high order spectral element method. *Journal of Computational Physics*, 228:7333–7356, 2009.

J. M. Weiss and W. A. Smith. Preconditioning applied to variable and constant density flows. *AIAA Journal*, 33(11):2050–2057, 1995.

O. Zienkiewicz, K. Morgan, B. Satya Say, R. Codina, and M. Vázquez. A general algorithm for compressible and incompressible flow - Part II. tests on the explicit form. *Int. J. Numer. Meth. Fluids*, 20:887–913, 1995.